UNIVERSITY OF SÃO PAULO
ESCOLA POLITÉCNICA

Reinaldo Chen

Design of reinforced concrete structures based on three-dimensional stress fields

São Paulo
2024

Reinaldo Chen

Design of reinforced concrete structures based on three-dimensional stress fields

Versão corrigida

Tese apresentada à Escola Politécnica da Universidade de São Paulo para a obtenção do título de Doutor em Ciências.

Área de Concentração:
Engenharia de Estruturas

Orientador:
Prof. Dr. Túlio Nogueira Bittencourt

São Paulo
2024

Este exemplar foi revisado e corrigido em relação à versão original, sob responsabilidade única do autor e com a anuência de seu orientador.

São Paulo, 05 de agosto de 2024.

gov.br Documento assinado digitalmente
REINALDO CHEN
Data: 04/08/2024 23:43:17-0300
Verifique em https://validar.iti.gov.br

Assinatura do autor: ______________________

gov.br Documento assinado digitalmente
TULIO NOGUEIRA BITTENCOURT
Data: 06/08/2024 17:58:07-0300
Verifique em https://validar.iti.gov.br

Assinatura do orientador ______________________

Catalogação-na-publicação

Chen, Reinaldo
Dimensionamento de estruturas de concreto armado baseado em campos de tensão tridimensionais / R. Chen -- versão corr. -- São Paulo, 2024.
241 p.

Tese (Doutorado) - Escola Politécnica da Universidade de São Paulo. Departamento de Engenharia de Estruturas e Geotécnica.

1.Concreto armado 2.Elementos sólidos 3.Dimensionamento 4.Campos de tensão tridimensionais 5.Sólidos 3D I.Universidade de São Paulo. Escola Politécnica. Departamento de Engenharia de Estruturas e Geotécnica II.t.

Acknowledgements

I would like to thank Professor Túlio Nogueira Bittencourt for his supervision and advice, and for providing the structure of the laboratory for the research.

I am especially grateful to Professor João Carlos Della Bella for the continued support and guidance, from my very first class of reinforced concrete back in 1998 until the final draft of this work. For the long hours of supervision with intellectual generosity, patience, and kindness.

I gratefully acknowledge the help of Marina Vendl for programming the application for the automatic design used in this dissertation, Bárbara Yano for sharing her international experience as a structural designer, Daniel Della Bella for the support with the figures, and the colleagues at the laboratory - Ruan for his readiness to help with the lab issues, and Nathanaell for his improvements in the text and support with the mathematics.

I thank Marcio Cardoso and João Victor with whom I could always share the difficulties during the program and find words of understanding and encouragement.

I express my gratitude to Ivan Mazzela for sharing his experience as a doctoral candidate and for assisting me, along with Daniel Di Carlo, Carlos Augusto Campanhã and José Carlos Andrade, in reconciling studies and professional work.

I thank Alberto Ngai and Natália Simoni for their advice and support. I thank Tara Brabazon for the numerous vlogs available on the Internet, which helped me understand formal and practical aspects of a doctoral program.

Finally, I am grateful to my parents Chen Yin Chun and Anita for their loving support and prayers.

“The righteous will live by faith.” (Romans 1:17, New International Version)

Resumo

CHEN, Reinaldo. **Dimensionamento de estruturas de concreto armado baseado em campos de tensão tridimensionais**. 2024. 241 p. Tese (Doutorado em Engenharia de Estruturas) – Escola Politécnica, Universidade de São Paulo, São Paulo, 2024.

O dimensionamento de peças de concreto armado em relação ao Estado Limite Último geralmente é realizado por meio de análises de modelos estruturais compostos por elementos unidimensionais (barras), bidimensionais (cascas) ou tridimensionais (sólidos). Quando elementos sólidos são utilizados na análise estrutural, as solicitações na estrutura são fornecidas através de tensores de tensões com seis componentes (σ_x, σ_y, σ_z, τ_{xy}, τ_{xz}, τ_{yz}). Essa tese revisita o método de dimensionamento denominado Método do Campo de Tensões (MCT), que combina análise linear e dimensionamento limite ponto-a-ponto através de um mecanismo resistente já estabelecido na literatura. A análise linear determina as tensões solicitantes na estrutura, enquanto a análise limite calcula a armadura necessária para equilibrar as tensões solicitantes e verifica o concreto contra o esmagamento. A tese apresenta duas principais contribuições originais ao conhecimento: (1) deduz analiticamente e interpreta fisicamente as equações do mecanismo resistente em uma nova abordagem, organizando-as em quatro casos de acordo com as tensões internas mobilizadas no concreto; (2) aplica o MCT para o dimensionamento de peças estruturais reais, desde a fase inicial da análise estrutural até o detalhamento final das armaduras em arranjos construtivos. As soluções obtidas pelo MCT são avaliadas por análises não-lineares que confirmam a sua segurança em relação ao estado limite último, e mostram seu desempenho em serviço melhorado em comparação com soluções obtidas por métodos de dimensionamento alternativos. O MCT pode ser aplicado de modo efetivo e prático para o dimensionamento de uma ampla gama de estruturas, sendo mais adequado para aquelas com geometria e carregamentos complexos.

Palavras-chave: Concreto armado. Elementos sólidos. Dimensionamento. Campos de tensão tridimensionais. Sólidos 3D.

Abstract

CHEN, Reinaldo. **Design of reinforced concrete structures based on three-dimensional stress fields**. 2024. 241 p. Tese (Doutorado em Engenharia de Estruturas) – Escola Politécnica, Universidade de São Paulo, São Paulo, 2024.

The Ultimate Limit State design of reinforced concrete members usually derives from linear elastic analyses of models composed of linear (bars), surface (shell), and volume (three-dimensional solid) elements. When solid elements are used in the structural analysis, the action effects are provided point-to-point within the structural model as a stress tensor with six stress components (σ_x, σ_y, σ_z, τ_{xy}, τ_{xz}, τ_{yz}). This dissertation revisits the design method denoted herein as the Stress Field Method (SFM), which combines linear analysis and point-to-point limit design through a resisting mechanism that is already established in the literature. Linear analysis determines the action effects throughout the structure, while limit design calculates the required reinforcement to equilibrate these effects and checks concrete against crushing. The dissertation presents two main original contributions to the knowledge: (1) it analytically deduces and physically interprets the design equations of the resisting mechanism in a new approach, organizing them into four well-delimited cases according to the internal stresses mobilized in the concrete; (2) it applies the SFM to the design of real structural members, from the very initial phase of structural analysis to the final detailing of the reinforcement into constructive arrangements. The SFM solutions are assessed by nonlinear analyses to confirm their safety in Ultimate Limit State, and to show their improved performance in serviceability states over solutions obtained from alternative design methods. The SFM can be effectively and practically applied to the design of a wide range of structures, being more suitable for those with complex geometries and loadings.

Keywords: Reinforced concrete. Solid elements. Design. Three-dimensional stress field. 3D solids.

List of figures

List of abbreviations and acronyms

1D	one-dimensional
2D	two-dimensional
3D	three-dimensional
ABNT	Associação Brasileira de Normas Técnicas
ACI	American Concrete Institute
C	column
CEB	Comité Euro-Internationale du Béton
CEN	European Commission for Normalization
EC2	Eurocode 2
FEM	finite element method
fib	Fédération Internationale du béton (created from the merger of CEB and FIP)
FIP	Fédération Internationale de la Précontrainte
LoA	level of approximation
MC	Model Code
MCFT	modified compression field theory
mnt.	monitor
MPa	megapascal
MCT	método do campo de tensões (stress field method)
NLFEA	nonlinear analysis finite element analysis
P	pile
reinf.	reinforcement
rhs	right -hand side
SecM	sectional method
SFM	stress field method
SLA	sequentially linear analysis
SLS	serviceability limit state
STM	strut-and-tie method
ULS	ultimate limit state
(C)	compression
(T)	tension

List of symbols

<u>*Roman letters and symbols*</u>

A_c	area of the concrete cross section
$A_{c.ef}$	effective area of concrete in tension
a_g	maximum aggregate size
a_{si}	area of the reinforcement in the cross section ($i = x, y, z$)
c	cohesion, concrete cover
E_c	modulus of elasticity of concrete
E_s	modulus of elasticity of reinforcement steel
f_A	separation strength
f_c	concrete compressive strength
f_{c0}	concrete compressive elastic limit
$f_{c,ef}$	effective strength of concrete
f_{cm}	concrete uniaxial compressive strength
f_{cp}	plastic strength of concrete
f_{ctd}	design value of the concrete tensile strength
f_{ctm}	concrete tensile strength
f_d	design values of actions, material properties, geometrical quantities, and variables which account for the model uncertainties
f_{sy}	reinforcement yield stress
$[f_t]$	equivalent reinforcement stress tensor
f_t	concrete tensile strength
f_{tx}, f_{ty}, f_{tz}	equivalent reinforcement stresses in the x-, y- and z-direction
f_{yd}	design yield strength of reinforcement bars
G_c	concrete shear modulus
G_f	fracture energy
I_1, I_2, I_3	first, second, and third invariants of the applied stresses, respectively
I_{c1}, I_{c2}, I_{c3}	first, second, and third invariants of the concrete stresses, respectively
J_2	second deviatoric stress invariant
k	parameter considering the influence of concrete cover (in $\ell_{s,max}$ calculation)
k	parameter describing a modified Coulomb material; strength ratio
k_1, k_2, k_3	coefficients multiplying concrete stresses
ℓ_1, m_1, n_1	components of $\overrightarrow{n_{c1}}$
ℓ_2, m_2, n_2	components of $\overrightarrow{n_{c2}}$
ℓ_3, m_3, n_3	components of $\overrightarrow{n_{c3}}$
$\ell_{s,max}$	transfer length
L_c, L_t	crack band size in compression and tension, respectively
M_x, M_y, M_{xy}	bending and torsional moments
n_{ci}	direction cosines of the concrete stress tensor ($i = 1, 2, 3$)
$\overrightarrow{n_{ci}}$	normal of the plane where σ_{ci} acts ($i = 1, 2, 3$); crack direction
N_x, N_y, N_{xy}	axial and in-plane shear forces for shell elements
N_x, V_x, V_y	axial and transverse shear forces for linear elements
p	auxiliary stress variable
P_d	design resistance
P_u	ultimate load
s	crack spacing
$s_{r,max}$	maximum crack spacing

$\mathrm{sgn}(\tau)$	sign of the shear stress components $\mathrm{sgn}(\tau) = \mathrm{sgn}(\tau_{xy}, \tau_{xz}, \tau_{yz})$
w	crack width calculated from the crack band theory
w_c	crack opening at the complete release of stress
w_d	design crack width
W_d	plastic displacements corresponding to the equivalent plastic strains
w_i	mean crack width in the principal direction i
x, y, z	rectangular coordinate system

Greek symbols

α, β', λ	material parameters
α_e	modular ratio
δ_i	enclosed angle between the principal direction of the applied stresses and those of the concrete stresses
$\varepsilon_{\perp}, \varepsilon_{c,\perp}$	mean strain and the mean concrete strain
ε_{c0}	concrete strain corresponding to the peak stress
ε_{cm}	average concrete strain within $\ell_{s,max}$
ε_{cs}	concrete strain due to shrinkage
ε_{cp}	concrete plastic strain at compressive strength
ε_{cu}	concrete maximum strain
ε_f	strains in concrete in tension due to microcracking
$\varepsilon_{ij}^{\,e}$	elastic strain component
$\varepsilon_{ij}^{\,f}$	fracturing strain component
$\varepsilon_{ij}^{\,p}$	plastic strain component
ε_{sm}	average steel strain within $\ell_{s,max}$
ε_{sy}	reinforcement yield strain
ε_t	concrete strain at tension strength
$\varepsilon_x, \varepsilon_y$	strain in the reinforcement directions
η_{fc}	factor accounting for brittleness of concrete in compression
η_ε	factor accounting for softening of concrete compression
μ	frictional coefficient
ν	factor modifying concrete strength (effectiveness factor); Poisson´s ratio
$\rho_{s,ef}$	effective reinforcement ratio
$\rho_{sx}, \rho_{sy}, \rho_{sz}$	reinforcement ratio in the x-, y- and z-direction
σ	normal stress
$\sigma_1, \sigma_2, \sigma_3$	applied principal stresses
$\sigma_{c1}, \sigma_{c2}, \sigma_{c3}$	concrete principal stresses
$\sigma_{cx}, \sigma_{cy}, \sigma_{cz}$	concrete stresses in the x-, y- and z-direction
σ_s	steel stress in a crack
σ_{si}	maximum tensile stress in any layer of the reinforcing steel
σ_{sr}	maximum steel stress in a crack
$\sigma_x, \sigma_y, \sigma_z$	applied normal stresses in the x-, y- and z-direction
$[\sigma]$	applied stress tensor (matrix characterizing the stress state in a point)
$[\sigma_c]$	concrete stress tensor
τ	shear stress
τ_1, τ_2, τ_3	smallest, intermediate, and largest absolute value of shear stress components
τ_{bms}	mean bond strength
τ_{ij}	maximum shear stress developed in a crack due to aggregate interlock
$\tau_{xy}, \tau_{xz}, \tau_{yz}$	applied shear stress components
φ	angle of friction
ϕ	diameter of reinforcing bars

Contents

1 Introduction

1.1 Design methods for reinforced concrete structures

Reinforced concrete members are usually designed by methods combining linear elastic structural analysis and plastic design. While the structural analysis assuming linear elastic material behavior determines the action effects on the whole or parts of the structure, the plastic design allows for quantifying reinforcement and concrete requirements.

Structures may be idealized and modeled by the composition of linear elements (1D bars), surface elements (2D membranes, plates or shells) or volume elements (3D solids) for the structural analysis. For linear elements, action effects are given as six sectional force components (axial and shear forces N_x, V_x, V_y; bending and torsional moments M_x, M_y, M_{xy}); for surface elements, as eight sectional force components (axial and in-plane shear forces N_x, N_y, N_{xy}; bending and torsional moments M_x, M_y, M_{xy}; transverse shear V_x, V_y); for volume elements, as a stress tensor with six stress components (normal stresses σ_x, σ_y, σ_z; shear stresses τ_{xy}, τ_{xz}, τ_{yz}).

Design is then performed by subdividing the structure into individual structural members and connecting areas: the Bernoulli regions (B-regions), where sections remain approximately plane after loading, and the disturbed regions (D-regions), where the assumption that the sections remain plane after deformation is no longer valid. For *B-regions* of individual members such as beams, columns, piles, slabs and walls, design relies on well-established methods for analyzing sectional forces. For *simple D-regions* such as frame corners, slabs with openings, shear walls, corbels and regular pile caps, design is usually developed based on strut-and-tie models.

For *complex D-regions*, which include the whole or parts of structures with complex geometry and/or complex loadings such as multiple-pile caps, hydroelectric facilities including spillways, powerhouses and intake structures, and bridge anchor blocks, however, design is carried out with more difficulty. Design may be performed by the strut-and-tie method, nonlinear analysis methods, or a method based on three-dimensional elastic stress fields. Each design method is discussed as follows.

Design based on strut-and-tie models

The strut-and-tie method (STM) idealizes the structure as an assembly of one-dimensional struts representing concrete in compression, and one-dimensional ties representing reinforcement in tension. It more commonly derives from the combination of elastic analysis (determining the applied forces) and plastic design (quantifying materials by assuming rigid-plastic material behavior).

Numerous references in the literature guide the application of the STM by practical recommendations and worked examples applying the method to the design of real members (SCHLAICH; SCHAFER, 1984; FIP, 1999; REINECK, 2002; REINECK; NOVAK, 2010; *fib*, 2011, 2021). However, applying the STM to complex structures is not straightforward and may be restricted due to practical limitations: (i) multiple models can, theoretically, be developed for a single given loading, and the more complex the structure, the more difficult it is to develop strut-and-tie models. As noted by Schlaich, Schäfer and Jennewein (1987, p.95): “Doubts could arise, however, as to whether the correct model has been chosen out of several possible ones”; (ii) numerous models are required for the comprehensive design of a member since all relevant design situations and loading cases must be considered, and ST models are unique for each load case of the structure; (iii) it is mandatory to ensure the deformation capacity of the designed member, such that the idealized flow of forces in a proposed model can be in fact be attained; and (iv) it is also mandatory to check the strength of all nodes within the model.

In practice, those limitations are usually tackled by general practices: building models as the composition of existing simpler models; recurring to superposition of models; searching for models that minimize the strain energy; reducing the number of developed models by identifying envelope loadings for representative behaviors; providing a minimum amount of reinforcement to allow for the ductility of the structure so that plastic stress redistribution can effectively occur. Still, solutions may fail to represent the actual response of concrete (LOURENÇO et al., 2023, p. 3761). Application of the STM may incur an inaccurate design of the structural member: “if the orientation of the model varies significantly from the actual stress field, then the structure must undergo substantial deformation in order to develop the poorly assumed model” (REINECK; NOVAK, 2011, p. 1-4); also, if critical load scenarios cases are mistakenly disregarded, an unsafe solution will be achieved.

Design based on nonlinear analysis

Nonlinear finite element analysis (NLFEA) offers an advanced approach for designing reinforced concrete members, beyond the capabilities of the STM. It builds on numerical models that satisfy equilibrium of forces, compatibility of displacements and nonlinear constitutive laws describing the material behavior, and implements an incremental and iterative procedure to analyze the structural behavior.

Full nonlinear analyses are acknowledged by normative codes for the design of new structures: EC2 (2004, Section 5.7) directly states that nonlinear methods of analysis may be used for both ultimate and serviceability verifications; MC2010 (2013, Section 3.1.2) associates it to the highest order level-of-approximation approach but only advises its use "for the final design of very complex structures or for the assessment of critical existing structures". However, true nonlinear analyses are still rarely applied to the design of new structures due to four main reasons: (i) the complexity of the analyses, that require "high-level expertise, and intensive modelling and interpretation time" (*fib*, 2021, p. 76); (ii) they rely on the input of complex material parameters, which may significantly affect the results; (iii) they require specialized and expensive software, which is usually only affordable to few universities and design offices; (iv) they also require the definition of the reinforcement layout, which is unknown in the design phase, as an input parameter. All those aspects render nonlinear analyses as a tool for the assessment of existing structures or solutions (with a predetermined concrete geometry and reinforcement detailing), rather than for ULS design.

Design based on three-dimensional elastic stress fields

As an alternative to the aforementioned design approaches for complex D-regions, a method based on *three-dimensional elastic stress fields* and limit design stands out for its simplicity and efficiency; herein, it is denoted simply as the *stress field method* (SFM[1]). Linear analysis assumes constant uncracked concrete stiffness to determine the action effects over the structure and does not require information about reinforcement quantities and arrangements, which are not known at the beginning of the design process, as an input parameter; it can be performed by numerous types of finite element software analyzing structural models composed of solid elements. Limit design, in turn, proportionates concrete and reinforcement in the resistant mechanism equilibrating the applied stress tensors. The SFM brings the immediate advantage of neither requiring the elaboration of numerous models, as in the STM, nor the performance of complex nonlinear analyses. It is the object of this dissertation.

[1] The design method for reinforced concrete structures combining linear analysis and plastic design has not yet been given a formal name and abbreviation in the literature. Throughout the dissertation, it will be referred to simply as the stress field method (SFM). Distinction between the SFM object of this dissertation and the SFM associated with the STM shall be automatically implied.

1.2 Design method based on three-dimensional elastic stress fields

The text presented in this sub-section is reproduced from Chen, Bittencourt and Della Bella (2023b). It presents the literature review for the SFM.

A concrete structure may be idealized from the composition of linear (bars), shell (membranes, plates, and shells), and solid elements. The utilization of finite solid elements may be justified when designing structural members with complex geometry and loadings such as those comprising industrial or hydraulic facilities (Figure 1), for which the application of unidimensional or bidimensional elements turns out to be insufficient to capture the load path within the structure. A linear analysis may be performed to determine the internal stress distribution throughout the three-dimensional structure for the ultimate limit state design, according to design codes (ACI 318, 2014; EC2, 2004; *fib* MC 2010, 2013; NBR-6118, 2023). The stress field obtained from the analysis consists of six stress components at each integration point of the solid elements comprising the structural model. Limiting state conditions are not directly expressed in terms of sectional forces, and the problem of dimensioning the required reinforcement and checking concrete in the presence of the applied stresses is then posed.

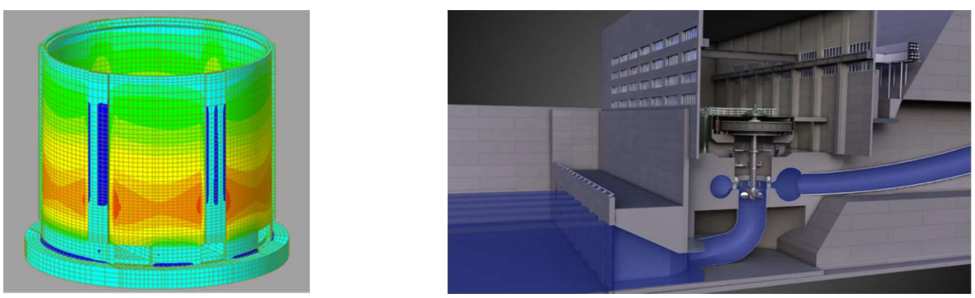

(a) (b)

Source: (a) Dianafea (2017); (b) Wikimedia Commons (2022).

Figure 1 – Finite solid element models for: (a) clinker storage silo of the Ramliya Cement Plant; (b) a concrete hydroelectric structure.

A solution for the design would be to provide reinforcement to resist the major principal stress in the principal directions. However, in design practice it is impossible to provide reinforcement following the randomly oriented principal tensile stresses within the structure, even more if it is considered that a structural member is designed for multiple loading conditions. Alternatively, reinforcement could be arranged in three orthogonal directions to resist the major principal tensile stress in the three reinforcement directions. But this solution is also disregarded in design practice since uneconomical layouts would be assuredly attained, especially when crack directions draw close to any of the reinforcement directions. In another attempt, designers utilizes the incomplete method of defining working sections, integrating the normal stress patterns over their surfaces and then calculating the reinforcement from the total sectional forces. For example, de Boer (2010) proposed the so-called "Theory on composing results to lower model type results" where one should proceed to the back-substitution of stresses from a solid model to reference elements: either by integration of stress components along the height of a structure to a bidimensional model at the level of a reference plane (Figure 2a), or by integration of stresses along both height and width of an elected cross-section to a unidimensional model at the level of a reference line (Figure 2b). Dolgikh and Podvysotskii (2011) proposed, independently, the "Method of equivalent shells", which consisted basically in the same procedure as the one proposed by de Boer, and applied it to the design of a concrete spillway (Figure 3). The method of composing results in reference elements, however, has restricted application to members with uniform geometry and loadings, so that a sectional design may effectively be performed. It cannot be applied in discontinuity regions such as joints of frames or zones of application of concentrated loads. As pointed out by Lisichkin (2001, p.116), the results obtained by integration methods are "not rigorous since they did not incorporate either the tangential stresses or the effects of the resistance in the reinforcement to shearing in other directions."

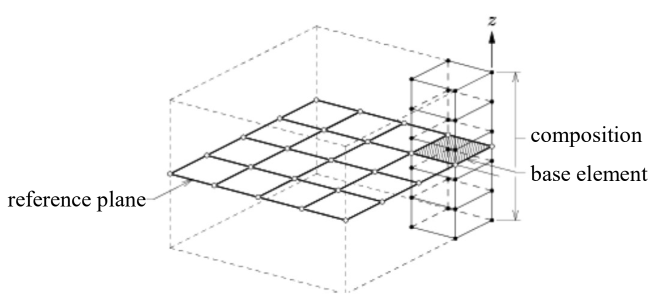

(a)

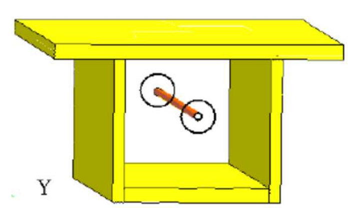

(b)

Source: de Boer (2010).

Figure 2 – Composition of results from solid elements: (a) in a quadrangular reference plane or (b) in a reference line.

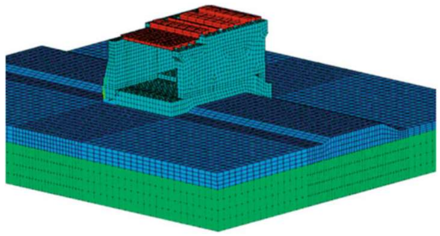

(a)

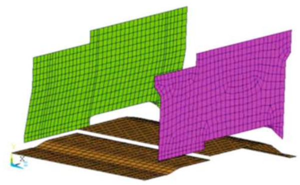

(b)

Source: Dolgikh and Podvysotskii (2011).

Figure 3 – Finite element model for a concrete spillway: (a) with solid elements; (b) with equivalent shell elements.

The solution for the ULS then relied on the definition of a resistant mechanism equilibrating the applied stress tensors. Smirnov (1983), addressed, for the first time, equations for the reinforcement design in concrete solid elements from three-dimensional stress tensors, focusing on the application in hydroelectric structures. Kamezama et al. (1994) proposed additional formulas for the computation of the required reinforcement, but they were still limited to stress combinations yielding reinforcement in three directions. Marti, Mojsilović and Foster (2002) and Foster, Marti and Mojsilović (2003) published two thorough detailed works on the subject, clearly identifying biaxial and uniaxial compression design cases, and graphically representing the solutions with the aid of Mohr circles. Their formulation was later reproduced in the *fib* Bulletin 45 (2008), which was a practical guide to finite element modelling of reinforced concrete structures. In this publication, however, no new information about the subject was brought. Hoogenboom and de Boer (2008, 2010) categorized the solution into three subgroups, namely “corner”, “edge” and “interior solution”, according to the requirement of reinforcement in one, two or three orthogonal directions, respectively. They also implemented this solution in a numerical algorithm searching for the solution that minimized the total required steel. Su et al. (2010) presented a genetic algorithm to examine all possible solutions and to find, among them, the one that provided the optimal reinforcement. Zalesov and Rubin (1994) and Lisichkin (2001) treated the theme with a different approach, where reinforcement incorporated shearing resistance. Since the solution was not analytical, but rather based upon coefficients determined experimentally, the derived equations are not presented in this work. Finally, Nielsen and Hoang (2011) presented the complete formulation in the third edition of the book *Limit Analysis and Concrete Plasticity* – former editions, dated 1984 and 1999, still did not address this theme. The authors brought out the physical interpretation of the applied shear stresses and elegantly deduced analytically the complete set of design formulas. The application of these design formulas, however, relied on three additional variables (the Euler angles) and axes transformations, which brought some complexity for the equations.

1.3 Research questions and original contribution to knowledge

Throughout my 24 years of experience as a reinforced concrete structural engineer, a question has been recurrent: Why are finite solid elements, even though readily available in most finite element software, rarely used in design practice?

Early investigation developed for the research proposal confirmed the existence of a design method for solid elements at a point level, the SFM. The original question, could then be rewritten with more theoretical rigor to constitute the main *research question* of the dissertation: Why is the existing design method based on three-dimensional linear stress fields for reinforced structures rarely used in design practice? Other accompanying questions were: Are there design tools for applying the method? And how good is the solution brought by this method in terms of material efficiency and structural performance?

Four main *gaps in the knowledge* were clearly identified. Two of them regarded the formulation of the resisting mechanisms: (i) the difficulty in handling design equations, mainly when dealing with positive, negative, or absolute values of the shear stress components, and (ii) the difficulty in physically interpreting the design cases. The two other gaps concerned the application of the method: (iii) the lack of research applying the method to the design of complex real structural members, and (iv) the absence of guidelines orienting reinforcement detailing.

This dissertation's original contribution to knowledge is to further extend the design method combining linear analysis and limit design for reinforced concrete structures. First, by deducing and interpreting the design equations of the resisting mechanisms in a novel and simpler approach, at a point level. Second, by applying them to the design of real structural members, from the initial stage of determining the applied stresses to the last stage of reinforcement detailing. The design method, albeit better suited for the design of 3D discontinuity regions or complex structures, is applicable to all reinforced concrete structures. Its disclosure by the new approach is believed to have the potential to simplify the way complex structures are designed and to open new ways of arranging reinforcement.

1.4 Scope

This work presents a ULS design method for reinforced concrete structural members, from the very initial stage of determining the internal applied stresses to the final stage of reinforcement detailing. It encompasses a theoretical part, in which the formulation of the resisting mechanisms for the applied stresses at a point is presented in a new approach, and an application part, whereby the formulation is applied to the design and reinforcement detailing of five structural members. Key aspects of the detailing process are covered, which may orient the detailing of any other structural element.

The design method is based on a *stress-based approach* for designing finite solid elements (3D) discretizing continuum structural volumes, rather than on *force-based approaches* for designing bar elements (1D) and surface elements (2D). Throughout the design process, three simple tools were required: a commercial finite element software to perform linear analyses, a developed application for the automatic point-to-point design, and an opensource software for postprocessing results throughout the structural members.

The dissertation then presents the assessment of the achieved solution by nonlinear numerical simulations to confirm the ultimate state safety of the design and to evaluate the structural performance in both serviceability and design conditions. Complementarily, it compares achieved and traditional alternative design solutions. The choice for numerical nonlinear analyses over laboratory tests or tests of existing structures is justified by their reduced implementation cost, and their capability to simulate large structures and structures with complex geometry and loadings.

This work does not aim at new developments on nonlinear analyses: no new numerical methods, numerical solution strategies, formulation of types of solid elements and material models are proposed. Instead, existing ones are implemented for the specific purpose of assessing the dissertation design method.

The dissertation addresses the SLS design in the context of three-dimensional stress fields. The existing formulation is presented, along with guidance for its implementation; it will be implemented into the automatic design framework in future works.

At the closure of the dissertation, formulation, application, and assessment of the design method are critically reviewed, confirming its strength, importance, and wide range of applicability.

1.5 Organization of chapters

This dissertation reviews, further extends, applies, and critically evaluates the method combining linear analysis and limit design (SFM) for designing reinforced concrete structures. It is organized as follows. Chapter 2 presents the theoretical basis for applying limit analysis to the design of reinforced concrete structures. It identifies the design method object of this dissertation as a lower-bound solution of the theory of plasticity and discusses failure conditions for the resisting materials.

Chapter 3 presents the resisting mechanism for the ULS design for applied stresses at a point in an original approach. The design equations are deduced analytically and organized according to the stresses developed in concrete. Chapter 4, in turn, provides the background for SLS verification when working with stress-based approaches.

Chapter 5 applies the SFM to the ULS design of five structural members. For each of them, concrete is checked against crushing while reinforcement is computed and detailed in constructive arrangement. Chapter 6 assesses by fully nonlinear analyses the solution obtained for the five structural members, whereby information about the load-carrying capacity and structural performance is obtained.

Finally, Chapter 7 summarizes the main aspects of the design method including implementation, strengths, and weaknesses. It also presents guidelines for applying the SFM to design practice and brings suggestions for improvement of normative code sections dealing with 3D solids.

2 Limit analysis for three-dimensional stress fields

Ensuring the safety of structures hinges on accurately defining the load-carrying capacity of their individual elements. Limit analysis is a fundamental tool in this direction, providing information about the strength of rigid-plastic materials. This chapter presents the background and assumptions that identify the SFM as a lower bound solution of limit analysis for designing reinforced concrete structures.

The theory, theorems, and methods of limit analysis, which are credited to Gvozdev (1960), Drucker, Greenberg and Prager (1952), and Sayir and Ziegler (1969), are initially presented in Section 2.1. Failure conditions, essential for the application of limit analysis, are reviewed in Section 2.2, starting from a general theory that is extended sequentially to Coulomb materials, modified Coulomb materials, concrete and reinforced concrete.

The introduction of the modified Coulomb failure criterion for concrete is credited to Chen and Drucker (1969). The application of limit analysis to reinforced concrete, in turn, is attributed to M.P. Nielsen (1978) and B. Thürlimann (1978). It was reviewed and further developed by researchers including Marti (1977, 1980), Kaufmann (1998), Meyboom (2002), Monotti (2004), Larsen (2010) and Braestrup (1994, 2021).

2.1 Plasticity and limit analysis

The theory of plasticity is concerned with the strength and deformation of rigid-plastic materials. A rigid plastic material is idealized as one that remains undeformed until a yield stress is reached, after which deformations can occur without accompanying stress increase. An infinity of strains is therefore compatible with σ_y. The plastic strain rate, $\dot{\varepsilon}$, also referred to as the incremental plastic strain, can be determined for a rigid-plastic structure but specific strain values cannot be calculated. The strength and deformation of a rigid-plastic structure can be described by its yield conditions and the associated flow rule, respectively. The yield conditions describe the stress states at which plastic flow commences, while the flow rule describes the ratios between the plastic rates of the corresponding collapse mechanism (MEYBOOM, 2002).

A body of rigid-plastic material is subjected to a loading that can be carried only by stresses at the yield point; the body is then said to be subjected to *collapse by yielding*. The corresponding load is called the *collapse load* of the body, and the theory of *collapse by yielding* is termed *limit analysis* (NIELSEN, 1984). In the context of this chapter, the term *yield* can be equally used as *rupture* or *failure* when characterizing a *load*, a *surface*, a *condition,* or a *criterion*.

2.1.1 Extremum principles for rigid-plastic materials

The theorems of limit analysis derive from the application of two principles, the principle of virtual work and the principle of maximum energy dissipation, for rigid-plastic bodies. They can be enunciated as follows:

- <u>*Lower bound theorem*</u>: any load corresponding to a statically admissible state of stress distribution within the yield surface is smaller than the ultimate load, that is, it will not be able to cause collapse of the body.
- <u>*Upper bound theorem*</u>: any load resulting from considering a kinematically admissible state of deformation and setting the work done by the external forces equal to the internal energy dissipation is greater than the ultimate load.
- <u>*Uniqueness theorem*</u>: any load for which a complete solution, that is, a statically admissible state of stress everywhere at or below yield and a compatible, kinematically admissible state of deformation can be found, is equal to the ultimate load.

A stress distribution is considered statically admissible if it satisfies both equilibrium and static boundary conditions. A state of deformation is considered kinematically admissible if it satisfies kinematic relations and kinematic boundary conditions.

2.1.2 Limit analysis and design methods

The solution of load-carrying capacity problems in plastic theory can then be divided into two methods, as summarized by Kaufmann (1998, p.35).

The *static method* of theory of plasticity is based on the lower bound theorem. Starting from statically admissible states of stress, one attempts to maximize the associated ultimate load. This method is suitable for design and provides safe solutions for the actual ultimate load. The *kinematic method* of theory of plasticity is based on the upper bound theorem. Starting from kinematically admissible states of deformation or failures mechanisms, one attempts to minimize the associated ultimate load. This method yields unsafe or upper bound solutions for the actual ultimate load.

2.2 Yield conditions

2.2.1 Failure (yield) criteria

A general theory for failure was proposed by Mohr in 1882, who assumed that failure occurs when the stresses in a section satisfy the condition $f(\sigma,\tau) = 0$, where $f(\sigma,\tau)$ is a characteristic function of the material, and where σ and τ are the normal stress and the shear stress, respectively, in the section. Many suggestions have been made for the shape of the Mohr failure envelope, including those proposed by Cowan (1953), Johansen (1958) and Paul (1961). In any case, rupture criteria appear as hypotheses whose application to various materials need to be evaluated from experimental data.

Different failure criteria that do not rely on the absolute values of stresses have been proposed. Some were based on energy considerations or distortion energy. However, the criteria based on the stresses are of particular interest for later application to structural concrete.

2.2.2 Failure (yield) criteria for Coulomb and modified Coulomb materials

Coulomb advanced the frictional hypothesis, by which sliding failure occurs in a section where $|\tau|$ exceeds the *sliding resistance*. The condition for sliding failure is expressed by:

$$|\tau| + \mu\sigma - c = 0 \tag{2.1}$$

where c is the cohesion, μ is the frictional coefficient, and σ is the normal stress perpendicular to the sliding plane, counted negative as a compressive stress. A material that satisfies the sliding failure condition is termed a *Coulomb material*.

For a large group of materials, reasonable failure conditions are attained by combining Coulomb's frictional hypothesis for sliding failure with a bound for the maximum tensile stress in the case of separation failure, known as separation strength f_A. This combination results in the modified Coulomb failure criterion:

$$\begin{cases} |\tau| + \mu\sigma - c = 0 \\ \sigma - f_A = 0 \end{cases} \tag{2.2}$$

A separation failure occurs when the largest principal stress component, σ_1, reaches the separation strength. A material complying with the above criterion is called a *modified Coulomb material*, and the failure criterion is depicted in the σ-τ coordinate system in Figure 4a. When examining the applied stress field at a point, defined by the principal stresses σ_1, σ_2, and σ_3, and represented by the Mohr's circles in Figure 4b, failure will not occur if the circle with diameter

(σ_1 - σ_3) lies within the boundary lines. Alternatively, the sliding criterion in Equation (2.2) can be transformed into relationships between the principal stresses σ_1 and σ_3. From Figure 4c, by projection on one of the lines corresponding to sliding failure:

$$1/2(\sigma_1 - \sigma_3) = c\cos\varphi - 1/2(\sigma_1 + \sigma_3)\sin\varphi \qquad (2.3)$$

Introducing $\mu = tg\ \varphi$ and $k = \left(\mu + \sqrt{1+\mu^2}\right)^2$, where φ is called the angle of friction, the conditions for sliding failure can be written:

$$\begin{cases} k\sigma_1 - \sigma_3 - 2c\sqrt{k} = 0 \\ \sigma_1 - f_A = 0 \end{cases} \qquad (2.4)$$

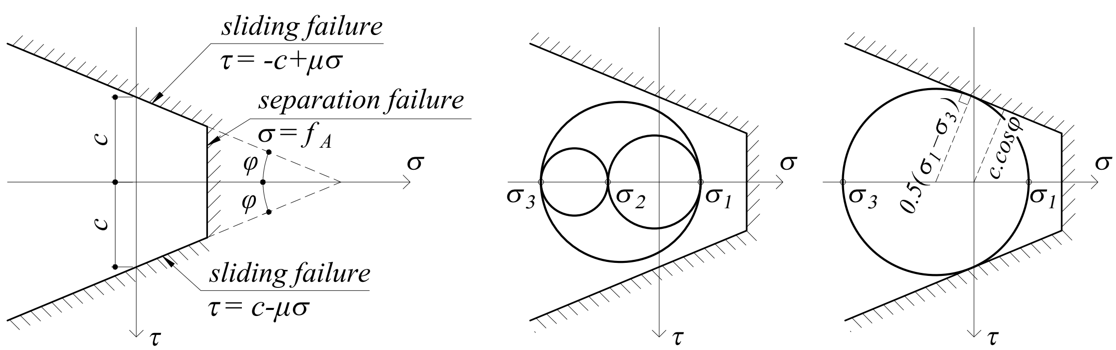

(a) (b) (c)

Source: (a, b) Nielsen (1984); (c) adapted from Nielsen (1984).

Figure 4 – (a) Failure criterion for a modified Coulomb material; (b) Mohr´s circles of principal stresses within the yield lines; (c) Mohr's circle at sliding failure.

2.2.3 Failure (yield) conditions for concrete

Strengths tests of plain concrete are well documented in the literature. To name a few, the reports by Kupfer et al. (1969) on biaxial stresses, and those by Gerstle et al. (1978) on triaxial stresses can be listed. The experimental data indicated the essential features of a failure surface of concrete materials, based on which a variety of failure criteria have been proposed. These models are classified based on the number of material constants appearing in the expression, ranging from one-parameter to five-parameter models.

Low strength concrete can be considered a modified Coulomb material, described by a two-parameter model: parameter k has the value of about 4 corresponding to an angle of friction of $\varphi = 37^{o}$, and a friction coefficient of $\mu = 0.75$ (Nielsen, 1984). The modified Coulomb failure criteria for concrete are then defined in the form of a sliding surface and a separation surface, respectively, as:

$$\begin{cases} 4\sigma_1 - \sigma_3 = f_c \\ \sigma_1 = f_{ct} \end{cases} \tag{2.5}$$

where f_c is the concrete compressive strength, and f_{ct} is the concrete tensile strength. The failure criterion is represented in Figure 5, with dashed lines representing the plane stress field in both σ-τ coordinate system (Figure 5a) and principal stress coordinate system (Figure 5b), forming a hexagon in the latter case.

The criterion adopted for concrete under uniaxial or biaxial compression in this study is the modified Coulomb criterion with a zero-tension cutoff. The tensile concrete strength is conservatively neglected due to its small values compared to the compressive strength, and due to the brittle nature of concrete behavior in tension, which is very distant from the rigid-plastic idealization. The modified criterion is represented graphically in Figure 5, using continuous lines. In the principal stress coordinate system, the hexagon is approximated by a square in the third quadrant since the tensile strength is assumed to be zero (Figure 5b). Concrete is considered to be an isotropic material; the modified Coulomb criterion is thus equally valid in all directions**.**

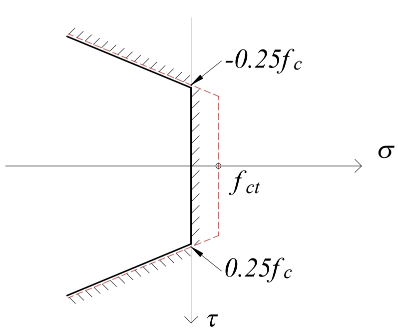

(a)

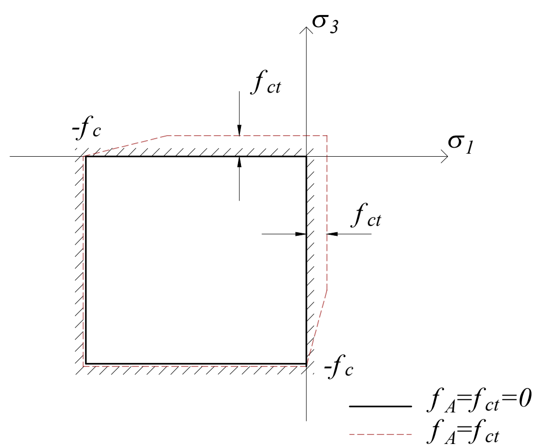

(b)

Source: adapted from Nielsen (1984).

Figure 5 – Modified Coulomb failure critetion for plain concrete: (a) in the σ, τ - coordinate system; (b) in the principal stress space.

The Ottosen four-parameter model, particularly, is the failure criterion for concrete under multiaxial states of stress indicated in both Model Code 90 (CEB-FIP, 1993) and Model Code 2010 (*fib*, 2013). It is valid for normal weight and self-compacting concrete, subjected to monotonic stress increase until failure, and is reproduced below in the MC-90 format:

$$\alpha \frac{J_2}{f_{cm}^2} + \lambda \frac{\sqrt{J_2}}{f_{cm}} + \beta' \frac{I_1}{f_{cm}} - 1 = 0 \tag{2.6}$$

where:

$$\begin{gathered}\lambda = \begin{cases} c_1 \cos\left(1/3 \arccos\left(c_2 \cos 3\theta\right)\right) & \text{for } \cos 3\theta \geq 0 \\ c_1 \cos\left(\pi/3 - 1/3 \arccos\left(-c_2 \cos 3\theta\right)\right) & \text{for } \cos 3\theta < 0 \end{cases} \\ \cos 3\theta = \frac{3\sqrt{3}}{2} \frac{J_3}{J_2^{3/2}} \end{gathered} \tag{2.7}$$

Parameters J_2, J_3 and I_1 represent the second and third invariants of the stress deviator and the first invariant of the stress tensor, respectively, characterizing the state of stress considered. Coefficients α, β, c_1 and c_2 are material parameters which depend on the strength ratio $k = f_{ctm}/f_{cm}$, where f_{ctm} is the mean value of concrete tensile strength, and f_{cm} is the mean value of concrete compressive strength:

$$\begin{gathered}\alpha = \frac{1}{9k^{1.4}}; \quad \beta = \frac{1}{3.7k^{1.1}} \\ c_1 = \frac{1}{0.7k^{0.9}}; \quad c_2 = c_1 - 6.8\left(k - 0,07\right)^2 \end{gathered} \tag{2.8}$$

$$I_1 = \sigma_x + \sigma_y + \sigma_z$$

$$J_2 = \frac{1}{3}\left(\sigma_x^2 + \sigma_y^2 + \sigma_z^2 - \sigma_x\sigma_y - \sigma_x\sigma_z - \sigma_y\sigma_z + 3\tau_{yz}^2 + 3\tau_{xz}^2 + 3\tau_{xy}^2\right)$$

$$\begin{aligned} J_3 = {} & \frac{2}{27}\left(\sigma_x^3 + \sigma_y^3 + \sigma_z^3\right) - \frac{1}{9}\left(\sigma_x^2\sigma_y + \sigma_x^2\sigma_z + \sigma_y^2\sigma_x + \sigma_y^2\sigma_z + \sigma_z^2\sigma_x + \sigma_z^2\sigma_y\right) + \frac{4}{9}\sigma_x\sigma_y\sigma_z + \\ & - \frac{2}{3}\left(\sigma_x\tau_{yz}^2 + \sigma_y\tau_{xz}^2 + \sigma_z\tau_{xy}^2\right) + \frac{1}{3}\left(\sigma_x\tau_{xy}^2 + \sigma_x\tau_{xz}^2 + \sigma_y\tau_{xy}^2 + \sigma_y\tau_{yz}^2 + \sigma_z\tau_{xz}^2 + \sigma_z\tau_{yz}^2\right) + 2\tau_{xy}\tau_{xz}\tau_{yz} \end{aligned}$$

Alternatively, the invariants can be expressed as a function of the principal stresses:

$$\begin{gathered} I_1 = \sigma_1 + \sigma_2 + \sigma_3 \\ J_2 = \frac{1}{6}\left[\left(\sigma_1 - \sigma_2\right)^2 + \left(\sigma_2 - \sigma_3\right)^2 + \left(\sigma_3 - \sigma_1\right)^2\right] \\ J_3 = \left(\sigma_1 - \sigma_m\right)\left(\sigma_2 - \sigma_m\right)\left(\sigma_3 - \sigma_m\right), \quad \text{where } \sigma_m = \frac{\sigma_1 + \sigma_2 + \sigma_3}{3} \end{gathered} \tag{2.9}$$

This model is far more sophisticated, accounting for the influence of the intermediate principal stress. It will be used for concrete subjected to triaxial compression in the ultimate limit state design method of Chapter 3.

2.2.4 Failure (yield) conditions for reinforcement

In the limit analysis, reinforcement is assumed to be a rigid-perfectly plastic material with yield stress f_{sy}. The yield criterion simply defines that rupture occurs when reinforcement axial stresses reach the yield stress. The stress-strain relation for reinforcement is depicted in Figure 6.

It is assumed that reinforcing bars can carry only longitudinal tensile stresses - dowel action and contributions from compressed reinforcement are both neglected. This assumption is acceptable based on the lower bound theorem since it results in stresses in the reinforcement which are statically admissible and safe if the stresses are smaller than or equal to the yield stress.

An additional assumption, specifically important for the stress field design method, is that reinforcing bars are continuously distributed over the volume (smeared rebars), placed at such small spacings that the forces in them can be replaced by an equivalent yield stress distribution in the concrete ρf_{sy}. In this expression, $\rho = A_s / A_c$ is the reinforcement ratio, where A_c is the area of the section of concrete perpendicular to the bars of area A_s.

Concerning reinforcement bond and anchorage, perfect bond is assumed to exist between rebars and concrete. The anchorage is checked as an *a posteriori* procedure: if the yield condition of bond is violated, an alternative procedure is to reduce rebar forces by increasing the total reinforcement area.

The assumption of rigid-plastic behavior is a simplification justified for reinforcement since the total strains are significantly higher than the elastic limit strain ε_{sy}.

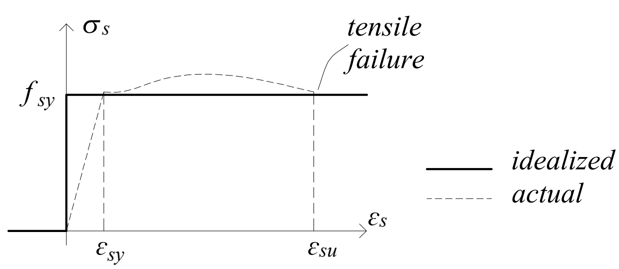

Figure 6 – Material model for reinforcement: stress-strain curve.

2.2.5 Failure (yield) conditions for reinforced concrete

When applying methods of limit analysis to structural concrete, which is a composite material, concrete and reinforcement are typically considered together as a continuum. Kaufmann (1998), states, in the context of limit analysis, that the resistance of structural concrete is given by the linear combination of the resistances of concrete and reinforcement. “Although concrete cannot reasonably be claimed to be a rigid, perfectly plastic material, classic plasticity theory (limit analysis), adopting the modified Coulomb failure criterion, gives surprisingly realistic insights into the behavior of structural concrete at failure.” (BRAESTRUP, 2021, p. 2522).

The simplifications assumed for concrete in Section 2.2.3 are extended to reinforced concrete by introducing a reduced concrete strength known as effective or plastic concrete strength. Kaufmann and Mata-Falcón (2017, p.4) contextualized that:

> Pioneers like Nielsen and Thürlimann and his co-workers dared to apply the theory of plasticity to reinforced concrete. They were of course fully aware of the limited ductility of concrete and even reinforcement. Therefore, they completely neglected the tensile strength of concrete and addressed further concern regarding ductility by providing minimum reinforcement and using conservative limit for the so-called effective concrete compressive strength, as well as upper limits for the reinforcement quantities and corresponding compression zone depths.

The simplifications assumed for *reinforcement* in Section 2.2.4 and their impact on the evaluation of the ultimate load of the structure were discussed by Kaufmann (1998, p.40):

> In a real structure, reinforcing bars are not infinitely thin, and considerable transverse shear stresses may occur in the reinforcement (“dowel action”). Bond stresses are limited by the bond strength, resulting in finite development lengths. The crack spacings are not infinitely small and tension stiffening effects occur. On the other hand, the analysis of a structure is simplified to a great extent by these assumptions, and their influence on the ultimate load is often negligible.

Nielsen (1984, p. 39) also referred to the simplifications assumed for concrete and reinforcement material models in plastic analysis, affirming that “a more accurate description of the detailed behavior is not essential when the primary purpose is to determine the load-carrying capacity of a reinforced concrete structure.”

Yield conditions are defined differently according to the structural element being analyzed. They can be explicitly obtained for reinforced membranes and slabs with a given reinforcement. For shells and structures under three-dimensional stress, however, simple yield conditions in closed analytical form are still unavailable, so that we turn to the inverse problem: to investigate the reinforcement necessary to carry given stresses.

2.3 Application of limit analysis to structural concrete

2.3.1 Plastic strength of concrete

A conservative material model for plain concrete is required for use with limit analysis, one that somehow conservatively approximates the real behavior to an idealized plastic behavior. As pointed out by Nielsen (1984, p.30): "many solutions based on the plastic theory have been derived which show a remarkably good correlation with test results when the plastic solutions are modified by inserting in the formulas a concrete strength that is smaller than the strength measured by standard tests." The effective (plastic) strength of concrete is given by:

$$f_{c,ef} = \upsilon f_c \tag{2.10}$$

where $v = \eta_{fc}\, \eta_{\varepsilon} \leq 1$ is the effectiveness factor which, according to Nielsen (1984) and *fib* (2021), accounts for:

- Geometry and size effects (the larger the dimensions, the lower the effective strength).
- Loading and loading history of the structure (for example, effective strength varies for different shear span/depth ratios in a beam without shear reinforcement loaded by bending and shear; also, effective strength varies when changes in cracking directions throughout specific loading histories are observed).
- The reinforcement ratio, yield stress, and arrangement (the higher the number of bars distributed in a section, the higher the effective strength).
- The brittleness of concrete in compression, accounted for by the brittleness factor η_{fc}, such that the plastic strength of concrete, f_{cp}, is given by the *fib* Bulletin 100 (2021):

  $$f_{cp} = \eta_{fc} \cdot f_c, \quad \text{with } \eta_{fc} = \left(30/f_c\left[MPa\right]\right)^{1/3} \leq 1 \tag{2.11}$$

  Plain concrete does not behave as a rigid-plastic material; rather, the stress-strain relation for plain concrete in uniaxial compression is characterized by the absence of a yield plateau and by a descending branch characterizing the strain softening; that is, an unloading curve after the maximum value of the stresses is reached, where stresses decrease with increasing strains until a brittle crushing occurs at the maximum strain value, ε_{cu}. The stress-strain curve is represented in Figure 7a, where the dashed line represents the actual behavior, and the continuous line represents the assumed plastic behavior.
- The compression softening effect is accounted for by the factor η_{ε}. The effective plastic strength of concrete, $f_{c,ef}$, is expressed as:

$$f_{c,ef} = \eta_{\varepsilon} f_{cp} = \eta_{\varepsilon}\left(\eta_{fc}\ f_c\right) = \upsilon f_c \tag{2.12}$$

Concrete strength is reduced in the presence of reinforcement and particularly when it is in tension leading to cracking that disturbs the transmission of the compression field, softens the response, and reduces its capacity. The resulting yield criteria for cracked concrete under plane stress conditions can be seen as a shrinkage of the square yield surface, as illustrated in Figure 7b.

The effectiveness factor utilized in the present dissertation is the one applied to the design of reinforcement in 3D solid elements considering that one or more reinforcement layers are yielding, as proposed by the Model Code 2010 (*fib*, 2013, Section 7.3.9.1):

$$\nu = \left(1 - 0.032\left|\delta_i\right|\right)\frac{1.18}{1.14 + 0.00166 f_{yd}} \tag{2.13}$$

It is not clear from the text in the MC2010, however, whether it accounts for both the strength reduction due to transverse tensile stresses and the material brittleness. Equations 2.9 and 2.12 were directly applied, knowing that this topic should be further clarified in the normative codes.

The *fib* Bulletin 100 (2021, p. 19) presented this equation in an altered format. The revised expression excluded the dependence on δ_i, explicitly incorporated the dependence on the strains in the reinforcement directions, and included both lower and upper bounds to it:

$$\eta_{\varepsilon} = 0.6 \le \frac{1.18}{1.14 + 3.40\max\left(\varepsilon_x, \varepsilon_y\right)} \le 1 \tag{2.14}$$

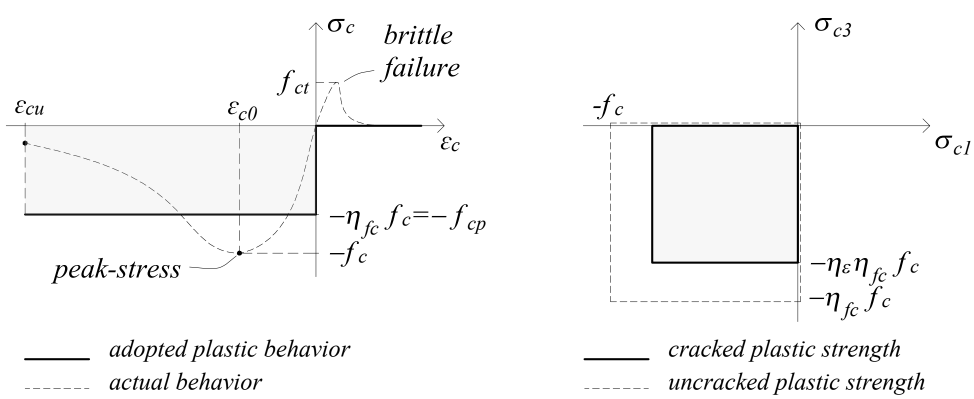

(a) (b)

Source: adapted from *fib* (2021).

Figure 7 – Material model for concrete: (a) stress-strain curve for uniaxially loaded concrete; (b) 3D yield condition for plain cracked concrete.

2.3.2 Limit analysis for three-dimensional stress fields

The SFM for the design of reinforced concrete structures is presented in Chapter 3 of this dissertation. The method begins by determining a stress field equilibrating the applied loads using linear elastic analysis. Subsequently, it calculates the required reinforcement and concrete to carry the given stresses below the yield surface. It is an application of the *lower bound theorem* since equilibrium and static boundary conditions are satisfied and the yield conditions are implicitly accounted for. That puts the design method on a solid theoretical basis: it is guaranteed that the solution thus obtained is on the safe side, and that the structural element will not collapse. Application of limit analysis to the design of reinforced concrete structures, however, still faces certain limitations, as outlined below:

- It is not directly applicable for service verifications. Checking of deformations and crack widths should be addressed by different approaches, as later addressed in Chapter 4.
- It relies on conservative estimation of the concrete compressive strength affected by transverse strains. References values for the effectiveness factor in solids under multiaxial stress states still lack experimental confirmation.
- It requires sufficient deformation capacity of all structural members and elements, and the theory of plasticity by itself does not address the questions related to the required and provided deformation capacities (KAUFMANN, 1998). It is known, however, that "reinforced concrete can exhibit considerable ductility if failure is governed by yielding of reinforcement, which can be achieved if concrete's material properties are conservatively defined, and careful attention is paid to the detailing of the reinforcing steel", and that "The ductile response of reinforced concrete has been demonstrated by decades of testing of large-scale specimens" (MEYBOOM, 2002, p.5). The *fib* Bulletin 100 (2021, Section 2.2) provides complementary insights about the ductility in structural concrete, stating that rules are required to ensure that the deformation capacity is not exceeded. Those rules might include provision of minimum reinforcement and limits to the inclination of the compression field, rotation of the compression field with respect to the uncracked state, amount of moment redistribution in redundant girders and compression zone depth.

It is timely to close this chapter with Braestrup's incisive statement found in his extensive review on concrete plasticity (2021). Based on a solid theoretical foundation, he pragmatically states that: "the main justification for applying limit analysis to concrete structures is that it works."

3 Design method: formulation for ULS

This chapter presents the complete formulation of the resisting mechanism for a given stress tensor. Equations for the ULS reinforcement and concrete design at an individual point within the structural member are deduced analytically in a new approach. Extension of this approach to encompass the entire stress field within the member, as shown in Chapter 5, will establish the SFM for a member design. The text is reproduced from the article entitled *Design of reinforced concrete structures based on three-dimensional stress fields*, Chen R, Nogueira Bittencourt T, Della Bella JC, Structural Concrete, Copyright ©2023, International Federation for Structural Concrete, Wiley.

3.1 The applied stresses

The applied stresses at a point, deriving from a linear elastic analysis, are assumed to be known: three normal stresses (σ_x, σ_y, σ_z) and three shear stress components (τ_{xy}, τ_{xz}, τ_{yz}) referred to a rectangular coordinate system (x, y, z). In an elementary cube, the stresses can be represented as shown in Figure 8. The sign convention for the applied stresses is defined as follows: normal stresses are considered positive as tensile; shear stresses τ_{xy} and τ_{xz} are positive in the positive coordinate directions in a section with the x-axis as an outwardly directed normal of the element face; shear stresses τ_{xy} and τ_{yz} are positive in the positive coordinate directions in a section with the y-axis as an outwardly directed normal of the element face; shear stresses τ_{xz} and τ_{yz} are positive in the positive coordinate directions in a section with the z-axis as an outwardly directed normal of the element face.

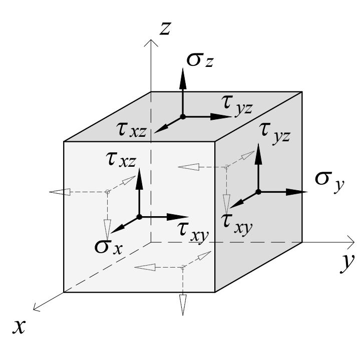

Source: Chen, Nogueira Bittencourt, and Della Bella (2023a).

Figure 8 – The applied stresses at a point.

3.2 The resisting mechanism

In the proposed resisting mechanism, the applied stress tensor is equilibrated by resisting components from reinforcement and concrete. If all the principal stresses at a point are compressive, the internal stresses are carried by the unreinforced concrete alone. Yet, if at least one of the applied principal stresses at a point is tensile, concrete will be cracked, and reinforcement will be subjected to the yield stress. For some applied stress combinations, which will be properly identified in the following formulation, an infinity of solutions exists, each one corresponding to an equilibrated scheme associated with a specific crack direction. An optimum design is then achieved for the specific crack direction that minimizes the reinforcement consumption.

The assumptions for defining the resisting mechanism are: (1) reinforcement is perfectly plastic, uniformly distributed within the element in three mutually orthogonal *x*-, *y*-, and *z*-directions and capable of carrying exclusively axial stresses; (2) concrete does not resist any tensile stress; (3) perfect bond exists between concrete and reinforcement; (4) cracks are uniformly distributed in a cracked region as "smeared cracks"; and (5) there is no aggregate interlock and no dowel action of the reinforcement on the crack surface, so that no tangential stress acts on the crack plane. The resisting mechanism is then such that the applied stress field $[\sigma]$ is resisted by stress fields in both concrete $[\sigma_c]$ and reinforcement $[f_t]$ as follows:

$$\underbrace{\begin{bmatrix} \sigma_x & \tau_{xy} & \tau_{xz} \\ \tau_{xy} & \sigma_y & \tau_{yz} \\ \tau_{xz} & \tau_{yz} & \sigma_z \end{bmatrix}}_{[\sigma]} = \underbrace{\begin{bmatrix} \sigma_{cx} & \tau_{xy} & \tau_{xz} \\ \tau_{xy} & \sigma_{cy} & \tau_{yz} \\ \tau_{xz} & \tau_{yz} & \sigma_{cz} \end{bmatrix}}_{[\sigma_c]} + \underbrace{\begin{bmatrix} f_{tx} & 0 & 0 \\ 0 & f_{ty} & 0 \\ 0 & 0 & f_{tz} \end{bmatrix}}_{[f_t]} \tag{3.1}$$

where f_{ti} ($i = x, y, z$) are the stresses acting on the cube faces with area A_{ci}, which are equivalent to the forces in the discrete reinforcement with cross-sectional area A_{si} and subjected to the stress σ_{si}.

$$\begin{aligned} f_{tx} &= \frac{A_{sx}\sigma_{sx}}{A_{cx}} = \rho_{sx}\sigma_{sx} \\ f_{ty} &= \frac{A_{sy}\sigma_{sy}}{A_{cy}} = \rho_{sy}\sigma_{sy} \\ f_{tz} &= \frac{A_{sz}\sigma_{sz}}{A_{cz}} = \rho_{sz}\sigma_{sz} \end{aligned} \tag{3.2}$$

The tensor of concrete stresses can be written as:

$$[\sigma_c] = \begin{bmatrix} \sigma_{cx} & \tau_{xy} & \tau_{xz} \\ \tau_{xy} & \sigma_{cy} & \tau_{yz} \\ \tau_{xz} & \tau_{yz} & \sigma_{cz} \end{bmatrix} = \begin{bmatrix} \sigma_x - f_{tx} & \tau_{xy} & \tau_{xz} \\ \tau_{xy} & \sigma_y - f_{ty} & \tau_{yz} \\ \tau_{xz} & \tau_{yz} & \sigma_z - f_{tz} \end{bmatrix} \tag{3.3}$$

The concrete principal stresses σ_{c1}, σ_{c2}, σ_{c3} are the roots of the characteristic equation:

$$\sigma_c^3 - I_{c1}\sigma_c^2 + I_{c2}\sigma_c - I_{c3} = 0 \tag{3.4}$$

where I_{c1}, I_{c2} and I_{c3} are the invariants of the tensor of the concrete stresses:

$$\begin{aligned} I_{c1} &= \sigma_{cx} + \sigma_{cy} + \sigma_{cz} \ = \ \sigma_{c1} + \sigma_{c2} + \sigma_{c3} \\ I_{c2} &= \sigma_{cx}\sigma_{cy} + \sigma_{cy}\sigma_{cz} + \sigma_{cx}\sigma_{cz} - \tau_{xy}^2 - \tau_{yz}^2 - \tau_{xz}^2 \ = \ \sigma_{c1}\sigma_{c2} + \sigma_{c1}\sigma_{c3} + \sigma_{c2}\sigma_{c3} \\ I_{c3} &= \det[\sigma_c] = \sigma_{cx}\sigma_{cy}\sigma_{cz} + 2\tau_{xy}\tau_{xz}\tau_{yz} - \sigma_x\tau_{yz}^2 - \sigma_y\tau_{xz}^2 - \sigma_z\tau_{xy}^2 \ = \ \sigma_{c1}\sigma_{c2}\sigma_{c3} \end{aligned} \tag{3.5}$$

The resisting mechanism, which is illustrated in Figure 9, leads to safe solutions as later discussed in Section 7.1.

The complete formulation is divided into four design cases, according to the internal stress state mobilized in concrete to equilibrate the applied stresses.

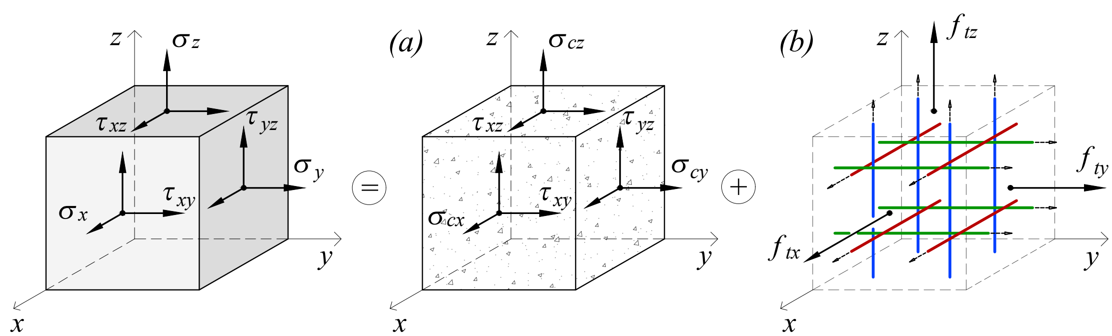

Source: Chen, Nogueira Bittencourt, and Della Bella (2023a).

Figure 9 – Resisting mechanism for the applied stress: (a) concrete stresses and (b) equivalent reinforcement stresses.

3.3 Design case: Concrete stress $\sigma_{c1} = 0$, and σ_{c2}, $\sigma_{c3} < 0$

3.3.1 Reinforcement in three directions

When the largest principal applied stress $\sigma_1 > 0$, reinforcement must be provided. If the applied stress field $[\sigma]$ is equilibrated by concrete stresses such that the principal stresses $\sigma_{c1} = 0$, $\sigma_{c2} < 0$*, and* $\sigma_{c3} < 0$*,* parallel crack planes will be formed at a point. Concrete will be subjected to a biaxial compression stress state, with principal stresses σ_{c2} and σ_{c3}, between two consecutive crack planes (see Figure 10). Considering that the normal vector of the crack planes (or, simply, the crack direction) is $\overrightarrow{n_{c1}} = (\ell_1, m_1, n_1)$, it is found that at the crack face:

$$[\sigma]\cdot\overrightarrow{n_{c1}} = [f_t]\cdot\overrightarrow{n_{c1}} + [\sigma_c]\cdot\overrightarrow{n_{c1}} \tag{3.6}$$

Assuming that no shear stress is transferred on a crack face, either by concrete-to-concrete friction, or by dowel action of the reinforcing bars crossing the crack, the concrete stress acting on this plane $[\sigma_c]\,\overrightarrow{n_{c1}}$ equals zero, and consequently:

$$[\sigma]\cdot\overrightarrow{n_{c1}} = [f_t]\cdot\overrightarrow{n_{c1}} \tag{3.7}$$

which can be rewritten as:

$$\begin{cases} \sigma_x \ell_1 + \tau_{xy} m_1 + \tau_{xz} n_1 = f_{tx} \ell_1 \\ \tau_{xy} \ell_1 + \sigma_y m_1 + \tau_{yz} n_1 = f_{ty} m_1 \\ \tau_{xz} \ell_1 + \tau_{yz} m_1 + \sigma_z n_1 = f_{tz} n_1 \end{cases} \tag{3.8}$$

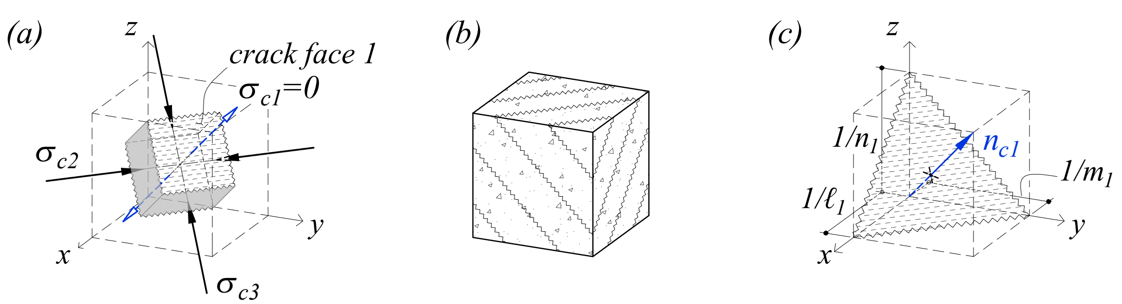

Source: Chen, Nogueira Bittencourt, and Della Bella (2023a).

Figure 10 – Design case with $\sigma_{c1} = 0$: (a) concrete principal stresses, (b) crack pattern, and (c) trihedron defined by a crack plane with crack direction in the first octant.

The equivalent reinforcement stresses are:

$$\begin{cases} f_{tx} = \sigma_x + \tau_{xy}\dfrac{m_1}{\ell_1} + \tau_{xz}\dfrac{n_1}{\ell_1} \\ f_{ty} = \sigma_y + \tau_{xy}\dfrac{\ell_1}{m_1} + \tau_{yz}\dfrac{n_1}{m_1} \\ f_{tz} = \sigma_z + \tau_{xz}\dfrac{\ell_1}{n_1} + \tau_{yz}\dfrac{m_1}{n_1} \end{cases} \tag{3.9}$$

The total reinforcement consumption is:

$$\sum f_t = \tau_{xy}\left(\frac{m_1}{\ell_1} + \frac{\ell_1}{m_1}\right) + \tau_{xz}\left(\frac{n_1}{\ell_1} + \frac{\ell_1}{n_1}\right) + \tau_{yz}\left(\frac{n_1}{m_1} + \frac{m_1}{n_1}\right) + \sigma_x + \sigma_y + \sigma_z \tag{3.10}$$

which is minimized if:

$$\begin{cases} \dfrac{\partial}{\partial \ell_1}\sum f_t = \tau_{xy}\left(-\dfrac{m_1}{\ell_1^2} + \dfrac{1}{m_1}\right) + \tau_{xz}\left(-\dfrac{n_1}{\ell_1^2} + \dfrac{1}{n_1}\right) = 0 \\ \dfrac{\partial}{\partial m_1}\sum f_t = \tau_{xy}\left(\dfrac{1}{\ell_1} - \dfrac{\ell_1}{m_1^2}\right) + \tau_{yz}\left(-\dfrac{n_1}{m_1^2} + \dfrac{1}{n_1}\right) = 0 \\ \dfrac{\partial}{\partial n_1}\sum f_t = \tau_{xz}\left(\dfrac{1}{\ell_1} - \dfrac{\ell_1}{n_1^2}\right) + \tau_{yz}\left(\dfrac{1}{m_1} - \dfrac{m_1}{n_1^2}\right) = 0 \end{cases} \tag{3.11}$$

The above conditions are simultaneously satisfied if:

$$-\frac{m_1}{\ell_1^2} + \frac{1}{m_1} = 0; \quad -\frac{n_1}{\ell_1^2} + \frac{1}{n_1} = 0; \quad \frac{1}{m_1} - \frac{m_1}{n_1^2} = 0 \tag{3.12}$$

which leads to the following relationship between the components of the crack vector:

$$\ell_1 = \pm m_1; \quad \ell_1 = \pm n_1; \quad m_1 = \pm n_1 \tag{3.13}$$

This means that an economical design is obtained when $\overrightarrow{n_{c1}}$ is one of the eight vectors equally inclined to coordinate axes x, y, z. The concrete stress tensor is obtained by inserting the f_t values (3.9) into (3.3):

$$[\sigma_c] = \begin{bmatrix} -\tau_{xy}\dfrac{m_1}{\ell_1} - \tau_{xz}\dfrac{n_1}{\ell_1} & \tau_{xy} & \tau_{xz} \\ \tau_{xy} & -\tau_{xy}\dfrac{\ell_1}{m_1} - \tau_{yz}\dfrac{n_1}{m_1} & \tau_{yz} \\ \tau_{xz} & \tau_{yz} & -\tau_{xz}\dfrac{\ell_1}{n_1} - \tau_{yz}\dfrac{m_1}{n_1} \end{bmatrix} \tag{3.14}$$

From the above Equation, it can be observed that the concrete stress field [σ_c] depends only on the tangential stresses of the applied stress field [σ]. The invariants of the concrete stress tensor are:

$$\begin{aligned}
&I_{c3}=0\\
&I_{c2}=\tau_{xy}\tau_{xz}\left(\frac{n_1}{m_1}+\frac{\ell_1^2}{m_1 n_1}+\frac{m_1}{\mathrm{n}_1}\right)+\tau_{xy}\tau_{yz}\left(\frac{n_1}{\ell_1}+\frac{\ell_1}{n_1}+\frac{m_1^2}{\ell_1\,\mathrm{n}_1}\right)+\tau_{xz}\tau_{yz}\left(\frac{n_1^2}{\ell_1 m_1}+\frac{\ell_1}{m_1}+\frac{m_1}{\ell_1}\right)\\
&I_{c1}=-\tau_{xy}\tau_{xz}\left(\frac{m_1}{\ell_1}+\frac{\ell_1}{m_1}\right)-\tau_{xz}\left(\frac{n_1}{\ell_1}+\frac{\ell_1}{n_1}\right)-\tau_{yz}\left(\frac{n_1}{m_1}+\frac{m_1}{n_1}\right)
\end{aligned} \tag{3.15}$$

Analyzing Equation (3.5), concrete is subjected to a biaxial compression stress state with the largest principal stress $\sigma_{c1} = 0$ and σ_{c2}, $\sigma_{c3} < 0$, if:

$$\begin{aligned}
&I_{c3}=0\\
&I_{c2}=\sigma_{c2}\sigma_{c3}>0\\
&I_{c1}=\sigma_{c2}+\sigma_{c3}<0
\end{aligned} \tag{3.16}$$

For a crack direction in the ***first octant***, $\overrightarrow{n_{c1}} = \left(1/\sqrt{3}\,,1/\sqrt{3}\,,1/\sqrt{3}\right)$ = (0.577, 0.577, 0.577). The reinforcement equivalent stresses, from Equation (3.9), become:

$$\begin{cases}
f_{tx}=\sigma_x+\left(\tau_{xy}+\tau_{xz}\right) & (a)\\
f_{ty}=\sigma_y+\left(\tau_{xy}+\tau_{yz}\right) & (b)\\
f_{tz}=\sigma_z+\left(\tau_{xz}+\tau_{yz}\right) & (c)
\end{cases} \tag{3.17}$$

The concrete stress tensor is:

$$\left[\sigma_c\right]=\begin{bmatrix}
-\left(\tau_{xy}+\tau_{xz}\right) & \tau_{xy} & \tau_{xz}\\
\tau_{xy} & -\left(\tau_{xy}+\tau_{yz}\right) & \tau_{yz}\\
\tau_{xz} & \tau_{yz} & -\left(\tau_{xz}+\tau_{yz}\right)
\end{bmatrix} \tag{3.18}$$

and the principal stresses are given by:

$$\left.\begin{matrix}\sigma_{c2}\\ \sigma_{c3}\end{matrix}\right\}=-\left(\tau_{xy}+\tau_{xz}+\tau_{yz}\right)\pm\sqrt{\left(\tau_{xy}+\tau_{xz}+\tau_{yz}\right)^2-3\left(\tau_{xy}\tau_{xz}+\tau_{xz}\tau_{yz}+\tau_{yz}\tau_{xy}\right)} \tag{3.19}$$

The invariants of the concrete stress tensor are, for the crack direction in the first octant:

$$I_{c3} = 0$$
$$I_{c2} = 3\left(\tau_{xy}\tau_{xz} + \tau_{xy}\tau_{yz} + \tau_{xz}\tau_{yz}\right) \tag{3.20}$$
$$I_{c1} = -2\left(\tau_{xy} + \tau_{xz} + \tau_{yz}\right)$$

Condition $I_{c2} > 0$ is met if:

$$\tau_{xy}\tau_{xz} + \tau_{xy}\tau_{yz} + \tau_{xz}\tau_{yz} > 0 \tag{3.21}$$

Condition $I_{c1} < 0$ is met if:

$$\tau_{xy} + \tau_{xz} + \tau_{yz} > 0 \tag{3.22}$$

The aforementioned conditions are simultaneously met for the following sign combination of the shear stress components: sgn(τ) = (sign of τ_{xy}, sign of τ_{xz}, sign of τ_{yz}) = (+,+,+), (+,+,-), (+,-,+), or (-,+,+). This is graphically represented in the space of the shear stress components (Figure 11), where four sub-regions satisfying simultaneously $I_{c2} > 0$ and $I_{c1} < 0$ are identified: region I with sgn(τ) = (+,+,+), region II with sgn(τ) = (+,-,+), region III with sgn(τ) = (-,+,+), and region IV with sgn(τ) = (+,+,-).

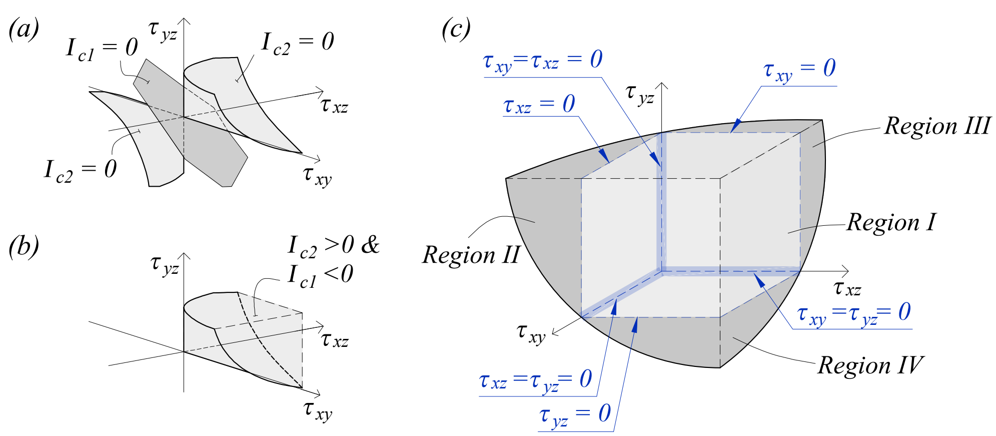

Source: Chen, Nogueira Bittencourt, and Della Bella (2023a).

Figure 11 – (a) $I_{c1} = 0$ and $I_{c2} = 0$; (b) region and (c) sub-regions satisfying $I_{c2} > 0$ & $I_{c1} < 0$.

The internal stresses developed in concrete and reinforcement are further analyzed:

- When τ_{xy}, τ_{xz}, and $\tau_{yz} > 0$, conditions (3.21) and (3.22) are always met, which means that concrete is subjected to a biaxial compression stress state. Equilibrium of the concrete internal stresses in a trihedron delimited by a crack plane is represented in Figure 12a. The stresses applied to the trihedron faces are transferred internally by three compression struts - AB, BC and CA. Stresses may be projected onto the coordinate planes as indicated in Figure 12b. Note that each and every shear stress component increases the tensile stresses in the reinforcement f_t equilibrating it.

- When sgn(τ) = (+,-,+), (-,+,+), or (+,+,-), the condition $I_{c2} > 0$ is evaluated by means of an artifice: sorting the shear stress components in ascending order, from τ_1 to τ_3, Equation (3.21) can be rewritten as:

$$\tau_1\tau_2 + \tau_1\tau_3 + \tau_2.\tau_3 > 0 \tag{3.23}$$

from which it is found:

$$\begin{aligned}
&\underbrace{\tau_1}_{<0}\underbrace{\left(\tau_2+\tau_3\right)}_{>0} > \underbrace{-\tau_2\tau_3}_{<0} \quad \Rightarrow \quad \left|\tau_1\right| < \frac{\tau_2\tau_3}{\tau_2+\tau_3} && (a)\\
&\underbrace{\tau_2}_{>0}\left(\tau_1+\tau_3\right) > \underbrace{-\tau_1\tau_3}_{>0} \quad \Rightarrow \quad \left(\tau_1+\tau_3\right)>0 \quad \Rightarrow \quad \left|\tau_1\right| < \tau_3 && (b)\\
&\underbrace{\tau_3}_{>0}\left(\tau_1+\tau_2\right) > \underbrace{-\tau_1\tau_2}_{>0} \quad \Rightarrow \quad \left(\tau_1+\tau_2\right)>0 \quad \Rightarrow \quad \left|\tau_1\right| < \tau_2 && (c)
\end{aligned} \tag{3.24}$$

This means that concrete will be subjected to a biaxial compression stress state provided that Equation (3.24)a is satisfied and provided that the smallest shear stress component τ_1 is also the one with the smallest absolute value, as required by Equations (3.24)b and (3.24)c. Notice that τ_1 alleviates the tensile stresses in the respective reinforcement:

– If τ_{xy} is the negative shear stress component, it alleviates f_{tx} and f_{ty}, and reduces the compression in the AB direction (see Figure 13a).

– If τ_{xz} is the negative shear stress component, it alleviates f_{tx} and f_{tz}, and reduces the compression in the BC direction (see Figure 13b).

– If τ_{yz} is the negative shear stress component, it alleviates f_{ty} and f_{tz}, and reduces the compression in the AC direction (see Figure 13c).

For crack directions in the ***second*** to the ***eighth octants***, design equations are presented in Appendix A. It is found that design Equation (3.17) for crack direction in the first octant can be used for crack directions in *any octant* if it is adopted:

- When $\tau_{xy}.\tau_{xz}.\tau_{yz} > 0$: positive values for all shear components;
- When $\tau_{xy}.\tau_{xz}.\tau_{yz} < 0$: negative value for the shear stress component with the smallest absolute value (τ_1), and positive values for the remaining components (τ_2, τ_3).

Note: the design Equations for the plane stress state, as proposed by Baumann (1972a, 1972b), can be derived from Equation (3.9). This is demonstrated in Appendix B.

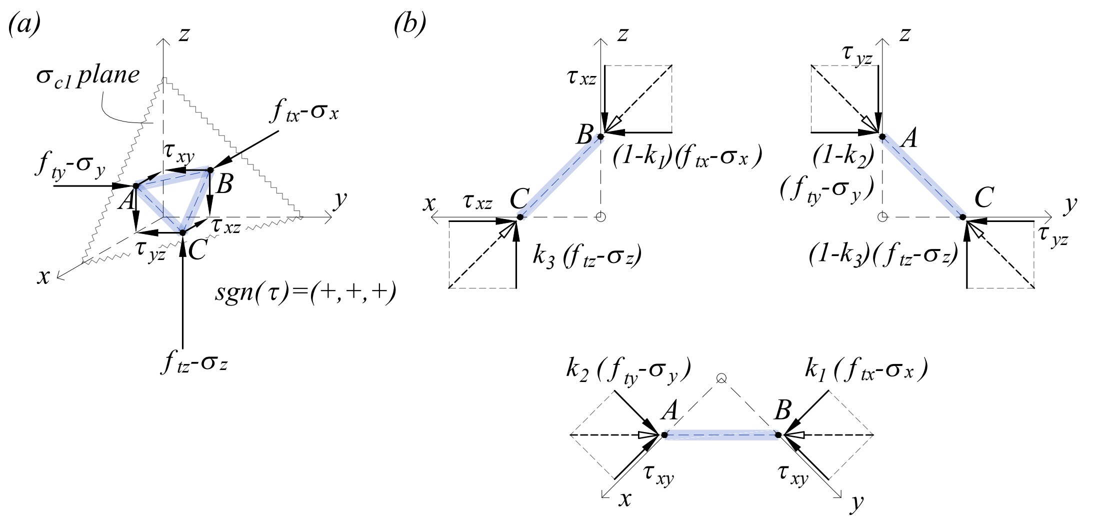

Source: Chen, Nogueira Bittencourt, and Della Bella (2023a).

Figure 12 – Concrete stresses when the applied shear stress components are all positive.

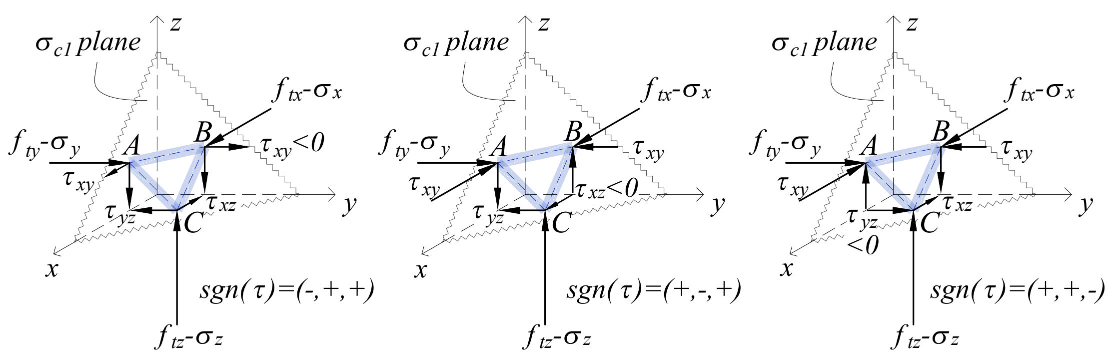

(a) (b) (c)

Source: Chen, Nogueira Bittencourt, and Della Bella (2023a).

Figure 13 – Concrete stresses when one of the applied shear stress components is negative: (a) $\tau_{xy} < 0$, (b) $\tau_{xz} < 0$, or (c) $\tau_{yz} < 0$.

Particular case: zero shear stresses (either $\tau_{xy} = 0$, or $\tau_{xz} = 0$, or $\tau_{yz} = 0$). For a crack direction in the first octant $\overrightarrow{n_{c1}} = (\ell_1, m_1, n_1) = (0.577, 0.577, 0.577)$, the internal stresses developed in concrete and reinforcement are analyzed below:

- When $\tau_{xy} = 0$ in Equation (3.20), the concrete stress tensor invariants are:

$$\begin{aligned} I_{c2} &= 3\,\tau_{xz}\tau_{yz} \\ I_{c1} &= -2\left(\tau_{xz} + \tau_{yz}\right) \end{aligned} \tag{3.25}$$

Condition $I_{c2} > 0$ is met if sgn(τ) = (0,+,+) or (0,-,-), whereas $I_{c1} < 0$ if sgn(τ) = (0,+,+). Concrete will be under a biaxial compression stress state if sgn(τ) = (0,+,+).

- When $\tau_{xz} = 0$ in Equation (3.20), the concrete stress invariants are:

$$\begin{aligned} I_{c2} &= 3\,\tau_{xy}\tau_{yz} \\ I_{c1} &= -2\left(\tau_{xy} + \tau_{yz}\right) \end{aligned} \tag{3.26}$$

Condition $I_{c2} > 0$ is met if sgn(τ) = (+,0,+) or (-,0,-), whereas $I_{c1} < 0$ if sgn(τ) = (+,0,+). Concrete will be under a biaxial compression stress state if sgn(τ) = (+,0,+).

- When $\tau_{yz} = 0$ in Equation (3.20), the concrete stress invariants are:

$$\begin{aligned} I_{c2} &= 3\,\tau_{xy}\tau_{xz} \\ I_{c1} &= -2\left(\tau_{xy} + \tau_{xz}\right) \end{aligned} \tag{3.27}$$

Condition $I_{c2} > 0$ is met if sgn(τ) = (+,+,0) or (-,-,0), whereas $I_{c1} < 0$ if sgn(τ) = (+,+,0). Concrete will be under a biaxial compression stress state if sgn(τ) = (+,+,0).

Table C1 in Appendix C presents the design equations when an applied shear stress is zero for crack directions in the ***second*** to the ***eighth octants***. It is found that all cases can be designed with Equation (3.17) of the crack direction in the first octant assuming the zero-shear stress combined with the other two shear stress components with positive values. By doing so, if one equivalent reinforcement stress f_{tx}, f_{ty}, or f_{tz} results negative, equivalent reinforcement stresses should be calculated as described in Section 3.3.2. If, however, two equivalent reinforcement stresses f_{tx}, f_{ty}, or f_{tz} result negative, equivalent reinforcement stresses should be calculated as described in Section 3.3.3. See Section 3.4.1 for stress states with $\tau_{xy} = \tau_{xz} = 0$, or $\tau_{xz} = \tau_{yz} = 0$, or $\tau_{xz} = \tau_{yz} = 0$.

3.3.2 Reinforcement in two directions

Reinforcement in the x-direction dispensed

When in Equation (3.17) the equivalent reinforcement stress f_{tx} turns out to be negative, while (f_{ty}, f_{tz}) > 0, it is possible to dispense the reinforcement in the x-direction by assuming $f_{tx} = 0$ in (3.8):

$$\begin{cases} \sigma_x \ell_1 + \tau_{xy} m_1 + \tau_{xz} n_1 = 0 & (a) \\ \tau_{xy} \ell_1 + \sigma_y m_1 + \tau_{yz} n_1 = f_{ty} m_1 & (b) \\ \tau_{xz} \ell_1 + \tau_{yz} m_1 + \sigma_z n_1 = f_{tz} n_1 & (c) \end{cases} \tag{3.28}$$

from which:

$$\ell_1 = -\frac{\tau_{xy}}{\sigma_x} m_1 - \frac{\tau_{xz}}{\sigma_x} n_1 \tag{3.29}$$

The equivalent reinforcement stresses are:

$$\begin{cases} f_{tx} = 0 \\ f_{ty} = \sigma_y + \tau_{yz} \dfrac{n_1}{m_1} + \tau_{xy} \left(-\tau_{xy} - \tau_{xz} \dfrac{n_1}{m_1} \right) \dfrac{1}{\sigma_x} \\ f_{tz} = \sigma_z + \tau_{yz} \dfrac{m_1}{n_1} + \tau_{xz} \left(-\tau_{xy} \dfrac{m_1}{n_1} - \tau_{xz} \right) \dfrac{1}{\sigma_x} \end{cases} \tag{3.30}$$

The concrete stress tensor, in the general form, is:

$$[\sigma_c] = \begin{bmatrix} \sigma_x & \tau_{xy} & \tau_{xz} \\ \tau_{xy} & -\tau_{yz} \dfrac{n_1}{m_1} + \dfrac{\tau_{xy}^2}{\sigma_x} + \tau_{xy}\tau_{xz} \dfrac{n_1}{m_1} & \tau_{yz} \\ \tau_{xz} & \tau_{yz} & -\tau_{yz} \dfrac{m_1}{n_1} + \dfrac{\tau_{xy}\tau_{xz}}{\sigma_x} \dfrac{m_1}{n_1} + \dfrac{\tau_{xz}^2}{\sigma_x} \end{bmatrix} \tag{3.31}$$

The invariants of the concrete stress tensor are, in the general form:

$$\begin{aligned} I_{c3} &= 0 \\ I_{c2} &= \left(-\sigma_x \tau_{yz} + \tau_{xy}\tau_{xz} - \frac{\tau_{yz}\tau_{xz}^2}{\sigma_x} + \frac{\tau_{xy}\tau_{xz}^3}{\sigma_x^2} \right) \frac{n_1}{m_1} + \left(-\sigma_x \tau_{yz} + \tau_{xy}\tau_{xz} - \frac{\tau_{xy}^2\tau_{yz}}{\sigma_x} + \frac{\tau_{xy}^3\tau_{xz}}{\sigma_x^2} \right) \frac{m_1}{n_1} + \\ &\quad + \frac{2\tau_{xy}^2\tau_{xz}^2}{\sigma_x^2} - \frac{2\tau_{xy}\tau_{xz}\tau_{yz}}{\sigma_x} \\ I_{c1} &= \sigma_x - \tau_{yz} \left(\frac{n_1}{m_1} + \frac{m_1}{n_1} \right) + \frac{\tau_{xy}^2}{\sigma_x} + \frac{\tau_{xy}\tau_{xz}}{\sigma_x} \left(\frac{n_1}{m_1} + \frac{m_1}{n_1} \right) + \frac{\tau_{xz}^2}{\sigma_x} \end{aligned} \tag{3.32}$$

Notice that, from Equation (3.17)a, condition f_{tx} =0 occurs when:

$$\sigma_x < -\left(\tau_{xy} + \tau_{xz} \right) \tag{3.33}$$

The analysis of Equation (3.33) shows that the normal stress σ_x is always compressive because:

– If all shear stresses are positive, then positive values of τ_{xy} and τ_{xz} lead to $\sigma_x < 0$.

– If τ_{xy} is the negative shear stress component, then $\sigma_x < 0$, since $|\tau_{xy}| < \tau_{xz}$.

– If τ_{xz} is the negative shear stress component, then $\sigma_x < 0$, since $|\tau_{xz}| < \tau_{xy}$.

Note: the maximum σ_x delimiting this design case is independent of the τ_{yz} value.

<u>*Solution 1: Economical solution*</u>. Variables m_1 and n_1 may be determined minimizing the total required reinforcement. The derivative of the total reinforcement with respect to the variable m_1 must equal zero:

$$\frac{\partial}{\partial m_1}\sum f_t = \frac{\partial}{\partial m_1}\left(f_{ty} + f_{tz}\right) = -\tau_{yz}\frac{n_1}{m_1^2} + \frac{\tau_{xy}}{\sigma_x}\left(\tau_{xz}\frac{n_1}{m_1^2}\right) + \tau_{yz}\frac{1}{n_1} + \frac{\tau_{xz}}{\sigma_x}\left(-\tau_{xy}\frac{1}{n_1}\right) = 0 \tag{3.34}$$

The above condition is met independently of the stress state if:

$$\tau_{yz}\left(\frac{1}{n_1} - \frac{n_1}{m_1^2}\right) + \frac{\tau_{xy}\tau_{xz}}{\sigma_x}\left(\frac{n_1}{m_1^2} - \frac{1}{n_1}\right) = 0\,; \quad \frac{m_1^2 - n_1^2}{n_1 m_1^2} = 0; \quad m_1 = \pm n_1 \tag{3.35}$$

The derivative of the total reinforcement with respect to variable n_1 must also equal zero:

$$\frac{\partial}{\partial n_1}\sum f_t = \tau_{yz}\frac{1}{m_1} + \frac{\tau_{xy}}{\sigma_x}\left(-\tau_{xy}\frac{1}{m_1}\right) - \tau_{yz}\frac{m_1}{n_1^2} + \frac{\tau_{xz}}{\sigma_x}\left(\tau_{xy}\frac{m_1}{n_1^2}\right) = 0 \tag{3.36}$$

The above condition leads to the same result from (3.35):

$$\tau_{yz}\left(\frac{1}{m_1} - \frac{m_1}{n_1^2}\right) + \frac{\tau_{xy}\tau_{xz}}{\sigma_x}\left(\frac{m_1}{n_1^2} - \frac{1}{m_1}\right) = 0\,; \quad \frac{n_1^2 - m_1^2}{m_1 n_1^2} = 0; \quad m_1 = \pm n_1 \tag{3.37}$$

Therefore, there are four feasible directions for the first principal crack $\overrightarrow{n_{c1}}$: $(\ell_1, m_1, n_1) = (\ell_1, 1, 1)$, $(\ell_1, 1, -1)$, $(\ell_1, -1, 1)$, or $(\ell_1, -1, -1)$. Case $m_1 = n_1 = 1$ is then analyzed. Equation (3.29) can be rewritten as:

$$\ell_1 = -\left(\tau_{xy} + \tau_{xz}\right)/\sigma_x \tag{3.38}$$

from which ℓ_1 is found to be always positive because:

- If all shear stresses are positive, then positive values of τ_{xy} and τ_{xz} lead to $\ell_1 > 0$.
- If τ_{xy} is the negative shear stress component: since $|\tau_{xy}| < \tau_{xz}$ and $\sigma_x < 0$, then $\ell_1 > 0$.
- If τ_{xz} is the negative shear stress component: since $|\tau_{xz}| < \tau_{xy}$ and $\sigma_x < 0$, then $\ell_1 > 0$.

This locates the first principal crack direction $\overrightarrow{n_{c1}}$ in the ***first octant***.

The equivalent reinforcement stresses, from Equation (3.30), are:

$$\begin{cases} f_{tx} = 0 \\ f_{ty} = \sigma_y + \tau_{yz} + \tau_{xy} \underbrace{\left(\tau_{xy} + \tau_{xz}\right) / -\sigma_x}_{>1} \\ f_{tz} = \sigma_z + \tau_{yz} + \tau_{xz} \underbrace{\left(\tau_{xy} + \tau_{xz}\right) / -\sigma_x}_{>1} \end{cases} \tag{3.39}$$

The concrete stress tensor for a crack direction in the first octant is:

$$[\sigma_c] = \begin{bmatrix} \sigma_x & \tau_{xy} & \tau_{xz} \\ \tau_{xy} & -\tau_{yz} + \dfrac{\tau_{xy}^2}{\sigma_x} + \dfrac{\tau_{xy}\tau_{xz}}{\sigma_x} & \tau_{yz} \\ \tau_{xz} & \tau_{yz} & -\tau_{yz} + \dfrac{\tau_{xy}\tau_{xz}}{\sigma_x} + \dfrac{\tau_{xz}^2}{\sigma_x} \end{bmatrix} \tag{3.40}$$

The invariants of the concrete stress tensor are:

$$\begin{aligned} & I_{c3} = 0 && (a) \\ & I_{c2} = \underbrace{\left(2 + \frac{\left(\tau_{xy} + \tau_{xz}\right)^2}{\sigma_x^2}\right)}_{>0} \left(-\sigma_x \tau_{yz} + \tau_{xy}\tau_{xz}\right) && (b) \\ & I_{c1} = \left(\sigma_x - 2\tau_{yz}\right) + \underbrace{\frac{1}{\sigma_x}\left(\tau_{xy} + \tau_{xz}\right)^2}_{<0} && (c) \end{aligned} \tag{3.41}$$

From Equation (3.41)b, condition $I_{c2} > 0$ is verified to be met if:

$$\sigma_x \tau_{yz} \le \tau_{xy}\tau_{xz} \tag{3.42}$$

The analysis of Equation (3.41)c indicates that condition $I_{c1} < 0$ is always met because:

- If all shear stresses are positive, then $(\sigma_x - 2\,\tau_{yz}) < 0$, and I_{c1} results negative.
- If τ_{xy} is the negative shear stress, then $\tau_{yz} > 0$, and all terms of I_{c1} are smaller than zero.
- If τ_{xz} is the negative shear stress, then $\tau_{yz} > 0$, and all terms of I_{c1} are smaller than zero.
- If τ_{yz} is the negative shear stress, knowing that the $|\tau_{yz}| < \tau_{xy}$ and $|\tau_{yz}| < \tau_{xz}$:

$$2\left|\tau_{yz}\right| < (\tau_{xy} + \tau_{xz});\ -(\tau_{xy} + \tau_{xz}) < -2\left|\tau_{yz}\right|;\ -(\tau_{xy} + \tau_{xz}) < 2\tau_{yz} \tag{3.43}$$

Since $\sigma_x < -(\tau_{xy} + \tau_{xz})$, it is possible to state that $\sigma_x < 2\,\tau_{yz}$, and, consequently, $(\sigma_x - 2\,\tau_{yz}) < 0$, which in (3.41)c gives $I_{c1} < 0$.

The internal stresses developed in concrete and reinforcement are further analyzed:

- When τ_{xy}, τ_{xz}, and $\tau_{yz} > 0$, condition (3.42) is satisfied, and since $I_{c1} < 0$, concrete is confirmed to be under a biaxial compression stress state. Each and every shear stress component increases the tensile stresses in reinforcement f_t equilibrating it.
- When sgn(τ) = (+,-,+), (-,+,+), or (+,+,-):
  - If $\tau_{xy} < 0$, this negative shear stress component reduces the required *y*-reinforcement.

$$\begin{cases} f_{ty} = \sigma_y + \tau_{yz} + \tau_{xy} \underbrace{\left(\tau_{xy} + \tau_{xz}\right)\big/-\sigma_x}_{>0} \\ f_{tz} = \sigma_z + \tau_{yz} + \tau_{xz} \underbrace{\left(\tau_{xy} + \tau_{xz}\right)\big/-\sigma_x}_{>0}, \text{ where } \left|\tau_{xy}\right| < \tau_{xz} \end{cases} \quad (3.44)$$

  - If $\tau_{xz} < 0$, this negative shear stress component reduces the required *z*-reinforcement.

$$\begin{cases} f_{ty} = \sigma_y + \tau_{yz} + \tau_{xy} \underbrace{\left(\tau_{xy} + \tau_{xz}\right)\big/-\sigma_x}_{>0}, \text{ where } \left|\tau_{xz}\right| < \tau_{xy} \\ f_{tz} = \sigma_z + \tau_{yz} + \tau_{xz} \underbrace{\left(\tau_{xy} + \tau_{xz}\right)\big/-\sigma_x}_{>0} \end{cases} \quad (3.45)$$

  - If $\tau_{yz} < 0$, this component reduces both *y*- and *z*- required reinforcement.

$$\begin{cases} f_{ty} = \sigma_y + \tau_{yz} + \underbrace{\tau_{xy} \left(\tau_{xy} + \tau_{xz}\right)\big/-\sigma_x}_{>0} \\ f_{tz} = \sigma_z + \tau_{yz} + \underbrace{\tau_{xz} \left(\tau_{xy} + \tau_{xz}\right)\big/-\sigma_x}_{>0} \end{cases} \quad (3.46)$$

Design equations for crack directions in the ***second*** to the ***eighth octants*** can be found analogously. It can be shown that the design Equation (3.39) for a crack direction in the first octant can be used for crack directions in *any octant* if it is adopted:

- When $\tau_{xy}.\tau_{xz}.\tau_{yz} > 0$: positive values for all shear stress components;
- When $\tau_{xy}.\tau_{xz}.\tau_{yz} < 0$: a negative value for the shear stress component with the smallest absolute value, and positive values for the remaining ones.

Solution 2: Complementary solution. This solution is adopted when, for a crack direction in the ***first octant***, Equation (3.42) is not satisfied, that is, when:

$$\sigma_x \tau_{yz} > \tau_{xy} \tau_{xz} \quad (3.47)$$

A crack direction defined by $n_1/m_1 = -\tau_{xy}/\tau_{xz}$ is chosen. This direction cancels ℓ_1 out, so that the plane of σ_{c1} becomes perpendicular to the direction of zero reinforcement.

$$\ell_1 = -\frac{\tau_{xy}}{\sigma_x}\left(-\frac{\tau_{xz}}{\tau_{xy}}n_1\right) - \frac{\tau_{xz}}{\sigma_x}n_1 = 0 \tag{3.48}$$

The equivalent reinforcement stresses are obtained from (3.30):

$$\begin{cases} f_{tx} = 0 \\ f_{ty} = \sigma_y - \dfrac{\tau_{yz}\tau_{xy}}{\tau_{xz}} \\ f_{tz} = \sigma_z - \dfrac{\tau_{xz}\tau_{yz}}{\tau_{xy}} \end{cases} \tag{3.49}$$

The concrete stress tensor is:

$$[\sigma_c] = \begin{bmatrix} \sigma_x & \tau_{xy} & \tau_{xz} \\ \tau_{xy} & \dfrac{\tau_{xy}\tau_{yz}}{\tau_{xz}} & \tau_{yz} \\ \tau_{xz} & \tau_{yz} & \dfrac{\tau_{xz}\tau_{yz}}{\tau_{xy}} \end{bmatrix} \tag{3.50}$$

The concrete stress invariants are:

$$\begin{aligned} & I_{c3} = 0 && (a) \\ & I_{c2} = \sigma_x\tau_{yz}\frac{\tau_{xy}}{\tau_{xz}} + \sigma_x\tau_{yz}\frac{\tau_{xz}}{\tau_{xy}} - \tau_{xy}^2 - \tau_{xz}^2 && (b) \\ & I_{c1} = \sigma_x + \frac{\tau_{xy}\tau_{yz}}{\tau_{xz}} + \frac{\tau_{xz}\tau_{yz}}{\tau_{xy}} && (c) \end{aligned} \tag{3.51}$$

From (3.47) and (3.51)b, it is found that:

$$I_{c2} > \left(\tau_{xy}\tau_{xz}\right)\frac{\tau_{xy}}{\tau_{xz}} + \left(\tau_{xy}\tau_{xz}\right)\frac{\tau_{xz}}{\tau_{xy}} - \tau_{xy}^2 - \tau_{xz}^2; \quad I_{c2} > \tau_{xy}^2 + \tau_{xz}^2 - \tau_{xy}^2 - \tau_{xz}^2; \quad I_{c2} > 0 \tag{3.52}$$

From (3.51)c, considering that all individual terms are negative, it is found that $I_{c1} < 0$. Since $I_{c2} > 0$ and $I_{c1} < 0$, concrete is confirmed to be subjected to a biaxial compression stress state.

Design equations for crack directions in the ***second*** to the ***eighth octants*** can be found analogously. It can be shown that the design Equation (3.49) for a crack direction in the first octant can be used for crack directions in *any octant* if it is adopted:

- When $\tau_{xy}.\tau_{xz}.\tau_{yz} > 0$: positive values for all shear components;
- When $\tau_{xy}.\tau_{xz}.\tau_{yz} < 0$: a negative value for the shear stress component with the smallest absolute value, and positive values for the remaining ones.

Reinforcement in the y-direction dispensed

When $f_{ty} < 0$ and $(f_{tx}, f_{tz}) > 0$ in Equation (3.17), it is possible to dispense the reinforcement in the y-direction, and $f_{ty} = 0$ is assumed so that:

$$\begin{cases} f_{tx} = \sigma_x + \tau_{xz} + \tau_{xy}\left(\tau_{xy} + \tau_{yz}\right) / -\sigma_y \\ f_{ty} = 0 \\ f_{tz} = \sigma_z + \tau_{xz} + \tau_{yz}\left(\tau_{xy} + \tau_{yz}\right) / -\sigma_y \end{cases} \tag{3.53}$$

Concrete will be subjected to a biaxial compression stress ($I_{c2} > 0$ and $I_{c1} < 0$) state while:

$$\sigma_y \tau_{xz} \le \tau_{xy}.\tau_{yz} \tag{3.54}$$

If the condition above is not met, the following design equation should be adopted:

$$\begin{cases} f_{tx} = \sigma_x - \tau_{xy}\tau_{xz} / \tau_{yz} \\ f_{ty} = 0 \\ f_{tz} = \sigma_z - \tau_{xz}\tau_{yz} / \tau_{xy} \end{cases} \tag{3.55}$$

Reinforcement in the z-direction dispensed

When $f_{tz} < 0$ and $(f_{tx}, f_{ty}) > 0$ in Equation (3.17), it is possible to dispense the reinforcement in the z-direction, and $f_{tz} = 0$ is assumed so that:

$$\begin{cases} f_{tx} = \sigma_x + \tau_{xy} + \tau_{xz}\left(\tau_{xz} + \tau_{yz}\right) / -\sigma_z \\ f_{ty} = \sigma_y + \tau_{xy} + \tau_{yz}\left(\tau_{xz} + \tau_{yz}\right) / -\sigma_z \\ f_{tz} = 0 \end{cases} \tag{3.56}$$

Concrete will be subjected to a biaxial compression stress ($I_{c2} > 0$ and $I_{c1} < 0$) state while:

$$\sigma_z \tau_{xy} \le \tau_{xz}.\tau_{yz} \tag{3.57}$$

If the condition above is not met, the following design equation should be adopted:

$$\begin{cases} f_{tx} = \sigma_x - \tau_{xy}\tau_{xz} / \tau_{yz} \\ f_{ty} = \sigma_y - \tau_{xy}\tau_{yz} / \tau_{yz} \\ f_{tz} = 0 \end{cases} \tag{3.58}$$

3.3.3 Reinforcement in one direction

Reinforcement in the z-direction

When the equivalent reinforcement stresses f_{tx} and f_{ty} turn out to be negative in (3.17) while f_{tz} is still positive, reinforcement in the *x*- and *y*-directions are dispensed, and $f_{tx} = f_{ty} = 0$ is assumed in Equation (3.8):

$$\begin{cases} \sigma_x \ell_1 + \tau_{xy} m_1 + \tau_{xz} n_1 = 0 & (a) \\ \tau_{xy} \ell_1 + \sigma_y m_1 + \tau_{yz} n_1 = 0 & (b) \\ \tau_{xz} \ell_1 + \tau_{yz} m_1 + \sigma_z n_1 = f_{tz} n_1 & (c) \end{cases} \tag{3.59}$$

From Equations (3.59)a and (3.59)b, isolating ℓ_1 shows that:

$$-\frac{\tau_{xy} m_1 + \tau_{xz} n_1}{\sigma_x} = -\frac{\sigma_y m_1 + \tau_{yz} n_1}{\tau_{xy}} \tag{3.60}$$

so that the relation between components m_1 and n_1 of the first principal direction vector is:

$$\frac{m_1}{n_1} = \frac{-\sigma_x \tau_{yz} + \tau_{xy} \tau_{xz}}{-\tau_{xy}^2 + \sigma_x \sigma_y} \tag{3.61}$$

From Equation (3.59)a:

$$\frac{\ell_1}{n_1} = -\frac{\tau_{xy}}{\sigma_x} \frac{m_1}{n_1} - \frac{\tau_{xz}}{\sigma_x} \tag{3.62}$$

The equivalent reinforcement stresses, from (3.59)c, are then calculated by:

$$\begin{cases} f_{tx} = 0 \\ f_{ty} = 0 \\ f_{tz} = \sigma_z + \tau_{xz} \dfrac{\ell_1}{n_1} + \tau_{yz} \dfrac{m_1}{n_1} = \sigma_z + \dfrac{2\tau_{xy}\tau_{xz}\tau_{yz} - \sigma_x \tau_{yz}^2 - \sigma_y \tau_{xz}^2}{\sigma_x \sigma_y - \tau_{xy}^2} \end{cases} \tag{3.63}$$

The concrete stress tensor is:

$$[\sigma_c] = \begin{bmatrix} \sigma_x & \tau_{xy} & \tau_{xz} \\ \tau_{xy} & \sigma_y & \tau_{yz} \\ \tau_{xz} & \tau_{yz} & -\dfrac{2\tau_{xy}\tau_{xz}\tau_{yz} - \sigma_x\tau_{yz}^2 - \sigma_y\tau_{xz}^2}{\sigma_x\sigma_y - \tau_{xy}^2} \end{bmatrix} \tag{3.64}$$

The invariants of the concrete stress tensor are:

$$\begin{aligned} I_{c3} &= 0 \\ I_{c2} &= \sigma_x\sigma_y - \frac{2\sigma_x\tau_{xy}\tau_{xz}\tau_{yz} - \sigma_x^2\tau_{yz}^2 - \sigma_x\sigma_y\tau_{xz}^2}{\sigma_x\sigma_y - \tau_{xy}^2} - \frac{2\sigma_y\tau_{xy}\tau_{xz}\tau_{yz} - \sigma_x\sigma_y\tau_{yz}^2 - \sigma_y^2\tau_{xz}^2}{\sigma_x\sigma_y - \tau_{xy}^2} \\ &\quad - \tau_{xy}^2 - \tau_{xz}^2 - \tau_{yz}^2 \\ I_{c1} &= \sigma_x + \sigma_y - \frac{2\tau_{xy}\tau_{xz}\tau_{yz} - \sigma_x\tau_{yz}^2 - \sigma_y\tau_{xz}^2}{\sigma_x\sigma_y - \tau_{xy}^2} \end{aligned} \tag{3.65}$$

The applied normal stresses are then evaluated. From (3.17)a, condition $f_{tx} = 0$ occurs when σ_x is compressive (see 3.3.2):

$$\sigma_x \le -\left(\tau_{xy} + \tau_{xz}\right); \quad \left|\sigma_x\right| \ge \tau_{xy} + \tau_{xz}; \quad \left|\sigma_x\right| \ge \tau_{xy} \tag{3.66}$$

From (3.17)b, it may be shown, likewise, that $f_{ty} = 0$ occurs when σ_y is also compressive:

$$\sigma_y \le -\left(\tau_{xy} + \tau_{yz}\right); \quad \left|\sigma_y\right| \ge \tau_{xy} + \tau_{yz}; \quad \left|\sigma_y\right| \ge \tau_{xy} \tag{3.67}$$

Multiplying the latter two equations:

$$\sigma_x\sigma_y \ge \tau_{xy}^2 \tag{3.68}$$

Condition $I_{c2} > 0$ is evaluated as follows: rearranging I_{c2} into a common denominator, its numerator can be expressed as a sum of squared terms, so that it will be always positive:

$$\left(\sigma_x\tau_{yz} - \tau_{xy}\tau_{xz}\right)^2 + \left(\sigma_y\tau_{xz} - \tau_{xy}\tau_{yz}\right)^2 + \left(\sigma_x\sigma_y - \tau_{xy}^2\right)^2 \tag{3.69}$$

The sign of the denominator is also always positive. Since both numerator and denominator are positive, condition $I_{c2} > 0$ is confirmed to be met.

Condition $I_{c1} < 0$ is then evaluated as follows: rearranging I_{c1} into a common denominator, it is found that $I_{c1} < 0$ if:

$$\begin{aligned}&\sigma_x^2\sigma_y - \sigma_x\tau_{xy}^2 + \sigma_x\sigma_y^2 - \sigma_y\tau_{xy}^2 - 2\tau_{xy}\tau_{xz}\tau_{yz} + \sigma_x\tau_{yz}^2 + \sigma_y\tau_{xz}^2 = \\ &\quad = \sigma_x\sigma_y\left(\sigma_x + \sigma_y\right) - \tau_{xy}^2\left(\sigma_x + \sigma_y\right) + \left(-2\tau_{xy}\tau_{xz}\tau_{yz} + \sigma_x\tau_{yz}^2 + \sigma_y\tau_{xz}^2\right) < 0\end{aligned} \tag{3.70}$$

Multiplying all terms by $\sigma_x < 0$:

$$\sigma_x^2\sigma_y\left(\sigma_x + \sigma_y\right) - \sigma_x\tau_{xy}^2\left(\sigma_x + \sigma_y\right) + \left(-2\sigma_x\tau_{xy}\tau_{xz}\tau_{yz} + \sigma_x^2\tau_{yz}^2 + \sigma_x\sigma_y\tau_{xz}^2\right) > 0 \tag{3.71}$$

Substituting (σ_x . σ_y) as the sum of two terms ($\tau^2_{xy} + p$), where $p > 0$, Equation (3.71) turns into:

$$\underbrace{\left(\sigma_x^2 + \sigma_x\sigma_y\right)}_{>0}\underbrace{\left(\sigma_x\sigma_y - \tau_{xy}^2\right)}_{>0} + \underbrace{\left(\sigma_x\tau_{yz} - \tau_{xy}\tau_{xz}\right)^2 + p.\tau_{xz}^2}_{>0} > 0 \tag{3.72}$$

which confirms that $I_{c1} < 0$. Since $I_{c2} > 0$ and $I_{c1} < 0$, concrete is assured to be subjected to a biaxial compression state.

Reinforcement in the y-direction

Similarly, if (f_{tx}, f_{tz}) < 0 in (3.17), it is assumed that $f_{tx} = f_{tz} = 0$. Concrete is subjected to a biaxial compression stress state, and the equivalent stress in the *y*-direction reinforcement is given by:

$$f_{ty} = \sigma_y + \frac{2\tau_{xy}\tau_{xz}\tau_{yz} - \sigma_x\tau_{yz}^2 - \sigma_z\tau_{xy}^2}{\sigma_x\sigma_z - \tau_{xz}^2} \tag{3.73}$$

Reinforcement in the x-direction

If (f_{ty}, f_{tz}) < 0 in (3.17), it is assumed that $f_{ty} = f_{tz} = 0$. Concrete is subjected to a biaxial compression stress state, and the equivalent stress in the *x*-direction reinforcement is given by:

$$f_{tx} = \sigma_x + \frac{2\tau_{xy}\tau_{xz}\tau_{yz} - \sigma_y\tau_{xz}^2 - \sigma_z\tau_{xy}^2}{\sigma_y\sigma_z - \tau_{yz}^2} \tag{3.74}$$

3.4 Design case: Concrete stresses $\sigma_{c1} = \sigma_{c2} = 0$, $\sigma_{c3} < 0$

When the largest principal applied stress $\sigma_1 > 0$, reinforcement must be provided. If the applied stress field [σ] is equilibrated by concrete stresses such that the principal stresses σ_{c1} and σ_{c2} are zero, two mutually orthogonal set of crack planes, with normal $\overrightarrow{n_{c1}} = (\ell_1, m_1, n_1)$ and $\overrightarrow{n_{c2}} = (\ell_2, m_2, n_2)$, will be formed in the element. The concrete stress state of an element between cracks is one of uniaxial compression with $\sigma_{c3} < 0$, as shown in Figure 14.

The invariants of the concrete stress tensor are:

$$
\begin{aligned}
&I_{c3} = 0 \\
&I_{c2} = 0 \\
&I_{c1} = \sigma_{c1} + \sigma_{c2} + \sigma_{c3} = 0 + 0 + \sigma_{c3} = \sigma_{c3} < 0
\end{aligned} \tag{3.75}
$$

For the first set of planes, it can be written:

$$
[\sigma] \cdot \overrightarrow{n_{c1}} = [f_t] \cdot \overrightarrow{n_{c1}} + [\sigma_c] \cdot \overrightarrow{n_{c1}} \tag{3.76}
$$

in $\overrightarrow{n_{c1}}$, since $\overrightarrow{\rho_{c1}} = \vec{\sigma} + \vec{\tau} = 0$,

$$
[\sigma] \cdot \overrightarrow{n_{c1}} = [f_t] \cdot \overrightarrow{n_{c1}} \tag{3.77}
$$

For the second set of planes, it can be written:

$$
[\sigma] \cdot \overrightarrow{n_{c2}} = [f_t] \cdot \overrightarrow{n_{c2}} + [\sigma_c] \cdot \overrightarrow{n_{c2}} \tag{3.78}
$$

in $\overrightarrow{n_{c2}}$, since $\overrightarrow{\rho_{c2}} = \vec{\sigma} + \vec{\tau} = 0$,

$$
[\sigma] \cdot \overrightarrow{n_{c2}} = [f_t] \cdot \overrightarrow{n_{c2}} \tag{3.79}
$$

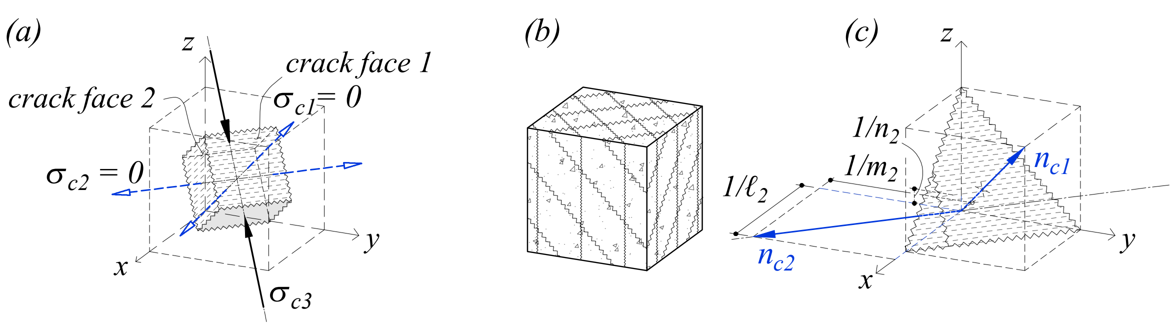

Source: Chen, Nogueira Bittencourt, and Della Bella (2023a).

Figure 14 – Design case with $\sigma_{c1} = \sigma_{c2} = 0$: (a) concrete principal stresses, (b) crack pattern, and (c) trihedron defined by a crack plane with crack direction in the first octant.

First, see that Equation (3.9) was obtained projecting the stress tensor in the direction of $\overrightarrow{n_{c1}}$:

$$
\begin{cases}
f_{tx} = \sigma_x + \tau_{xy} \dfrac{m_1}{\ell_1} + \tau_{xz} \dfrac{n_1}{\ell_1} \\[2ex]
f_{ty} = \sigma_y + \tau_{xy} \dfrac{\ell_1}{m_1} + \tau_{yz} \dfrac{n_1}{m_1} \\[2ex]
f_{tz} = \sigma_z + \tau_{xz} \dfrac{\ell_1}{n_1} + \tau_{yz} \dfrac{m_1}{n_1}
\end{cases} \tag{3.80}
$$

Repeating the same procedure for the plane with direction $\overrightarrow{n_{c2}}$, the reinforcement stresses on this plane are obtained:

$$\begin{cases} f_{tx} = \sigma_x + \tau_{xy}\dfrac{m_2}{\ell_2} + \tau_{xz}\dfrac{n_2}{\ell_2} & (a) \\ f_{ty} = \sigma_y + \tau_{xy}\dfrac{\ell_2}{m_2} + \tau_{yz}\dfrac{n_2}{m_2} & (b) \\ f_{tz} = \sigma_z + \tau_{xz}\dfrac{\ell_2}{n_2} + \tau_{yz}\dfrac{m_2}{n_2} & (c) \end{cases} \quad (3.81)$$

First, by equating f_t from (3.80) and (3.81), it is found that:

$$\begin{aligned} \frac{\tau_{xy}}{\tau_{xz}} &= \frac{n_2\ell_1 - n_1\ell_2}{m_1\ell_2 - m_2\ell_1} & (a) \\ \frac{\tau_{xy}}{\tau_{yz}} &= \frac{n_2m_1 - n_1m_2}{\ell_1m_2 - \ell_2m_1} & (b) \\ \frac{\tau_{xz}}{\tau_{yz}} &= \frac{m_2n_1 - m_1n_2}{\ell_1n_2 - \ell_2n_1} & (c) \end{aligned} \quad (3.82)$$

Second, vector $\overrightarrow{n_{c3}}$= (ℓ_3, m_3, n_3) can be expressed in terms of the components from the vector product:

$$\overrightarrow{n_{c3}} = \overrightarrow{n_{c1}} \times \overrightarrow{n_{c2}} = \left(m_1n_2 - m_2n_1,\ \ell_2n_1 - \ell_1n_2,\ \ell_1m_2 - \ell_2m_1\right) \quad (3.83)$$

The shear stresses relations (3.82)a and (3.82)b can be rewritten as a function of the coordinates of $\overrightarrow{n_{c3}}$:

$$\begin{aligned} \frac{\tau_{xy}}{\tau_{xz}} &= \frac{m_3}{n_3} & (a) \\ \frac{\tau_{xy}}{\tau_{yz}} &= \frac{\ell_3}{n_3} & (b) \end{aligned} \quad (3.84)$$

Therefore, it is possible to determine the direction $\overrightarrow{n_{c3}}$:

$$\overrightarrow{n_{c3}} = \left(\frac{\tau_{xy}}{\tau_{yz}}n_3,\ \frac{\tau_{xy}}{\tau_{xz}}n_3,\ n_3\right) \quad (3.85)$$

Dividing each of the three components of $\overrightarrow{n_{c3}}$ by (τ_{xy}. n_3), it is found that the direction of the compression is given by a vector with coordinates proportional to:

$$\overrightarrow{n_{c3}} = \left(\frac{1}{\tau_{yz}}, \frac{1}{\tau_{xz}}, \frac{1}{\tau_{xy}} \right) \tag{3.86}$$

Since $\sigma_{c1} = \sigma_{c2} = 0$, directions $\overrightarrow{n_{c1}}$ and $\overrightarrow{n_{c2}}$ may be any set of two arbitrary mutually orthogonal vectors, contained in a plane whose normal is $\overrightarrow{n_{c3}}$. A particular direction vector $\overrightarrow{n_{c2}} = (\ell_2, m_2, n_2) = (-n_3, 0, \ell_3)$ is chosen, which is perpendicular to $\overrightarrow{n_{c3}}$ as shown by the following scalar product:

$$\overrightarrow{n_{c2}} \bullet \overrightarrow{n_{c3}} = -n_3.\ell_3 + 0.m_3 + \ell_3.n_3 = 0 \tag{3.87}$$

Retaking Equation (3.81)a, and inserting (3.84)b:

$$f_{tx} = \sigma_x + \tau_{xy} \frac{0}{-n_3} + \tau_{xz} \frac{\ell_3}{-n_3} = \sigma_x - \frac{\tau_{xy}\tau_{xz}}{\tau_{yz}} \tag{3.88}$$

Adopting a new $\overrightarrow{n_{c2}} \perp \overrightarrow{n_{c3}}$ to avoid division by zero:

$$\overrightarrow{n_{c2}} = (\ell_2, m_2, n_2) = (0, -n_3, m_3)$$

Retaking Equation (3.81)b and inserting (3.84)a:

$$f_{ty} = \sigma_y + \tau_{xy} \frac{0}{-n_3} + \tau_{xz} \frac{m_3}{-n_3} = \sigma_y - \frac{\tau_{xy}\tau_{yz}}{\tau_{xz}} \tag{3.89}$$

Retaking Equation (3.81)c and inserting (3.84)a:

$$f_{tz} = \sigma_z + \tau_{xz} \frac{0}{m_3} + \tau_{yz} \frac{-n_3}{m_3} = \sigma_z - \frac{\tau_{xz}\tau_{yz}}{\tau_{xy}} \tag{3.90}$$

So that the equivalent reinforcement stresses are defined for this case:

$$\begin{cases} f_{tx} = \sigma_x - \dfrac{\tau_{xz}\tau_{xy}}{\tau_{yz}} \\ f_{ty} = \sigma_y - \dfrac{\tau_{xy}\tau_{yz}}{\tau_{xz}} \\ f_{tz} = \sigma_z - \dfrac{\tau_{xz}\tau_{yz}}{\tau_{xy}} \end{cases} \tag{3.91}$$

The concrete stress state is obtained by inserting (3.91) into (3.3):

$$[\sigma_c]=\begin{bmatrix} \dfrac{\tau_{xy}\tau_{xz}}{\tau_{yz}} & \tau_{xy} & \tau_{xz} \\ \tau_{xy} & \dfrac{\tau_{xy}\tau_{yz}}{\tau_{xz}} & \tau_{yz} \\ \tau_{xz} & \tau_{yz} & \dfrac{\tau_{xz}\tau_{yz}}{\tau_{xy}} \end{bmatrix} \tag{3.92}$$

The invariants of the concrete stress tensor are:

$$\begin{aligned} &I_{c3}=I_{c2}=0 \\ &I_{c1}=\sigma_{c3}=\frac{\tau_{xy}\tau_{xz}}{\tau_{yz}}+\frac{\tau_{xy}\tau_{yz}}{\tau_{xz}}+\frac{\tau_{xz}\tau_{yz}}{\tau_{xy}} \end{aligned} \tag{3.93}$$

Note from Equation (3.5) that $I_{c2}=I_{c3}=0$. Therefore, Equations (3.91) are applicable to all cases whereby $\tau_{xy}.\tau_{xz}.\tau_{yz}<0$, without restrictions. In some cases, there are solutions in either biaxial or uniaxial compression but, in these situations, reinforcement and principal stresses $|\sigma_{c3}|$ are larger for the uniaxial compression, especially when one of the tangential stresses gets closer to zero. Therefore, when $\tau_{xy}.\tau_{xz}.\tau_{yz}<0$, it should be prioritized the design for concrete under biaxial compression while Equation (3.24) applies.

In the particular case of uniaxial compression, all shear stresses contribute to σ_{c3}. Figure 15a presents an element subjected to a uniaxial compression stress state, where σ_{c3} is the principal stress and two crack planes are formed. Compression acts on an inclined plane characterized by a direction vector $\overrightarrow{n_{c3}}$. The stress state in the element is represented in a cube with unit dimension (Figure 15b). The resultant of the concrete stress in the plane xz is:

$$\vec{\rho}_B=\left(\sigma_x-f_{tx},\tau_{xy},\tau_{xz}\right)=\left(\frac{\tau_{xz}\tau_{xy}}{\tau_{yz}},\tau_{xy},\tau_{xz}\right)=\tau_{xz}\left(\frac{\tau_{xy}}{\tau_{yz}},\frac{\tau_{xy}}{\tau_{xz}},1\right) \tag{3.94}$$

Retaking Equation (3.85), the two vectors $\overrightarrow{\rho_B}$ and $\overrightarrow{n_{c3}}$ are verified to be parallel. The same verification applies to points A and C, from where it is found that $\overrightarrow{\rho_A}$, $\overrightarrow{\rho_B}$, $\overrightarrow{\rho_C}$ and $\overrightarrow{n_{c3}}$ are all parallel. By equilibrium, it is found that:

$$\sigma_{c3}=\rho_A+\rho_B+\rho_C \tag{3.95}$$

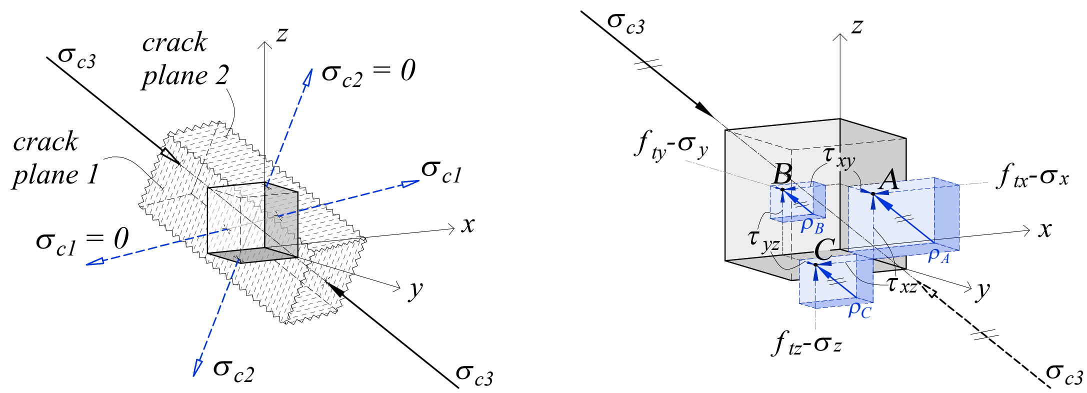

Source: Chen, Nogueira Bittencourt, and Della Bella (2023a).

Figure 15 – Two tensile concrete principal stresses: (a) uniaxial concrete compression σ_{c3}; (b) components equilibrating σ_{c3}.

3.4.1 Particular case: either $\tau_{xy} = \tau_{xz} = 0$, or $\tau_{xz} = \tau_{yz} = 0$, or $\tau_{xy} = \tau_{yz} = 0$

This case is identified in the shear stress space in Figure 11c. It corresponds to the highlighted continuous blue lines, which coincide simultaneously with the coordinate axes and the surface representing $I_{c2} = 0$. From Equation (3.20), for a crack direction in the ***first octant***, when $\tau_{xy} = \tau_{yz} = 0$ it is found that:

$$\begin{aligned} I_{c2} &= 0 \\ I_{c1} &= -2\tau_{yz} \end{aligned} \tag{3.96}$$

Since $I_{c2} = 0$, concrete will be subjected to a uniaxial compression stress state ($\sigma_{c1} = \sigma_{c2} = 0$). See Table C1 in Appendix C for the design cases with two simultaneous shear stress components in the ***second*** to the ***eighth octants***. All cases can be treated considering Equation (3.17) for crack directions in the first octant by assuming a positive value for the non-zero shear stress component. If one component in (f_{tx}, f_{ty}, f_{tz}) results negative, equivalent reinforcement stresses f_{ti} should be calculated as described in Section 3.3.2. If, however, two components in (f_{tx}, f_{ty}, f_{tz}) result negative, equivalent reinforcement stresses f_{ti} should be calculated as described in Section 3.3.3.

3.5 Design case: Concrete stresses $\sigma_{c1} = \sigma_{c2} = \sigma_{c3} = 0$

When the applied normal stresses are simultaneously tensile ($\sigma_i > 0$), and the applied shear stresses are zero ($\tau_{xy} = \tau_{xz} = \tau_{yz} = 0$), the concrete stresses are $\sigma_{c1} = \sigma_{c2} = \sigma_{c3} = 0$. In this case, cracks are formed in three mutually orthogonal directions (see Figure 16).

The invariants of the concrete stress tensor are $I_{c3} = I_{c2} = I_{c1} = 0$, and the applied stresses are resisted by the reinforcement alone:

$$\begin{cases} f_{tx} = \sigma_x \\ f_{ty} = \sigma_y \\ f_{tz} = \sigma_z \end{cases} \tag{3.97}$$

The concrete stress tensor is:

$$[\sigma_c] = \begin{bmatrix} 0 & 0 & 0 \\ 0 & 0 & 0 \\ 0 & 0 & 0 \end{bmatrix} \tag{3.98}$$

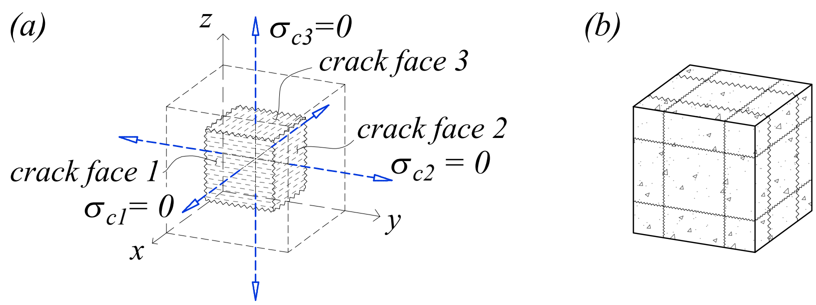

Source: Chen, Nogueira Bittencourt, and Della Bella (2023a).

Figure 16 – Design case with $\sigma_{c1} = \sigma_{c2} = \sigma_{c3} = 0$: (a) zero concrete stresses, and (b) crack pattern.

3.6 Design case: Concrete stresses $\sigma_{c1}, \sigma_{c2}, \sigma_{c3} < 0$

When the applied stress tensor is such that all concrete principal stresses are compressive (σ_{c1}, σ_{c2}, $\sigma_{c3} < 0$), concrete will be subjected to a triaxial compression stress state. The element remains uncracked, as shown in Figure 17, and no reinforcement is required:

$$f_{tx} = f_{ty} = f_{tz} = 0 \tag{3.99}$$

The concrete stress tensor is:

$$[\sigma_c] = \begin{bmatrix} \sigma_{c1} & 0 & 0 \\ 0 & \sigma_{c2} & 0 \\ 0 & 0 & \sigma_{c3} \end{bmatrix} \tag{3.100}$$

The invariants of the concrete stress tensor are:

$$
\begin{aligned}
&I_{c3} = 0 \\
&I_{c2} = \sigma_{c1}\sigma_{c2} + \sigma_{c1}\sigma_{c3} + \sigma_{c2}\sigma_{c3} < 0 \\
&I_{c1} = \sigma_{c1} + \sigma_{c2} + \sigma_{c3} < 0
\end{aligned}
\tag{3.101}
$$

This design case occurs when f_{tx}, f_{ty}, and f_{tz} all become negative in Equations (3.74), (3.73), and (3.63). The condition delimiting this design case is:

$$\sigma_x\sigma_y\sigma_z + 2\tau_{xy}\tau_{xz}\tau_{yz} - \sigma_x\tau_{yz}^2 - \sigma_y\tau_{xz}^2 - \sigma_z\tau_{xy}^2 < 0$$

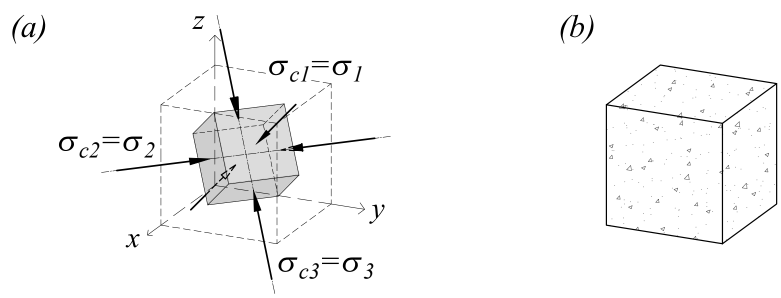

Source: Chen, Nogueira Bittencourt, and Della Bella (2023a).

Figure 17 – Design case: (a) compressive concrete stresses σ_{c1} , σ_{c2} , σ_{c3}; (b) uncracked element.

3.7 Dimensioning

3.7.1 Reinforcement design

Reinforcement is designed on the assumption of using the bars up to the design value, and stresses must be limited to:

$$f_{tx} \le \rho_{sx} f_{yd}; \quad f_{ty} \le \rho_{sy} f_{yd}; \quad f_{tz} \le \rho_{sz} f_{yd} \tag{3.102}$$

where ρ_{sx}, ρ_{sy}, ρ_{sz} are the reinforcement ratio in the x-, y- and z-directions, respectively, and f_{yd} is the design value of the reinforcement steel yield stress.

3.7.2 Concrete check

Concrete stresses are required to satisfy:

$$-\sigma_{c3} \le \nu f_{cd} \tag{3.103}$$

where f_{cd} is the design compression strength of concrete, and ν is the efficiency factor introduced to account for both confinement effects, as in the case of concrete in biaxial or triaxial compression, disturbance effects as those caused by transmission of tension fields through compression fields, and micro-cracking in the concrete paste due to shrinkage. Then, v accounts for the imperfect assumption that concrete behaves as a rigid-plastic material and ensures that ductility demands are met. The following values of v are indicated by the Model Code 2010 (*fib*, 2013):

- If no reinforcement has yielded and at least one principal stress is in tension, then:

$$\nu = \frac{1.18}{1.14 + 0.00166\sigma_{si}} \leq 1 \tag{3.104}$$

where σ_{si} is the maximum tensile stress (in MPa) in any layer of the reinforcing steel

- If one or more layers of reinforcement yield:

$$\nu = \left(1 - 0.032\left|\delta_i\right|\right)\frac{1.18}{1.14 + 0.00166 f_{yd}} \tag{3.105}$$

where δ_i (i = 1, 2, 3) is given by Equation (3.107).

- If all principal stresses are compressive, v may be taken as 1.0 or determined in accordance with more elaborate expressions for the strength under multiaxial states of stress, such as the one given by Ottosen (OTTOSEN, 1977; *fib*, 2013):

$$\alpha \frac{J_2}{f_{cm}^2} + \lambda \frac{\sqrt{J_2}}{f_{cm}} + \beta' \frac{I_1}{f_{cm}} - 1 = 0 \tag{3.106}$$

where I_1 and J_2 characterize the state of stress considered, and f_{cm} is the concrete uniaxial compressive strength.

In a solid subjected to increasing loads, the stress field is continuously redistributed, starting from an initial approximately elastic state, followed by cracking of concrete, and yielding of steel. Throughout this process, elements shall be capable of allowing for sufficient plastic strains to prevent local rupture before the calculated stress distribution has been attained. Foster, Marti and Mojsilović (2003) warn that "*designers must critically examine the load path being assumed to satisfy themselves that a sufficient level of ductility is available to meet the demands of the imposed tractions.*" For this purpose, they presented an expression for the enclosed angle between the principal direction of the applied stresses and those of the concrete stresses:

$$\delta_i \leq \cos^{-1}\left|n_{ix}n_{cix} + n_{iy}n_{ciy} + n_{iz}n_{ciz}\right| \tag{3.107}$$

where n_{ci} (i = 1, 2, 3) are the direction cosines of the concrete stress tensor. They suggested a limit of 25 degrees to δ_i, value that was later revised by the Model Code 2010 (*fib*, 2013) to 15 degrees (see Figure 18).

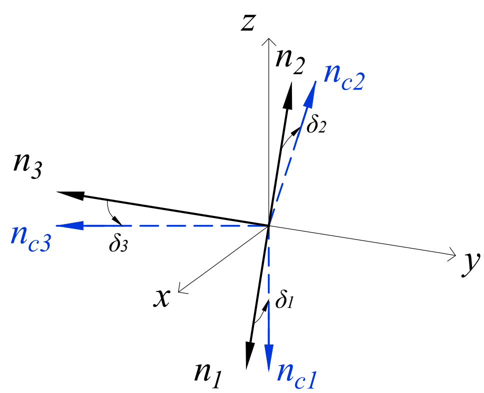

Source: adapted from Foster et al. (2003).

Figure 18 – Comparison of concrete principal stress directions and the principal stress directions for the case of optimum reinforcement.

3.8 Summary of design equations

The design equations in Sections 3.3 to 3.6 were written as a function of the six components of the applied stress tensor. The definition of the limits of application of each design equation is examined herein. For the first design case (σ_{c1} = 0, and σ_{c2}, σ_{c3} < 0), these limits are visualized in the shear stress space, as indicated in Section 3.3.1, since they rely on the shear stress components alone. However, for other design cases, the limits of application also depend on the concomitant applied normal stresses. One way to visualize the application of the design formulas is by ordering them as a function of the normal stresses applied to each coordinate direction, as shown in Figure 19. Arranging the f_{tx}, f_{ty}, and f_{tz} design equations in terms of σ_x when τ_{yz} > 0, for example, it is found that: for both tensile and "small" compressive stresses, Equation (3.17) applies; for "high" compressive stresses, the effect of shear stresses in the reinforcement is surpassed, and reinforcement in the x-direction is dispensed (Equation (3.39) applies). From eq. (3.74), it is observed that this is valid while f_{tx} remains positive, that is, while:

$$\sigma_x > \left(2\tau_{xy}\tau_{xz}\tau_{yz} - \sigma_y\tau_{xz}^2 - \sigma_z\tau_{xy}^2\right) / \left(\sigma_y\sigma_z - \tau_{yz}^2\right) \tag{3.108}$$

It should be emphasized that design equations, however, must be applied considering the behavior of the resisting mechanism in the three coordinate directions simultaneously.

Equations for computing the required reinforcement are then summarized in a framework suited for design practice in Table 1. The column "Condition 1" identifies positive and negative values for the calculated reinforcement stresses, whereas the column "Condition 2" identifies triaxial, biaxial or uniaxial compression stress states in concrete.

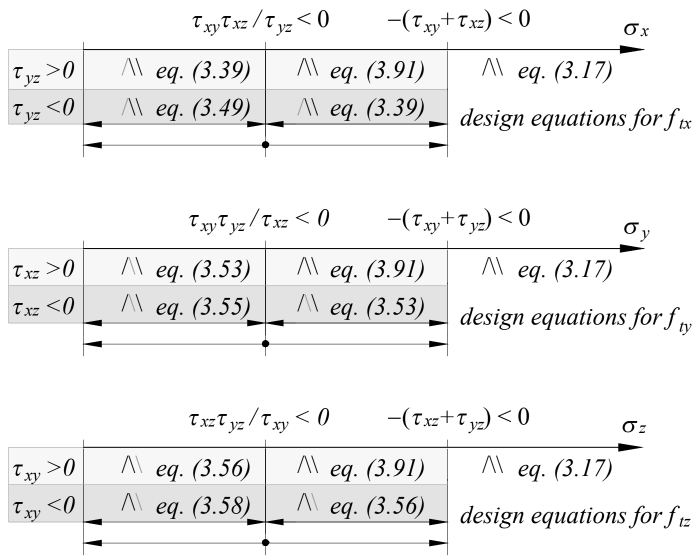

Source: Chen, Nogueira Bittencourt, and Della Bella (2023a)

Figure 19 – f_{tx}, f_{ty}, and f_{tz} design equations: intervals of application as a function of the applied normal stress in a chosen direction.

Table 1 – Summary of design equations

	Condition 1	*Condition 2*	f_{tx}	f_{ty}	f_{tz}
/\\	$\sigma_x \geq -(\tau_{xy}+\tau_{xz})$ $\sigma_y \geq -(\tau_{xy}+\tau_{yz})$ $\sigma_z \geq -(\tau_{xz}+\tau_{yz})$	$\tau_{xy}\tau_{xz}+\tau_{xy}\tau_{yz}$ $+\tau_{xz}\tau_{yz}>0$	$\sigma_x+\tau_{xy}+\tau_{xz}$	$\sigma_y+\tau_{xy}+\tau_{yz}$	$\sigma_z+\tau_{xz}+\tau_{yz}$
/\\	$\sigma_x < -(\tau_{xy}+\tau_{xz})$ $\sigma_y > -(\tau_{xy}+\tau_{yz})$ $\sigma_z > -(\tau_{xz}+\tau_{yz})$	$\sigma_x\tau_{yz} \leq \tau_{xy}\tau_{xz}$	0	$\sigma_y+\tau_{yz}+\tau_{xy}\dfrac{\tau_{xy}+\tau_{xz}}{-\sigma_x}$	$\sigma_z+\tau_{yz}+\tau_{xz}\dfrac{\tau_{xy}+\tau_{xz}}{-\sigma_x}$
/\\	$\sigma_x > -(\tau_{xy}+\tau_{xz})$ $\sigma_y < -(\tau_{xy}+\tau_{yz})$ $\sigma_z > -(\tau_{xz}+\tau_{yz})$	$\sigma_y\tau_{xz} \leq \tau_{xy}\tau_{yz}$	$\sigma_x+\tau_{xz}+\tau_{xy}\dfrac{\tau_{xy}+\tau_{yz}}{-\sigma_y}$	0	$\sigma_z+\tau_{xz}+\tau_{yz}\dfrac{\tau_{xy}+\tau_{yz}}{-\sigma_y}$
/\\	$\sigma_x > -(\tau_{xy}+\tau_{xz})$ $\sigma_y > -(\tau_{xy}+\tau_{yz})$ $\sigma_z < -(\tau_{xz}+\tau_{yz})$	$\sigma_z\tau_{xy} \leq \tau_{xz}\tau_{yz}$	$\sigma_x+\tau_{xy}+\tau_{xz}\dfrac{\tau_{xz}+\tau_{yz}}{-\sigma_z}$	$\sigma_y+\tau_{xy}+\tau_{yz}\dfrac{\tau_{xz}+\tau_{yz}}{-\sigma_z}$	0
/\\	$f_{tx}>0, f_{ty}<0$ in (3.56) or $f_{tx}>0, f_{tz}<0$ in (3.53)	---	$\sigma_x+\dfrac{2\tau_{xy}\tau_{xz}\tau_{yz}-\sigma_y\tau_{xz}^2-\sigma_z\tau_{xy}^2}{\sigma_y\sigma_z-\tau_{yz}^2}$	0	0
/\\	$f_{ty}>0, f_{tx}<0$ in (3.56) or $f_{ty}>0, f_{tz}<0$ in (3.39)	---	0	$\sigma_y+\dfrac{2\tau_{xy}\tau_{xz}\tau_{yz}-\sigma_x\tau_{yz}^2-\sigma_z\tau_{xy}^2}{\sigma_x\sigma_z-\tau_{xz}^2}$	0
/\\	$f_{tz}>0, f_{tx}<0$ in (3.53) or $f_{tz}>0, f_{ty}<0$ in (3.39)	---	0	0	$\sigma_z+\dfrac{2\tau_{xy}\tau_{xz}\tau_{yz}-\sigma_x\tau_{yz}^2-\sigma_y\tau_{xz}^2}{\sigma_x\sigma_y-\tau_{xy}^2}$
/\\ /\\	---	$\sigma_x\tau_{yz} > \tau_{xy}\tau_{xz}$	$\sigma_x-\dfrac{\tau_{xy}\tau_{xz}}{\tau_{yz}} \not< 0$	$\sigma_y-\dfrac{\tau_{yz}\tau_{xy}}{\tau_{xz}} \not< 0$	$\sigma_z-\dfrac{\tau_{xz}\tau_{yz}}{\tau_{xy}} \not< 0$
/\\ /\\	---	$\sigma_y\tau_{xz} > \tau_{xy}\tau_{yz}$			
/\\ /\\	---	$\sigma_z\tau_{xy} > \tau_{xz}\tau_{yz}$			
/\\	---	$\sigma_x\sigma_y\sigma_z+$ $+2\tau_{xy}\tau_{xz}\tau_{yz}$ $-\sigma_x\tau_{yz}^2-\sigma_y\tau_{xz}^2$ $-\sigma_z\tau_{xy}^2<0$	0	0	0

Notes: (1) Symbol convention: /\\ x-reinforcement; /\\ y-reinforcement; /\\ z-reinforcement.

(2) Sign convention for normal stresses: (+) for tension, (-) for compression.

(3) Sign convention for shear stresses:

a) Sign (τ_{xy}, τ_{xz}, τ_{yz}) = (+,+,+), or (+,-,-), or (-,+,-), or (-,-,+) → $\tau_{xy}.\tau_{xz}.\tau_{yz} > 0$ → consider (+,+,+);

b) Sign (τ_{xy}, τ_{xz}, τ_{yz}) = (+,+,-), or (+,-,+), or (-,+,+), or (-,-,-) → $\tau_{xy}.\tau_{xz}.\tau_{yz} < 0$ → sort ($|\tau_{xy}|$, $|\tau_{xz}|$, $|\tau_{yz}|$) in ascending order → consider the smallest shear stress component with its negative sign, and the remaining ones with positive value;

c) When one or more τ_{ij} =0, consider positive value for the non-zero shear stress components.

(4) Concrete stresses: $\sigma_{cx}= \sigma_x - f_{tx}$; $\sigma_{cy}= \sigma_y - f_{ty}$; $\sigma_{cz}= \sigma_z - f_{tz}$; concrete verification as described in Section 3.7.2.

(5) Reinforcement design: $\rho_{sx} = f_{tx} / f_{yd}$; $\rho_{sy} = f_{ty} / f_{yd}$; $\rho_{sz} = f_{tz} / f_{yd}$; and $a_{si}= \rho_{si}.\ A_c$.

3.9 Application examples for selected stress states

Selected application examples are presented and noted in Table 2.

Table 2 – Noted application examples.

		Applied stresses			Auxiliary stresses			Reinforcement stresses			Concrete stresses/invariants		
Exam. #	**Design Eq.**	σ_x τ_{xy}	σ_y τ_{xz}	σ_z τ_{yz}	σ_x τ^*_{xy}	σ_y τ^*_{xz}	σ_z τ^*_{yz}	f_{tx}	f_{ty}	f_{tz}	σ_{cx} σ_{c1} I_{c1}	σ_{cy} σ_{c2} I_{c2}	σ_{cz} σ_{c3} I_{c3}
1	(3.17)	2.00	3.00	2.50	2.00	3.00	2.50	3.20	4.00	6.30	-1.20	-1.00	-3.80
		-0.80	2.00	1.80	-0.80	2.00	1.80				0.00	-0.29	-5.71
											-6.00	1.68	0.00
2	(3.17)	2.00	3.00	2.50									
		0.80	**-2.00**	1.80		″			″			″	
3	(3.17)	2.00	3.00	2.50									
		0.80	2.00	**-1.80**		″			″			″	
	Examples #1, 2, and 3 show that when $\tau_{xy}.\tau_{xz}.\tau_{yz} < 0$, the smallest shear stress component alone should be considered with a negative value, as indicated in note 3 of Table 1. Concrete is subjected to a biaxial compression stress state. Eq. (3.17) indicates that reinforcement is required in three directions.												
4	(3.39)	**-1.20**	3.00	2.50	-1.20	3.00	2.50	0.00	3.97	5.97	-1.20	-0.97	-3.47
		-1.00	2.00	1.80	-1.00	2.00	1.80				0.00	-0.08	-5.56
											-5.63	0.43	0.00
	Starting from the stress state of Example #1, σ_x is reduced until it becomes compressive. Reinforcement in the x-direction is dispensed; concrete is subjected to a biaxial compression stress state.												
5	(3.63)	**-1.20**	**-1.20**	2.50	-1.20	-1.20	2.50	0.00	0.00	5.88	-1.20	-1.20	-3.38
		-1.00	2.00	1.80	-1.00	2.00	1.80				0.00	-0.24	-5.54
											-5.78	1.32	0.00
	Starting from the stress state of Example #4, σ_y is reduced until it becomes compressive. Reinforcement in the y-direction is also dispensed; concrete is still subjected to a biaxial compression stress state.												
6	(3.91)	**-1.05**	3.00	2.50	-1.05	3.00	2.50	0.06	3.90	6.10	-1.11	-0.90	-3.60
		-1.00	2.00	1.80	-1.00	2.00	1.80				0.00	0.00	-5.61
											-5.61	0.00	0.00
	Starting from the stress state of Ex. #1, σ_x is reduced until it becomes compressive, but still larger than $\tau_{xy}.\tau_{xz} / \tau_{yz}$. Reinforcement is required in three directions; concrete is under a uniaxial compression stress state.												
7	(3.99)	**-3.00**	**-3.00**	**-3.00**	-3.00	-3.00	-3.00	0.00	0.00	0.00	-3.00	-3.00	-3.00
		-1.00	2.00	1.80	-1.00	2.00	1.80				-0.76	-2.01	-6.24
											-9.00	18.76	-9.48
	Starting from the stress state of Example #5, three compression stresses are applied. No reinforcement is required; concrete is subjected to a triaxial compression stress state.												
8	(3.97)	2.00	3.00	4.00	2.00	3.00	4.00	2.00	3.00	4.00	0.00	0.00	0.00
		0.00	**0.00**	**0.00**	0.00	0.00	0.00				0.00	0.00	0.00
											0.00	0.00	0.00
	The shear stress components are zero, and three tensile stresses are applied. Reinforcement is required in three directions; concrete is cracked in these three directions.												
9	(3.17)	0.00	0.00	0.00	0.00	0.00	0.00	1.50	1.00	3.50	-1.50	-1.00	-3.50
		-0.50	2.00	1.50	-0.50	2.00	1.50				0.00	-0.71	-5.29
											-6.00	3.75	0.00
10	(3.91)	0.00	0.00	0.00	0.00	0.00	0.00	1.33	0.75	3.00	-1.33	-0.75	-3.00
		-1.00	2.00	1.50	-1.00	2.00	1.50				0.00	0.00	-5.08
											-5.08	0.00	0.00
	In Example #9, $\tau_{xy}\,\tau_{xz} + \tau_{xy}\,\tau_{yz} + \tau_{xz}\,\tau_{yz} > 0$. Concrete is subjected to a biaxial compression stress state. In Example #10, $\tau_{xy}\,\tau_{xz} + \tau_{xy}\,\tau_{yz} + \tau_{xz}\,\tau_{yz} < 0$. Concrete is subjected to a uniaxial compression stress state.												

4 Design method: formulation for SLS

The design method for ULS presented in the previous chapter assumed rigid perfectly plastic material behavior for both reinforcement and concrete. Once the yielding point is reached, the material deforms plastically, and infinite strains are associated to the constant yielding stress, such that a univocal strain field cannot be associated with the stress field. Verifications for SLS are, therefore, outside the scope of limit analysis and, so far, no information has been attained concerning the actual deformation or crack widths within the structure.

The alternative solution for SLS verification is to recur to assessment based on stress field approaches since "Other than for verifying the Ultimate Limit State, stress fields can be used to assess the serviceability response of structures." (*fib*, 2021, p. 28). More specifically, linear elastic stress fields are used for the analyses. Eurocode 2, when referring to the strut-and-tie method, states that "Verifications in SLS may also be carried out […] if approximate compatibility for strut-and-tie models is ensured (in particular the position and direction of important struts should be oriented according to linear elasticity theory" (CEN, 2004, Section 5.6.4 (2)). Kleissl and Ravn (2017) interpret that "by approximate compatibility is referred to that the position and direction of important struts shall be oriented according to compressive stress trajectories in the uncracked state based on linear elastic theory." Eurocode 2 also states that "When using strut-and-tie models with the struts oriented according to the compressive stress trajectories in the uncracked state, it is possible to use the forces in the ties to obtain the corresponding steel stresses to estimate the crack width" (CEN, 2004, Section 7.3.1 (8)). Similarly, the linear elastic stress fields can be used to estimate crack widths since reinforcement for the ULS are oriented by the struts in the uncracked state, according to the linear elasticity theory.

Over one hundred crack width formulas were categorized, in a comprehensive work by van der Esch et al. (2023), into three groups according to their application, representation, and background. Categorization by background identified the assumptions behind each formula, and sub-categorized them as either based on experiments, on fracture mechanics, on bond stress-slip relationships, or on semi-analytical models.

This chapter presents a design method for computation of crack widths in three-dimensional analysis based on semi-analytical models. The formulation is first presented for linear elements and then extended to membrane elements. Further extension for three-dimensional elements subjected to three-dimensional stress states is finally presented, such that the performance of the member under service loads can thereof be assessed. This completes the ULS and SLS design of a structural member.

4.1 Crack spacing

Crack width calculation methods are found in design codes such as Eurocode 2 (CEN, 2004) and *fib* Model Code 2010 (*fib*, 2013). They were critically assessed by Tan, Hendriks and Kanstad (2018). They pointed out large discrepancies in the computation of crack widths by different methods and suggested that a more consistent approach should be employed, by explicitly solving the expression for slip. This is, however, outside the scope of this work, and focus is given to the normative MC2010 formulation (*fib*, 2013; BALÁZS et al., 2013).

4.1.1 Basic crack width formula

Crack widths and spacing vary throughout a structural element. "Hence formulas for calculating the crack width and spacing frequently express a representative value of the calculated crack width, which might slightly deviate from actual crack widths observed on a structure." (van der ESCH et al., 2023, p.5). The *fib* Model Code 2010 calculates the design crack width by the following equation:

$$w_d = 2l_{s,\max}\left(\varepsilon_{sm} - \varepsilon_{cm} - \varepsilon_{cs}\right) \tag{4.1}$$

where:

$\ell_{s,max}$ is the transfer length over which slip between steel and concrete occurs. The maximum crack spacing, is given by $s_{r,max} = 2\ \ell_{s,max}$.

ε_{sm} is the average steel strain within $\ell_{s,max}$.

ε_{cm} is the average concrete strain within $\ell_{s,max}$.

ε_{cs} is the concrete strain due to shrinkage.

The transfer length is determined by a semi-analytical approach, meaning that formulas "are partially based on bond stress–slip relations and calibrated with experimental crack width and spacing measurements." (van der ESCH et al., 2023, p.7). It is calculated as a linear additive combination of two terms: the first one accounting for the influence of concrete cover, and the second one for the bond stress-slip:

$$l_{s,\max} = k \cdot c + \frac{1}{4} \cdot \frac{f_{ctm}}{\tau_{bms}} \cdot \frac{\phi_s}{\rho_{s,ef}} \tag{4.2}$$

where k is an empirical parameter considering the influence of the concrete cover c (as a simplification, k = 1.0 can be assumed); and τ_{bms} is the mean bond strength between steel and concrete ($\tau_{bms} = 1.8\, f_{ctm}$ for stabilized cracking stage, and long-term loading).

The relative mean strain follows from:

$$\left(\varepsilon_{sm} - \varepsilon_{cm} - \varepsilon_{cm}\right) = \frac{\sigma_s - \beta\sigma_{sr}}{E_s} - \eta_r\, \varepsilon_{sr} \tag{4.3}$$

where σ_s is the steel stress in a crack; and σ_{sr} is the maximum steel stress in a crack in the crack formation stage, which is, for pure tension:

$$\sigma_{sr} = \frac{f_{ctm}}{\rho_{s,ef}}\left(1 + \alpha_e \rho_{s,ef}\right) \tag{4.4}$$

where:

- $\rho_{s,ef}$ $= A_s/A_{c,ef}$. $A_{c,ef}$ is the effective area of concrete in tension (*fib*, 2013, Fig. 7.6-4).
- α_e the modular ratio = E_s/E_c.
- β is an empirical coefficient to assess the mean strain over $\ell_{s,max}$ depending on the type of loading (*fib*, 2013, Table 7.6-2).
- η_r is a coefficient for considering the shrinkage contribution.
- ε_{sh} is the shrinkage strain.

Equation (4.2) has been evaluated by several researchers. The formulas were found to generally tend to yield good results for relatively small specimens, but inconsistent results, and rather to the conservative side, for larger members (ROSPARS; CHAUVEL, 2014; TAN; HENDRIKS; KANSTAD, 2018). Also, the consideration of the cover term has been contested: Debernardi and Taliano (2016) proposed improved expressions for calculating the transfer length where the cover term was suppressed, and τ_{bm} was reduced taking into account the influence of the secondary cracks on the mean deformation. The equation for the transfer length was rewritten as a function not only of the concrete tensile strength, but also of the reinforcement ratio and bar diameter.

4.1.2 Two orthogonal reinforcement directions

For members reinforced in two orthogonal directions where cracks are expected to form at an angle which differs substantially from the direction of the reinforcement, that is, an angle larger than 15º, the *fib* Model Code 2010 (*fib*, 2013, Section 7.6.4.4.3) suggests the use of the following expression for the transfer length:

$$l_{s,\max,\theta} = \left(\frac{\cos\theta}{l_{sx,k}} + \frac{\sin\theta}{l_{sy,k}} \right)^{-1} \tag{4.5}$$

where θ denotes the angle between the reinforcement in the x-direction and the direction of the principal tensile stress, and $\ell_{sx,k}$ and $\ell_{sy,k}$ denote the slip lengths in the two orthogonal directions, so that the design crack width can be calculated from:

$$w_d = 2 l_{s,\max,\theta} \left(\varepsilon_{\perp} - \varepsilon_{c,\perp} \right) \tag{4.6}$$

where $\varepsilon_{\perp}$ and $\varepsilon_{c,\perp}$ represent the mean strain and the mean concrete strain, evaluated in the direction orthogonal to the crack.

4.1.3 Three orthogonal reinforcement directions

The crack width formulation was extended to elements reinforced in three orthogonal directions by Hoogenboom and de Boer (2008, 2011). In their formulation, which is reproduced as follows, cracks are expected to form in up to three directions, and the mean crack spacing s_x, s_y, s_z for uniaxial tension in the reinforcement directions is calculated from the MC90 simplified equation for stabilized cracking (CEB-FIP, 1993):

$$l_{s,\max} = \frac{\phi_s}{3.6 \rho_{s,ef}} \tag{4.7}$$

$$s_x = \frac{2}{3} \times \frac{\phi_x}{3.6 \rho_x}; \quad s_y = \frac{2}{3} \times \frac{\phi_y}{3.6 \rho_y}; \quad s_z = \frac{2}{3} \times \frac{\phi_z}{3.6 \rho_z} \tag{4.8}$$

where ϕ_x, ϕ_y, ϕ_z are the diameter of the reinforcing bars in the *x*-, *y*-, *z*-directions, respectively. Crack spacing *s* in the principal direction *i* (*i*= 1, 2, 3) is computed from:

$$\frac{1}{s_i} = \frac{|\cos\alpha_i|}{s_x} + \frac{|\cos\beta_i|}{s_y} + \frac{|\cos\gamma_i|}{s_z} \tag{4.9}$$

where α, β and γ are the angles of the crack face normal vector.
The mean crack width in the principal direction *i* is:

$$w_i = s_i \left(\varepsilon_i - \varepsilon_c - \varepsilon_s \right) \tag{4.10}$$

For simplicity, they assumed that the concrete strain ($\varepsilon_c > 0$) and the concrete shrinkage ($\varepsilon_s < 0$) cancel each other out, such that the crack width is given by: $w_i = s_i \, \varepsilon_i$.

4.2 Crack width computation and control

Once the reinforcement is determined from the ULS design, an iterative approach may be employed to estimate the cracking behavior under the applied stress tensor. Hoogenboom and de Boer (2008) proposed a source code for the numerical computation of crack widths of elements under three-dimensional stresses, which is described as follows.

Concrete principal stresses and the principal strains are assumed to have the same direction, and crack directions, which are perpendicular to the principal directions, continuously follow the orientation of the principal strains, according to the rotating crack concept. Also assumed is that aggregate interlock can carry any shear stress in the crack. Concerning the material models for the serviceability limit state, the following constitutive relations are assumed: for the reinforcing bars, linear elastic constitutive relation, since yielding is supposed not to occur in the SLS; for concrete in compression, linear elastic (uncracked) constitutive relation in the principal directions, and Poisson's ratio is set to zero.

Equilibrium equation for the applied stresses resisting mechanism can be rewritten to:

$$\begin{bmatrix} \sigma_x & \tau_{xy} & \tau_{xz} \\ \tau_{xy} & \sigma_y & \tau_{yz} \\ \tau_{xz} & \tau_{yz} & \sigma_z \end{bmatrix} = P \begin{bmatrix} \sigma_{c1} & 0 & 0 \\ 0 & \sigma_{c2} & 0 \\ 0 & 0 & \sigma_{c3} \end{bmatrix} P^{-1} + \begin{bmatrix} \rho_x \sigma_{sx} \\ \rho_y \sigma_{sy} \\ \rho_z \sigma_{sz} \end{bmatrix} \tag{4.11}$$

where σ_{sx}, σ_{sy}, σ_{sz} are the mobilized stresses in the reinforcement in service condition ($< f_y$) and:

$$P = \begin{bmatrix} \cos\alpha_1 & \cos\alpha_2 & \cos\alpha_3 \\ \cos\beta_1 & \cos\beta_2 & \cos\beta_3 \\ \cos\gamma_1 & \cos\gamma_2 & \cos\gamma_3 \end{bmatrix} = \begin{bmatrix} l_1 & l_2 & l_3 \\ m_1 & m_2 & m_3 \\ n_1 & n_2 & n_3 \end{bmatrix} \tag{4.12}$$

The columns in P are the vectors of the concrete principal directions. Constitutive relation for tensioned concrete follows the Modified Compression Field Theory (VECCHIO; COLLINS, 1986):

$$\sigma_{ci} = f_{ctm} \Big/ \left(1 + \sqrt{500\varepsilon_i}\right) \tag{4.13}$$

where f_{ctm} is the concrete mean tensile strength, and ε_i ($i = 1, 2, 3$) are the principal strains, that is, the eigenvalues of the strain tensor:

$$\begin{bmatrix} \varepsilon_x & \tfrac{1}{2}\gamma_{xy} & \tfrac{1}{2}\gamma_{xz} \\ \tfrac{1}{2}\gamma_{xy} & \varepsilon_y & \tfrac{1}{2}\gamma_{yz} \\ \tfrac{1}{2}\gamma_{xz} & \tfrac{1}{2}\gamma_{xy} & \varepsilon_z \end{bmatrix} = P \begin{bmatrix} \varepsilon_1 & 0 & 0 \\ 0 & \varepsilon_2 & 0 \\ 0 & 0 & \varepsilon_3 \end{bmatrix} P^{-1} \tag{4.14}$$

where $\varepsilon = \sigma/E_c$; $\gamma = \tau/G_c$ (E_c and G_c are the concrete elastic and shear modulus, respectively).

The iterative process aims at solving the strain tensor numerically by the modified Newton-Raphson method with initial stiffness, as represented in Figure 20, where i represents the number of the iteration. Given the service stress state ($\boldsymbol{\sigma}^{SLS}$) and the reinforcement ratios calculated from the design method for the ULS presented in Chapter 3 (ρ_{sx}, ρ_{sy}, ρ_{sz}), the process starts by calculating the linear elastic strains for uncracked concrete ($\boldsymbol{\varepsilon}^0$). The effective stresses mobilized in the cracked concrete ($\boldsymbol{\sigma_c}^0$) and reinforcement ($\boldsymbol{f_t}^0$), corresponding to the linear strains, are then summed to give the total mobilized stress ($\boldsymbol{\sigma}^0$). The residual strain ($\Delta\boldsymbol{\varepsilon}^0$), corresponding to the residual stress ($\Delta\boldsymbol{\sigma}^0$), is used to update the previous strain to the first estimation of the strain of the cracked concrete ($\boldsymbol{\varepsilon}^1$). The incremental strains in the successive iterations are updated until the residual stress falls below a threshold defined by the designer. In the proposed procedure, the threshold value is defined by a variable computing the sum of the six stress components of the residual stress, set as 0.01 MPa.

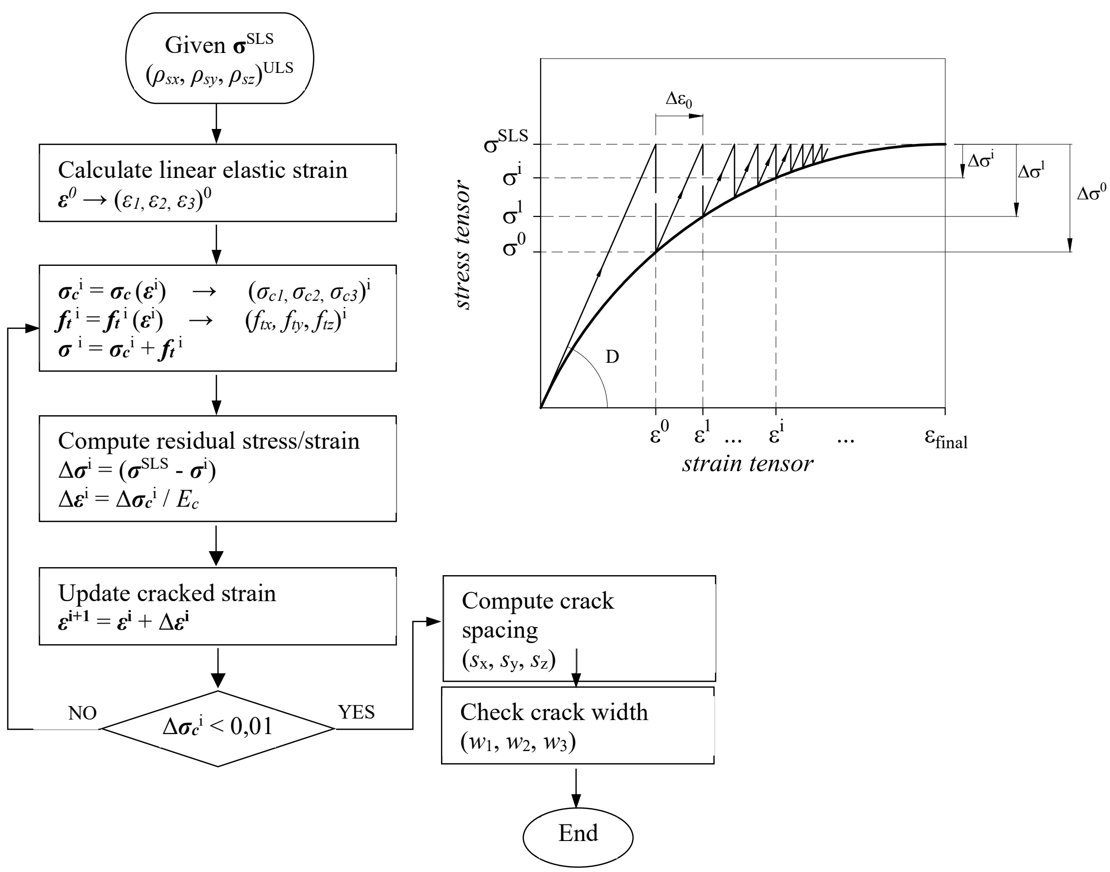

Figure 20 – Flowchart and graphical representation of the iterative procedure for crack width verification.

The crack width is limited to a maximum value $w_i \leq w_{max}$ (i = 1, 2, 3). If the condition is not fulfilled in a specific direction, the reinforcement amount should be increased in this direction, and the verification process should be restarted for the new reinforcement arrangement.

4.3 Discussion

The crack widths were verified following an iterative procedure at individual integration points of the structural model.

Alternatively, crack widths could have been computed by full numerical simulations of the designed structural members. However, as discussed in Section 1.1, those simulations require extensive modeling and analysis time and computational resources, making this solution impractical in design practice.

Two further comments on the standard formulas used to calculate crack widths are pointed out. First, it is noted that to disregard the first term in Equation (4.2), which is related to the concrete cover, is reasonable and advisable when applying the formulation for massive structures, whereby reinforcement is placed throughout the member volume. Second, it is indicated that Bastekår et al. (2019) presented a work evaluating under what circumstances, and to what extent, SLS requirements can exceed the ULS requirement.

Automatic crack width computation offers a powerful tool for verifying serviceability limit state (SLS) requirements. Although not implemented in the automatic ultimate limit state (ULS) design due to time constraints, the formulation presented can directly couple ULS and SLS verifications.

5 Design of structural members: examples

The SFM was applied to the design of five selected examples to allow for discussing aspects of the complete design process including: construction of the numerical model, treatment of singularities, handling of multiple load cases and complex geometries, provision of minimum reinforcement, checking for anchorage of rebars, and their detailing.

5.1 Methodology for ULS design of a structural member

The methodology for designing reinforced concrete structural members based on three-dimensional stress fields (SFM) followed three well-delimited steps, as described by Chen, Bittencourt and Della Bella (2023b):

> **Step 1: Linear analysis.** An initial linear analysis was performed with the software *STRAP* version 12.5 from *Atir Engineering Software Development Ltd.* (ATIR, 2005). The structure was modeled with finite solid elements assuming uncracked material, linear stress-strain relationships, and the mean value of the concrete modulus of elasticity. From this initial model two output **.lst* files were obtained: one containing the geometry definition (nodal coordinates and element nodal incidence), and the other containing the complete stress field deriving from the analysis (nodal stresses).
>
> **Step 2: Data processing – individual element SFM[1] design.** An application was developed with Java programming language for data treatment using *Java Development Kit JDK 17*. This application was built to: (i) read the data from the **.lst* files created in step 1; (ii) treat the data, computing stress invariants, principal stresses and directions, and equivalent resisting stresses in each model node (both reinforcement stresses f_{tx}, f_{ty}, f_{tz} and concrete stresses); (iii) automatically assemble the calculated quantities into a **.vtk* file to be later accessed by a post processor. The flowchart of the application structure is presented in Figure 21.
>
> **Step3: Data analysis and structural member SFM [1] design.** The **.vtk* file was loaded into software *ParaView* version 5.9.1 from *Kitware Inc.* This software, described by Ahrens, Geveci and Law (2005), is an open-source software system for 3D computer graphics, modeling, volume rendering and information visualization by operations such as clipping, slicing, filtering, or generating contours from the loaded data. At this point, a thorough analysis of the reinforcement requirements and concrete stresses sufficed for the global structural design and subsequent detailing by delimitation of zones with constant reinforcement ratio.

[1] Originally termed “RSM”, but herein referred to as “SFM”, following the dissertation nomenclature.

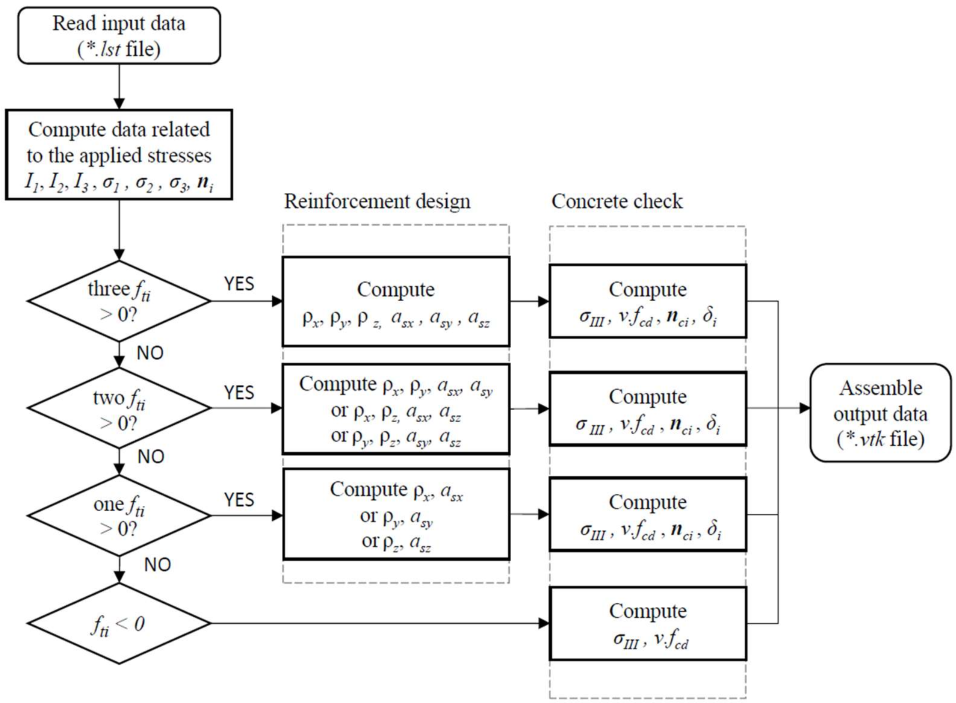

Source: adapted from Chen, Bittencourt, and Della Bella (2023b)

Figure 21 – Flowchart of the developed application.

STRAP was chosen for the static linear elastic finite element analysis because it offered a user-friendly interface for finite solid element mesh generation and boundary condition application, and was concurrently cost-effective. Although other software with more extensive modelling and post-processing capabilities do exist, cost considerations limited their selection. *ParaView*, in turn, was chosen for post-processing the results due to its accessibility as a free open-source software, and its strong resources for data manipulation and visualization.

Assessment of concrete behavior was obtained with the aid of two variables created to assess the concrete strength in the design process: the *Ottosen* variable for concrete strength under triaxial compression (if *Ottosen* < 0, no failure occurs); and the *ConcFailRel* variable for concrete under bi- or uniaxial compression (it indicates the ratio between concrete maximum compression in relation the assumed compression strength):

$$\begin{aligned} Ottosen &= \alpha \frac{J_2}{f_{cm}^2} + \lambda \frac{\sqrt{J_2}}{f_{cm}} + \beta' \frac{I_1}{f_{cm}} - 1 \\ ConcFailRel &= \frac{\sigma_{c3}}{\nu\, f_{cd}} \end{aligned} \tag{5.1}$$

5.2 Example 1: cantilever beam

The first example presents the application of the design method based on three-dimensional stress fields (SFM) to a simply supported beam with a 0.40 m x 0.80 m rectangular cross-section, span length of 8.35 m, and a cantilever with a length of 2.65 m. The left and right supports were 0.20 m and 0.30 m wide, respectively, both extending through the width of the concrete beam. A uniformly distributed design load of 112,5 kN/m acted over the span, and a concentrated design load of 270 kN acted on the cantilever, at 2.15 m from the support. The beam should be designed with normal-weight concrete C30 and B500 reinforcement (f_y = 500 MPa).

This practical example was chosen to illustrate the application of the design method to a linear structural member subjected to combined flexure and shear forces.

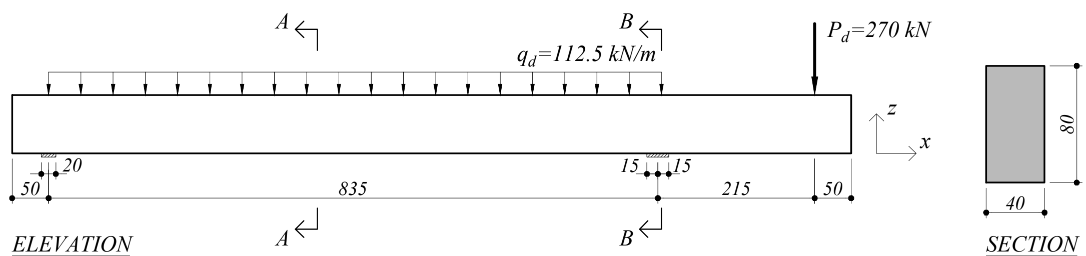

Figure 22 – Beam with cantilever: Geometry and loading (dimensions in cm).

5.2.1 Structural model for the linear analysis

The structural model elaborated for the linear elastic analysis was meshed with cubic elements with dimension of 0.10 m, leading to a model with 3,680 cubic solid elements, as shown in Figure 23. Four elements were distributed along the beam width, and eight elements along the beam height.

The concentrated design load was applied as a pressure load of q_1 = 270 / (0.10 x 0.40) = 6,750 kN/m²; the linear design load was applied as a pressure of q_2 = 112.5 / 0.40 = 281.3 kN/m². Specifically for this model, reaction forces which equilibrated the structural model in the *z*-direction were also applied as pressure loads: q_{left} = 405 / (0.20 x 0.40) = 5,063 kN/m², and q_{right} = 810 / (0.30 x 0.40) = 6,750 kN/m². Point supports were then defined to restrain the model, without mobilizing reaction forces at all. The beam was modeled with modulus of elasticity E_c = 26,070 MPa and Poisson's ratio ν = 0.2.

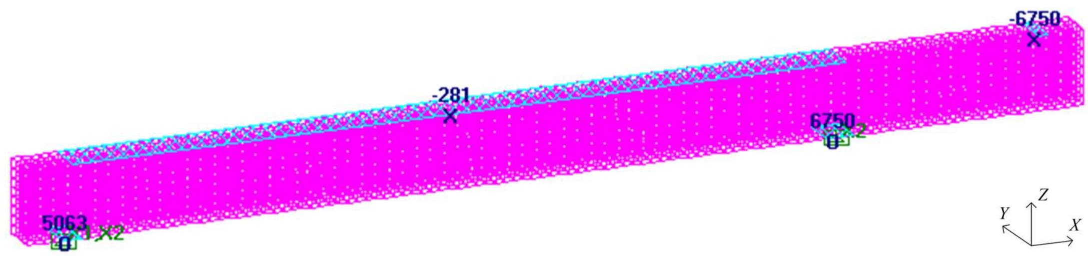

Figure 23 – Cantilever beam: structural model for the linear analysis: boundary conditions and applied loads.

5.2.2 Reinforcement design

Proceeding to Step 3 of the methodology described in Section 5.1, reinforcement stress distributions were analyzed in each coordinate direction with the aid of the post processor *ParaView*. Figures were prepared with color scales of the f_t values at the center of the elements.

f_{tx} distribution is shown in Figure 24, where elements with zero stress were filtered out. In the midspan region, reinforcement stresses developed in the x-direction along the lower mid-depth of the beam, reaching the peak value of 14.4 MPa. Above the right support, reinforcement stresses developed along the upper mid-depth of the beam, reaching the peak value of 11.3 MPa.

f_{ty} distribution is shown in Figure 25, where elements with stress smaller than 0.01 MPa were filtered out. Stresses in the y-direction were mostly null, as expected for the behavior of the linear member. Stresses f_{ty} amounted to only just 0.22 MPa, which is equivalent to 0.15 f_{ctd}. They were mainly found in the tension faces of the beam, along 0.10 m of the beam depth, but further developed in the projection of the applied loads.

f_{tz} distribution is shown in Figure 26, where elements with stress smaller than 0.05 MPa were filtered out. Regions with the higher stresses in the z-direction corresponded to those with higher shear forces. The peak value of 2.12 MPa occurred at the beam mid-depth, close to the left side of the right support. Stresses amounting to about 1.40 MPa occurred close to left support. Reinforcement resisting stresses of 1.40 MPa were also required and along the cantilever length, at the beam mid-depth, for the suspension of the concentrated load.

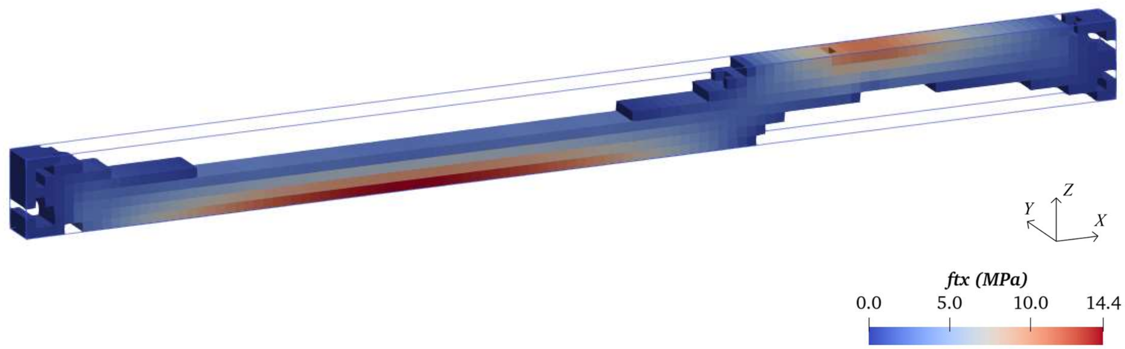

Figure 24 – Cantilever beam: reinforcement stresses f_{tx}.

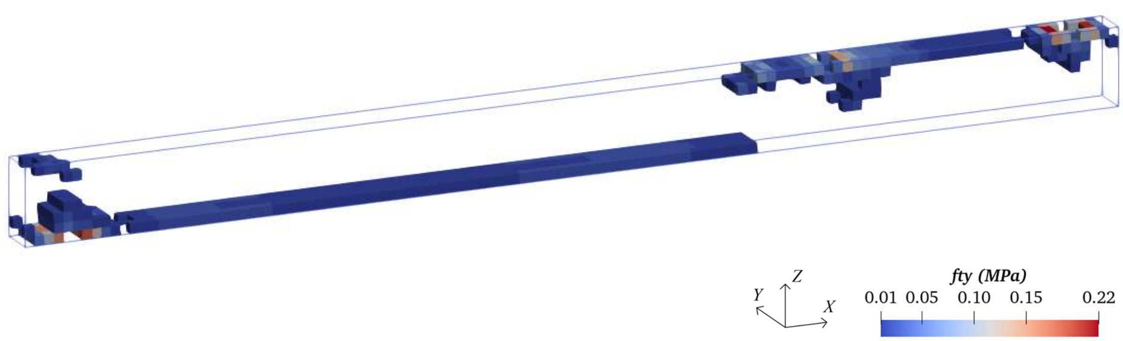

Figure 25 – Cantilever beam: reinforcement stresses f_{ty}.

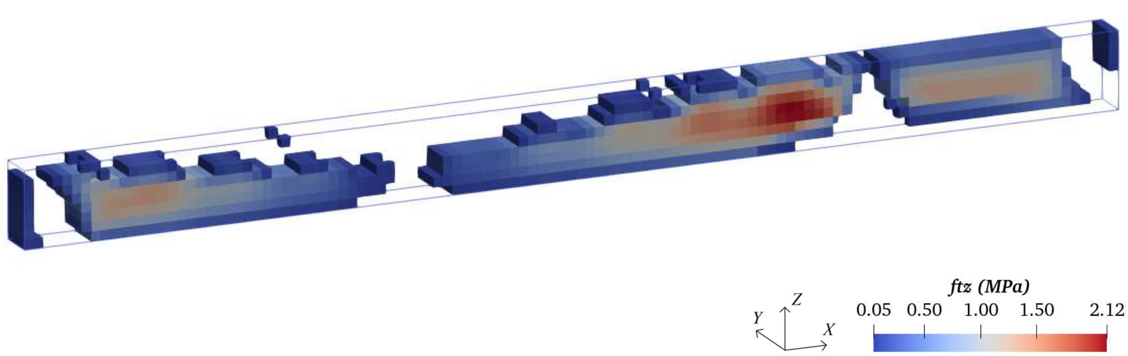

Figure 26 – Cantilever beam: reinforcement stresses f_{tz}

5.2.3 Concrete check

Verification of concrete against crushing was performed in two stages. First, elements under triaxial compression were filtered out and verified to respect the Ottosen failure criterion as shown in Figure 27: since the *Ottosen* variable was smaller than zero for all filtered elements, it is certified that the stress states did not exceed concrete multiaxial strength. Second, elements under biaxial and uniaxial compression were filtered out (Figure 28a). All elements with variable *ConcFailRel* < 1.0 were verified to respect the design compression strength of concrete, properly accounting for reduction introduced by the v efficiency factor. The elements filtered out in Figure 28b presented *ConcFailRel* ≥ 1.0, which indicated, at first sight, that they did not respect the failure criteria. Further analyses showed that the element with the highest *ConcFailRel* variable, for example, was subjected to the following stress state (in MPa):

$$\begin{bmatrix} \sigma_x & \tau_{xy} & \tau_{xz} \\ \tau_{xy} & \sigma_y & \tau_{yz} \\ \tau_{xz} & \tau_{yz} & \sigma_z \end{bmatrix} = \begin{bmatrix} -14.25 & 0 & -0.02 \\ 0 & 0 & 0 \\ 0 & 0 & 0 \end{bmatrix} \tag{5.2}$$

which corresponded to the principal stresses (in MPa):

$$\begin{bmatrix} \sigma_1 & 0 & 0 \\ 0 & \sigma_2 & 0 \\ 0 & 0 & \sigma_3 \end{bmatrix} = \begin{bmatrix} 2.8e-5 & 0 & 0 \\ 0 & 0 & 0 \\ 0 & 0 & -14.25 \end{bmatrix} \tag{5.3}$$

with a small tensile principal stress σ_1 and negligible associated reinforcement stress in the z-direction:

$$\left(f_{tx}, f_{ty}, f_{tz}\right) = \left(0, 0, 2.8e-5\right) \tag{5.4}$$

Indeed, the stress state given in Equation (5.3) can be considered as one of uniaxial compression: since in a real structure, those elements will not crack, concrete check for the elements from Figure 28b was performed following the Ottosen failure criteria.

The extended application of the *Ottosen* criterion is presented in Figure 29a: since all elements presented negative values for the *Ottosen* variable, it was guaranteed that the concrete strength was respected. The remainder elements, shown in Figure 29b adequately presented *ConcFailRel* < 1.0.

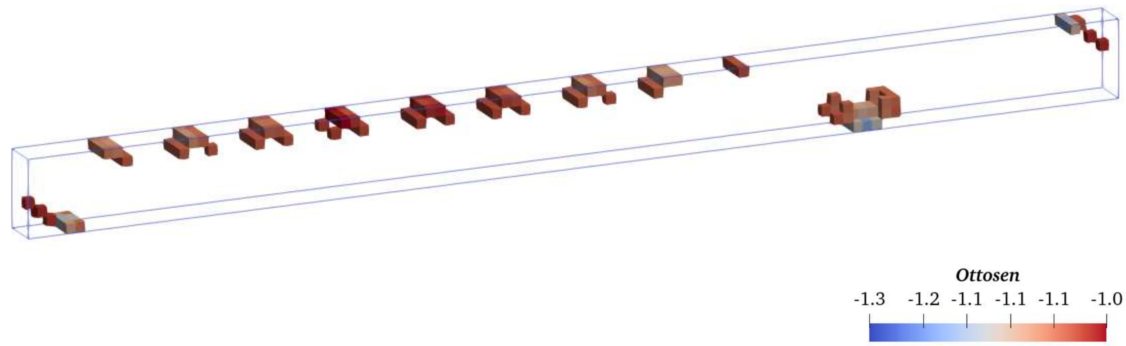

Figure 27 – Cantilever beam: *Ottosen* variable for concrete under triaxial compression

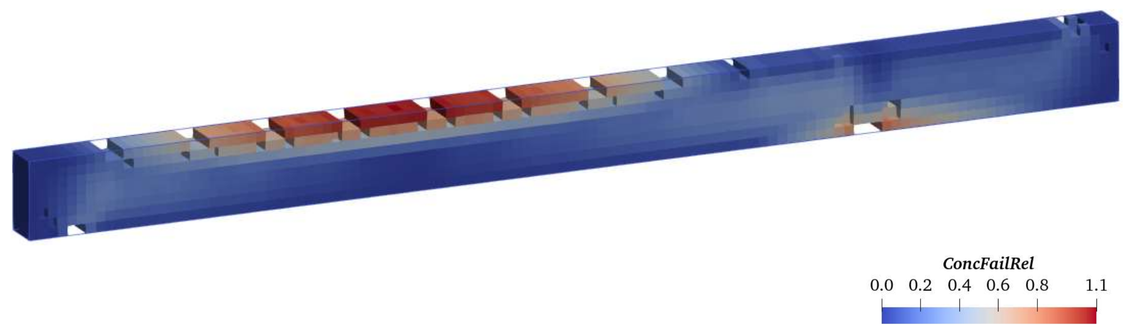

(a)

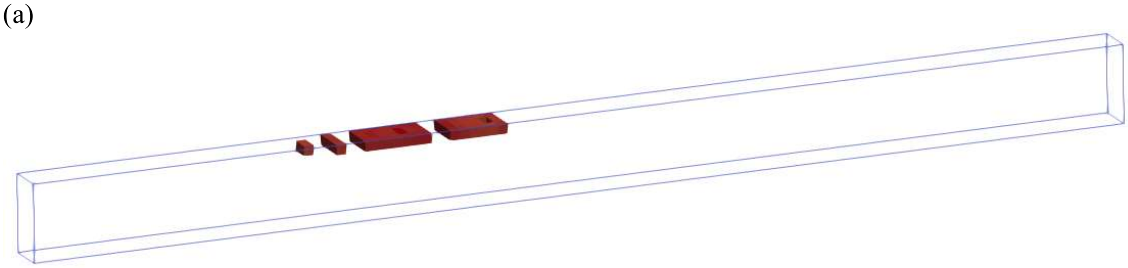

(b)

Figure 28 – Cantilever beam: (a) *ConcFailRel* for elements under bi- and uniaxial compresion; (b) elements with *ConcFailRel* ≥ 1.0.

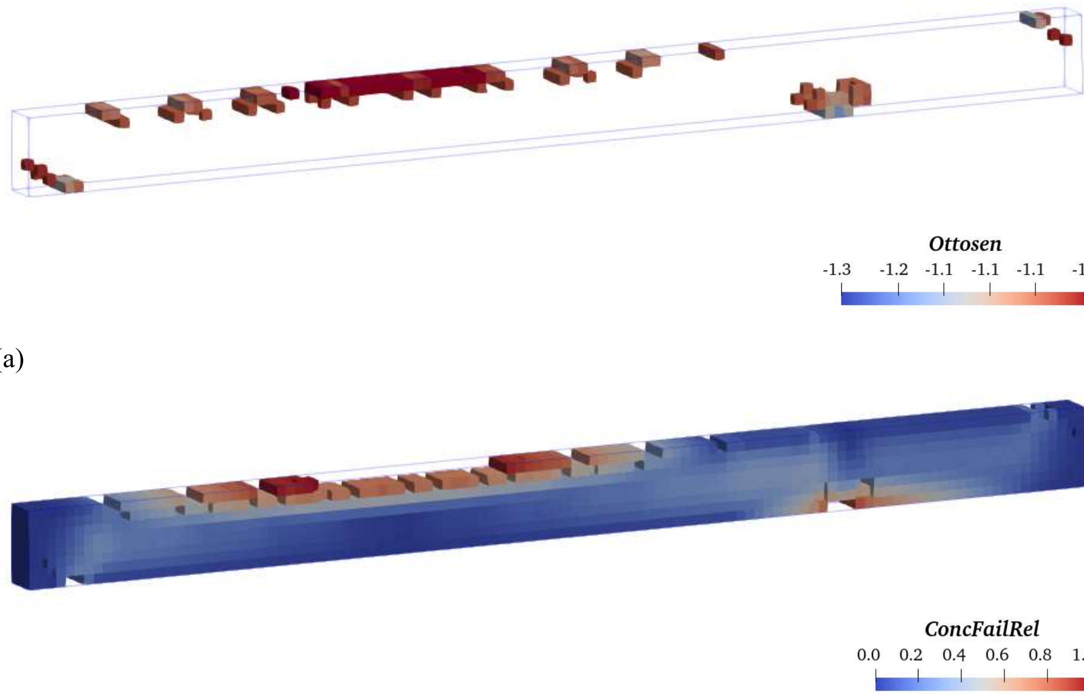

(a)

(b)

Figure 29 – Cantilever beam: (a) *Ottosen* variable extended to the elements indicated in Figure **28**b; (b) *ConcFailRel* for the remainder of the elements.

5.2.4 Detailing

Reinforcement stresses in the *x*-direction were analyzed in two transversal *YZ* cross-sections, one at the beam span (section *A-A*) and the other at the right support (section *B-B*). Different reinforcement arrangements were designed for each row of elements, that is, constant resisting reinforcement stresses were provided along 0.10 m intervals in the beam height. In the midspan (Figure 30), the arrangement was defined as follows:

$$
\begin{aligned}
f_{tx} &= 2.1MPa \rightarrow \rho_{sx} = 0.48\% \rightarrow A_{sx} = 1.9cm^2 \rightarrow 2\phi 12 \\
f_{tx} &= 6.2MPa \rightarrow \rho_{sx} = 1.40\% \rightarrow A_{sx} = 5.7cm^2 \rightarrow 3\phi 16 \\
f_{tx} &= 10.3MPa \rightarrow \rho_{sx} = 2.37\% \rightarrow A_{sx} = 9.5cm^2 \rightarrow 5\phi 16 \\
f_{tx} &= 14.4MPa \rightarrow \rho_{sx} = 3.31\% \rightarrow A_{sx} = 13.2cm^2 \rightarrow 5\phi 20
\end{aligned}
\tag{5.5}
$$

In section *B-B* (Figure 31), the arrangement was defined from the calculations below:

$$
\begin{aligned}
f_{tx} &= 11.3MPa \rightarrow \rho_{sx} = 2.59\% \rightarrow A_{sx} = 10.4cm^2 \rightarrow \quad 4\phi 20 \\
f_{tx} &= 7.8MPa \rightarrow \rho_{sx} = 1.79\% \rightarrow A_{sx} = 7.2cm^2 \quad \rightarrow \quad 4\phi 16 \\
f_{tx} &= 4.7MPa \rightarrow \rho_{sx} = 1.08\% \rightarrow A_{sx} = 4.3cm^2 \quad \rightarrow \quad 3\phi 16 \\
f_{tx} &= 1.8MPa \rightarrow \rho_{sx} = 0.41\% \rightarrow A_{sx} = 1.6cm^2 \quad \rightarrow \quad 2\phi 12
\end{aligned} \tag{5.6}
$$

Reinforcement stresses in the *y*-direction were analyzed in a longitudinal *XZ* cross-section (Figure 32a). Critical design values were grouped into three bands. Reinforcement stresses, amounting to 0.22 MPa at the outer bands, were resisted by the horizontal bends of the closed stirrups.

$$
\begin{aligned}
f_{ty} &= 0.22MPa \\
\rho_{sy} &= \frac{0.22}{434.8} = 0.05\% \\
A_{sy} &= 0.05\% \times 100 \times 10 = 0.5\ cm^2 / m
\end{aligned} \tag{5.7}
$$

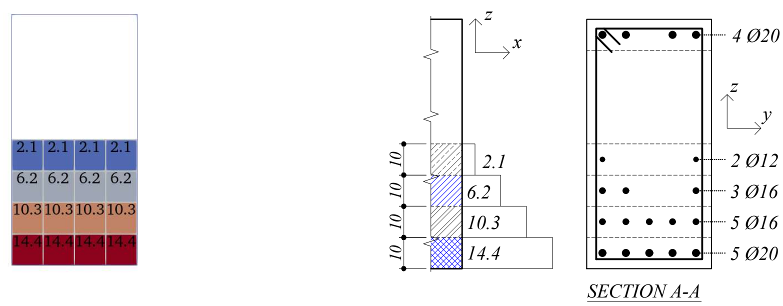

(a) (b) (c)

Figure 30 – Cantilever beam: (a) f_{tx} at midspan cross-section; (b) assumed f_{tx}; (c) *x*-reinf.

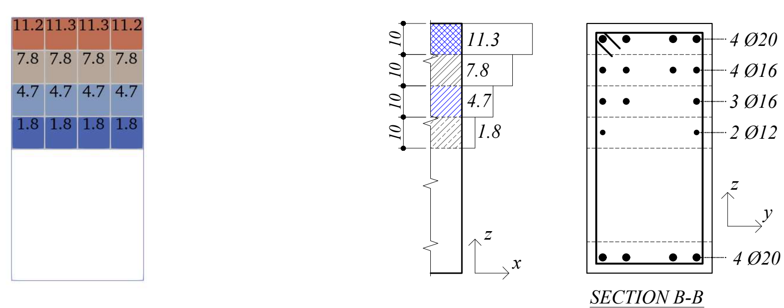

(a) (b) (c)

Figure 31 – Cantilever beam: (a) f_{tx} at right support cross-section; (b) assumed f_{tx}; (c) *x*-reinf.

Reinforcement stresses in the *z*-direction were analyzed in a longitudinal *XY* cross-section (Figure 32b). Critical design values were grouped into three bands along the beam span, and an additional band in the cantilever:

$$\begin{aligned} f_{tz} &= 1.40MPa \rightarrow \rho_{sz} = 0.32\% \rightarrow A_{sz} = 12.8\ cm^2/m \quad \rightarrow \quad \text{stirrup } \phi 12/20 \\ f_{tz} &= 0.91MPa \rightarrow \rho_{sz} = 0.21\% \rightarrow A_{sz} = 8.4\ cm^2/m \quad \rightarrow \quad \text{stirrup } \phi 10/20 \\ f_{tz} &= 2.12MPa \rightarrow \rho_{sz} = 0.49\% \rightarrow A_{sz} = 19.5\ cm^2/m \quad \rightarrow \quad \text{stirrup } \phi 12/12 \\ f_{tz} &= 1.33MPa \rightarrow \rho_{sz} = 0.30\% \rightarrow A_{sz} = 12.2\ cm^2/m \quad \rightarrow \quad \text{stirrup } \phi 12/20 \end{aligned} \tag{5.8}$$

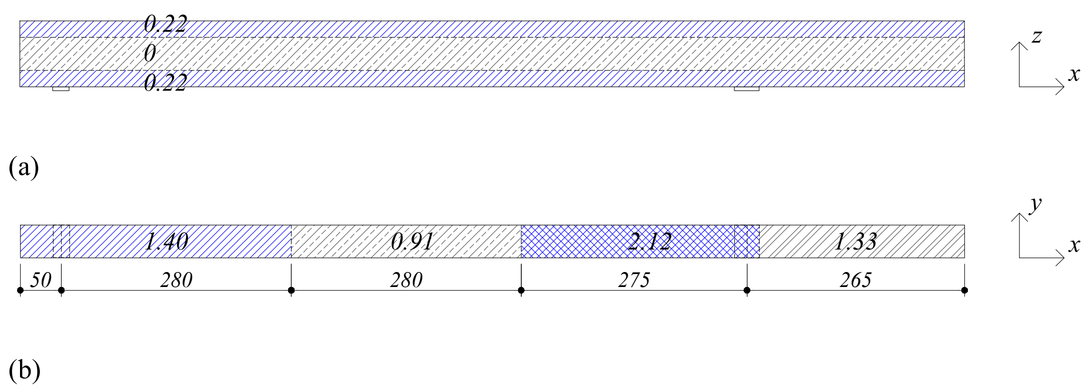

Figure 32 – Cantilever beam: assumed (a) f_{ty} and (b) f_{tz} for design.

Anchorage and complementary reinforcement

The formulation of the SFM considers a perfect bond between concrete and reinforcing bars. Design values of bond are used to calculate the anchorage length, even though they imply a much higher degree of conservatism than other failure modes such as rigid-plastic bond model or more refined bond models accounting for transverse pressures to reduce the anchorage length or to increment the bond strength, as discussed by the *fib* Bulletin 100 (*fib*, 2021, p.26).

Verifications does not rely on the geometrical definition of nodes converging uniform forces so that anchorage could be checked over or outside the nodal regions, as in the STM design. Rather, they must be undertaken at every point of the structural model requiring reinforcement. An adequate detailing is achieved by guaranteeing anchorage of rebars: if rebars cannot be adequately anchored, that is, if yield conditions of bond are not satisfied, either the area of the reinforcement should be increased to limit rebar axial forces, or anchorage should be provided by welded bars or mechanical anchors. In this particular example, the beam extended a sufficient length beyond the left support and concentrated applied force to anchor the reinforcement forces.

Two observations are made regarding *complementary rebars*. First, longitudinal rebars at the top and bottom faces, summing at least 4 $\phi 20$, extended throughout the longitudinal direction of the beam, conservatively, for the assemblage of the closed stirrups. Second, no skin reinforcement was detailed since the maximum distance between longitudinal bars, in the *z*-direction, resulted in 0.40 m, which was considered adequate for crack control.

Final detailing

The cantilever beam final detailing[1] is presented in Figure 33. The unusual arrangement will be later assessed and discussed in Section 6.2. By the end of the design process, reinforcement consumption was evaluated in terms of total cross-sectional area of the detailed rebars in the x-direction:

$$\begin{aligned} A_{sx,positive} &= 5\times 3.15 + 5\times 2.00 + 3\times 2.00 + 2\times 1.13 = 34.0\ cm^2 \\ A_{sy,negative} &= 4\times 3.15 + 4\times 2.00 + 3\times 2.00 + 2\times 1.13 = 28.9\ cm^2 \end{aligned} \tag{5.9}$$

These quantities will be compared to those obtained from the sectional design in Section 6.2.6.

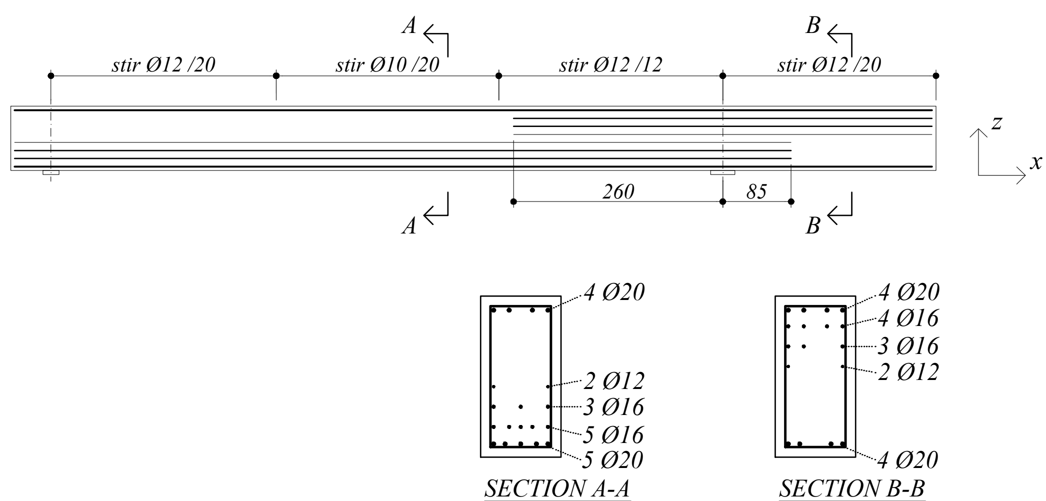

Figure 33 – Cantilever beam: final reinforcement arrangement

---

[1] Note on the nomenclature for stirrup arrangement: "*stir _ bar diameter (mm)/ bar spacing (cm)*". For example: "*stir ϕ10/20*" stands for "stirrups with diameter of 10 mm, spaced at 20 cm". Rebar sizes following European Standards.

The SFM was applied to the ULS design of a structural member that, in engineering practice, would certainly be designed by a sectional approach. However, application of the SFM provided insights into key aspects related to the design process, such as the construction of the numerical model for the linear analysis (including element size and support discretization), the delimitation of regions with uniform reinforcement stresses, the verification of concrete strength under triaxial stress states, and the effective transfer of forces between reinforcement and concrete.

5.3 Example 2: corbel

The second designed structural element was a double corbel. It measured 0.30 m deep, 0.40 m wide, and 0.40 m long, and was supported by a 0.40 m square column. The design was focused on the corbel, which was loaded on both sides with 500 kN, applied at 0.20 m from the column faces. Steel plates measuring 0.15 m x 0.20 m distributed the concentrated load to the top face of the corbel. Another steel plate was located at the bottom of the column to uniformly distribute the vertical reactions. The member should be designed with normal-weight concrete C30 (f_{ck} = 30 MPa) and B500 reinforcement (f_{yk} = 500 MPa).

This practical example was chosen to illustrate the application of the design method to a simple D-region.

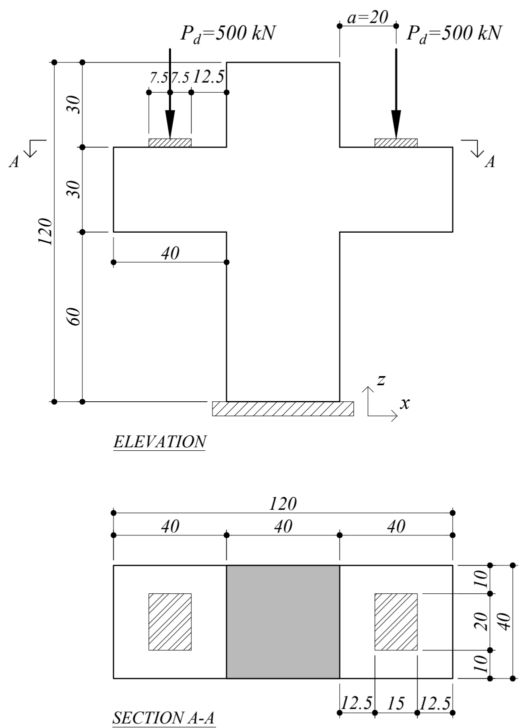

Figure 34 – Corbel: geometry and loading (dimensions in cm).

5.3.1 Structural model for the linear analysis

The structural model elaborated for the linear elastic analysis was meshed with cubic elements with dimension of 0.05 m, leading to a model with 2,436 cubic solid elements, as shown in Figure 35a. Eight elements were distributed along each dimension of the column, and six elements along the depth of the corbel. Concerning the boundary conditions, four pin supports were modeled symmetrically to the axis of the column, as shown in Figure 35b. The concentrated loads were applied as distributed pressures of q = 500/0.15/0.20 ≈ 16,700 kN/m².

Column and corbel were modeled with modulus of elasticity E_c = 26,070 MPa and Poisson´s ratio v = 0.2. Steel plates were modeled with a modulus of elasticity ten times greater than the steel modulus ($E_{s,equiv}$ = 10 x E_s = 2,100 GPa) to distribute both applied and reaction loads.

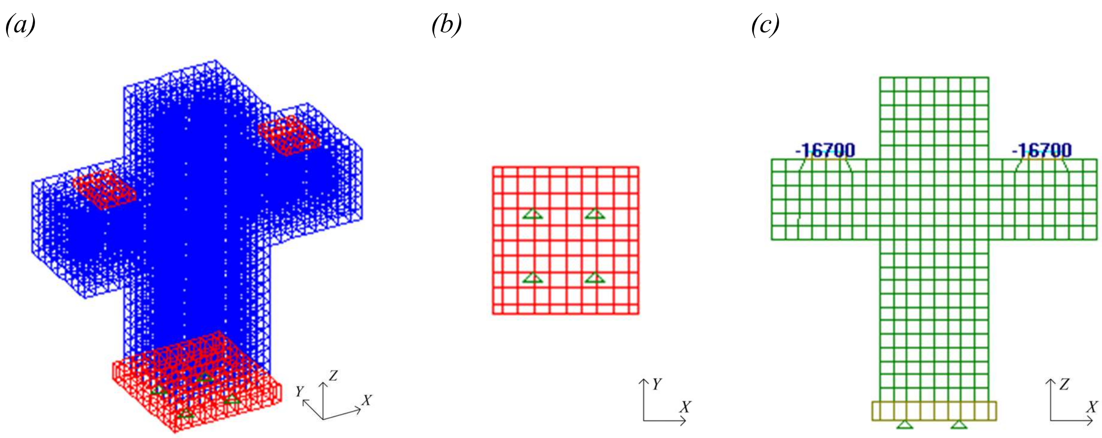

Figure 35 – Corbel: structural model for the linear analysis: (a) geometry perspective view; (b) boundary conditions; (c) loading.

5.3.2 Reinforcement design

Proceeding to Step 3 of the methodology described in Section 5.1, reinforcement stress distributions were analyzed in each coordinate direction with aid of the post-processor *ParaView*. Values at the center of the elements, rather than values at their nodes, were represented for the refined meshes.

The f_{tx} distribution is initially shown in Figure 36a, where elements with stresses lower than 1.5 MPa were filtered out for a clearer visualization (elements stressed below this cutoff value, which corresponds to a reinforcement ratio of ρ = 1.5/434.8 = 0.34%, were properly considered in the reinforcement detailing). The higher f_{tx} values were found at the top of the corbel, at the intersection between column and corbel, reaching the peak value of 19.2 MPa. The overall distribution showed that reinforcement in the x-direction was required in the upper two thirds of the corbel height, approximately. It was also required in the portion of the column up to 0.25 m above the corbel top face above the corbel, showing the diffusion of the corbel main tensile stresses into the column volume. In Figure 36b, only elements with f_{tx} higher than

6.0 MPa were shown to isolate the distribution of the peak values. Figure 36c presents the model sectioned at planes passing through the center of the first element of the corbel in both *x*- and *z*-directions. As can be seen, reinforcement stresses diminish from the column face towards the center of the column from 19.2 MPa to about 5.0 MPa, and from the corbel top face towards its bottom face from 19.2 MPa to zero.

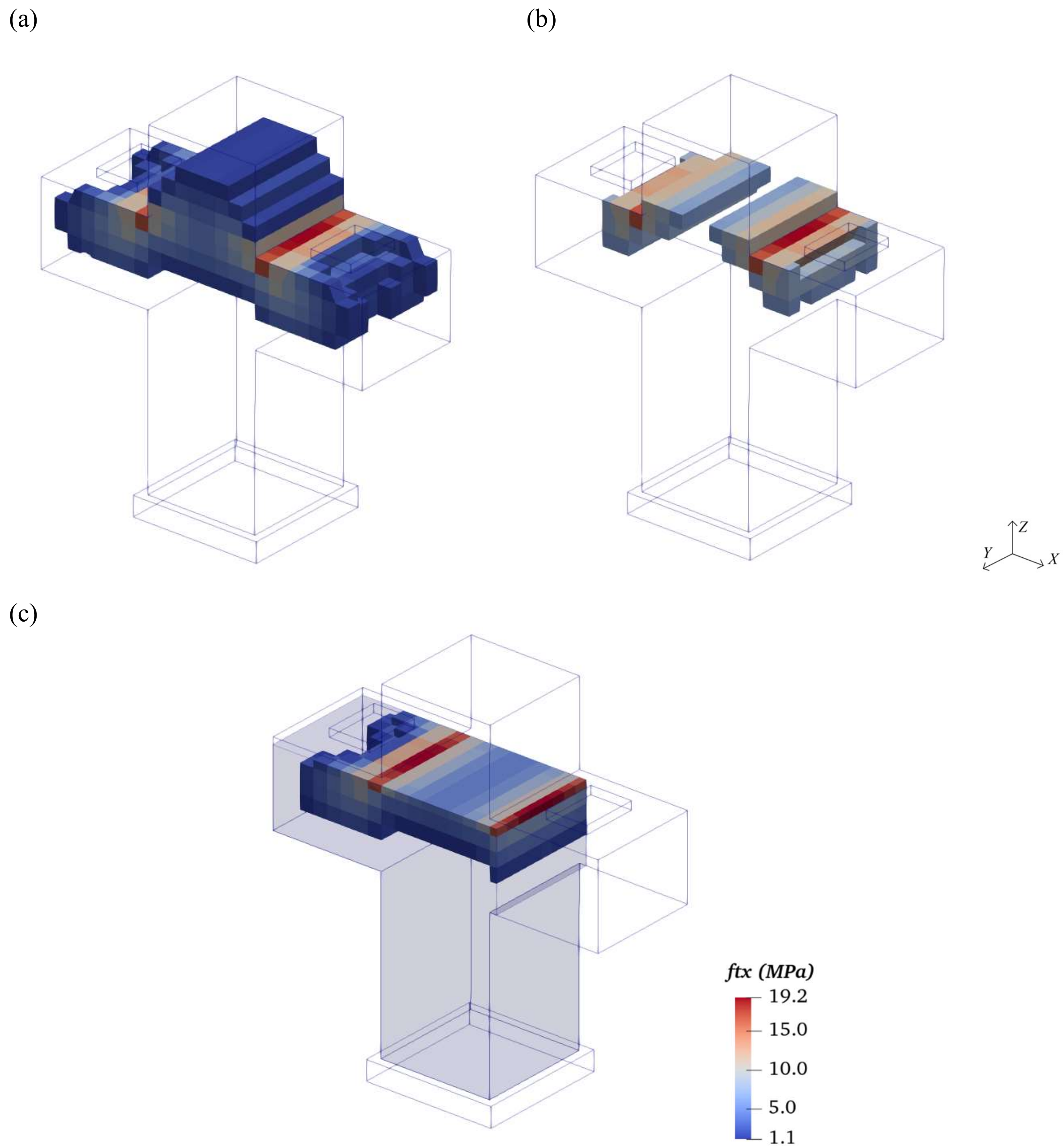

Figure 36 – Corbel reinforcement stress f_{tx}: (a) values above 1.1 MPa and (b) above 6.0 MPa; (c) clipped model.

The f_{ty} distribution is shown in Figure 37a, where elements with stresses lower than 0.5 MPa were filtered out. The higher f_{ty} values were found at the top of the corbel, at the column intersection, reaching the peak value of 2.7 MPa. It was associated, however, with a singularity of the numerical model affecting stresses in the elements neighboring the 90 degrees edge. In Figure 37b, elements with stresses lower than 1.0 MPa were filtered out to highlight the peak values in the projection of the load plate, which derived from the triaxial bottle-shaped tension-compression stress field developed in the partially loaded corbel.

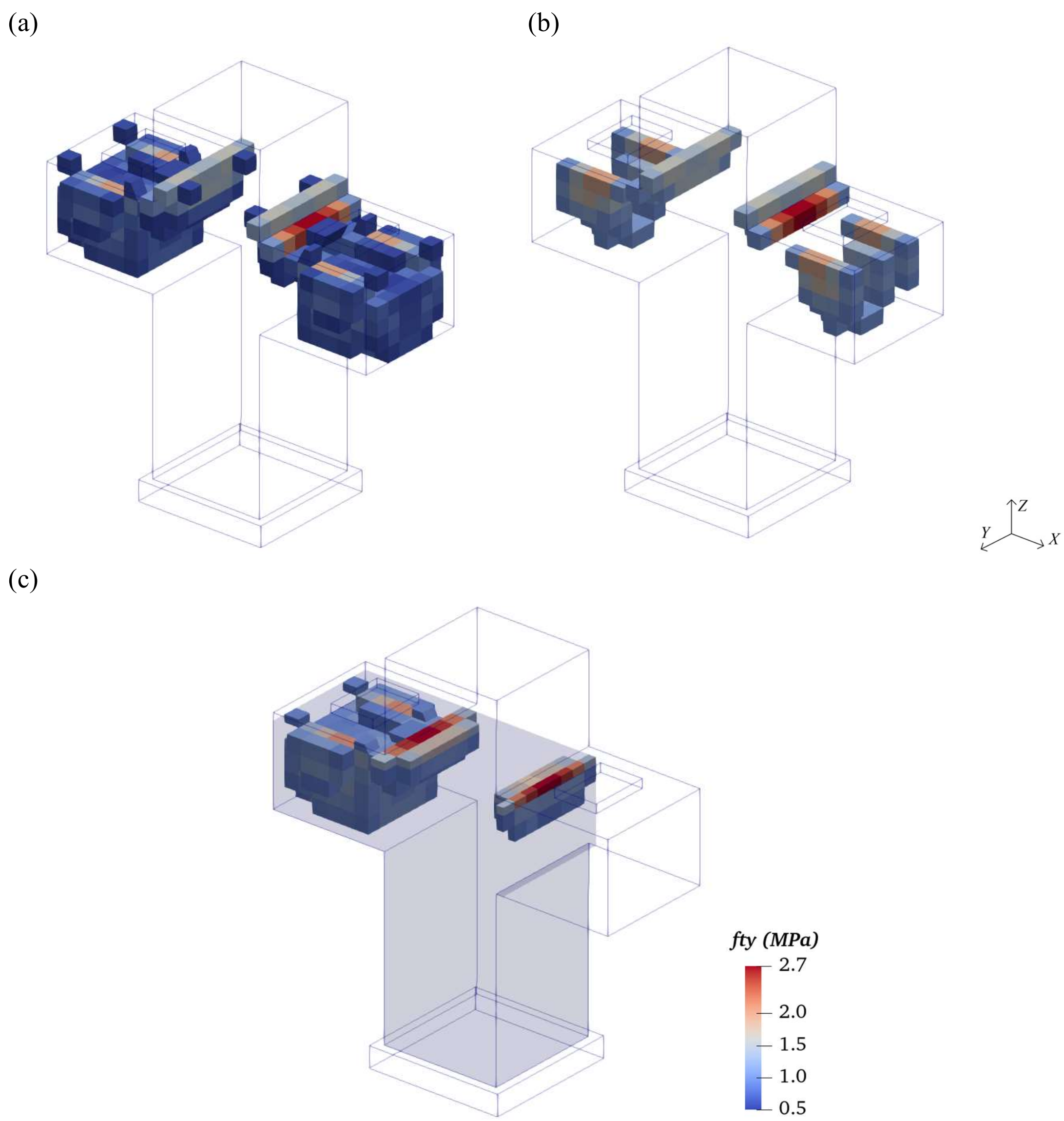

Figure 37 – Corbel reinforcement stress f_{ty}: (a) values above 0.5 MPa and (b) above 1.0 MPa; (c) clipped model.

The f_{tz} distribution is shown in Figure 38a, where elements with stresses lower than 1.0 MPa were filtered out. The higher f_{tz} values were found at the intersection between column and corbel, reaching the peak value of 10.4 MPa. Once again, the observed structural response was associated with the singularity of the numerical model in the elements neighboring the edge. Apart from this region, f_{tz} values lower than 1.0 MPa were observed in the portion between the plate and column face, which were required for the suspension of the applied loads (Figure 38b).

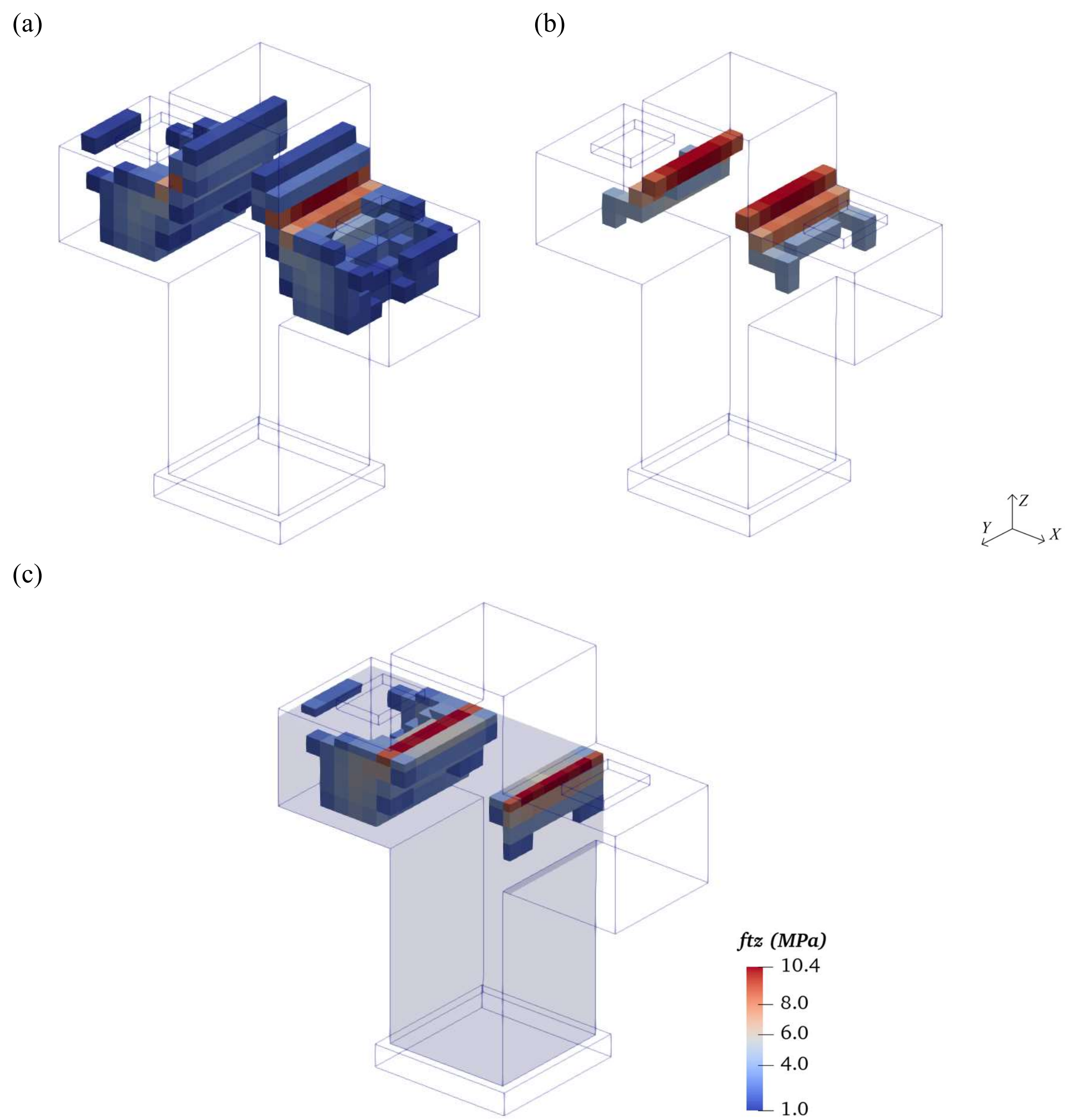

Figure 38 – Corbel reinforcement stress f_{tz}: (a) values above 1.0 MPa and (b) above 4.0 MPa; (c) clipped model.

5.3.3 Concrete check

Verification of concrete against crushing was performed in two steps. In the first one, elements under triaxial compression were filtered out and verified to respect the Ottosen failure criterion (Figure 39): the calculated Ottosen variable was smaller than zero for all elements, which indicated that the applied stresses did not surpass the concrete multiaxial strength. In the second step, elements under biaxial and uniaxial compression were filtered out and verified to respect the design compression strength of concrete, properly accounting for the reduction introduced by the *ν* efficiency factor (Figure 40).

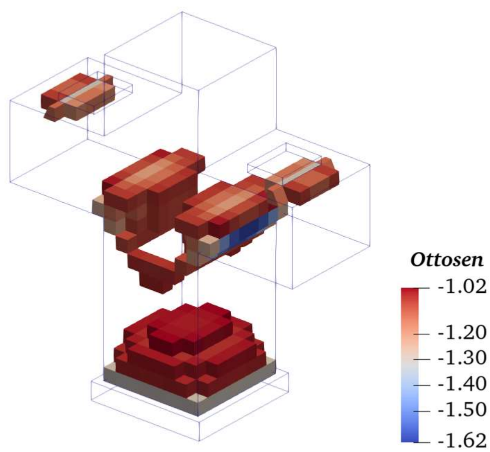

Figure 39 – Corbel: concrete check for elements under triaxial compression.

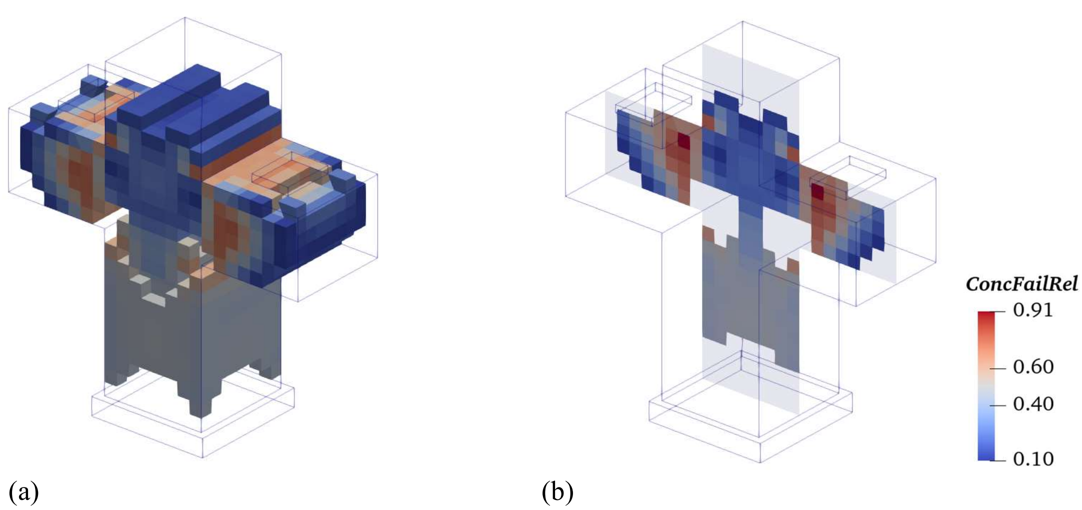

Figure 40 – Corbel: concrete check for elements under bi- and uniaxial compression: (a) overall distribution; (b) slice crossing the peak value.

5.3.4 Detailing

The reinforcement arrangement should then be defined from the stress distribution presented in Section 5.3.2. Reinforcement stresses in the *x*-direction were analyzed in transversal *YZ* cross-section, which passed through the center of the first column of corbel elements (Figure 41b). The section was subdivided into three bands along the corbel height, each of them enveloping two elements, thus extending to 0.10 m. Each band was assumed to be subjected to the average stress of the enveloped elements (Figure 41c): for example, the upper third of the corbel was reinforced for the average value of $f_{tx,upper}$:

$$\begin{aligned} &\overline{f}_{tx,upper} = \frac{19.2+7.9}{2} = 13.6MPa; \quad \rho_{sx} = \frac{13.6}{434.8} = 3.13\% \\ &A_{sx} = 3.13/100 \times 10 \times 40 = 12.5\ cm^2 \end{aligned} \tag{5.10}$$

which was arranged as 7 ϕ16 mm rebars. The peak value of 19.2 MPa was known to be affected by the numerical model singularity but was still computed in the calculations. This consideration will be further evaluated in this current section. Apart from the singularity itself, it should be noted that the election of a unique cross-section for the analysis was a conservative decision, since f_{tx} variation along the corbel width, with stresses ranging from 19.2 MPa, at the corbel core, to 16.8 MPa, at the corbel lateral faces (Figure 41b), was not accounted for reducing arrangements layouts locally.

Reinforcement stresses in the *y*-direction were analyzed in the longitudinal *XZ* cross-section located 0.075 m away from the corbel lateral face (Figure 42a) - the peak value of 2.7 MPa at the cross-section passing through the column axis was discarded since it corresponded to the numerical model singularity. The section was then subdivided into three bands along the height, yielding the design values presented in Figure 42b. Stresses at the upper and lower bands were covered by the horizontal folds of the vertical closed stirrups:

$$\begin{aligned} &\overline{f_{ty}} = \frac{1.9+0.6}{2} = 1.3MPa; \quad \rho_{sy} = \frac{1.3}{434.8} = 0.30\% \\ &A_{sy} = 0.30/100 \times 20 \times 40 = 2.40\ cm^2 < A_{s,stirup} = 1.13 + 1.13 + 0.5 + 0.5 = 3.30\ cm^2 \end{aligned} \tag{5.11}$$

For the central band, complementary reinforcement was detailed to resist the mean f_{ty} value acting on two elements (length of 0.10 m):

$$\begin{aligned} &\overline{f_{ty}} = \frac{1.8+1.3}{2} = 1.6MPa; \quad \rho_{sy} = \frac{1.6}{434.8} = 0.37\% \\ &A_{sy} = 0.37/100 \times 10 \times 40 = 1.47\ cm^2 \end{aligned} \tag{5.12}$$

which was arranged in 4 ϕ8 complementary horizontal stirrups (Figure 42c).

(a)

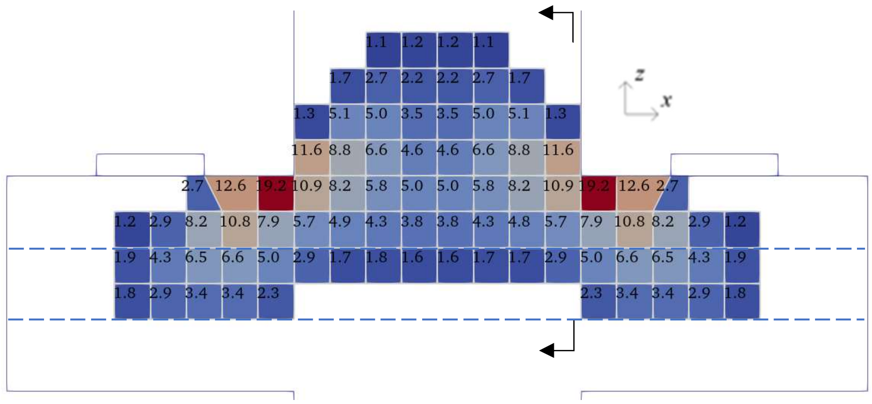

(b)

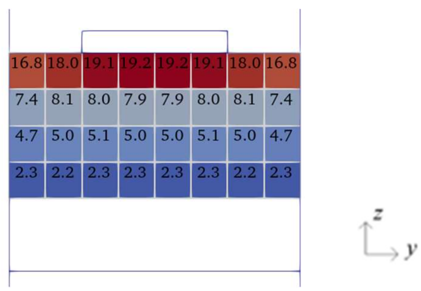

(c)

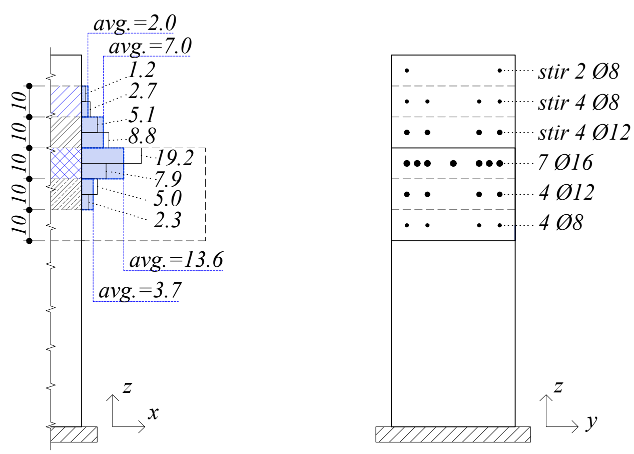

Figure 41 – Corbel: f_{tx} distribution in (a) longitudinal and (b) tranversal cross-sections; (c) assumed f_{tx} stresses for design.

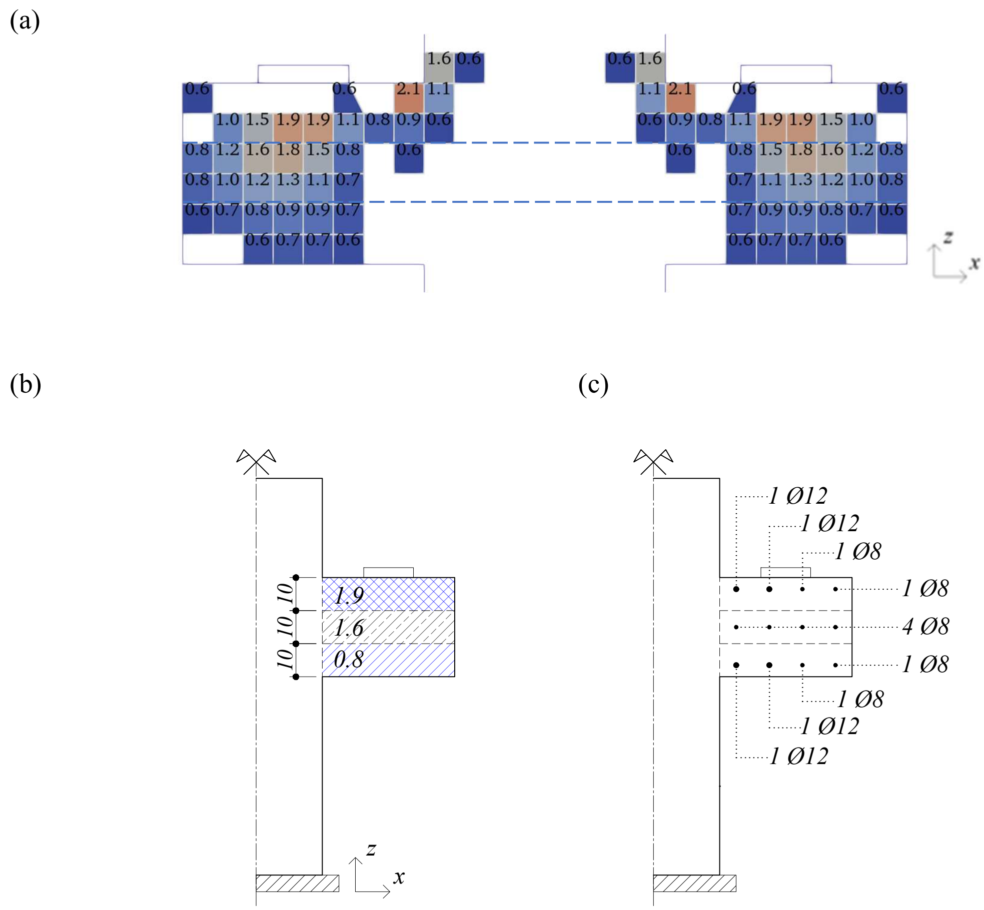

Figure 42 – Corbel: (a) f_{ty} distributions in a longitudinal cross-section; (b) assumed f_{ty} stresses for design; (c) adopted arrangement.

Reinforcement stresses in the *z*-direction were analyzed in the longitudinal *XY* cross-section at mid-height of the corbel (Figure 43a). Peak values surrounding the column/corbel superior corner were discarded since they corresponded to the numerical model singularity. The analyzed section was then subdivided into four bands along the corbel length, yielding the design values presented in Figure 43b. For the two bands adjacent to the column, for example, vertical reinforcement was calculated from:

$$\overline{f_{tz}} = \frac{2.8+3.9}{2} = 3.4MPa; \quad \rho_{sz} = \frac{3.35}{434.8} = 0.77\%$$
$$A_{sz} = \frac{0.77}{100} \times 10 \times 40 = 3.1\,cm^2 \tag{5.13}$$

which was arranged in 1 stirrup ϕ12 with 4 legs for each band. The complete set of stirrups for the corbel is presented in Figure 42c.

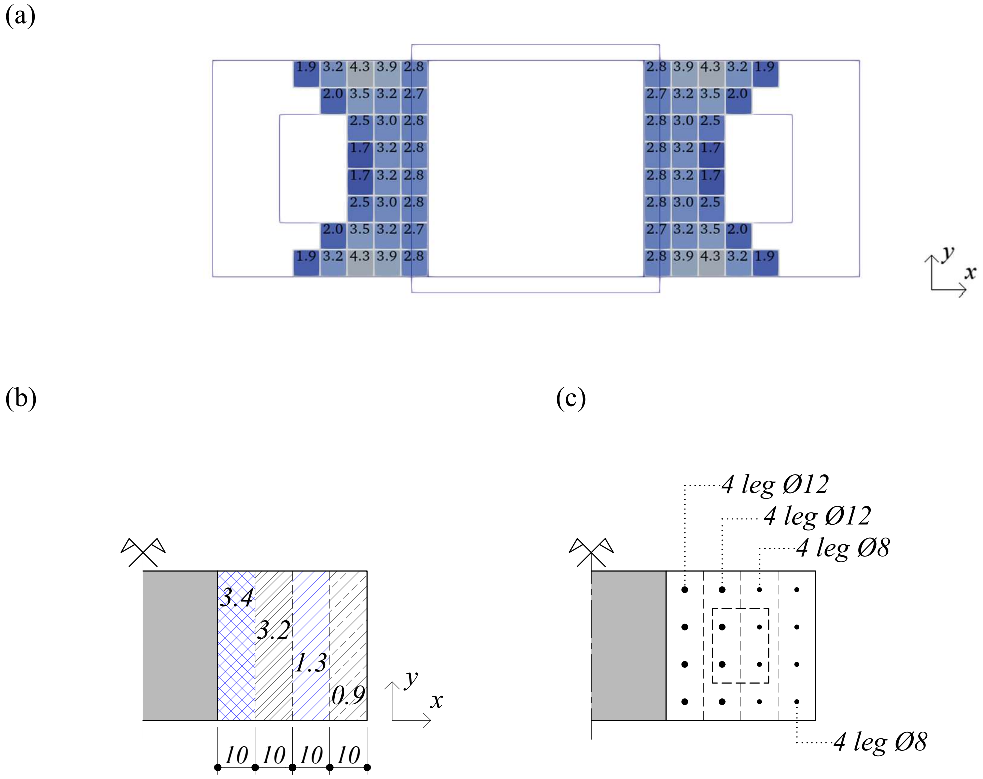

Figure 43 – Corbel: f_{tz} distribution at mid-height of the corbel; (b) assumed f_{tz} stresses for design; (c) adopted arrangement.

Complementary analysis for the singularity 1: column without upper portion

To assess the effects of the singularities, an additional numerical model was elaborated where the portion of the column above the corbel was suppressed. It was observed that:

- The maximum f_{tx} of 14.1 MPa (see Figure 44) occurred at a section passing through the axis of the column, and no longer in an element neighboring the singularity. This peak value was close to the assumed average value of 13.6 MPa obtained from Equation (5.10).
- The maximum f_{ty} of 2.0 MPa (see Figure 45) was approximately equal to the assumed value of 1.6 MPa obtained from Equation (5.12).
- The maximum f_{tz} of 3.6 MPa (see Figure 46) was approximately equal to the assumed value of 3.4 MPa obtained from Equation (5.13).

This showed that the criteria established for dealing with the singularity was adequate in this design case.

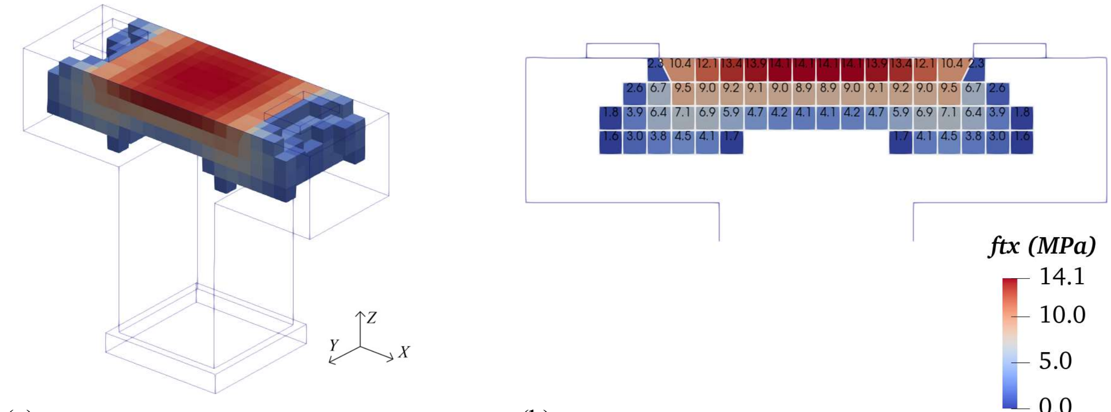

(a) (b)

Figure 44 – Corbel without upper column: f_{tx} distribution above (a) 1.5 MPa; (b) 7.0 MPa.

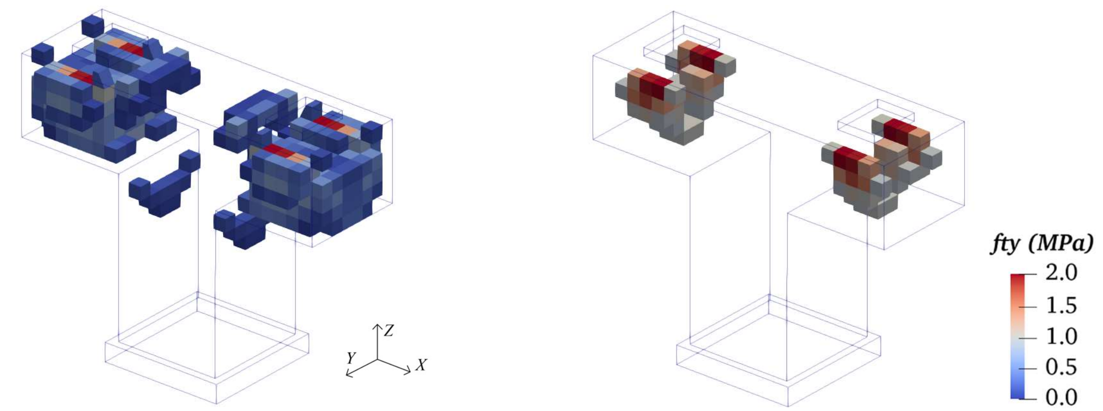

(a) (b)

Figure 45 – Corbel without upper column: f_{ty} above (a) 0.5 MPa and (b) 1.2 MPa.

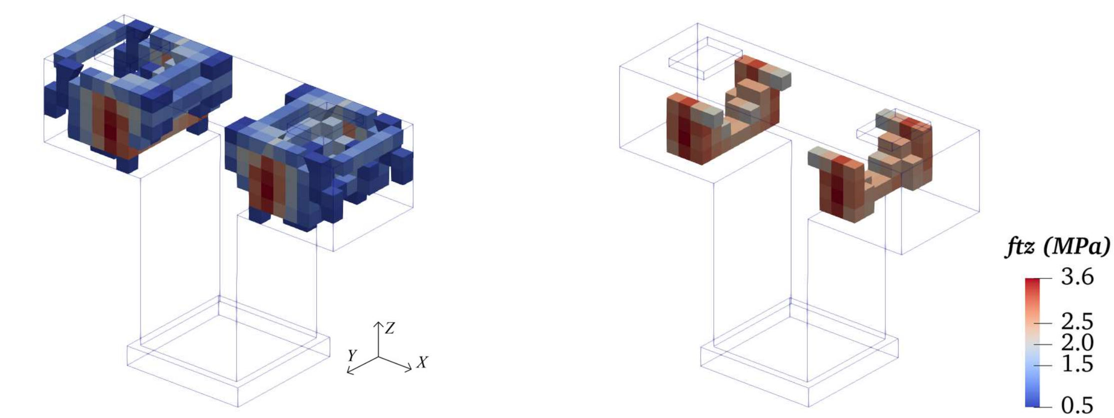

(a) (b)

Figure 46 – Corbel without upper column: f_{tz} above (a) 0.5 MPa and (b) 2.0 MPa.

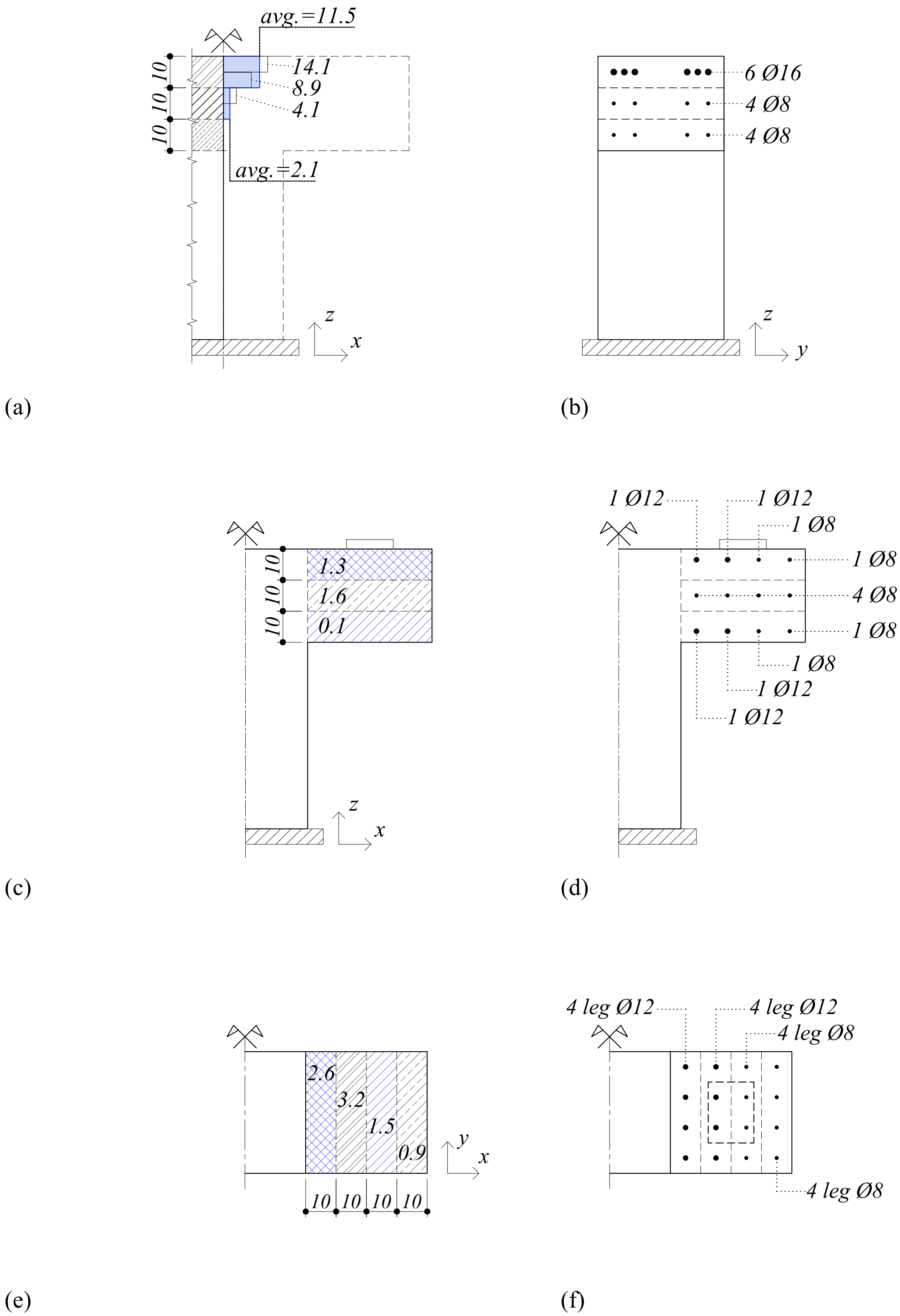

Figure 47 – Corbel without upper column: (a) f_{tx} design stresses; (b) x-reinf. arrangement; (c) f_{ty} design stresses; (d) reinforcement arrangement in the y-direction; (e) f_{tz} design stresses; (f) reinforcement arrangement in the z-direction.

Complementary analysis for the singularity 2: mesh refinement

To further evaluate the influence of the singularity on the design outcome, a new model was created with a refined mesh. Column and corbel were meshed with elements half the size of the original model (0.025 m), resulting in a model with 19,176 cubic solid elements (Figure 48a). Analyzing the results in the critical cross-section (Figure 48b), it was observed that the peak f_{tx} value increased from 19.2 MPa to 27.7 MPa; it was also observed that the equilibrium of forces in the *y*-direction was improved (the sum of *FZ* forces acting on the elements crossing the section was closer to the applied force of 500 kN).

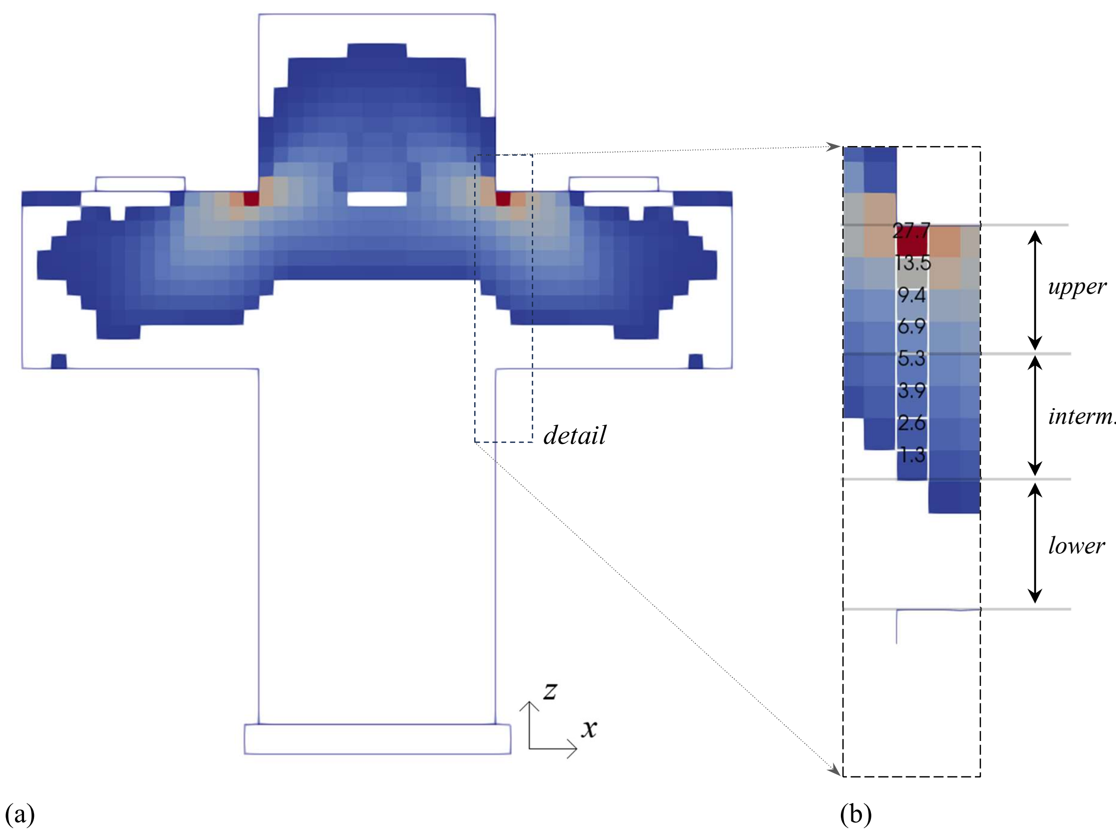

Figure 48 – Corbel with refined mesh: (a) f_{tx} distribution; (b) detail for the elements in the vertical alignment of the element with the peak value.

Final detailing

The corbel final detailing is presented in Figure 49. The main corbel tie was assumed to be anchored by a welded bar at each extremity. Minimum reinforcement was provided at the bottom of the corbel, following usual detailing prescriptions.

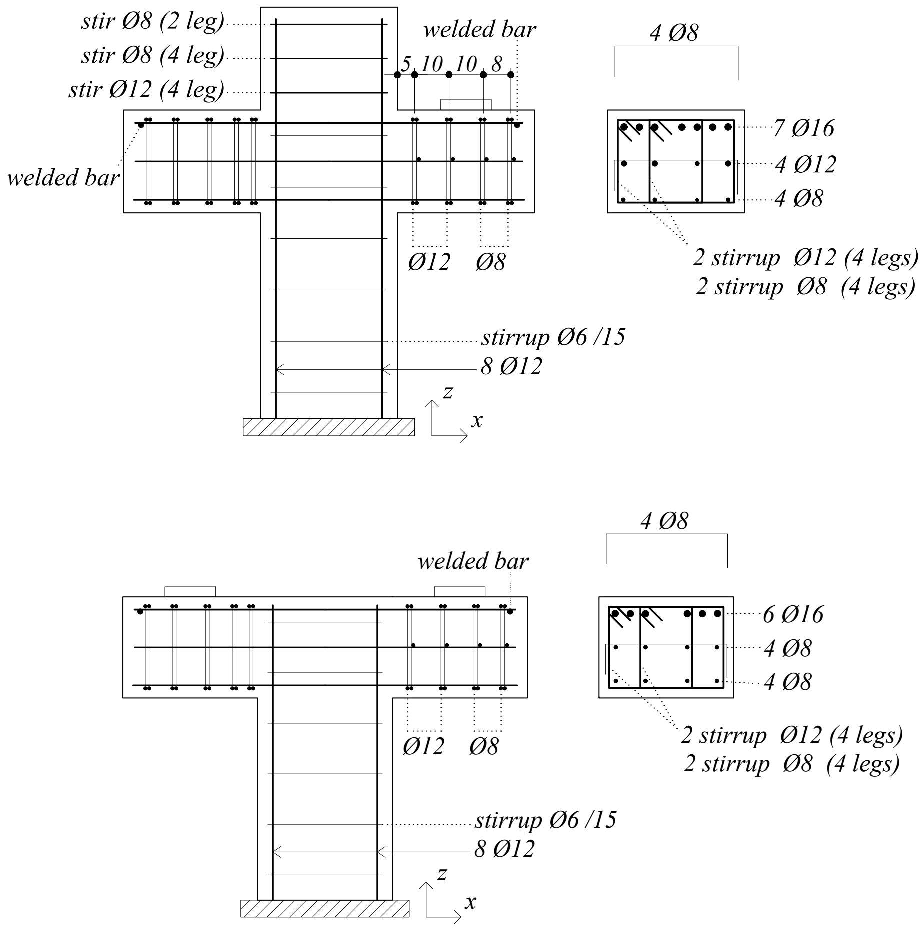

Figure 49 – Corbel: final detailing.

By the end of the design process, reinforcement consumption was evaluated in terms of total detailed reinforcement area. The proposed arrangement summed:

$$A_{sx,corbel} = 7\times 2.00 + 4\times 1.13 + 4\times 0.50 = 20.5\,cm^2 \tag{5.14}$$

This quantity will be later compared to the one obtained from an alternative design method in Section 6.3.6.

This second example addressed the following aspects for the SFM design: the management of singularities, the averaging of design stresses between neighboring elements, and the employment of welded bars for improving anchorage.

5.4 Example 3: beam under axial forces

This third design example employed the SFM to design a set of three beams with a total length of 3.10 m and a square cross-section of 0.20 m each. All beams were subjected to an axial force of 1,020 kN: while *beam I* was subdivided into two spans with equal length, *beams II* and *III* were subdivided into spans with length ratio of 1:2 (Figure 50). Beams should be designed with normal weight concrete C30 (f_{ck} = 30 MPa) and B500 reinforcement (f_{yk} = 500 MPa). This example was chosen to allow for discussion on ductility of concrete and reinforcement.

5.4.1 Structural model for the linear analysis

The structural analysis could have been performed by modeling the beams with solid elements. However, as a simplification, the structural models for the linear elastic analyses were constructed with linear elements.

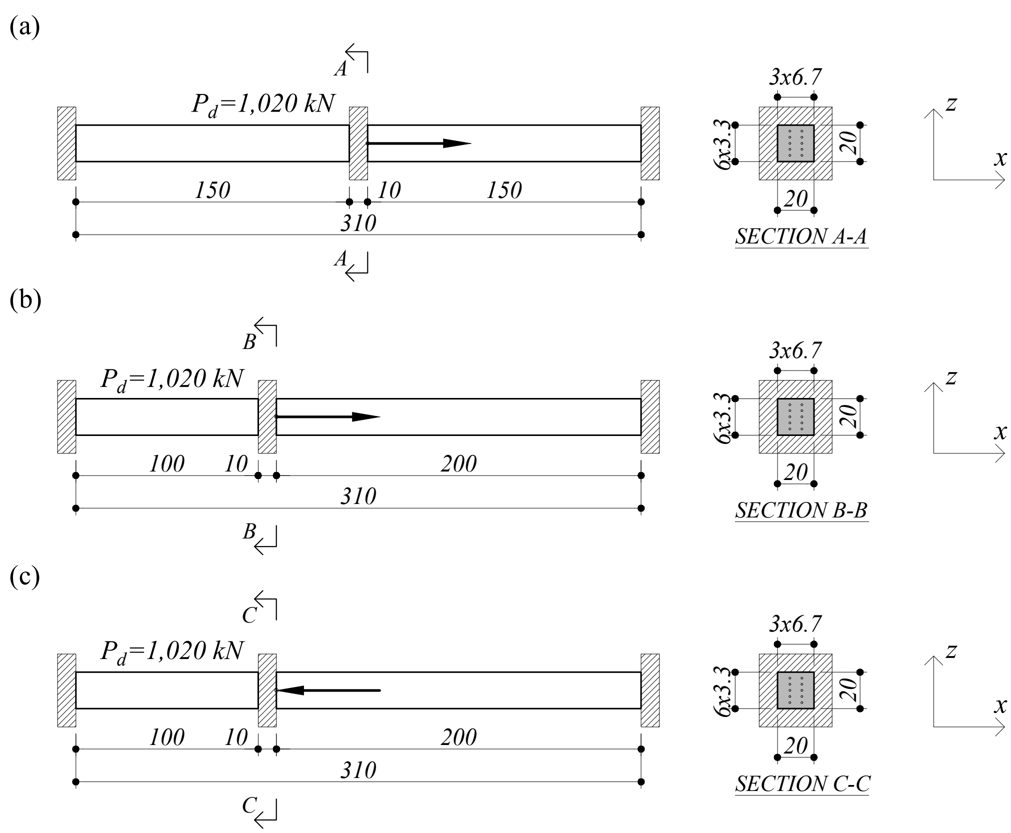

Figure 50 – Beam under axial forces: geometry and loading for: (a) beam *I*; (b) beam *II*; and (c) beam *III* (dimensions in cm).

Each structural model was composed of two single bars with modulus of elasticity of the uncracked concrete, E_c = 26,070 MPa, and Poisson´s ratio v = 0.2. The resulting normal forces diagrams are presented in Figure 51.

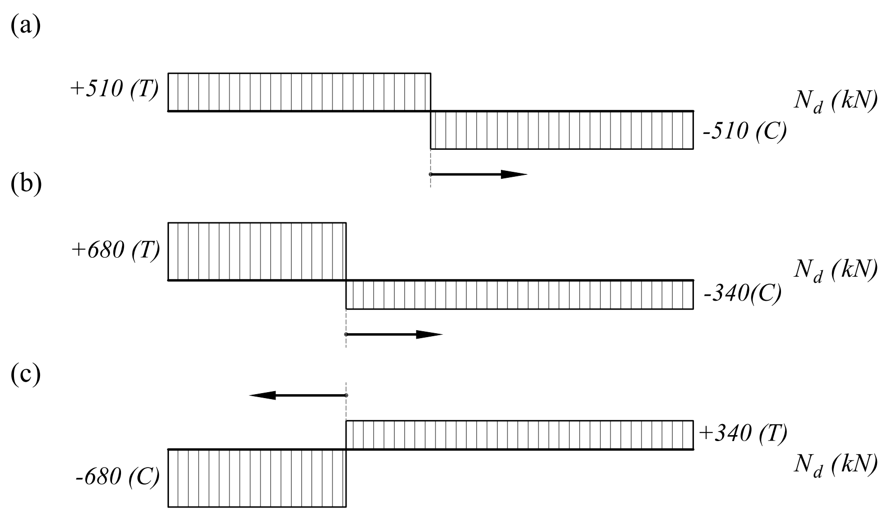

Figure 51 – Beam under axial forces: axial forces diagram for: (a) beam *I*; (b) beam *II*; and (c) beam *III*.

In the diagrams above, suffix (C) was used for compression forces, and suffix (T) for tension forces. Forces in each span were proportional to their relative axial rigidity EA/ℓ. Stresses for the SFM design were obtained by the simple division of the sectional forces by the beam sectional areas.

5.4.2 Reinforcement design

Beam I

The left span of the beam was subjected to a tensile force of +510 kN. The applied stresses on this side of the beam should be equilibrated by reinforcement stresses:

$$f_{tx} = \sigma_{x,right} = \frac{510}{0.20 \times 0.20} = 12,750 \frac{kN}{m^2} \tag{5.15}$$

which led to the arrangement of 4 ϕ20 rebars:

$$\begin{aligned} \rho_{sx} &= \frac{\sigma_x}{f_{yd}} = \frac{12.75}{434.8} = 0.029 \\ A_{sx} &= 0.029 \times 0.20 \times 0.20 = 11.7\ cm^2 \qquad \{4\phi 20 \end{aligned} \tag{5.16}$$

Beam II

The left side of the beam was subjected to a tensile force of +680 kN. The applied stresses on this side of the beam should be equilibrated by reinforcement stresses:

$$f_{tx} = \sigma_{x,right} = \frac{680}{0.20 \times 0.20} = 17,000 \frac{kN}{m^2} \tag{5.17}$$

which led to an arrangement of 8 ϕ16 rebars:

$$\begin{aligned} \rho_{sx} &= \frac{\sigma_x}{f_{yd}} = \frac{17.00}{434.8} = 0.039 \\ A_{sx} &= 0.039 \times 20 \times 20 = 15.6\ cm^2 \qquad \{8\phi 16 \end{aligned} \tag{5.18}$$

Beam III

The right side of the beam was subjected to a tensile force of +340 kN. The applied stresses on this side of the beam should be equilibrated by reinforcement stresses:

$$f_{tx} = \sigma_{x,right} = \frac{340}{0.20 \times 0.20} = 8,500 \frac{kN}{m^2} \tag{5.19}$$

which led to an arrangement of 4 ϕ16 rebars:

$$\begin{aligned} \rho_{sx} &= \frac{\sigma_x}{f_{yd}} = \frac{8.50}{434.8} = 0.020 \\ A_{sx} &= 0.020 \times 0.20 \times 0.20 = 7.8\ cm^2 \qquad \{4\phi 16 \end{aligned} \tag{5.20}$$

5.4.3 Concrete check

Concrete stresses should be limited to the design compressive strength. According to MC2010 (*fib*, 2013, Section 7.2.3.1.4), it is defined as:

$$f_{cd} = \alpha_{cc} \frac{f_{ck}}{\gamma_c} = 1.0 \frac{30}{1.4} = 21.4 MPa \tag{5.21}$$

where "α_{cc} is a coefficient taking account of long-term effects of compressive strength and of unfavorable effects from the way the loas is applied. For normal design situations it may be assumed that the increase of the compressive strength after 28 days compensates the effect of sustained loading, so that α_{cc} = 1.0 for new structures." "For concrete strength determined at an age greater than 28 days, the effect of hydration may not be able any more to compensate the effect of sustained loading, so that $\alpha_{cc} = \alpha_{ct}$ = 0.85 is more suitable." In this particular example, γ_c was assumed to be 1.4, in accordance with the Brazilian Code (ABNT, 2023).

Beam I

The right span of the beam was subjected to the following compressive stress:

$$|\sigma_{c3}| = |\sigma_{right}| = \frac{510}{0.20 \times 0.20} = 12,750 \frac{kN}{m^2} = 12.75 MPa = 0.59 f_{cd} \tag{5.22}$$

which was smaller than the limit compressive design strength of 21.4 MPa.

Beam II

The right span of the beam was subjected to the following compressive stress:

$$|\sigma_{c3}| = |\sigma_{right}| = \frac{340}{0.20 \times 0.20} = 8,500 \frac{kN}{m^2} = 8.5 MPa = 0.40 f_{cd} \tag{5.23}$$

which was smaller than the limit compressive design strength of 21.4 MPa.

Beam III

The left span of the beam was subjected to the following compressive stress:

$$|\sigma_{c3}| = |\sigma_{left}| = \frac{680}{0.20 \times 0.20} = 17,000 \frac{kN}{m^2} = 17.0 MPa = 0.79 f_{cd} \tag{5.24}$$

which was smaller than the limit compressive design strength of 21.4 MPa.

5.4.4 Detailing

The final detailing is presented in Figure 52. In the three beams, closed stirrups, spaced at 0.10 m, were provided along the tension spans with two stronger stirrups positioned near the central steel plate to resist tangential stresses in that region.

To isolate the specific behavior of concrete in compression in the assessment of the achieved solution in Section 6.4, reinforcement was not provided in the compression span. However, it is recognized that real structures typically require reinforcement in compressed zones as well, following code requirements for consideration of minimum eccentricities or minimum reinforcement ratios.

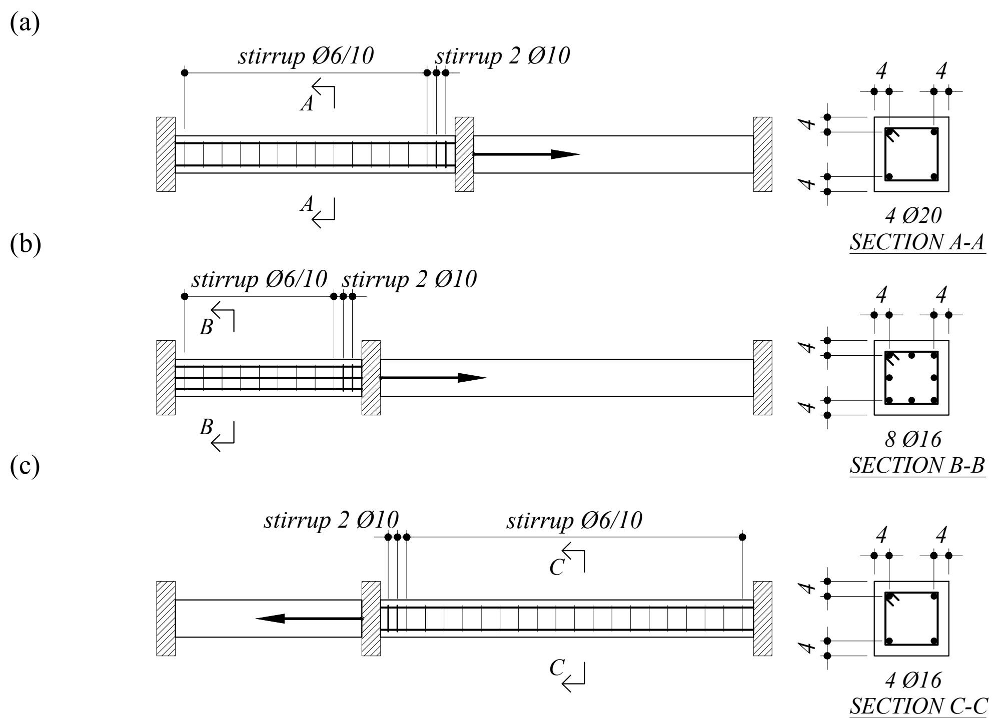

Figure 52 – Beam under axial forces: reinforcement detailing for (a) *beam I*; (b) *beam II*; and (c) *beam III.*

This third example presented the complete SFM design process for three beams subjected to axial forces. The key assumption in this solution, the use of an uncracked modulus of elasticity for both tension and compression zones, is critically evaluated in Section 6.4.

5.5 Example 4: six-pile cap

The fourth designed structural member was a pile cap with 8.00 m x 5.20 m plan dimensions and 2.40 m depth, responsible for transferring the loads from three rectangular columns to six 0.80 m square concrete piles, centers spaced at 2.80 m. The pile cap geometry was symmetrical about the *y*-axis, but asymmetrical about the *x*-axis. One of the columns was located outside the projection of the envelope of the pile group. The pile cap should be designed with normal-weight concrete C30 (f_{ck} = 30 MPa) and B500 reinforcement (f_{yk} = 500 MPa).

For the first load combination, a characteristic vertical load of 5,750 kN was applied on top of columns *C1* and *C2*, and a vertical characteristic load of 3,840 kN was applied on top of column *C3*. For the second load combination, a concomitant characteristic bending moment of -2,398 kN.m acting around the *x*-axis was applied on top of both *C1* and *C2*, and a concomitant moment of 704 kN.m acting around the *y*-axis was applied on top of *C3*.

This example was chosen to illustrate the application of the design method to a complex D-region, a volumetric structural element where load paths followed multiple three-dimensional directions.

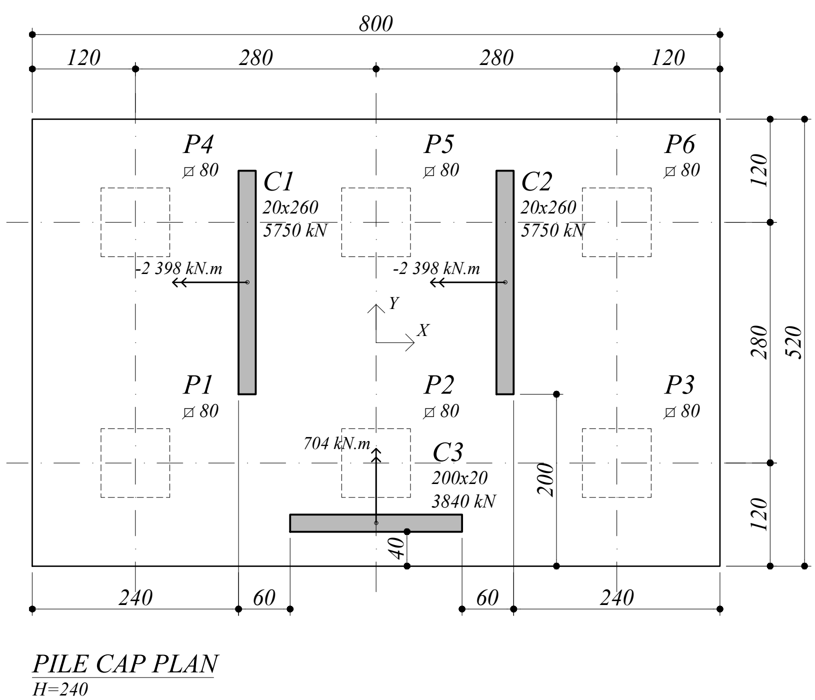

Figure 53 – Six-pile cap: geometry (dimensions in cm) and characteristc loads, second load combination.

5.5.1 Structural model for the linear analysis

Along with the pile cap itself, 2.00 m of the column length and 1.20 m of the pile length were modeled for the diffusion of the applied loads/reactions to the cap. Also, 0.20 m thick steel plates were included at the bottom of the piles.

The complete structural element comprised 13,656 cubic solid elements with 0.20 m in length (Figure 54). Twelve elements were distributed along the cap depth, and four elements were distributed along each dimension of the pile cross-section. Concerning the boundary conditions, a single fixed pin support was defined at the bottom of each steel plate to provide vertical restraint and to concurrently ensure that no bending moment would be transferred to the piles. Additional constraints guaranteed horizontal equilibrium for the structural model: pile *P1* was restricted in the *x*- and *y*-directions; pile *P3*, in the *y*-direction; and pile *P4*, in the *x*-direction (Figure 55b).

Columns and pile cap were modeled with modulus of elasticity E_c = 26,070 MPa and Poisson´s ratio ν = 0.2. Piles, in turn, were modeled with a reduced modulus of elasticity, calibrated to simulate a settlement of 9 mm for a working load of 2,600 kN ($E_{c,pile} = E_c/40$ = 650 MPa). Steel plates were modeled with a modulus of elasticity ten times greater than the steel modulus ($E_{s,equiv} = 10\ E_s$ = 2,100 GPa), to distribute the concentrated support reactions to the bottom face of the concrete piles.

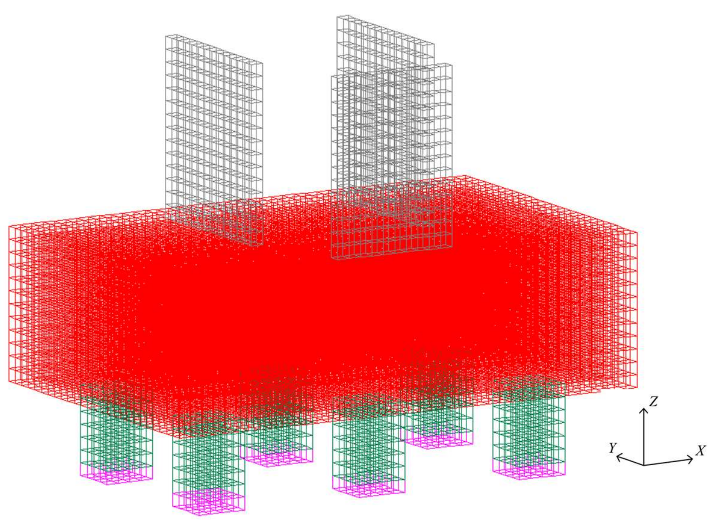

Figure 54 – Six-pile cap structural model for the linear analysis: perspective view.

Vertical loads (N) on top of columns were applied as uniform pressure loads, while flexural moments (M) were applied as binary forces, as shown in Figure 55c. Two load combinations were considered for the ULS design:

$$
\begin{aligned}
U1 &= 1.4 \times (N_k) \\
U2 &= 1.4 \times (N_k + M_k)
\end{aligned}
\tag{5.25}
$$

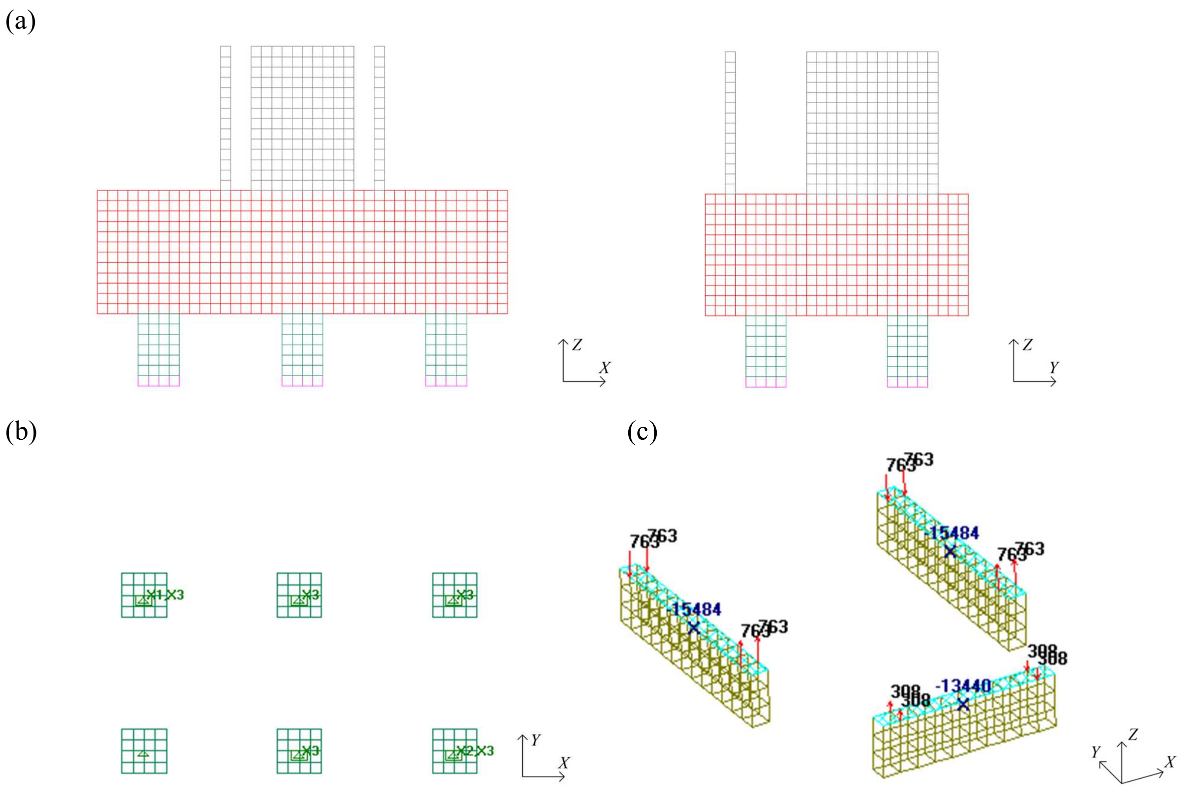

Figure 55 – Six-pile cap structural model for the linear analysis: (a) geometry; (b) boundary conditions; (c) loading *U2*.

5.5.2 Reinforcement design

Proceeding to Step 3 of the methodology described in Section 5.1, reinforcement stress distributions were analyzed in post-processor *ParaView* for each load combination.

Load combination U1

The f_{tx} distribution is shown in Figure 56, where elements with stresses lower than 0.20 MPa were filtered out. The higher f_{tx} values were found at the bottom of the pile cap, in the projection of *C3*. The peak value, particularly, was found between piles *P1* and *P2*, and between piles *P2* and *P3*, reaching 2.21 MPa. The overall distribution showed that the reinforcement in the *x*-direction was required in the lower two thirds of cap depth, approximately. Stresses in this region accounted for the flexural behavior of the structure.

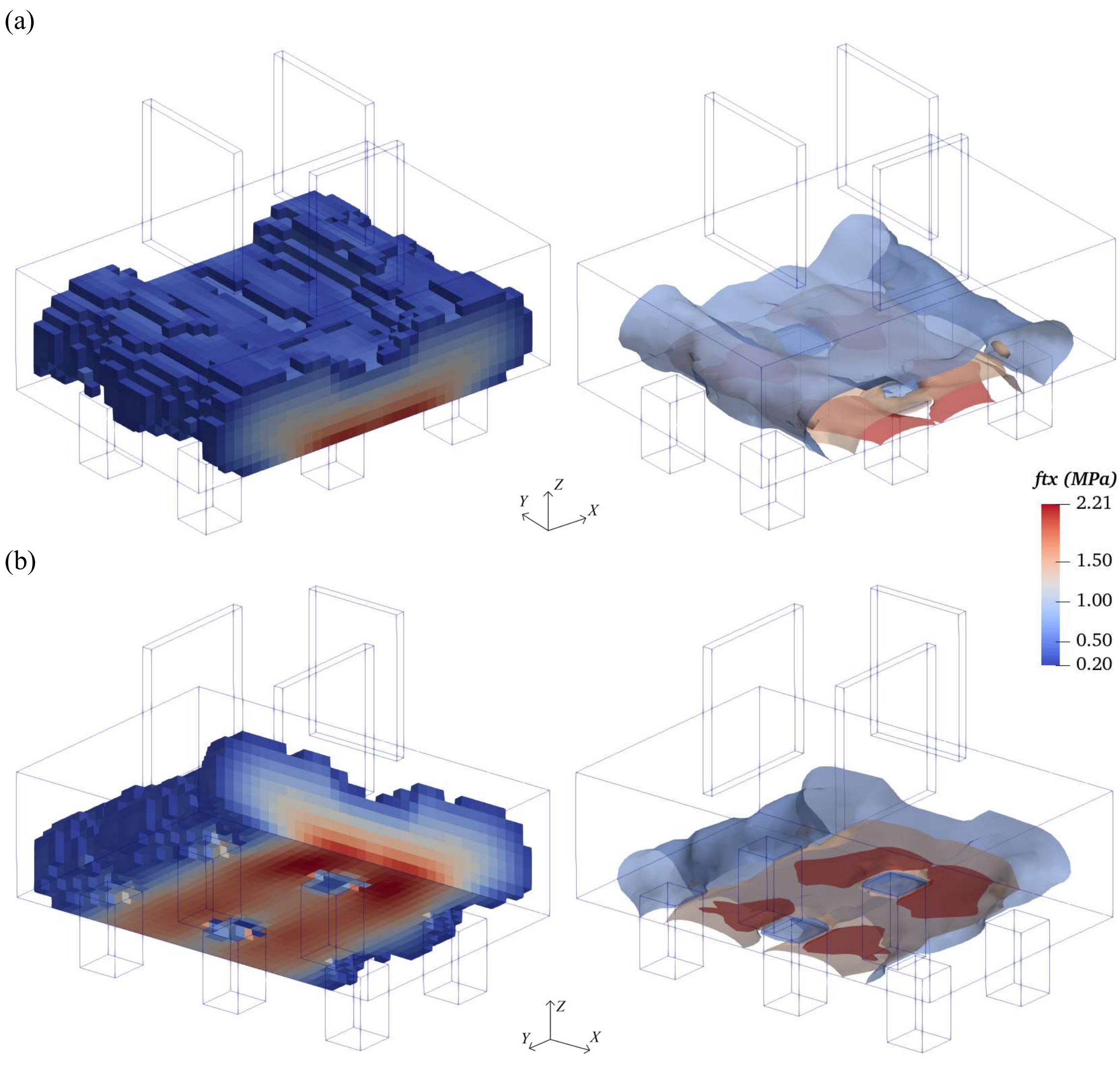

Figure 56 – Six-pile cap: f_{tx} distribution for load combination *U1* - (a) top view perspective; (b) bottom view perspective.

The f_{ty} distribution is shown in Figure 57. The higher f_{ty} values were found at the top of the pile cap, extending through the length of *C3*. Peak values, particularly, reached 0.82 MPa. The overall distribution showed that reinforcement in the *y*-direction was required throughout the cap volume: for the lower half of the cap, f_{ty} stresses were mainly accounted for the flexural behavior from columns *C1* and *C2* loads acting on the *y*-span between piles; for the upper half, stresses derived mainly from the load of *C3* acting eccentrically to the plane containing piles *P1-P2-P3* axis, thus generating a negative bending moment.

(a)

(b)

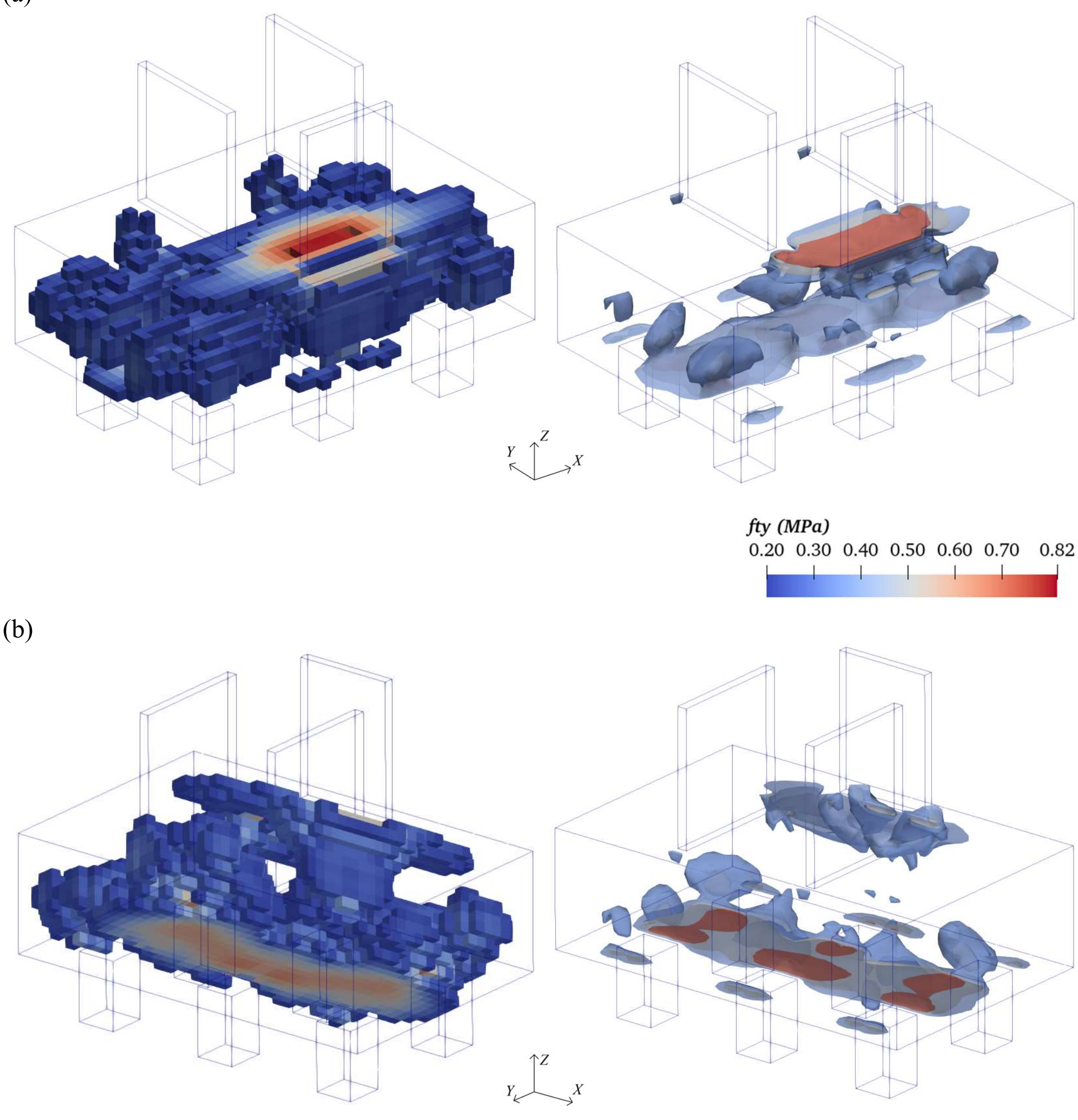

Figure 57 – Six-pile cap: f_{ty} distribution for load combination *U1* - (a) top view perspective; (b) bottom view perspective.

The f_{tz} distribution is shown in Figure 58, where elements with stresses lower than 0.10 MPa were filtered out. The highest f_{tz} values were found in the projection of column *C3*. The peak value, in particular, was found at the south face of the pile, reaching the value of 1.60 MPa. The overall distribution showed that, besides the aforementioned region, reinforcement stresses were found in the cap spans. This response was already expected for the suspension of vertical forces.

(a)

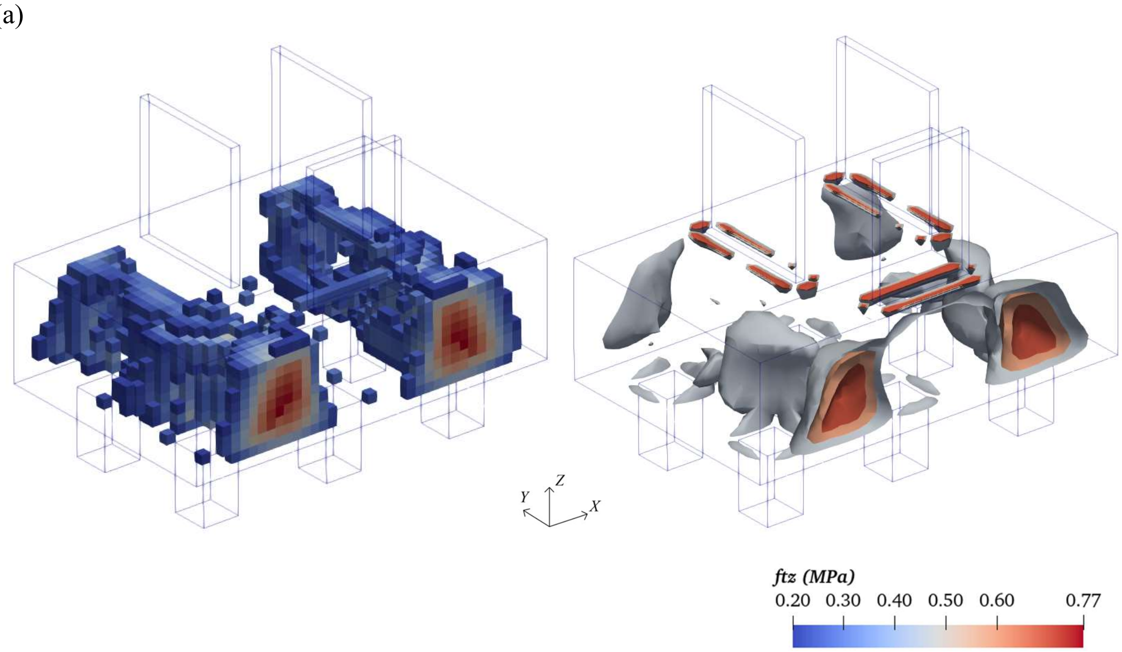

(b)

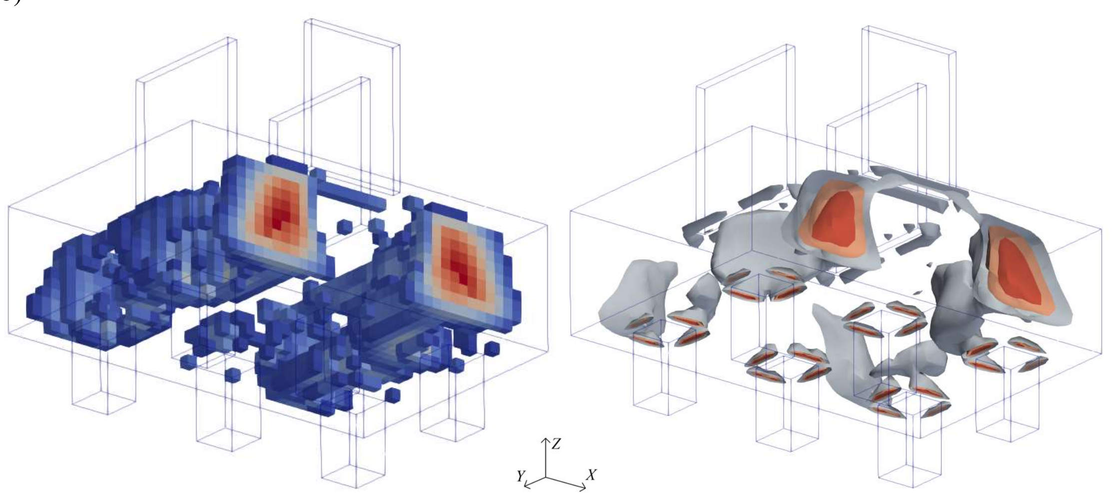

Figure 58 – Six-pile cap: f_{tz} distribution for load combination *U1* - (a) top view perspective; (b) bottom view perspective.

Load combination U2

The symmetrical response of the cap about the *y*-axis was lost. The overall reinforcement stress distribution was modified because bending moments applied at the top of *C1* and *C2* increased *P1*, *P2*, and *P3* reactions, while the bending moment applied at the top of *C3* increased *P3* and *P6* reactions. Figures were prepared, once again, filtering out elements with reinforcement stresses lower than 0.20 MPa.

The f_{tx} distribution is shown in Figure 59. The maximum f_{tx} value changed slightly from 2.21 to 2.13 MPa. Isosurfaces (Figure 59b) show the asymmetric response of the pile cap: in the projection of *C3*, a wider 'red isosurface' was identified between *P2* and *P3* than between *P1* and *P2*, whereas in the projection of *C1* and *C2* two 'red isosurfaces' were identified below the extremities of the columns with increased compression due to the column moments.

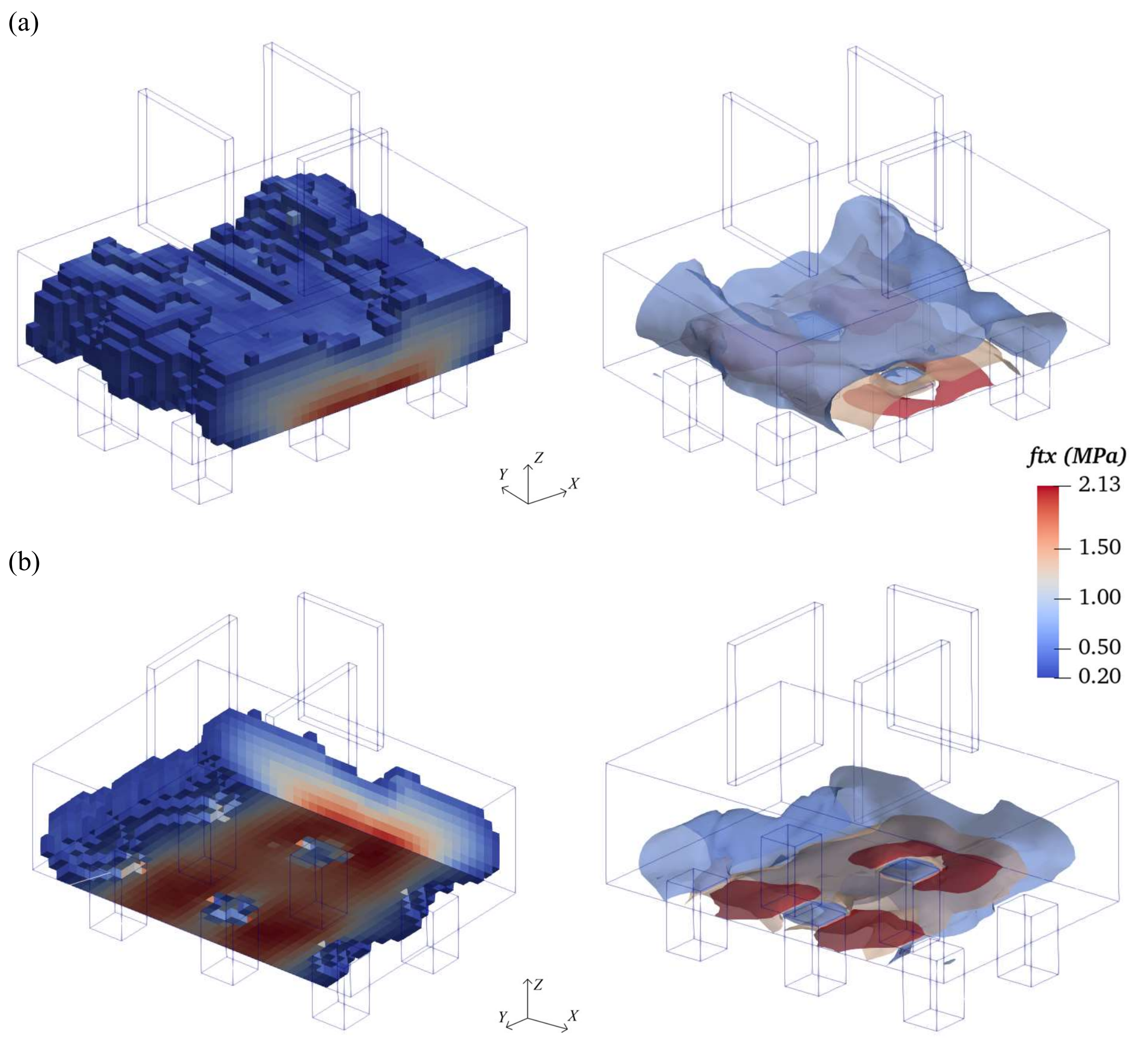

Figure 59 – Six-pile cap: f_{tx} for *U2* - (a) top view perspective; (b) bottom view perspective.

The f_{ty} distribution is shown in Figure 60. The maximum f_{ty} value increased from 0.82 to 1.03 MPa. Stresses that were distributed along *C3* length was now concentrated in the vicinities of the column extremity with increased compression. Also, increased f_{ty} stresses were found at the bottom of the cap, in regions neighboring piles *P4*, *P5* and *P6* below the extremities of the columns *C1* and *C2* with increased compression. Interestingly, comparing Figure 57b and Figure 60b, the reduction of f_{ty} stresses is observed in the *y*-span between piles.

(a)

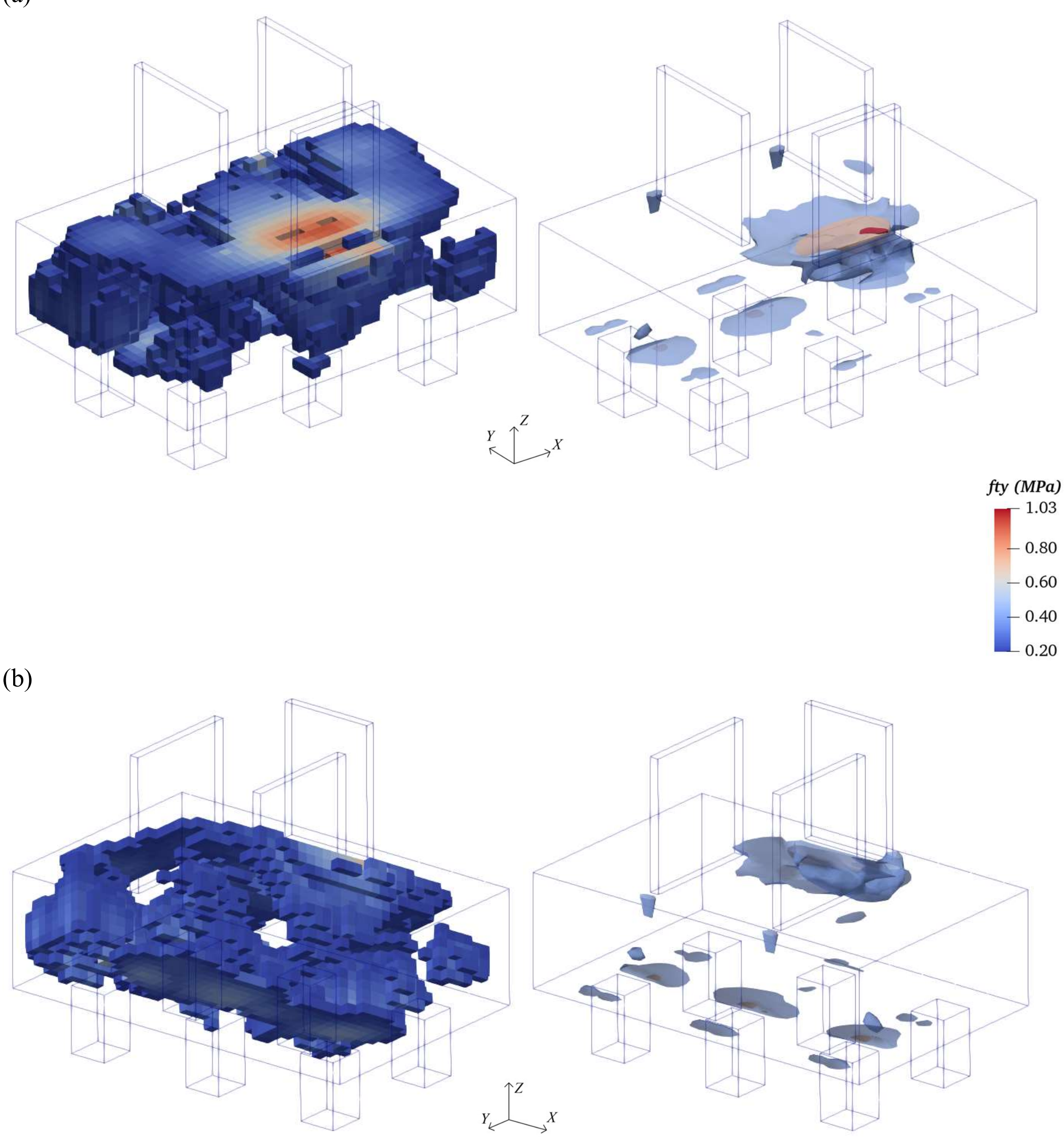

Figure 60 – Six-pile cap: f_{ty} distribution for load combination *U2* - (a) top view perspective; (b) bottom view perspective.

The f_{tz} distribution is shown in Figure 61. The maximum f_{tz} value changed slightly from 0.77 to 0.72 MPa. New ‘red isosurfaces’ were found at the north side face of cap, deriving from the increased compressive stresses of columns *C1* and *C2*. The reduction of the f_{tz} stresses at the bottom of the cap in the region of the piles, interestingly derived from the reduced compressive stresses of the same columns.

(a)

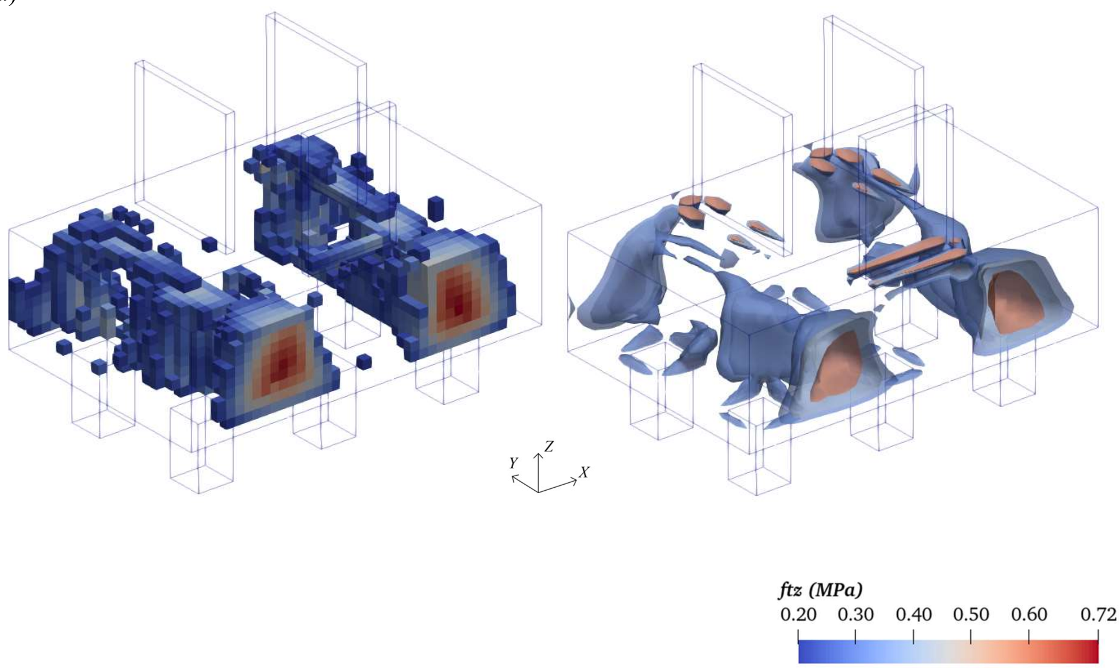

(b)

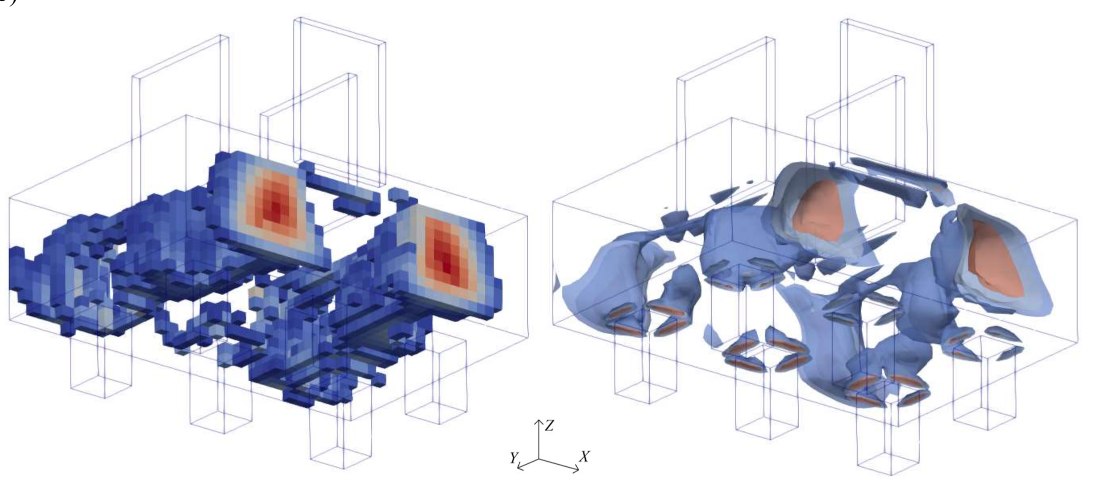

Figure 61 – Six-pile cap: f_{tz} distribution for load combination *U2* **-** (a) top view perspective; (b) bottom view perspective.

5.5.3 Concrete check

Load combination U1

Verification of concrete against crushing was performed in two steps. In the first one, elements under triaxial compression were filtered out in Figure 62 - they were mainly found immediately below the columns, and immediately above the piles. The calculated *Ottosen* variable was negative for them all, ranging from -1.58 to -1.00, indicating adequate concrete strength of the uncracked elements. The *element* subjected to the lowest σ_{c3} was located immediately below columns *C1* and *C2*, under the stress state (σ_{c1}, σ_{c2}, σ_{c3}) = (-1.48 MPa, -2.36 MPa, -7.16 MPa); the *node* with the lowest σ_{c3} was subjected to the stress state (σ_{c1}, σ_{c2}, σ_{c3}) = (-2.80 MPa, -4.35 MPa, -11.58 MPa).

In the second step of the verification, elements under biaxial and uniaxial compression were filtered out and verified to respect the design compression strength of cracked concrete, properly accounting for the reduction introduced by the *v* efficiency factor. Only elements with variable *ConcFailRel* > 0.12 were shown in Figure 63 to better illustrate the more stressed elements.

Load combination U2

Verification of concrete against crushing followed the same steps described in the analysis of load combination *U1*. None of the elements under triaxial compression, which once again were mainly found immediately below the columns, and immediately above the piles, exceeded the concrete strength according to the *Ottosen* failure criteria (Figure 64). The calculated *Ottosen* variable ranged from -1.90 to -1.00, indicating adequate concrete strength of the uncracked elements. The *element* subjected to the lowest σ_{c3} was located immediately below columns *C1* and *C2*, under the following stress state: (σ_{c1}, σ_{c2}, σ_{c3}) = (-2.39 MPa, -3.35 MPa, -11.98 MPa); the *node* with the lowest σ_{c3} was subjected to the stress state (σ_{c1}, σ_{c2}, σ_{c3}) = (-4.28 MPa, -7.05 MPa, -20,26 MPa).

In the second step of the verification, elements under biaxial and uniaxial compression were also verified to respect the design compression strength of cracked concrete. Only elements with variable *ConcFailRel* > 0.15 were shown in Figure 65, isolating the more stressed elements. The peak value of this variable increased from 0.36 to 0.48 (about 30%), due to the increased compression of the columns subjected to bending moments.

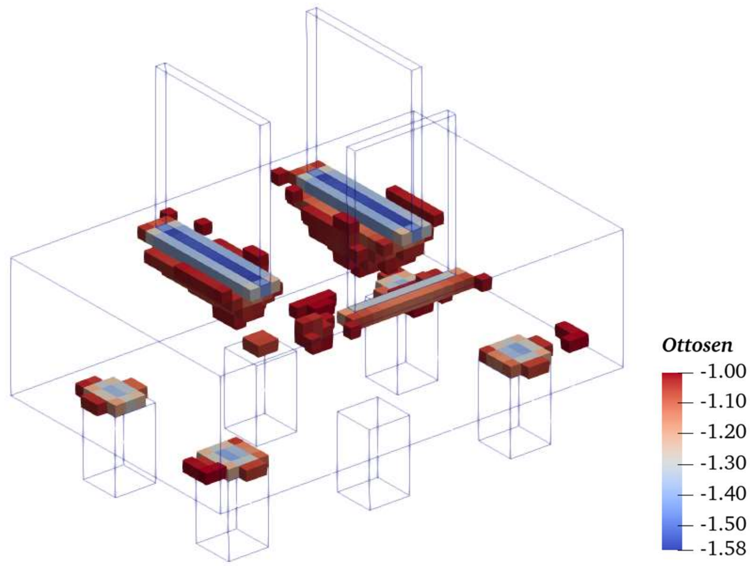

Figure 62 – Six-pile cap: concrete check for load combination *U1*- elements under triaxial compression.

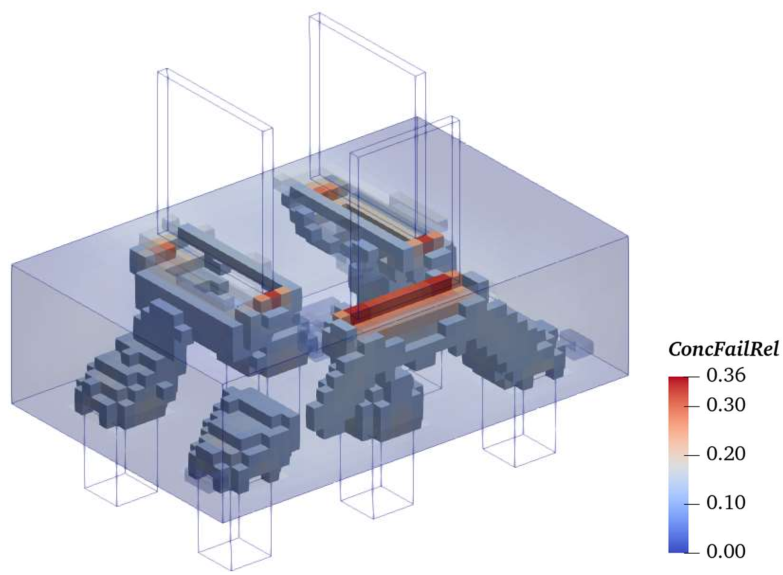

Figure 63 – Six-pile cap: concrete check for load combination *U1* - elements under biaxial or uniaxial compression.

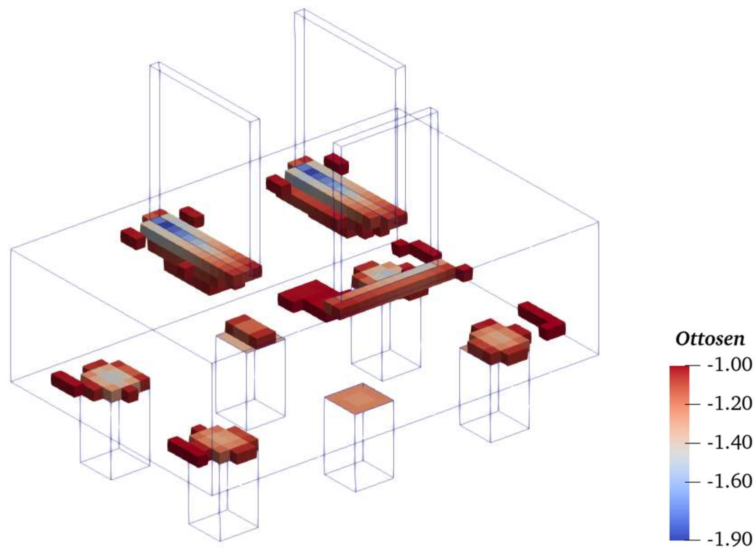

Figure 64 – Six-pile cap: concrete check for load combination *U2* - elements under triaxial compression.

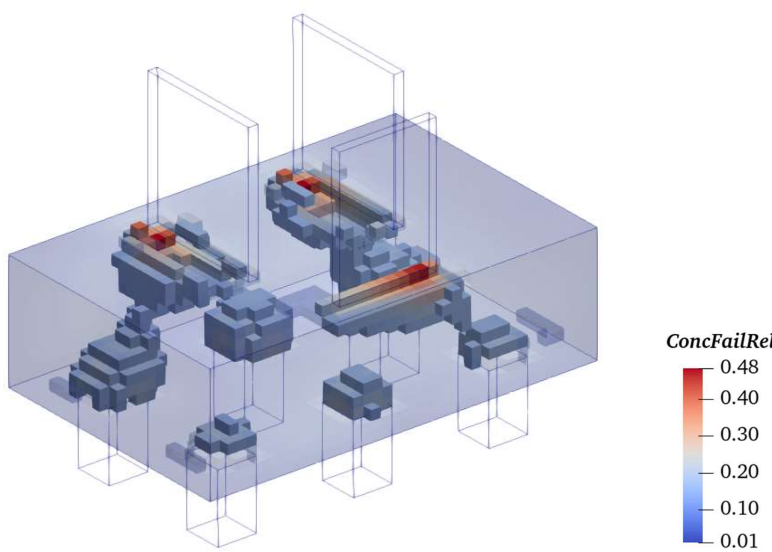

Figure 65 – Six-pile cap: concrete check for load combination *U2* - elements under biaxial or uniaxial compression.

5.5.4 Detailing

Once the f_t distribution was known, it was necessary to delimit zones of uniform reinforcement stress for design. The design stress for each zone should simultaneously cover reinforcement stresses from load combinations *U1* and *U2*.

To illustrate the process, the definition of the zone of uniform f_{tx} at the bottom of the cap is described. The height of the zone extended through 0.60 m of the cap depth, encompassing three rows of elements, which were isolated in Figure 66. For load combination *U1*, the peak value of 2.21 MPa occurred close to pile *P2*; for load combination *U2*, the peak values were also found in the projection of columns *C1* and *C2*, amounting to 2.13 MPa. The maximum stress, f_{tx} = 2.21 MPa, was assumed for the design of the whole of the analyzed zone. Such an assumption was quite conservative but guaranteed that the reinforced concrete strength would be nowhere exceeded. Consequently, no plastic stress redistribution was required between neighboring elements.

(a)

(b)

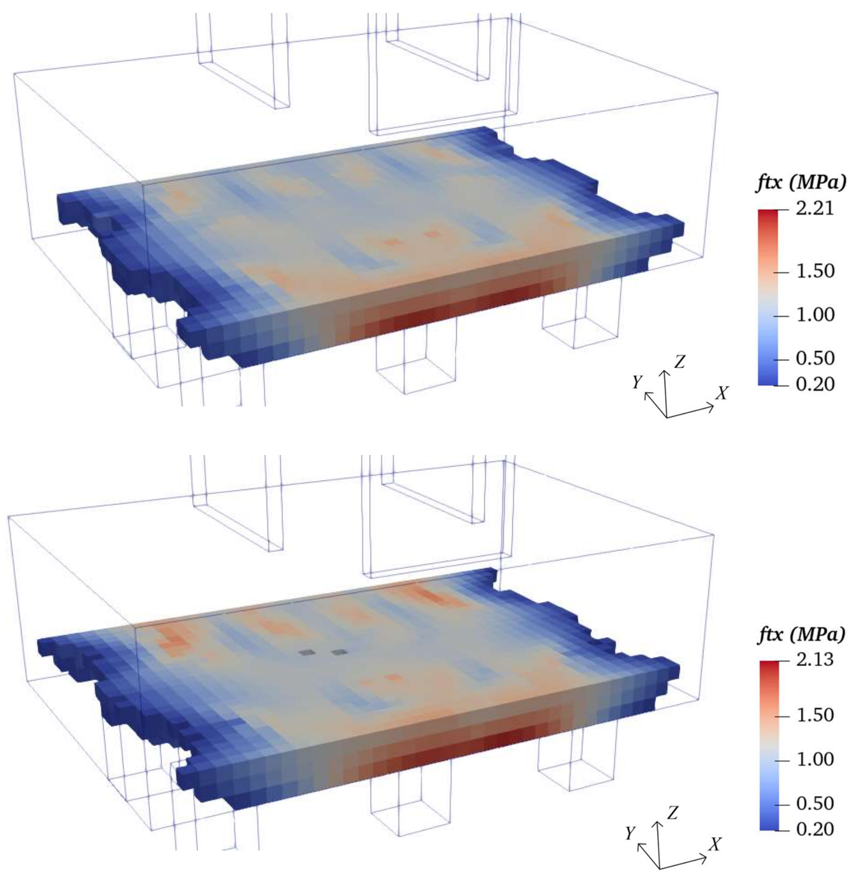

Figure 66 – Six-pile cap: definition of the enveloping f_{tx} value for the arrrangement in the lowest 0.60 m of the cap - load combination (a) *U1* and (b) *U2*.

The process of delimiting zones of uniform design stress was repeated for the three coordinate directions, in a quite handcrafted activity.

f_{tx} distribution was subdivided into three main zones in the lower part of the cap. The lowest one, particularly, was arranged with 3 layers of 16 mm rebars spaced at 0.20 m in *y*-direction and at 0.20 m in the *z*-direction (separation between layers).

$$\begin{aligned} & f_{tx} = 2.21 MPa \\ & \rho_{sx} = \frac{2.21}{434.8} = 0.51\% \\ & A_{sx} = \frac{0.51}{100} \times 100 \times 100 = 51\, cm^2 \qquad \{\text{provided by } \phi 16/20/20 \end{aligned} \tag{5.26}$$

Although no f_{tx} was observed at the top face of the pile cap, one layer of ϕ20 /40 was provisioned.

f_{ty} distribution was subdivided into three zones: one larger zone covering about 40% of the lower height of the cap, where 5 layers of 10 mm rebars spaced at 0.20 m were provided; one strengthened zone at the top of the cap, covering the length of the cap and thickened below the projection of *C3*, where 12 mm rebars were provided; another region in the projection of *C3*, where 12 mm rebars spaced at 0.40 m were provided in three layers.

f_{tz} distribution, was subdivided into four zones: two of them adjacent to columns *C1* and *C2*, where stirrups were provided by 16 mm rebars spaced at 0.40 m in the *x*- and *y*-directions; and the two others close to the extremities of C3, for the suspension of the vertical loads by 16 mm rebars spaced at 0.20 m in the *x*- and *y*-directions.

To facilitate concrete casting, reinforcement bars were positioned at multiples of 0.20. Concerning constructive process, horizontal meshes of *x*- and *y*-rebars can be independently pre-assembled on-site and lowered into their final position; industrialized welded meshes can be used for arranging rebars with diameter between 8 and 12 mm.

Anchorage

The SFM adopts the same principle for bar anchorage as discussed for the stringer-panel model: the anchorage length must be sufficient to transfer “the maximum tensile force that occurs in the reinforcing bar under consideration.” (*fib*, 2021, p.117). For this, enough length should be provided to ensure proper transfer of these tensile forces from the reinforcement to the surrounding concrete.

Particular attention was paid to verifying anchorage in the critical regions above the supports and below the applied loads. Since the cap extended 0.80 m beyond the pile faces, enough transfer length was provided for the bottom reinforcement. The same scenario was not found for top reinforcement in the y-direction, below column *C3*. In that case, provision of a welded bar in the x-direction, at the extremity of the top ties, would be recommended.

Final detailing

By the end of the design process, the reinforcement consumption was evaluated in terms of total detailed reinforcement area. The proposed arrangement summed:

$$\begin{aligned}
A_{sx,\inf} &= \left(18\times 2.00+8\times 1.13\right)\times 3+(26\times 1.13)\times 3+(13\times 1.13)\times 2=252.0\ cm^2 \\
A_{sy,\inf} &= (39\times 0.80)\times 5=156.0\ cm^2 \\
A_{sx,\sup} &= 13\times 1.13=14.7\ cm^2 \\
A_{sy,\sup} &= 39\times 1.13+(17\times 1.13)\times 2+(5\times 1.13)\times 3=99.4\ cm^2 \\
A_{sz} &= 16\times 1.13\times 2+(29\times 2.00)\times 2=152.2\ cm^2
\end{aligned} \tag{5.27}$$

These quantities are compared to those obtained from an alternative design method in Section 6.5.6. The final detailing rendered the arrangements[1] shown in Figure 67 and Figure 68.

Each load case was treated independently to isolate and allow for visualizing the individual structural responses. In design practice, however, the process could likely be automated to generate an envelope of point wise required reinforcement in all load cases. By automating this process, the SFM would efficiently and rigorously handle multiple load cases.

This fourth example addressed the following aspects for the SFM design: the capability of the method to deal with complex three-dimensional behavior and complex load cases, the still handcrafted process of defining reinforcement zones, the conservatism in the choice of arrangements, and the practical assembling of the reinforcement layouts.

[1] Note on the nomenclature for reinforcement arrangement: "*Number of rebars _ bar diameter (mm)/ bar spacing in the first transverse direction (cm)/ bar spacing in the second transverse direction (cm)*". For example, reinforcement in the z-direction arranged as "*24 ϕ10/20/40*" stands for "24 rebars with diameter of 10 mm, spaced at 20 cm in the x-direction, and at 40 cm in the y-direction".

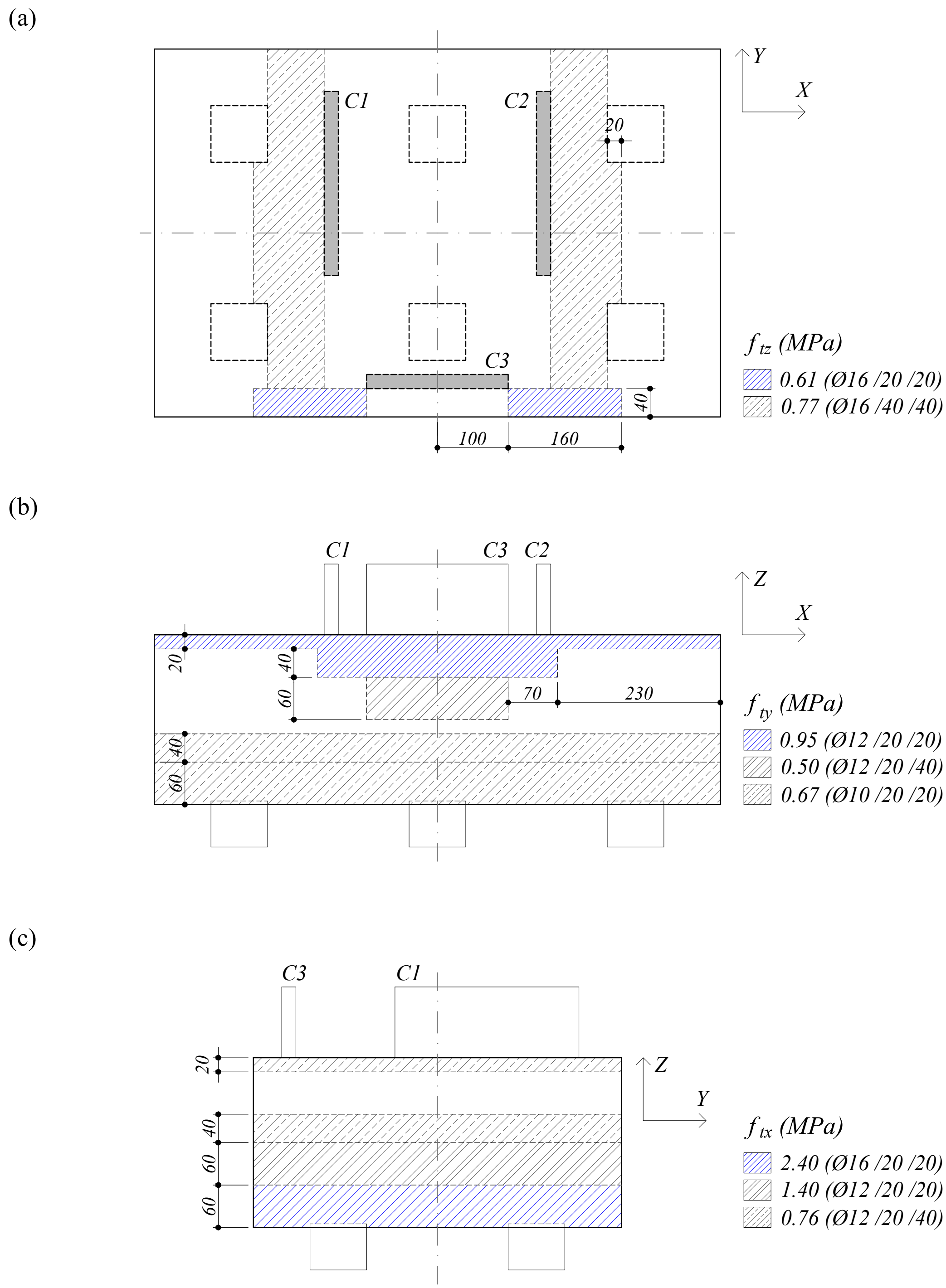

Figure 67 – Six-pile cap: sectorization of reinforcement stresses (a) in the *z*-direction; (b) in the *y*-direction; (c) in the *x*-direction.

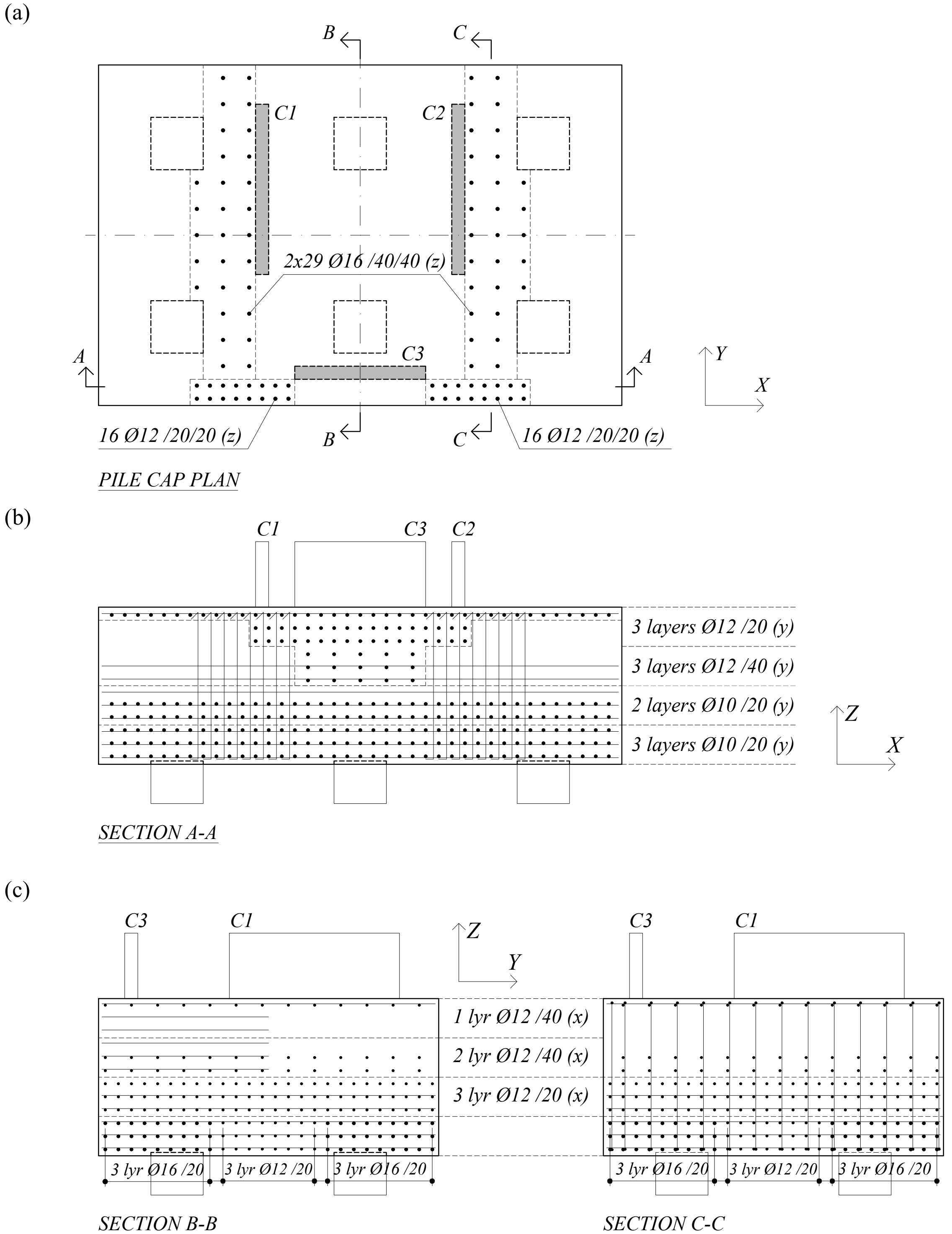

Figure 68 – Six pile cap: reinforcement detailing (a) in the *z*-direction; (b) in the *y*-direction; (c) in the *x*-direction.

5.6 Example 5: trunnion girder

Dams are built primarily to impound water for water storage and energy generation. The water level of the dams or reservoirs is controlled by flood discharger structures, such as the one presented in Figure 69, where the discharge flows through spillways by the opening and closure of spillway gates to adjust the discharge under the gate. A Tainter or radial gate, specifically, is "*is a segment of a cylinder mounted on radial arms that rotate on trunnions anchored to the piers.*" (U.S. Army Corps of Engineers, 2000, p. 2-1). Trunnions girders, on that account, are rigid structural elements that connect the gate arms to vertical reinforced concrete columns, as shown in Figure 70.

The fifth worked example presents the application of the design method based on three-dimensional stress fields to the design of a trunnion girder connected to an interior column, that is, a column supporting two adjacent gates simultaneously. It had a 4.20 m x 5.00 m rectangular cross-section, total length of 8.00 m, and was inclined 8 degrees from the horizontal plane. The girder rested on the column over two different contact surfaces: at its bottom face through a polyethylene film, and at its upstream face through concrete-to-concrete friction. Therein, the contact surface area was limited to two vertical bands, each of them measuring 1.20 m wide. This condition was achieved by the installation of a 1.60 m polystyrene sheet between the vertical contact bands, as shown in Figure 71.

Source: adapted from Andritz (2022).

Figure 69 – Laúca flood discharger.

(a) (b)

Source: (a) adapted from Jornal de Angola (2023); (b) adapted from Intertechne (2022).

Figure 70 – Zoom view of trunnion girders supporting tainter gates: (a) different opening positions; (b) downstream detailed view of the flow control structures.

Forces from the Tainter gate acted through the pivot point located 1.235 m from the upstream face of the girder. They are summarized in Table 3 for four different gate positions. *FN* were the characteristic applied normal forces, and *FT* the characteristic applied tangential forces. Each gate support included a 1.40 m x 2.60 m steel plate to uniformly distribute the concentrated loads to the girder.

Post-tensioning consisted of 4 x 7 tendons made of 21 strands with diameter of 15.2 mm in the longitudinal direction (*PL*), and 3 x 6 tendons made of 10 strands with diameter of 15.2 mm in the transverse direction (*PT*), where each strand cross-sectional area summed 1.4 cm². The anchor heads of the longitudinal tendons measured 0.40 m x 0.40 m, whereas the anchor heads of the transversal tendons measured 0.32 m x 0.32 m. For the current design, post-tensioning quantities were assumed to be already known, obtained from preceding calculations to control serviceability states and bearing stresses in the column-girder interface. Those calculations, however, are beyond the scope of this example. In the structural model, post-tensioning was simulated by the application of equivalent forces at the anchor heads. Girder should be designed with normal-weight concrete C30 (f_{ck} = 30 MPa), B500 reinforcement (f_{yk} = 500 MPa), and low relaxation post-tensioning steel (f_{pu} = 1 900 MPa).

This example was chosen to illustrate the application of the design method to another complex D-region: a structural member subjected to combined bending and twisting moments, axial and transverse shear forces. It did not aim at presenting a full design covering all load combinations as prescribed by design codes (ACI, 2006; U.S. ARMY, 2000). Rather, it illustrated the design process for two representative load combinations. The same design process could be easily and directly extended to cover multiple load combinations.

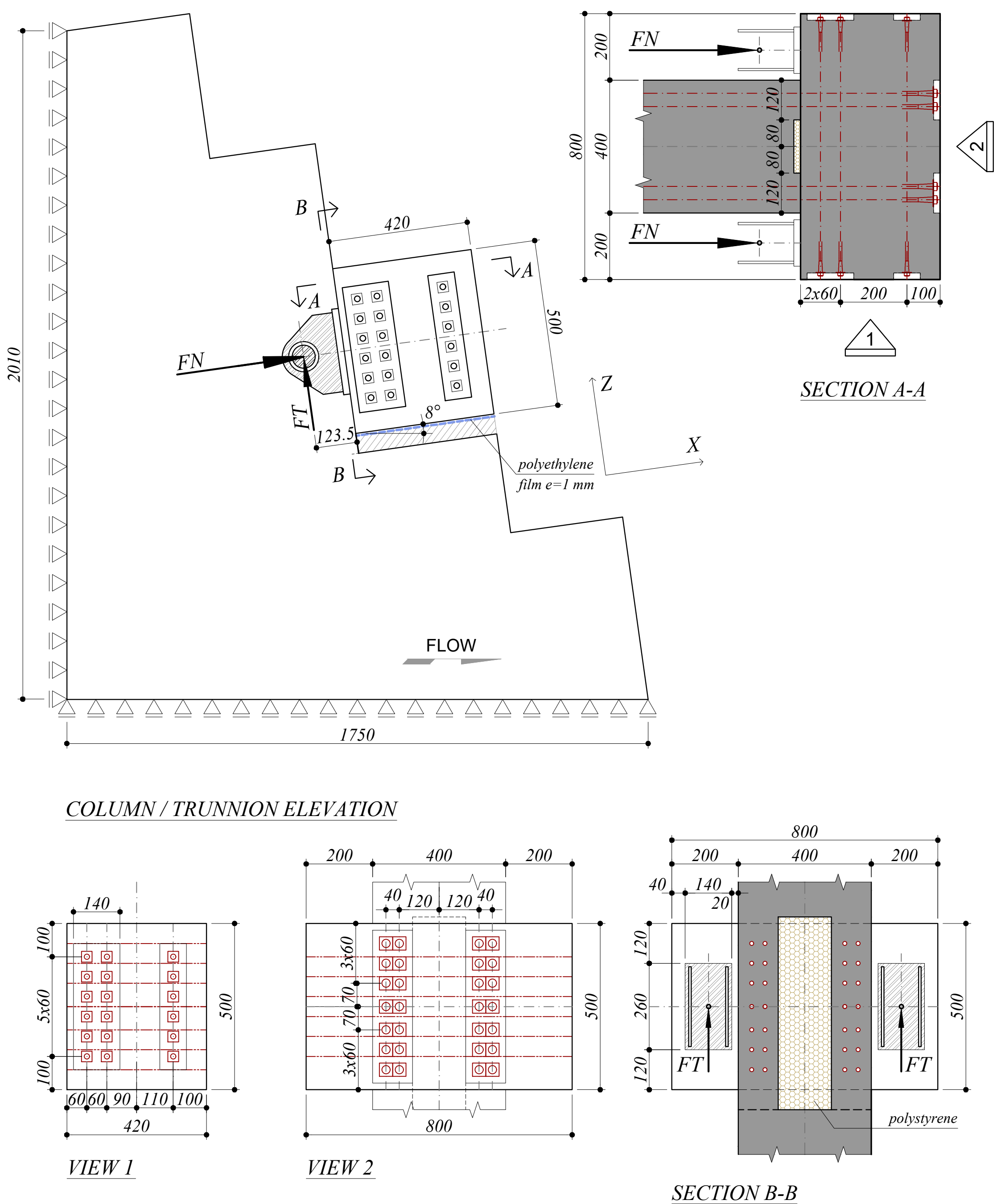

Figure 71 – Trunnion girder: geometry, post-tensionsing tendons and applied loads (dimensions in cm).

Table 3 – Loads applied to the trunnion girder for different gate opening position (loads per trunnion, characteristic values).

Position	opening [degrees]	*FN* [kN]	*FT* [kN]
#1	0	18,200	300
#2	15.83	11,000	-2,000
#3	30.67	5,700	-2,200
#4	45.63	2,600	-1,700

5.6.1 Structural model for the linear analysis

The structural model for the linear elastic analysis was meshed with cubic elements with dimension of 0.20 m, leading to a model with 62,758 cubic solid elements, as shown in Figure 72. Only one half of the structure was modeled due to geometry and loading symmetry. The girder, specifically, was modeled with 21 elements along the width, 25 elements along the height, and 20 elements along the length.

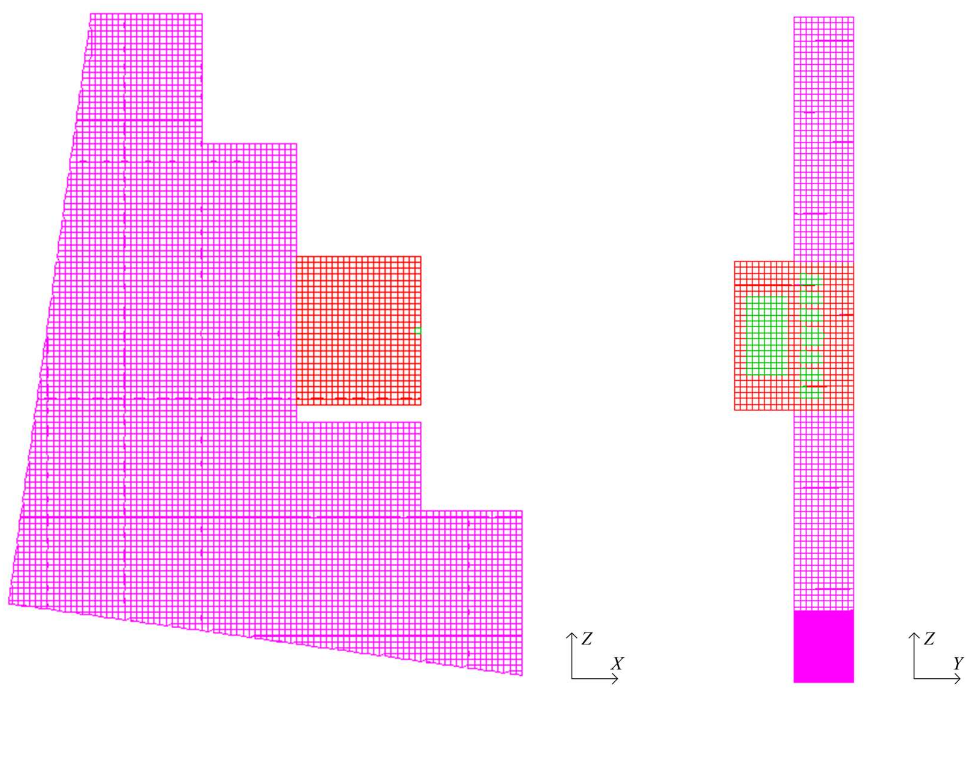

Figure 72 – Trunnion girder: structural model for the linear analysis.

The model was rotated 8 degrees clockwise about the z-axis, so that the beam directions would coincide with the global coordinate system. This artifice was employed because the formulation presented in Section 3 is restricted to reinforcement directions coinciding with the stress tensor coordinate system. Concerning the boundary conditions, a local coordinate system, rotated 8 degrees about the z-axis, was established to define the supports along the base and height of the column. Also, rigid links in the global z-direction were defined to connect the nodes of the bottom of the girder to nodes in the column with the same x and y coordinates. Lastly, restrictions were attributed to the nodes at the symmetry plane.

Column and girder were modeled with linear elastic material with modulus E_c = 4,760 $f_{ck}^{0,5}$ = 26,000 MPa, and 0.2 Poisson modulus. Steel plates at the post-tensioning anchor heads and at the gate support were modeled with a linear elastic material with an elastic modulus ten times greater than the steel modulus, to better distribute the applied loads (E_s = 2,100 GPa).

Note that, by modeling the structure with an axis of symmetry, it was assumed that two adjacent gates were assumed to be opened at identical positions. Design loads *FN* and *FT* acting on the pivot point were transformed to equivalent forces applied at the steel plate surface: *FN* and FT were directly subdivided into four subcomponents; flexural moment *FT x 1.235* was decomposed into binary forces with a 1.80 m lever arm along the z-direction. The resulting components were as show in Figure 73 and Table 4.

$$
\begin{aligned}
&FN_{\sup,x} = \frac{FN}{4} + 0.5\frac{FT \times 1.235}{1.8}; \quad FN_{\inf,x} = \frac{FN}{4} - 0.5\frac{FT \times 1.235}{1.8} \\
&FT_{\sup,z} = F_{\inf,z} = \frac{FT}{4}
\end{aligned}
\tag{5.28}
$$

Table 4 – Equivalent concentrated loads applied to the trunnion girder for different gate position.

		characteristic value (per node)			design value (per node)		
Position	**Opening** [degrees]	***FN***FN_{sup} [MN]	FN_{inf} [MN]	***FT*** [MN]	FN_{sup} [MN]	FN_{inf} [MN]	***FT*** [MN]
#1	0	4.65	4.45	0.08	6.51	6.23	0.11
#2	15.83	2.06	3.44	-0.50	2.89	4.81	-0.70
#3	30.67	0.67	2.18	-0.55	0.94	3.05	-0.77
#4	45.63	0.07	1.23	-0.43	0.09	1.73	-0.60

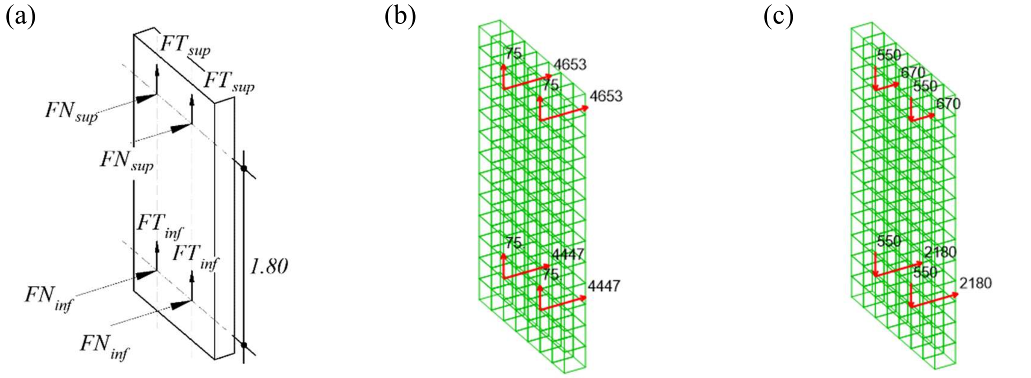

Figure 73 – Trunnion girder: loading (a) nomenclature; (b) gate position #1; (c) position #3.

Post-tensioning forces were applied as concentrated loads on the anchor plate, as presented in the following equation, assuming 20% of prestress losses, and permissible stress in prestressing steel equal to 0.74 f_{pu}, where f_{pu} is the ultimate stress of the prestressing strands:

$$F_{PL} = 21\,strand \times 1.4\,cm^2/strand \times 0.8 \times (0.74 \times 190)\,kN/cm^2 \cong 3,300\,kN$$
$$F_{PT} = 10\,strand \times 1.4\,cm^2/strand \times 0.8 \times (0.74 \times 190)\,kN/cm^2 = 1,575\,kN \tag{5.29}$$

In addition to post-tensioning and gate forces, the self-weight of the girder (G) was also computed. Two load combinations were selected for the ULS design, one for gate position #1, and another one for gate position #3. All loads were computed as unfavorable loads:

$$U1 = 1.4(FN + FT)_{gate\ position\ \#1} + 1.4G + 1.2(PL + PT)$$
$$U2 = 1.4(FN + FT)_{gate\ position\ \#3} + 1.4G + 1.2(PL + PT) \tag{5.30}$$

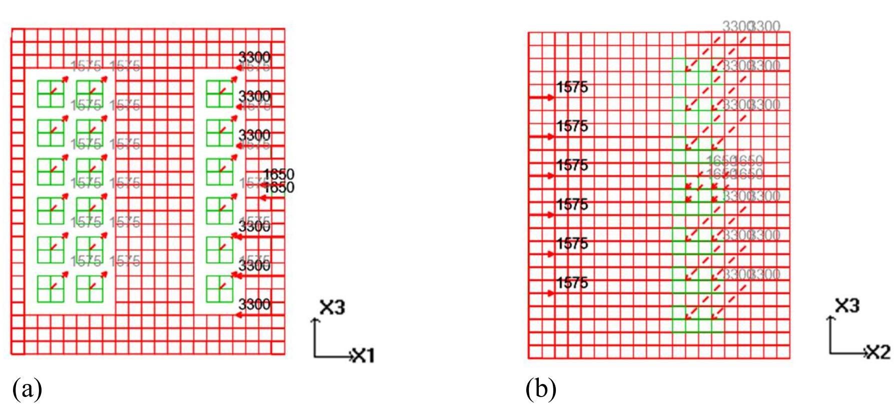

Figure 74 – Trunnion girder post-tensioning: (a) longitudinal PL; (b) transversal PT.

5.6.2 Reinforcement design

Proceeding to Step 3 of the methodology described in Section 5.1, reinforcement stress distributions were analyzed in post-processor *ParaView* for each load combination. Detailed results were extracted from the two chosen perspective views adjusted in Figure 75.

(a)

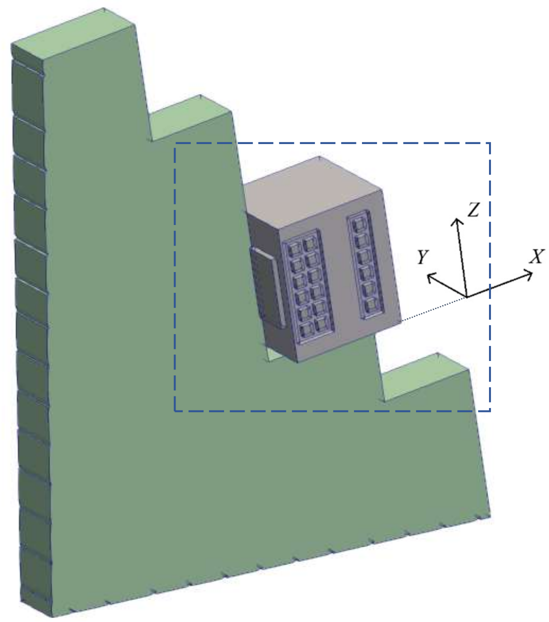

(b)

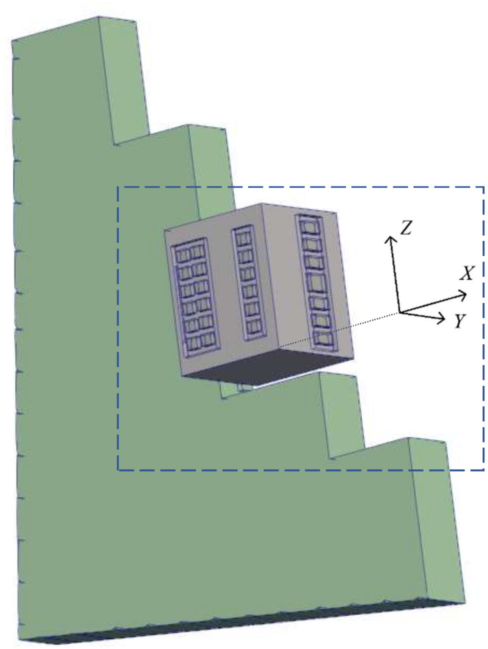

Figure 75 – Trunnion girder: overall views identifying detailed views - (a) upstream top perspective; (b) downstream bottom perspective.

Gate at position #1

The f_{tx} distribution is shown in Figure 76. The highest f_{tx} values were found in regions close to the south and downstream faces of the girder. The peak values, particularly, were found behind the trunnion steel plate, and between the second and third vertical lines of the transverse post-tensioning anchor heads, reaching the value of 1.23 MPa. In the south face, particularly, the response was already expected for a discontinuity region resulting from the application of the eccentric *PT* loads, which leads to side face tension stresses. The overall distribution showed that reinforcement stresses vanished towards the core of the girder.

(a)

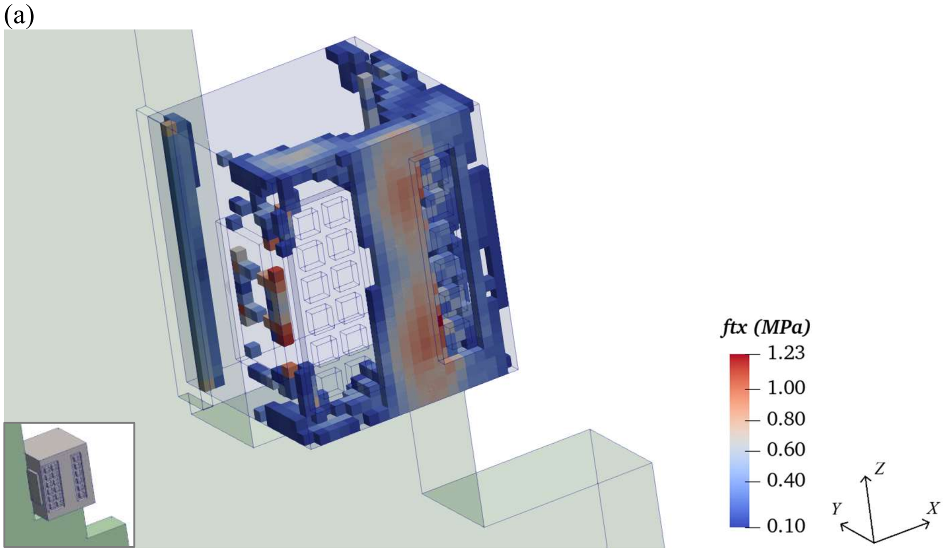

(b)

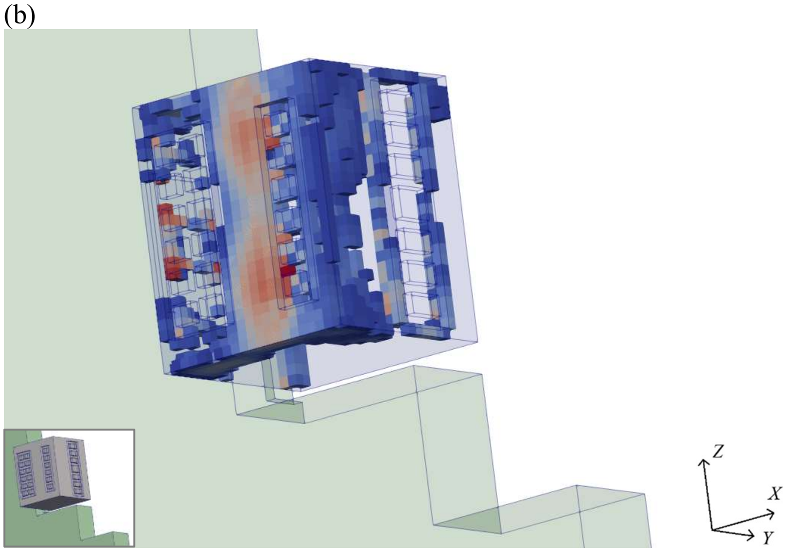

Figure 76 – Trunnion girder: f_{tx} distribution for gate position #1 – (a) upstream top perspective; (b) downstream bottom perspective.

The f_{ty} distribution is shown in Figure 77. The highest f_{ty} values of were found in the vicinity of column-girder contact surface. The peak value was observed at the axis of symmetry of the structure, reaching the value of 2.31 MPa. This response was already expected for a corbel subjected to a concentrated load, *FN*, which should be equilibrated by tensile forces in the y-direction. The overall distribution showed that the reinforcement stresses vanished towards the core of the girder.

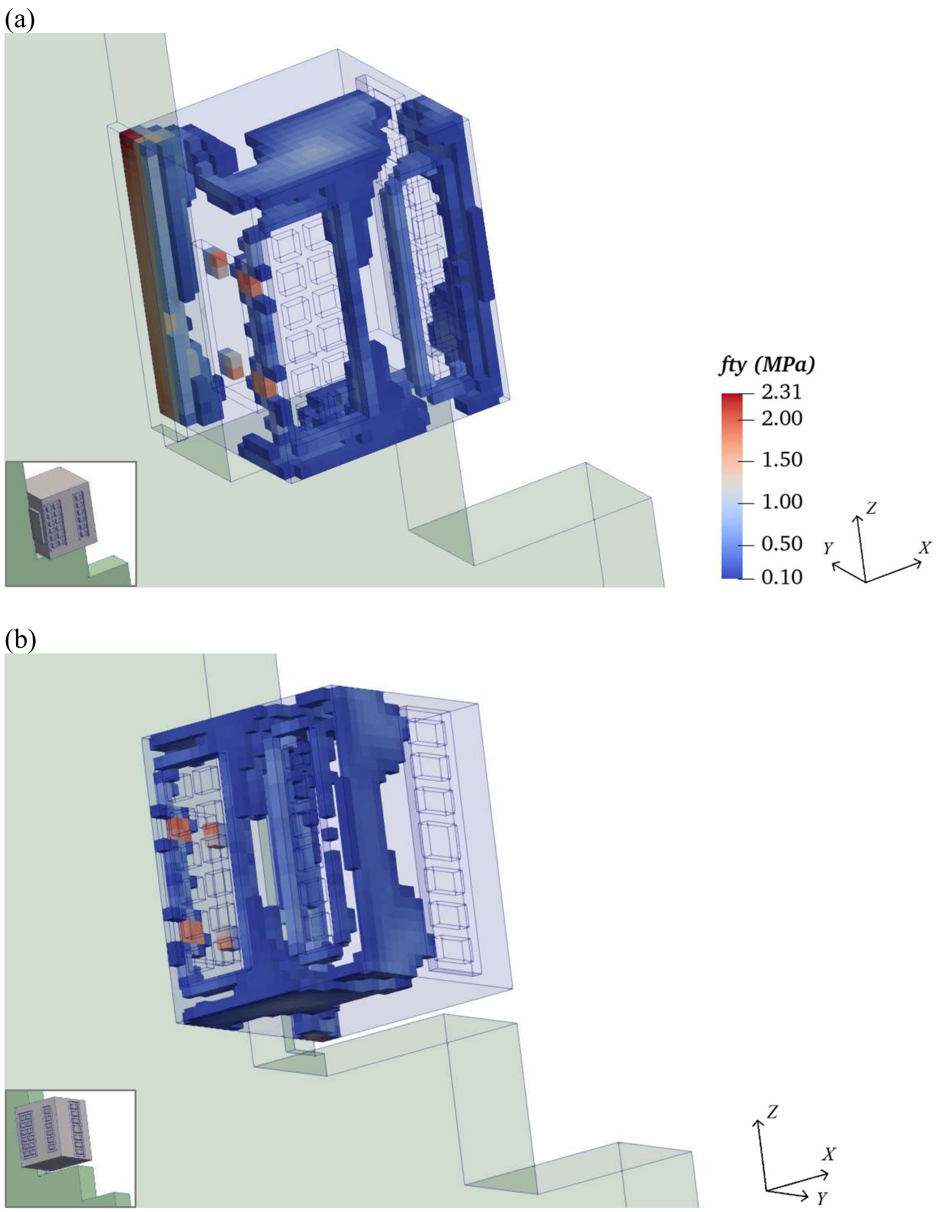

Figure 77 – Trunnion girder: f_{ty} distribution for gate position #1 – (a) upstream top perspective; (b) downstream bottom perspective.

The f_{tz} distribution is shown in Figure 78. Differently from the distribution presented in the previous directions, the greatest values of f_{tz} were distributed over the whole volume of the trunnion girder. The peak, particularly, was found behind the trunnion steel plate, reaching the value of 3.91 MPa. The peak values extended through a very reduced area, corresponding to just about four elements (0.40 cm), and were ascribed to the concentrated applied loads. The overall distribution showed that the reinforcement stresses were smaller at the core of the girder. This response was expected for the suspension of vertical forces.

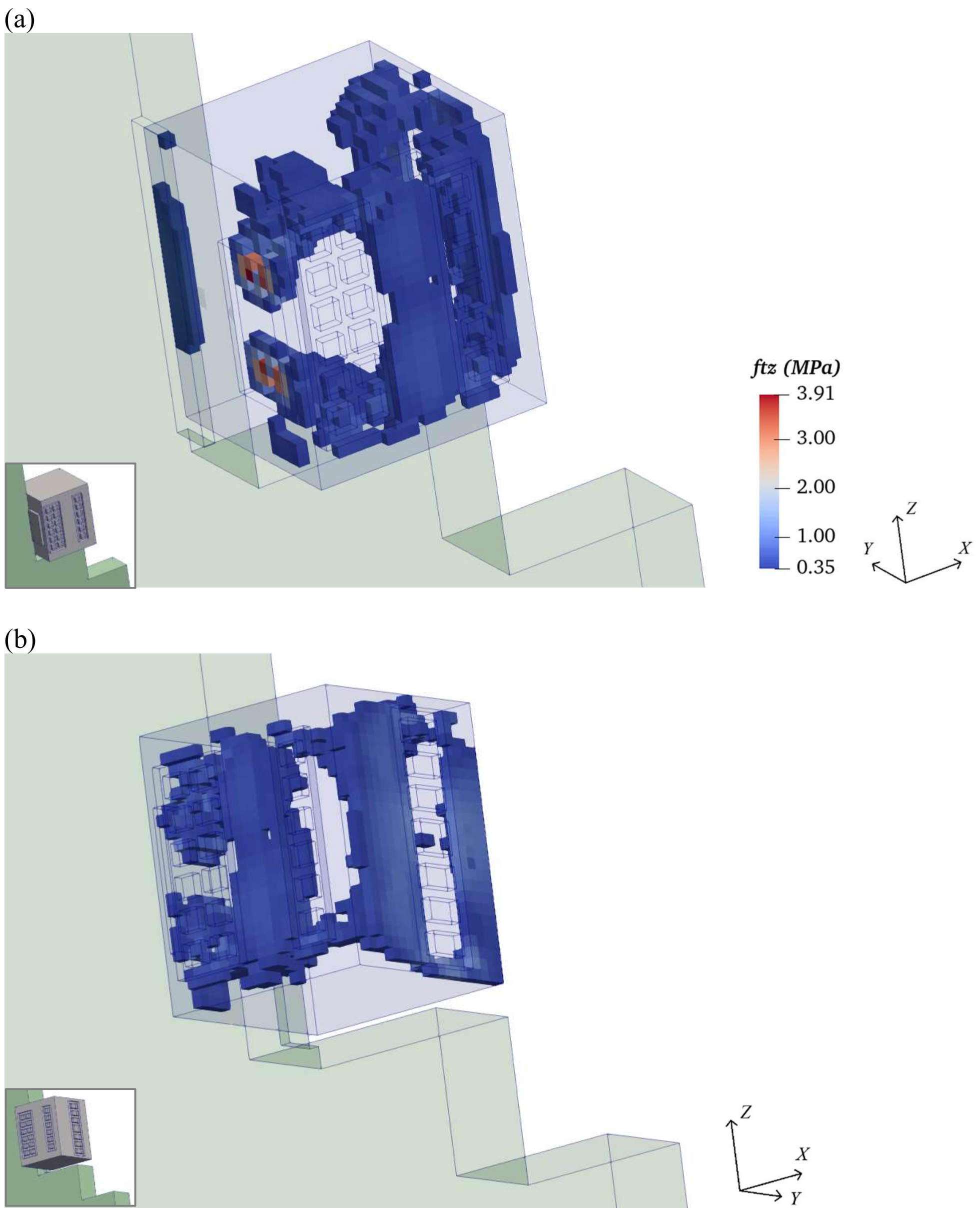

Figure 78 – Trunnion girder: f_{tz} distribution for gate position #1 – (a) upstream top perspective; (b) downstream bottom perspective.

Gate at position #3

When the gates are in *Position #3*, applied normal forces *FN* are much higher at the upper half of the girder, and *FT* introduces additional torsional moments to the girder.

The f_{tx} distribution is shown in Figure 79. The higher f_{tx} values were now intensively observed in the upper half of the girder. The peak value, particularly, increased from 1.23 MPa to 1.77 MPa (+43,9%).

(a)

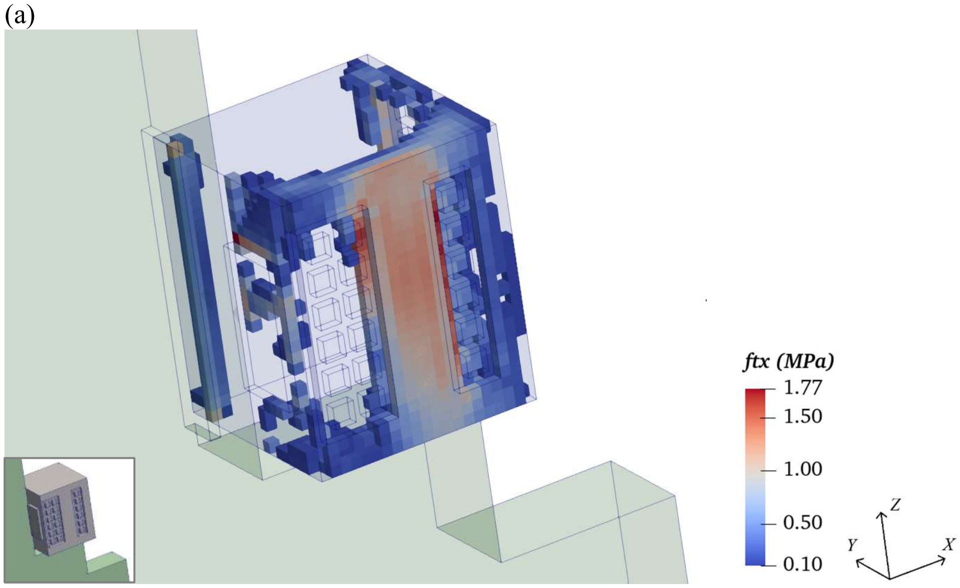

(b)

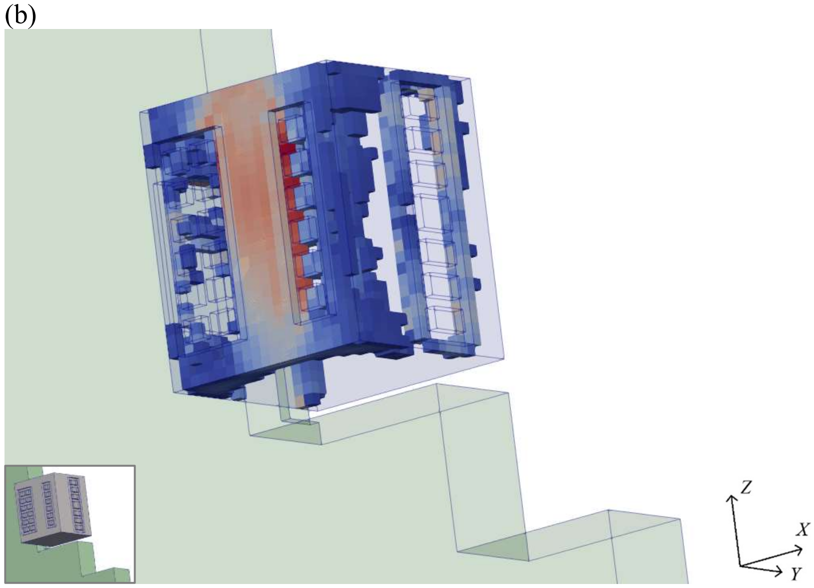

Figure 79 – Trunnion girder: f_{tx} distribution for gate position #3 – (a) upstream top perspective; (b) downstream bottom perspective.

The f_{ty} distribution is shown in Figure 80. The higher f_{ty} were more pronounced in the upper third of the girder, in the vicinity of the contact column-girder. The peak value, particularly, increased from 2.31 MPa to 2.76 MPa (+19,4%).

The f_{tz} distribution is shown in Figure 81. The higher f_{tz} values were found behind FN_{sup}. The peak value, particularly, reduced from 3.91 MPa to 2.61 MPa (-33,2%).

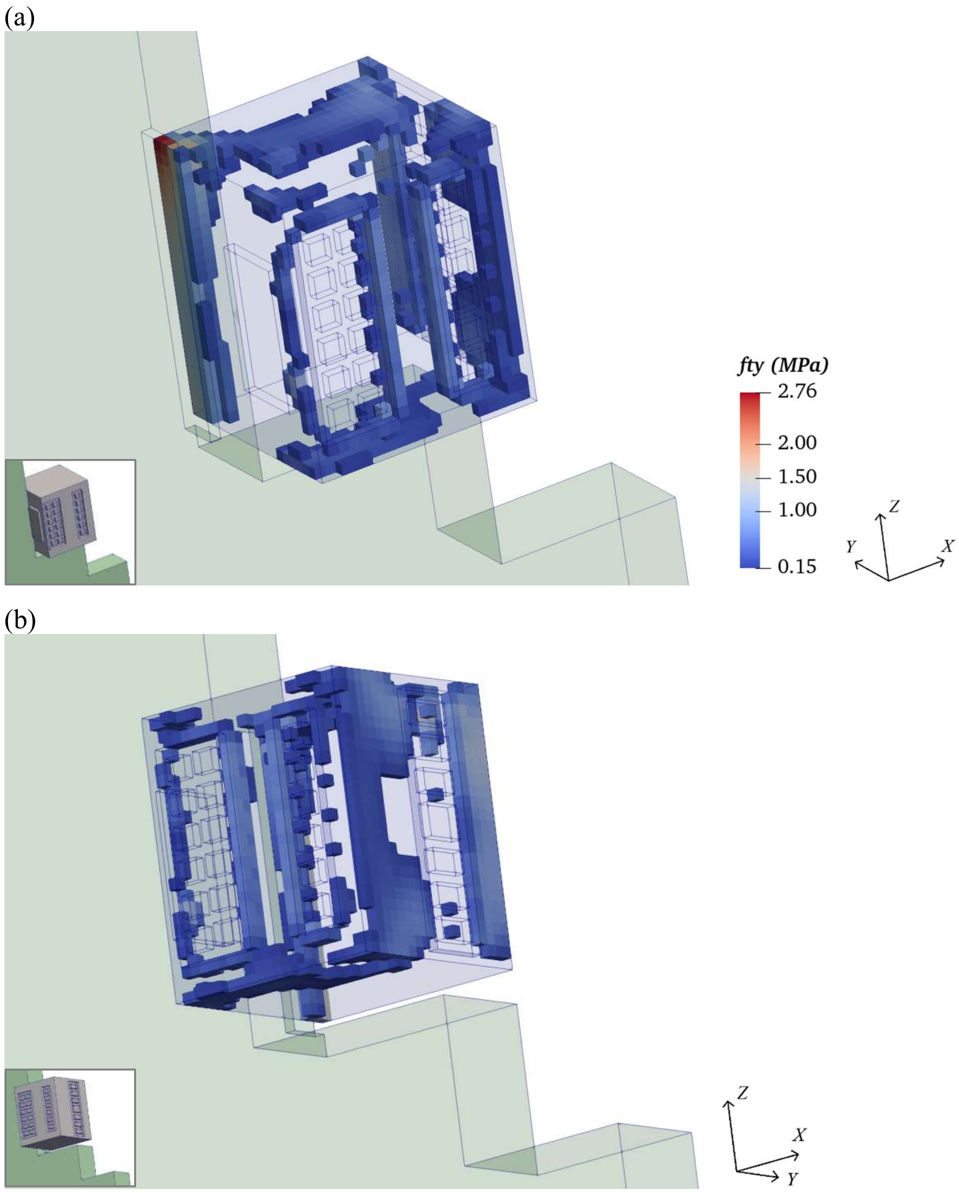

Figure 80 – Trunnion girder: f_{ty} distribution for gate position #3 – (a) upstream top perspective; (b) downstream bottom perspective.

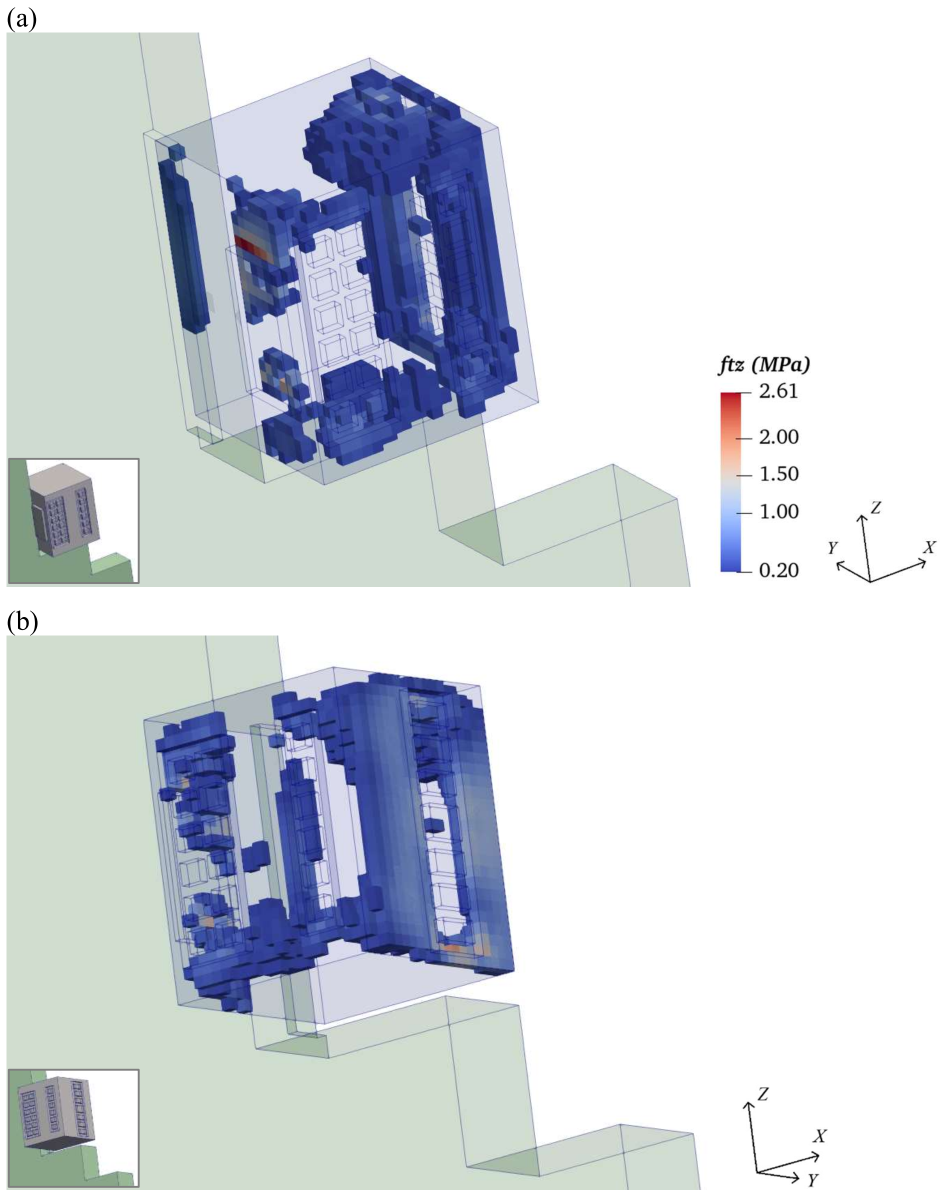

Figure 81 – Trunnion girder: f_{tz} distribution for gate position #3 – (a) upstream top perspective; (b) downstream bottom perspective.

5.6.3 Concrete check

Verification of concrete against crushing was performed in two steps. First, elements under triaxial compression were filtered out in Figure 82. They were mainly found in the projection of the *PL* anchor heads; some elements were also found in the projection of the first and second columns of the transverse post-tensioning *PT*. The calculated *Ottosen* variable was negative for all elements, for both load cases, and ranged from -2.31 to -1.00, indicating adequate concrete strength of the uncracked elements.

In the second step of the verification, elements under biaxial and uniaxial compression were filtered out and verified to respect the design compression strength of cracked concrete, properly accounting for the reduction introduced by the v efficiency factor.

(a)

(b)

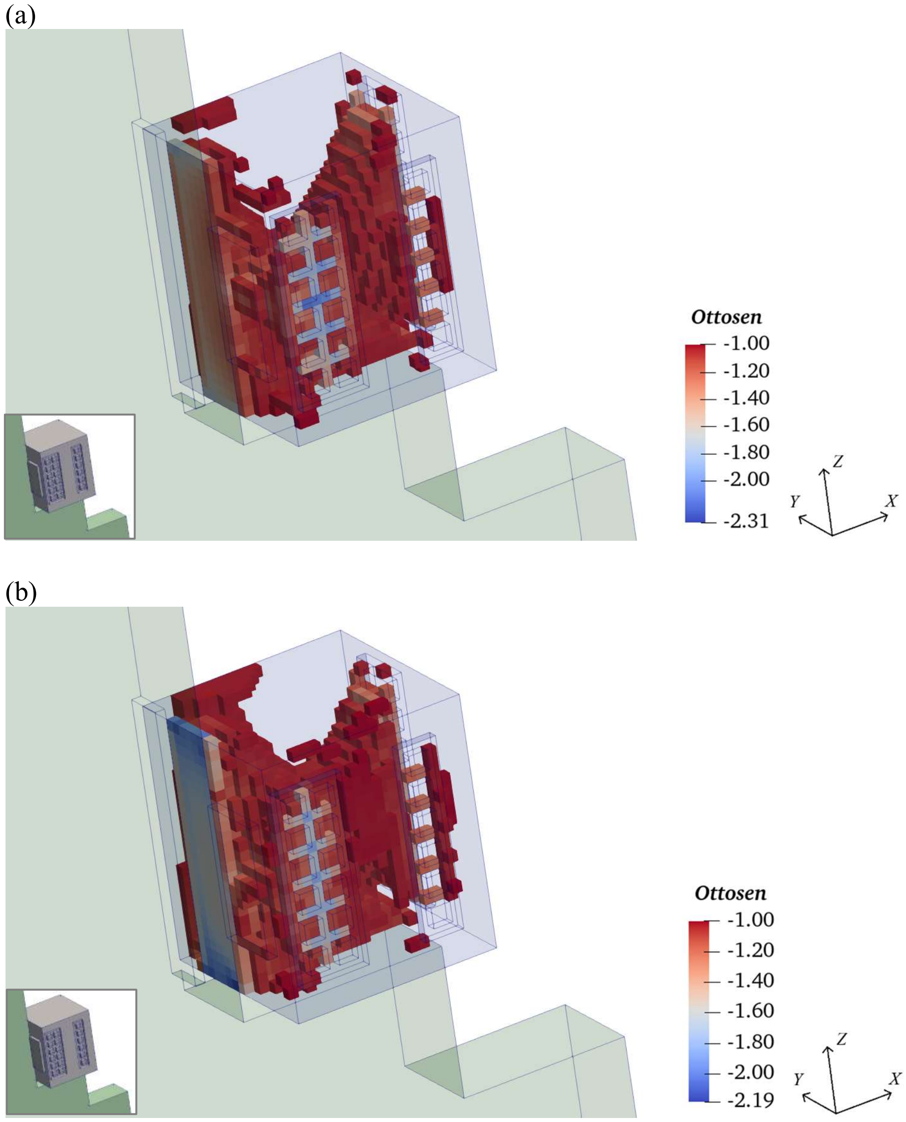

Figure 82 – Trunnion girder: concrete check for elements under triaxial compression for (a) gate position #1 and (b) gate position #3.

For gate position #1, variable *ConcFailRel* < 1.0 indicated the adequate concrete strength. Few elements presented *ConcFailRel* variable ranging from 1.0 and 1.17 (Figure 83b). Some of them were located behind the trunnion steel plate. Compressive stresses at those elements would certainly be reduced to allowable stresses if a more accurate modeling of the concentrated applied load were assumed; other few elements were located behind longitudinal anchor plates. However, it is anticipated that complementary spiral reinforcement prescribed by the suppliers of post-tensioning systems efficiently confines those regions, increasing the concrete compressive strength.

(a)

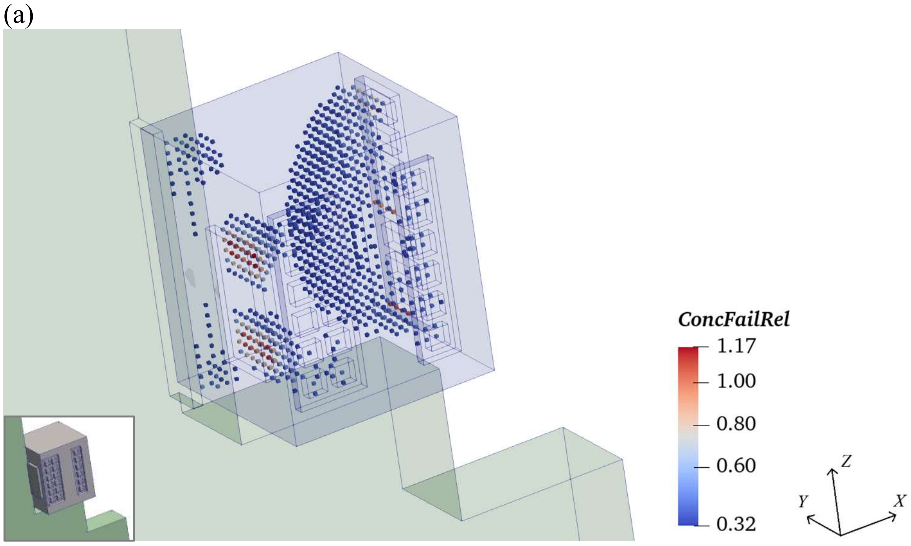

(b)

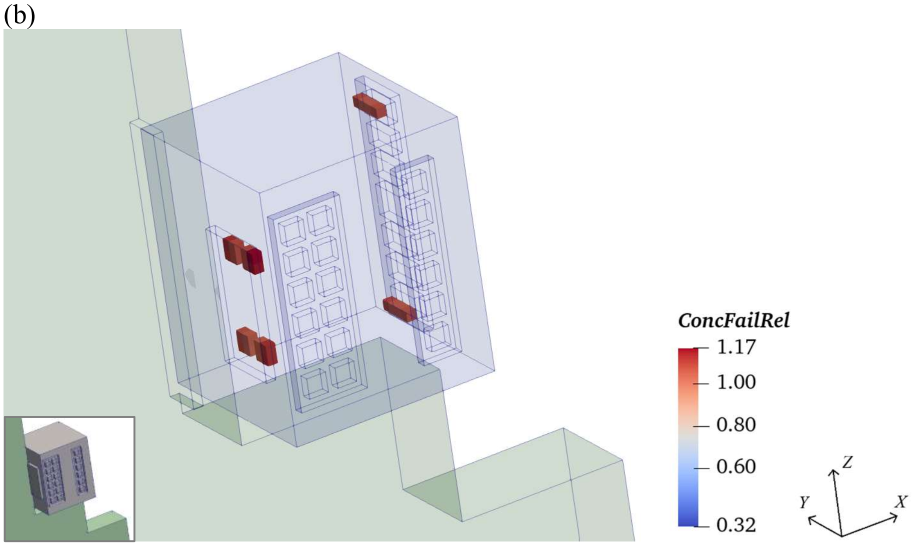

Figure 83 – Trunnion girder: concrete check for elements under bi/uniaxial compression for gate position #1 – (a) all elments; (b) elements with *ConcFailRel* > 1.

For gate position #3, variable *ConcFailRel* < 1.0 indicated the adequate concrete strength. Few elements presented *ConcFailRel* variable ranging from 1.0 and 1.12 (Figure 84b). They were located behind longitudinal anchor plates. However, it is once again anticipated that complementary spiral reinforcement will increase the concrete compressive strength to admissible values.

(a)

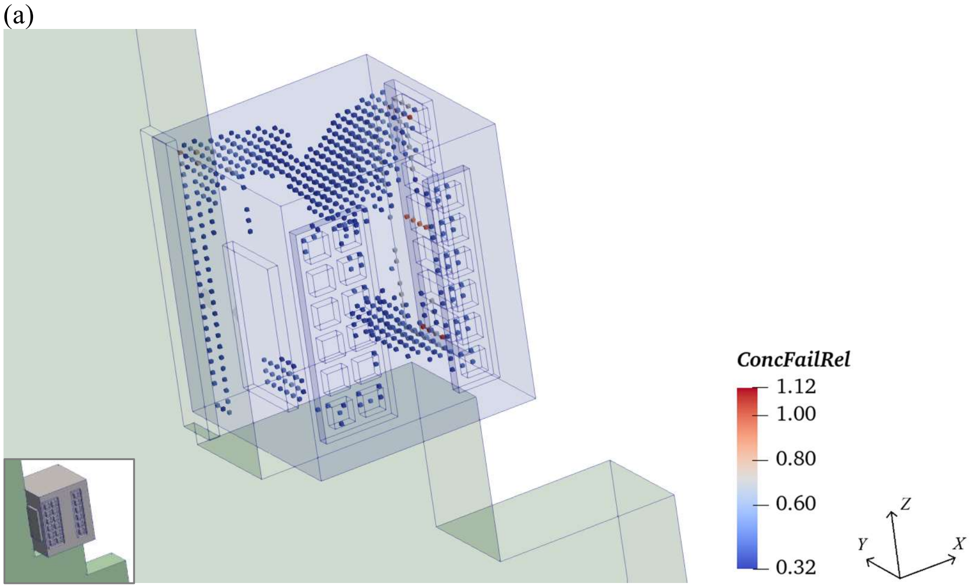

(b)

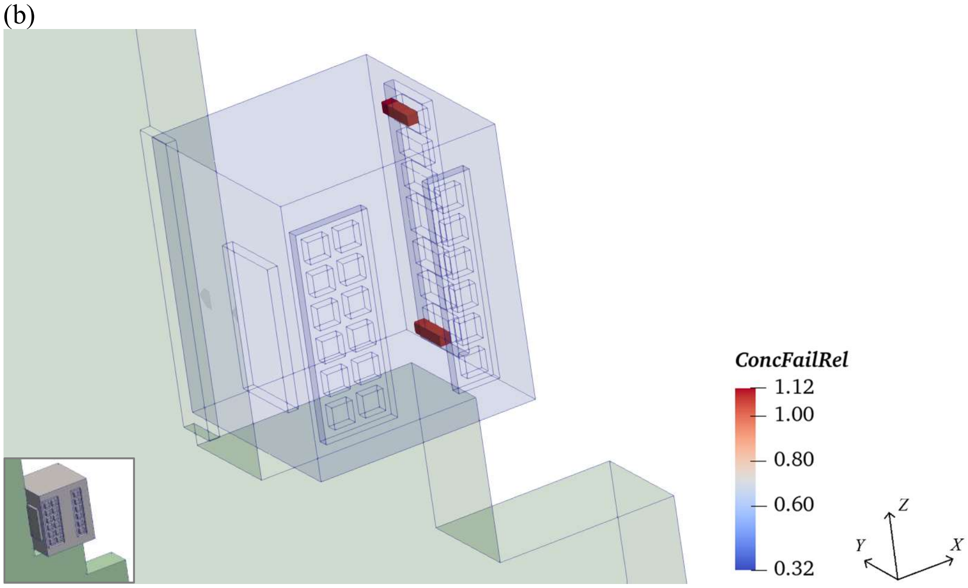

Figure 84 – Trunnion girder: concrete check for elements under bi/uniaxial compression for gate position #3 – (a) *ConcFailRel* < 0; (b) *ConcFailRel* > 1.

Figure 85 presents the distribution of the principal compressive concrete stress σ_{c3} for the two load combinations.

(a)

(b)

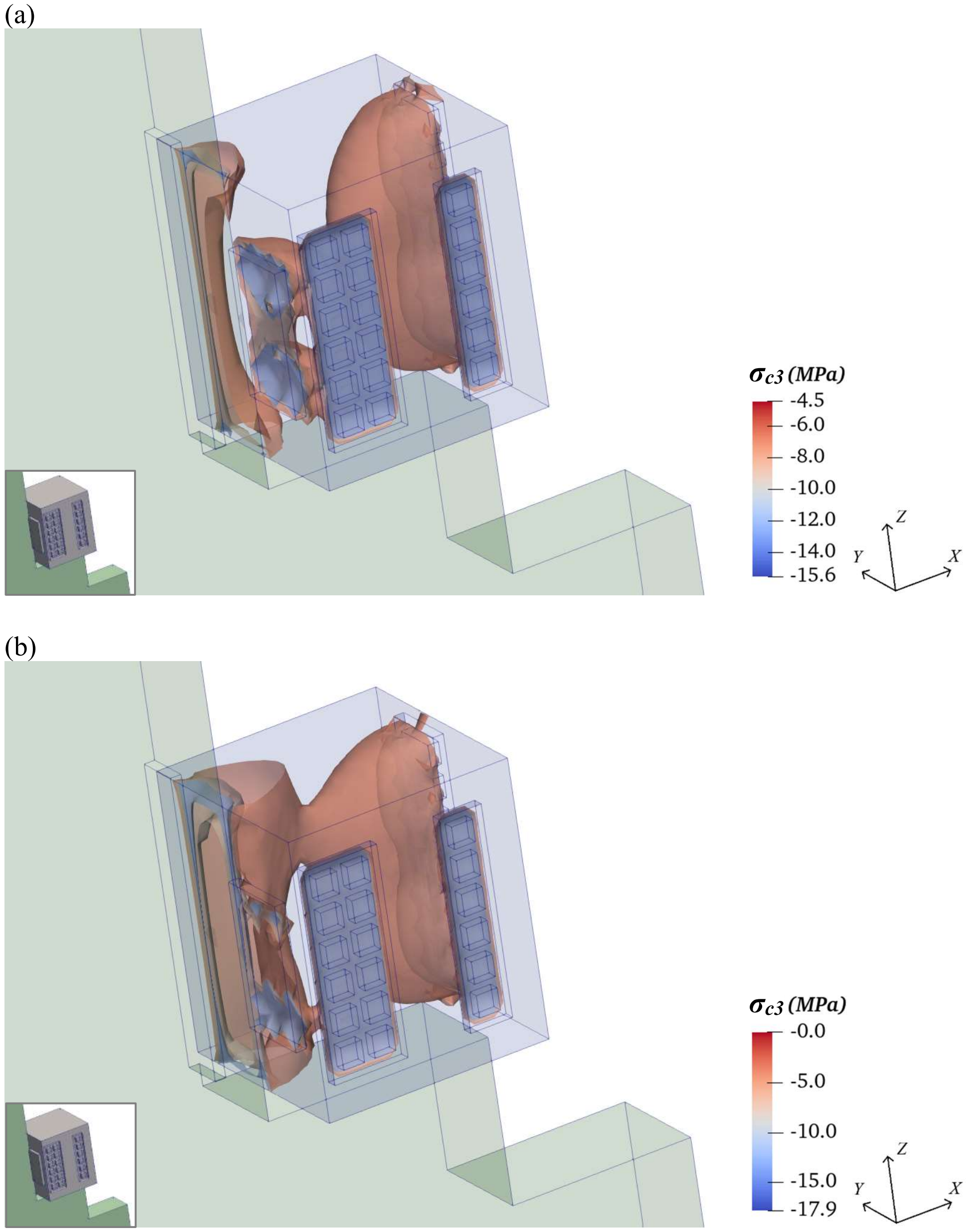

Figure 85 – Trunnion girder: smallest concrete principal stress for (a) gate position #1; (b) gate position #3.

5.6.4 Detailing

f_{tx} distribution was sectorized in the *YZ* plane for the reinforcement detailing as presented in Figure 86:

- A 0.40 m band straight after the *PT* anchor plates with 1.76 MPa.
- A 0.40 m transition band with 1.0 MPa.
- The remainder area with 0.34 MPa, except in two sub-regions: the projection of girder disconnected from the column by the polystyrene band, and localized strips at the top and bottom faces of the girder with 0.56 MPa.

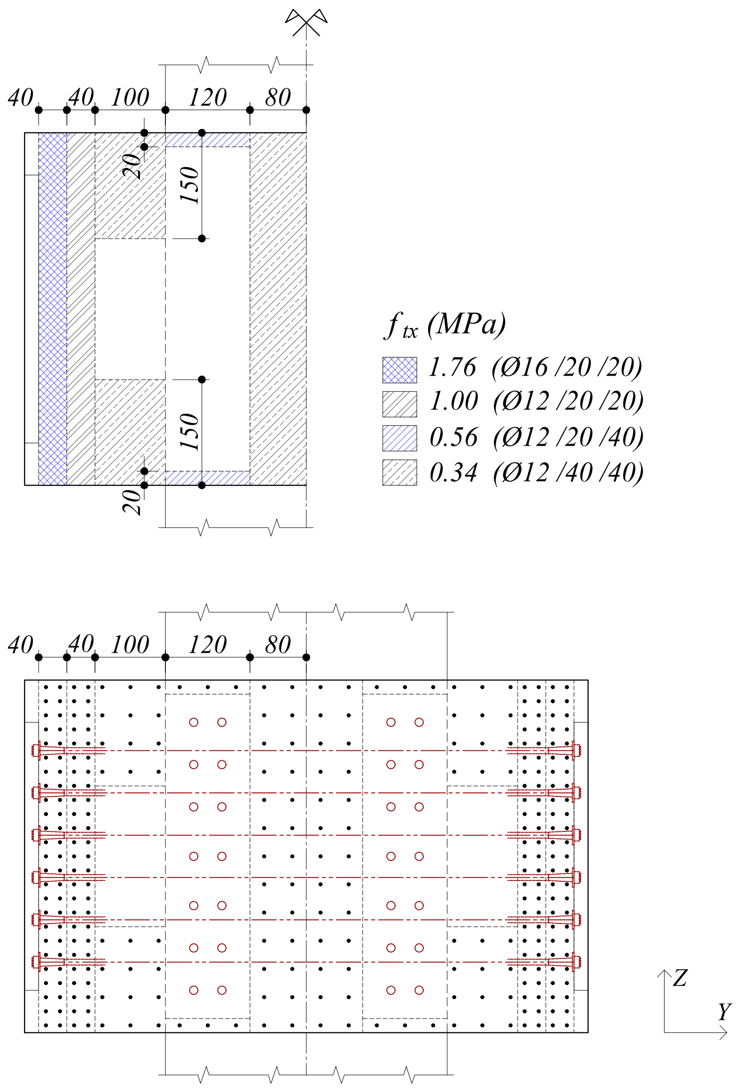

Figure 86 – Trunnion girder: (a) assumed f_{tx} distribution; (b) reinforcement arrangement.

The f_{ty} distribution was sectorized in the XZ plane for the reinforcement detailing as presented in Figure 87:

- At the upstream face of the girder, a 0.20 m band straight after the column-girder interface with 2.68 MPa was followed by a 0.20 m band with 1.54 MPa.
- At the downstream face of the girder, a 0.20 m band with 1.54 MPa was defined straight behind the PL anchor plates.
- At the top and bottom faces of the girder, 0.40 m bands were defined with 0.92 MPa.

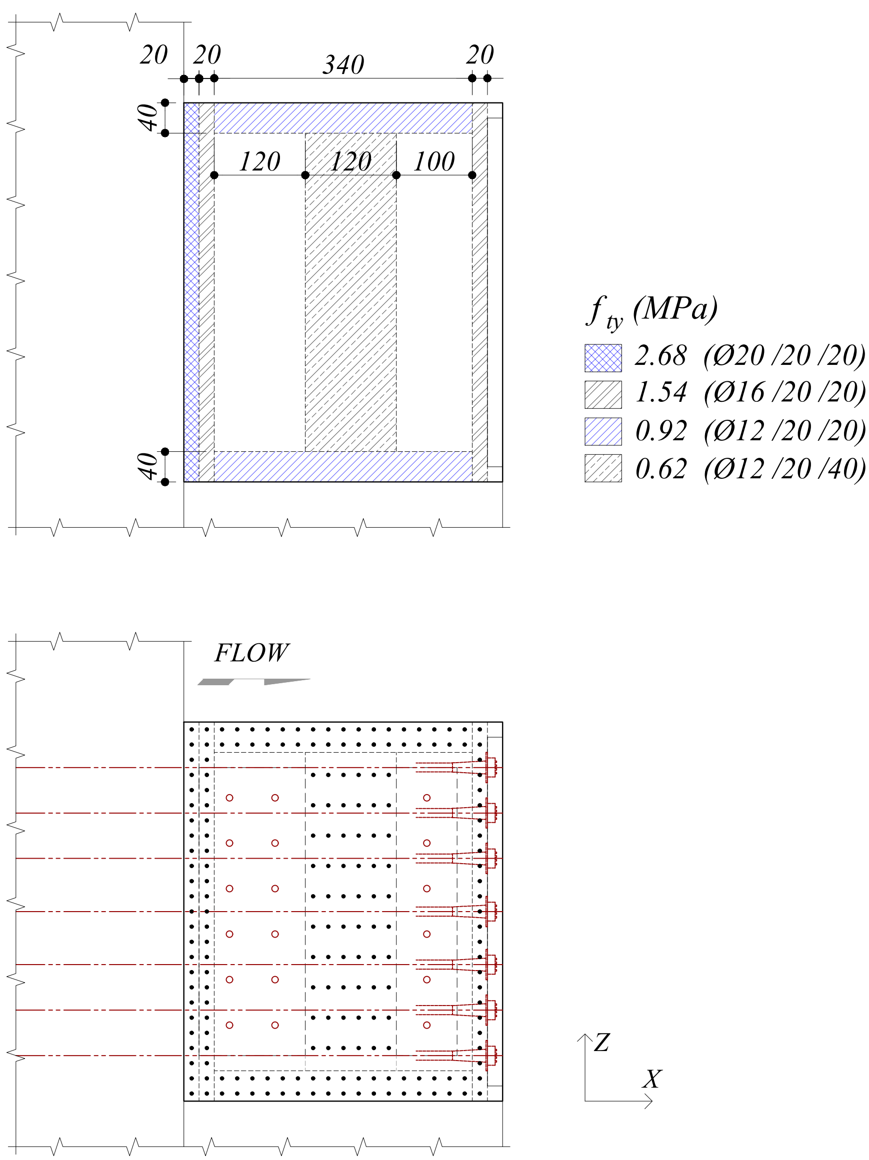

Figure 87 – Trunnion girder: (a) assumed f_{ty} distribution; (b) reinforcement arrangement.

The f_{tz} distribution was sectorized in the *XY* plane for the reinforcement detailing as presented in Figure 88:

- At the upstream face of the girder, behind the trunnion steel plate, a 0.20 m band with 3.11 MPa was followed by a 0.60 m band with 0.94 MPa. Behind the polyethylene plate, a 0.20 m band with 0.94 MPa was followed by a 0.60 m band with 0.40 MPa.
- At the downstream face of the girder, a 0.20 m band with 1.18 MPa followed by a 0.20 m band with 0.94 MPa. Behind the *PL* anchor plates, the bands assumed higher values: a 0.20 m band with 1.18 MPa followed by a 0.80 m band with 0.94 MPa.
- At the south face of the girder, a0.20 m band was defined with 0.94 MPa.
- In the remainder regions, a uniform distribution of 0.40 MPa, except for small areas close to the column, where reinforcement was dispensed.

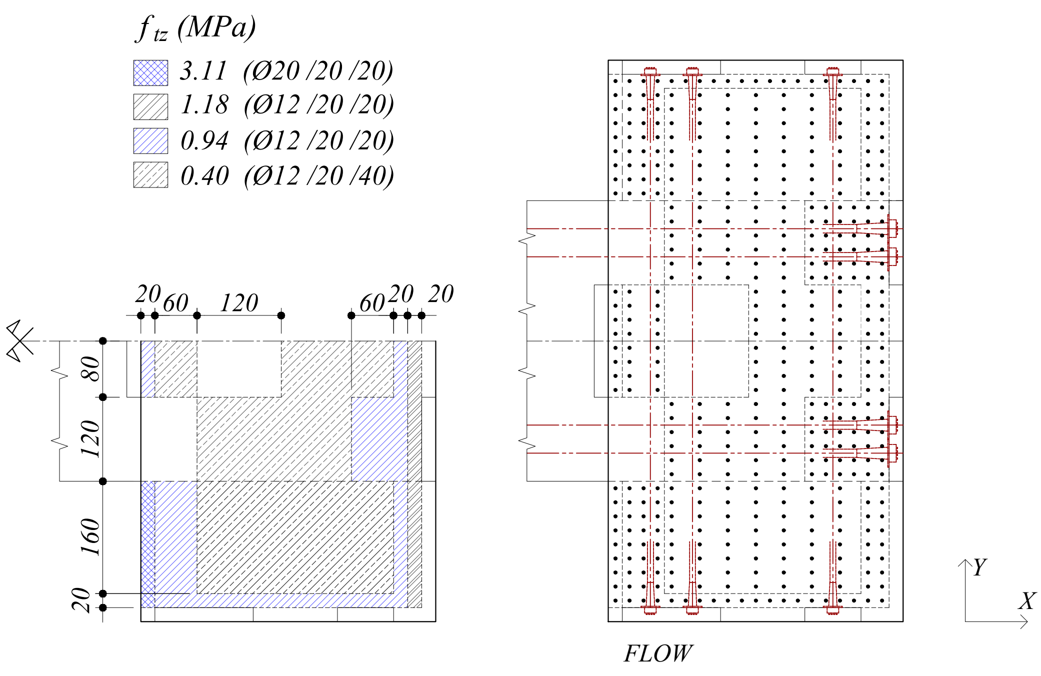

Figure 88 – Trunnion girder: (a) assumed ftz distribution; (b) reinforcement arrangement.

This fifth example addressed the application of the SFM design to a structure with real complex loading. The required reinforcement was successfully calculated and detailed into constructive arrangements, confirming the strength of the design method.

6 Design of structural members: validation

Structural members were designed for the ULS by the SFM in the last chapter: concrete was checked against crushing, and the required reinforcement was quantified and detailed in constructive arrangements. From the lower bound theorem of the theory of plasticity, it is known beforehand that a safe design was achieved for all members, meaning that the ultimate load was higher than the design load. However, it was neither possible to quantify the ratio between failure and design loads, nor to obtain information about the serviceability performance of the solutions achieved. In this chapter the structural members designed by the SFM are assessed by nonlinear analysis performed by a commercial finite element software to answer these questions.

6.1 Assessment by nonlinear analysis

Verifications assisted by numerical simulations are explicitly allowed by the MC2010 (*fib*, 2013). They are an alternative to physical testing in a laboratory or on a site, mainly for massive structures with complex geometry and loading. By adequately adjusting solution methods and material parameters it is possible to check the structural performance throughout the loading process up to failure.

Guidelines for performing nonlinear analyses are widely available in the literature (*fib*, 2008, 2021; de BOER et al., 2014). Solution strategies, in particular, were discussed by Vidosa, Kotsovos and Pavlović (1991) and Engen et al. (2015). The accuracy of nonlinear analyses depends on factors including the choice of material properties, mesh size, analysis methods, and convergence criteria. To ensure reliable predictions, calibration and validation of the nonlinear structural models were performed. This involved selecting appropriate parameters and conducting sensitivity analyses to understand how these parameters affect the structural response.

The structural members were modeled with preprocessor *GiD* (COLL et al., 2018) and analyzed with the software *ATENA* Studio (BENES; MIKOLASKOVA; ALTMAN, 2015), which is part of the *ATENA* program system from Červenka Consulting (ČERVENKA; JENDELE; ČERVENKA, 2020). *GiD* is an adaptive and user-friendly graphical interface for geometrical modelling, finite element mesh generation, and preparation of data for a variety of numerical simulation programs. Its use is enhanced with the installation of the *ATENA-GiD Interface* (ČERVENKA et al., 2020) into the *GiD* environment, which enables *ATENA*-specific commands for defining the material models, boundary conditions, and load conditions. *ATENA* provides comprehensive frameworks for nonlinear structural analysis, incorporating various material models, element types, and solution strategies. *ATENA Studio*, particularly, performs the nonlinear analyses of the numerical model, and provides graphical resources for post-processing the numerical results.

Full nonlinear analyses were chosen for assessing the SFM solutions for their completeness and accuracy, in detriment of other simplified three-dimensional nonlinear methods (MERGNY et al., 2015; MELÉNDEZ; MIGUEL; PALLARÉS, 2016; ABRA; FTIMA, 2020, 2022; COLAS et al., 2023) which remain in early stages of development, require implementation in finite element software, and lack widespread validation within the field.

6.1.1 Numerical model and numerical method

The finite element method was adopted for the numerical method of simulation. The continuum was discretized into solid elements, and loading and boundary conditions were applied to the model.

6.1.2 Material models

The constitutive models utilized for the nonlinear analyses are described in the following paragraphs, highlighting the key aspects of the formulation found in the *ATENA Program Documentation, Part 1: Theory* (ČERVENKA; JENDELE; ČERVENKA, 2020).

Concrete material model

The concrete was modeled with a fracture-plastic material model named *CC3DNonLin Cementitious2*. It combines a plasticity model for concrete crushing in compression with a Rankine fracture model for concrete cracking in tension. The material model formulation is based on the strain decomposition into elastic ($\varepsilon_{ij}{}^{e}$), plastic ($\varepsilon_{ij}{}^{p}$), and fracturing ($\varepsilon_{ij}{}^{f}$) components (de BORST, 1986):

$$\varepsilon_{ij} = \varepsilon_{ij}^{e} + \varepsilon_{ij}^{p} + \varepsilon_{ij}^{f} \tag{6.1}$$

The Menétrey-Willam failure criterion (1995) was used for the plasticity model for <u>*concrete crushing*</u>. It is a three-parameter model that has been calibrated in terms of the uniaxial strength f_c and f_t, and eccentricity e. It is represented in Figure 89a and given by:

$$F(\xi,\rho,\theta)=\left[\sqrt{1.5}\frac{\rho}{f_c}\right]^2+m\left[\frac{\rho}{\sqrt{6}f_c}r(\theta,e)+\frac{\xi}{\sqrt{3}f_c}\right]-c=0 \tag{6.2}$$

where:

ξ, ρ, θ are the Heigh-Westergaard coordinates: ξ is the hydrostatic stress invariant, ρ is the deviatoric stress invariant, and θ is the deviatoric polar angle.

m is a material parameter that measures cohesive and frictional strengths.

c is a parameter controlling hardening and softening effects.

e is a parameter defining the roundness of the failure surface.

The law for *concrete in compression* is described by two distinct branches:

(i) The elliptical ascending branch is based on strains and characterizes the concrete hardening for compression stresses exceeding the elastic limit $f_{c0} = 2\, f_t$, where f_t is the tensile strength, and E_c is the concrete Young's modulus. The curve is defined by two input parameters: the onset of nonlinear behavior f_{c0}, and the value of plastic strain at compressive strain ε_{cp}, as shown in Figure 89b. The hardening curve in *ATENA* is given by the following formula:

$$\sigma = f_{c0}+\left(f_c-f_{c0}\right)\sqrt{1-\left(\frac{\varepsilon_c-\varepsilon_{cp}}{\varepsilon_c}\right)^2} \tag{6.3}$$

where $\varepsilon_{cp} = f_c / E_c$. is the concrete plastic strain at compressive strength, f_c is derived from a cylinder test.

(ii) The linear descending branch is based on displacements and characterizes the concrete softening for compression stresses after reaching concrete strength f_c, as shown in Figure 89c. The equivalent plastic strains are transformed into displacements W_d by the length scale parameter L_c. This parameter corresponds to the projection of the element size into the direction of minimal principal stress, that is, the direction parallel to the crack. W_d can be determined by:

$$W_d=\left(\varepsilon_{eq}^p-\varepsilon_c^p\right)L_c \tag{6.4}$$

and may be assigned as 0.5 mm for normal strength concrete.

The Rankine-fracturing model for *concrete in tension* is used to identify zones with initiation of cracking in concrete - cracking occurs when the maximum principal tensile stress σ_1 exceeds the concrete tensile strength f_{ti} in the material direction i. The material behavior, in turn, is divided into two stages. Before cracking, it is assumed to be linear elastic, with stress-strain relationship given by the concrete elastic modulus E_c; after cracking, it is modeled based on the crack band theory (BAŽANT; Oh, 1983) combined with Hordjik's formulation for tension stiffening (1991). The *crack band theory* is a fracture-mechanics approach for localization of deformations in the failure state. In this formulation, the fracture is not modeled as a line crack (a sharp interelement crack), but as a band of continuously distributed parallel cracks (orthotropic smeared cracks). The crack width $w = \varepsilon_f L_t$ is obtained by accumulating strains ε_f due to microcracking over width L_t of the crack band. The direction of the failure planes is assumed to be normal to the principal stresses in tension. The stress-strain relationship within the crack band exhibits strain-softening, which reflects the loss of load-carrying capacity due to microcracking and damage accumulation. The material fracture properties are characterized by only three parameters – fracture energy G_f (the energy consumed in the formation and opening of all microcracks per unit area, required to create a unit area of stress-free crack), uniaxial strength limit f_t (derived from a failure function), and the width of crack band L_t (calculated as a size of the element projected into the crack direction). *Hordijk's softening model* builds upon the crack band theory for describing tension-stiffening behavior within the crack band. The strength of concrete under tension decreases sharply as the crack opening increases, according to an exponential crack opening law:

$$\frac{\sigma}{f_t} = \left[1 + \left(c_1 \frac{w}{w_c}\right)^3\right] \mathrm{e}^{-c_2 \frac{w}{w_c}} - \frac{w}{w_c}\left(1 + c_1^3\right) \mathrm{e}^{-c_2} \tag{6.5}$$

where:

- w is the crack width calculated from the crack band theory, $w = \varepsilon_f L_t$.
- w_c is the crack opening at the complete release of stress estimated by $w_c = 5.14\ G_f / f_t$.
- σ is the normal tensile stress at the crack band.
- c_1, c_2 are adjustment coefficients obtained experimentally ($c_1 = 3$, $c_2 = 6.93$).

The curve is represented in Figure 90b. The area under the curve is fracture energy G_f.

<u>Shear strength</u> of cracked concrete is calculated in *ATENA* using the Modified Compression Field Theory (VECCHIO; COLLINS, 1986). It corresponds to the maximum shear stress developed in a crack due to aggregate interlock:

$$\tau_{ij} \le \frac{0.18\sqrt{f_c}}{0.31 + \dfrac{24w}{a_g + 16}}, \quad i \ne j \tag{6.6}$$

where f_c is in MPa, a_g is the maximum aggregate size in mm, and w is the maximum crack width in mm at the given location.

Simulations were performed assuming a smeared fixed crack model, in which the crack direction is given by the principal stress direction at the onset of the crack initiation. In the uncracked concrete, the principal stress and strain directions coincide because of the assumption of isotropy in the concrete component. After cracking, the orthotropy is introduced, with material properties varying in the principal directions at the onset of cracking. It is possible that stresses in directions orthogonal to the crack direction also exceed the tensile strength, so that cracks are formed in up to three directions following the same softening model.

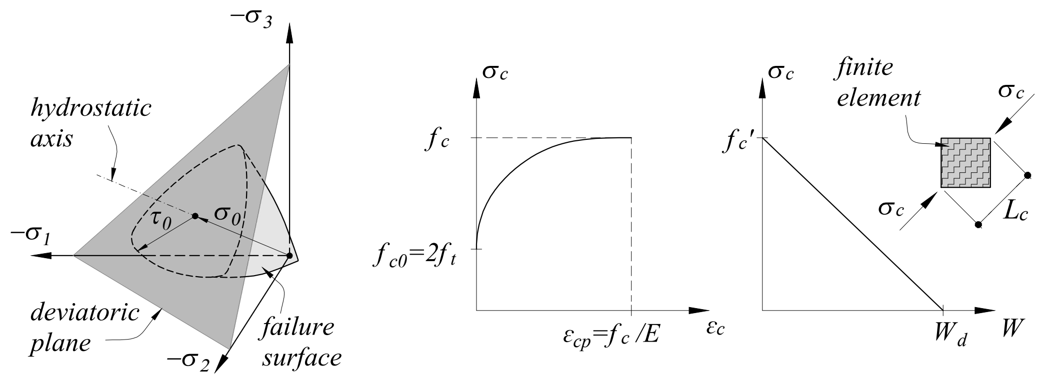

(a) (b) (c)

Source: (a,b) adapted from Červenka, Jandele and Červenka (2020); (c) Palomo (2024).

Figure 89 – Plasticity model for concrete in *ATENA*: (a) Menétry-Willam failure surface; (b) compression hardening; (c) compresssion softening.

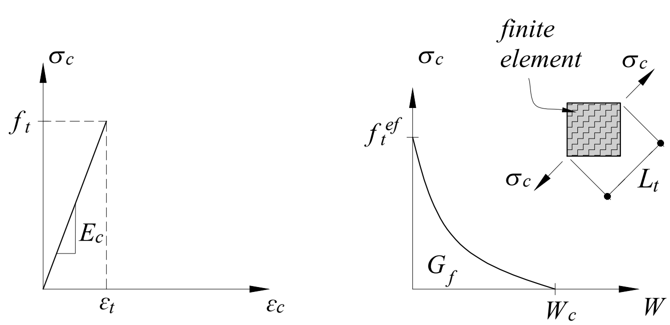

(a) (b)

Source: adapted from Červenka, Jandele and Červenka (2020).

Figure 90 – (a) Uniaxial stress-strain relationship for concrete in tension (elastic branch); (b) fracture model for concrete in *ATENA*: tensile softening according to Hordijk.

Steel plate material model

Steel plates were modeled as an isotropic elastic 3D material. The linear stress-strain curve in tension and compression was characterized by the Young's modulus of the steel material E, and its Poisson's ratio μ.

Reinforcement material model

Reinforcement was modeled as a material obeying a perfectly elasto-plastic behavior in one dimension. It followed a bi-linear constitutive relationship in both tension and compression, characterized by two regions: an initial elastic branch where stresses increase proportionally to the strains at a constant rate equal to the steel Young´s modulus E_s up to the yield point (ε_{sy}, f_{sy}), and a plastic branch where reinforcement stresses remain constant after the yield stress is reached, for strains increasing beyond the yielding strain up to the ultimate strain ε_{su}. No strain-hardening was considered, and flexural and shear stiffnesses were disregarded. Also, perfect bond was assumed.

Depending on the application, reinforcement was modeled by a discrete or a smeared approach. In both cases, the state of uniaxial stress was assumed. Discrete reinforcement in the form of reinforcing bars was modeled by truss elements incorporated into the concrete mesh. Smeared reinforcement, in turn, was modeled as a component of a composite material. It was characterized by two parameters: reinforcing ratio ρ, and direction angle β, and enhanced the tensile properties of concrete elements. The total material stiffness of the reinforced concrete was the sum of material stiffness of concrete and smeared reinforcement.

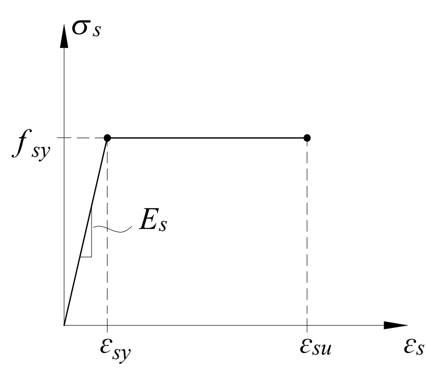

Figure 91 – Stress-strain relationship for reinforcement in tension.

6.1.3 Meshing

Discretization of the structure into finite elements must accurately describe the stresses in the structure. The maximum element size in the model must be chosen such that relatively smooth stress fields are obtained. In the worked examples, as an overall guideline, at least four elements were distributed over each dimension of the structural members. Mesh sensitivity studies were conducted to determine the optimum element size for the meshes, equilibrating accuracy of results and computational economy.

Unstructured meshes with 10-node tetrahedral elements were generated for the concrete volumes. Structured meshes with brick elements were preferred for the steel plate volumes. Meshes were generated automatically by the *ATENA* software.

For discrete reinforcement, rebars were drawn individually as continuous lines in the definition of the geometrical model. In the meshing process, their meshes were generated based on the existing mesh of solid elements: first, all nodes where the bar changes direction are found; second, the intersection of all straight parts of the bar with underlying solid elements are detected, such that all end nodes of embedded bar elements are defined; lastly, displacements of the nodes of the bar are linked to the underlying solid elements. For smeared reinforcement, no explicit rebar elements are defined since rebar properties are averaged over concrete element volumes.

Master-slave boundary conditions were defined for the contact of different structural volumes discretized with non-coinciding nodes.

6.1.4 Solvers and design strategies

Methods for solving the nonlinear equations in structural analysis involve solving linear equations within each iteration. The linear equations at each iteration are typically written in the form:

$$\boldsymbol{A}\ \underline{x} = \underline{b} \tag{6.7}$$

where $\boldsymbol{A}$ is the global structural matrix, $\underline{x}$ is the unknown solution vector, and $\underline{b}$ is the known vector, named the right-hand side (rhs) of the problem. They are solved using either a direct or an iterative *solver*. The *PARDISO* is a direct solver that factorizes the stiffness matrix into triangular matrices and solves the resulting linear systems at each iteration; it is highly efficient for small to medium-sized problems but memory-intensive for large matrices and was chosen as the preferential solver in the design examples. The *ICCG*, in turn, is an iterative solver that approximates the solution iteratively through a series of steps; it is recommended for large-scale problems, converging to a solution with less memory usage and was chosen for design examples 4 and 5.

Three different solution methods may be employed for solving the nonlinear equations: (*i*) the *full Newton-Raphson method*, which recomputes matrix $\boldsymbol{K}$ for every iteration; (*ii*) the *modified Newton-Raphson method*, which fixes matrix $\boldsymbol{K}$ for all iterations - it converges more slowly than the original Newton-Raphson method but requires "less computing time because it is necessary to assemble and to eliminate the stiffness matrix only once" (ČERVENKA; JENDELE; ČERVENKA. 2020); and (*iii*) the *arc-length method*, a well-established numerical technique for both geometrical and material non-linearity that assures good results even in cases in which traditional Newton-Raphson methods fail: it does not assume constant loading increments during iterations, and addresses instabilities during loading increments more efficiently.

The loading history for all design examples followed a scheme with small load steps for loads at the beginning of the loading process to capture the elastic behavior before cracking, and small load steps for load close to the ultimate load, whereby the effects of high localized nonlinearities due to cracking of concrete and yielding of steel occur. In structures with complex geometry and loading dozens of analyses were required to allow for drawing a detailed loading history. For all the analyses, proportional loading was assumed, meaning that the various loads applied to the structure maintained a constant ratio throughout the loading process. Note that this is an idealization of the real behavior. Blomfors, Engen and Plos (2016) showed how load history influenced the safety level of structures assessed by nonlinear analyses. When dealing with more complex loading scenarios, loading history may possibly be defined by a different approach.

Throughout the incremental procedure of the analyses, the convergence of solutions was checked at each iteration in terms of the vector increments for displacements, residual forces, residual stresses, and residual strains.

6.1.5 Safety format for nonlinear analysis

The safety format adopted for the analyses was the *partial factor method*. In this method, design resistance R_d is calculated using the design values as input parameters f_d for the nonlinear analysis:

$$R_d = r(f_d, ...) \tag{6.8}$$

where $r(f_d,\ldots)$ represents the nonlinear analysis model, and f_d refers to design values of actions, material properties, geometrical quantities, and variables which account for the model uncertainties, as described in MC2010 Sections 4.5.1.3 and 7.11.3.4 (*fib*, 2013). The ultimate load P_u obtained from the analysis by inputting the design mechanical properties is already the design resistance P_d.

When applying this safety format, the structural analysis is based on extremely low material parameters in all locations. This may cause deviations in the structural response, as pointed out by Hendriks, de Boer and Belletti (2016), but leads to a safe estimate in the absence of a more refined solution.

6.2 Example 1: cantilever beam

6.2.1 Structural model for the nonlinear analysis

The structural model for the nonlinear analysis was meshed with elements with dimension of 0.10 m: at least four elements were distributed along the beam width, and eight elements along the beam height (Figure 92a). Also, all the rebars from the reinforcement layout presented in Section 5.2.4 were discretized as linear elements (Figure 92b). The complete structural model summed 36,370 tetrahedral elements and 3,552 linear elements. It was named ‘model A’.

Concerning boundary conditions, displacements were constrained in the *x*-, *y*- and *z*-directions in the left line support (Figure 93a), and in the *z*-direction in the right line support.

Concrete was modeled with a “solid concrete” material model (f_{cd} = 20 MPa, f_{ct} = 1.33 MPa, E_c = 26,070 MPa, a_g = 20 mm, ε_{cp} = -1.54‰, f_{co} = -2.8 MPa, W_d = 5 mm). Embedded rebars were modeled with a “1D reinforcement” material model (f_{yd} = 435 MPa, E_s = 210 GPa, ε_{su} = 10‰). Steel plates at the supports were modeled with a “solid elastic” material model with increased modulus of 10 x E_s = 2 100 GPa, to better distribute the reaction forces).

Loads were applied as surface loads (Figure 93b), incrementally increasing up to failure. Analysis was performed with the *arc-length* solution method, utilizing the *PARDISO* solver. The behavior of the structural model was assessed with the aid of two monitoring entities: one monitoring point (*mnt.1*) located at the right end of the beam, at its bottom corner, to read displacements in the *z*-direction; and one monitoring line (*mnt.2*) located under the right steel plate to read the reaction forces in the *z*-direction. They are also presented in Figure 92a.

6.2.2 Results: failure load

The reinforced concrete beam failed at a load 1.26 times the design load. It failed by the yielding of the three lowest layers of longitudinal bars located at midspan. The upper longitudinal bars and stirrups did not yield. Selected results of the numerical analysis at failure load are shown in Figure 94 and Figure 95 and described as follows.

At the maximum sustained load in the analysis, the maximum displacement in the *z*-direction was -5.04 cm in the midspan; stresses of the tensioned reinforcement within the flexural span were around the value of the yield stress of the material (f_{yd} = 435 MPa). The stirrups confined the compression zone such that the concrete maximum compressive stress reached 23.6 MPa. Shear cracks were observed adjacent to both supports. Flexural cracks developed in the faces tensioned by flexure, and crack widths reached 0.50 mm. Plastic strains in the last converged iteration summed 1.69‰ in concrete, and 7.41‰ in the reinforcement.

(a)

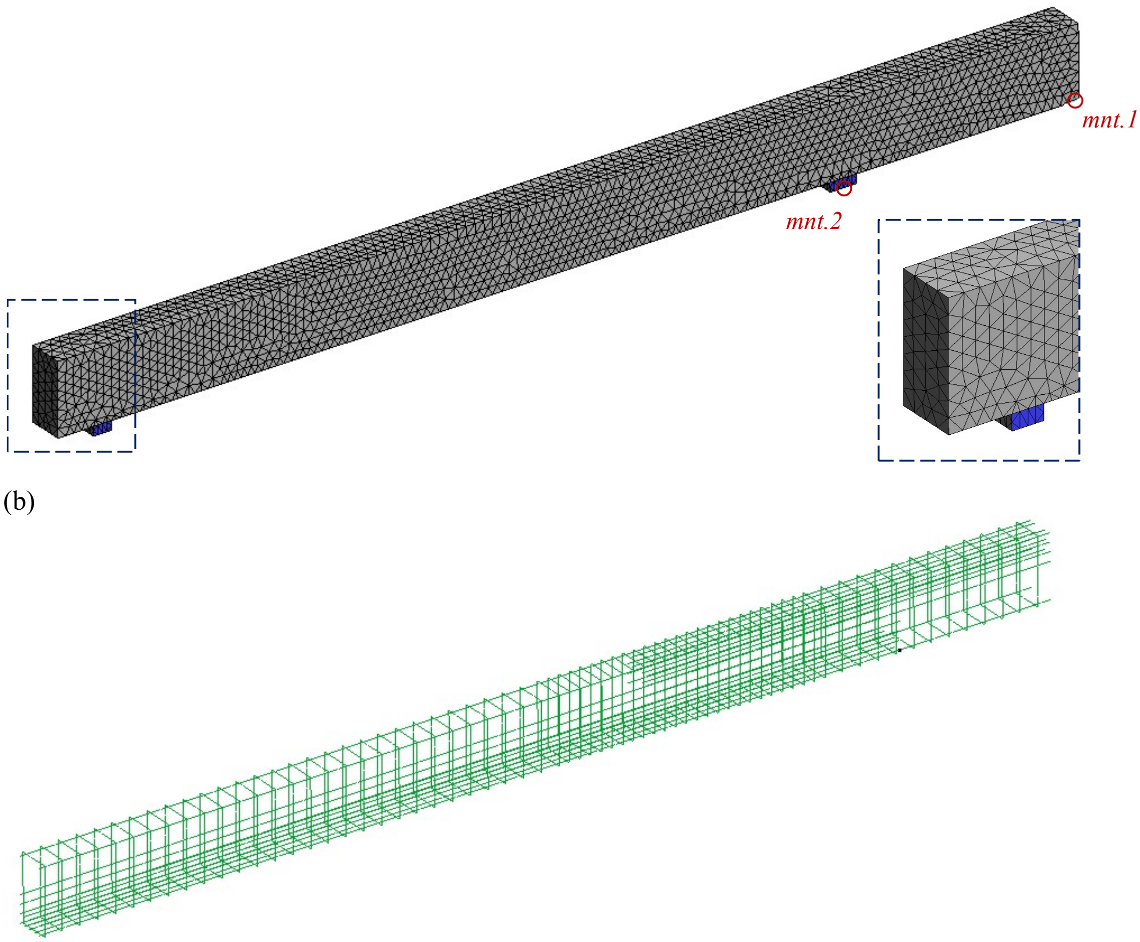

Figure 92 – Cantilever beam NLA structural model: (a) volume elements, close detail at support, monitoring point *mnt.1* and monitoring line *mnt.2*; (b) linear elements.

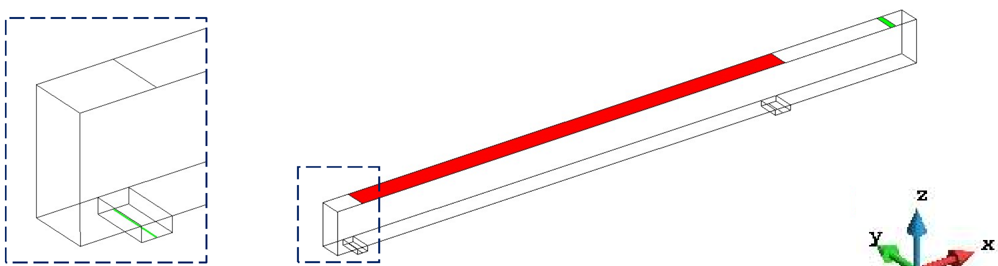

(a) (b)

Figure 93 – Cantilever beam NLA: (a) boundary condition; (b) surface loading.

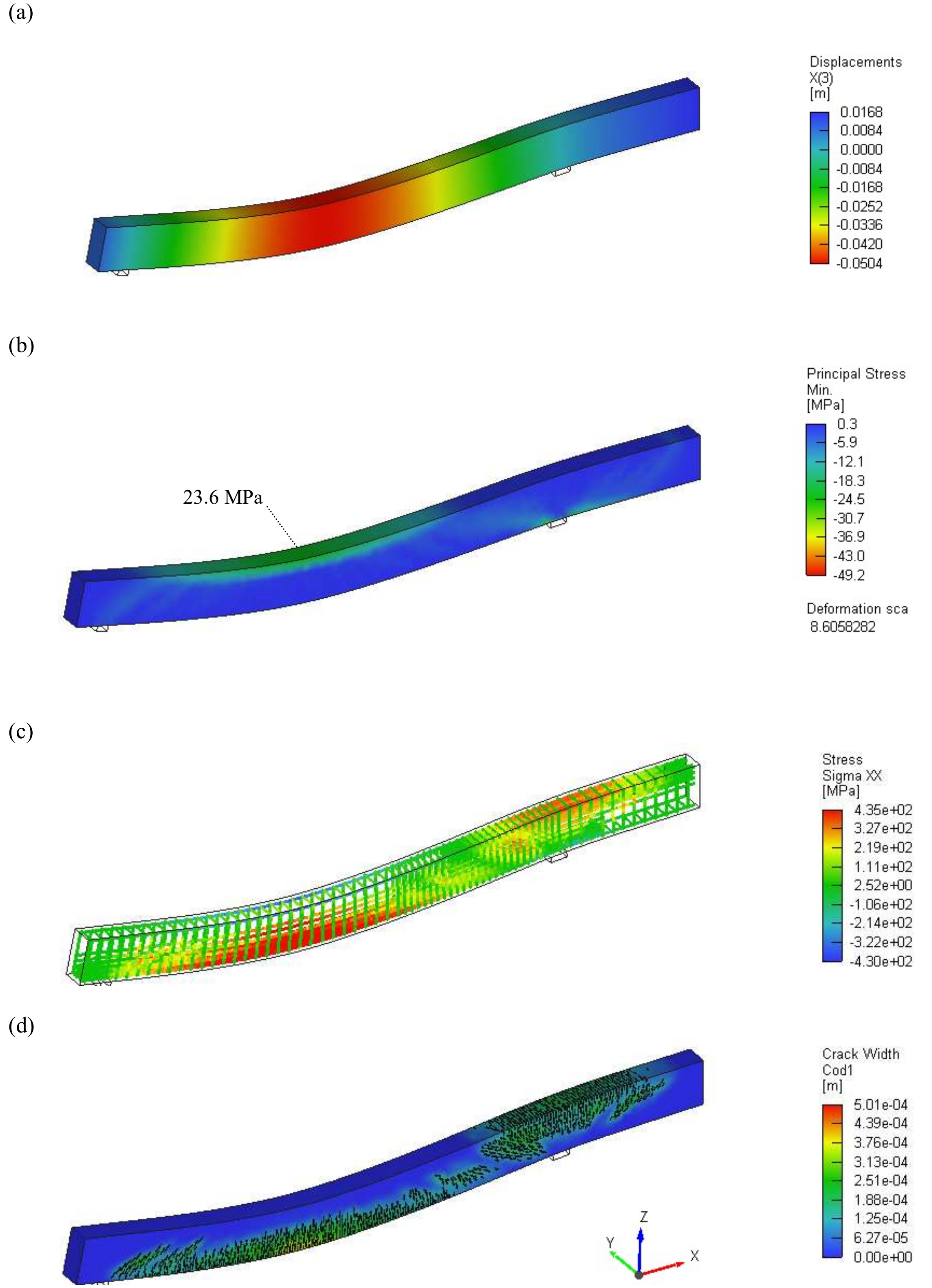

Figure 94 – Cantilever beam NLA at *failure load*: (a) deflections in the z-direction; (b) concrete principal stress σ_{c3}, (c) reinforcement stresses; (d) crack widths.

(a)

(b)

(c)

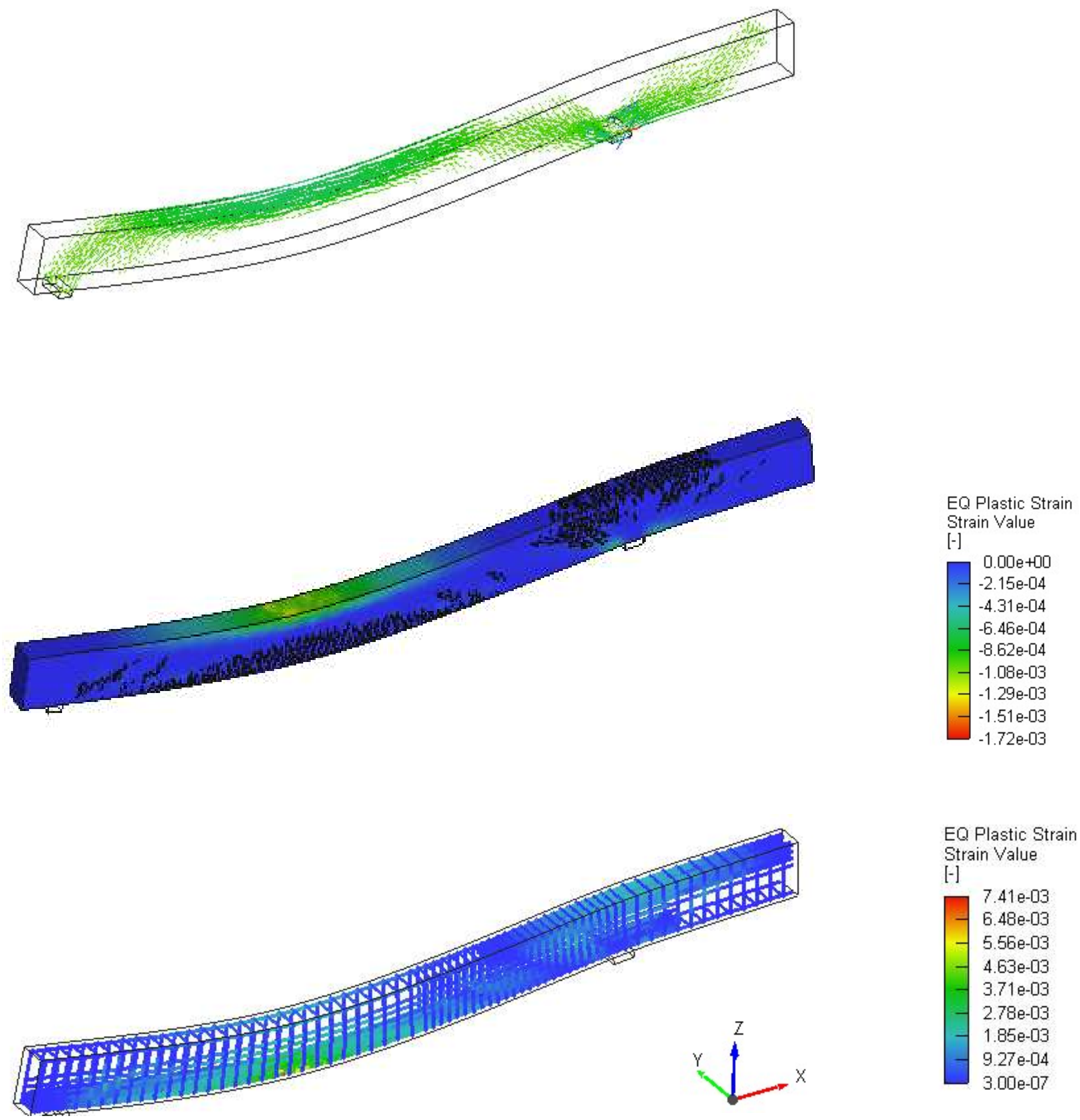

Figure 95 – Cantilever beam NLA at *failure load*: (a) concrete principal stress tensors; (b) concrete plastic strains; (c) reinforcement plastic strains.

6.2.3 Results: design load

Selected results at design load are shown in Figure 96 and described as follows.

The maximum displacement in the z-direction was -2.98 cm in the midspan. The concrete maximum compressive stress reached 17.3 MPa, while the reinforcement tensile stress in the lowest layer of the longitudinal bars reached the yield value (f_y = 435 MPa). The maximum crack width was 0.27 mm.

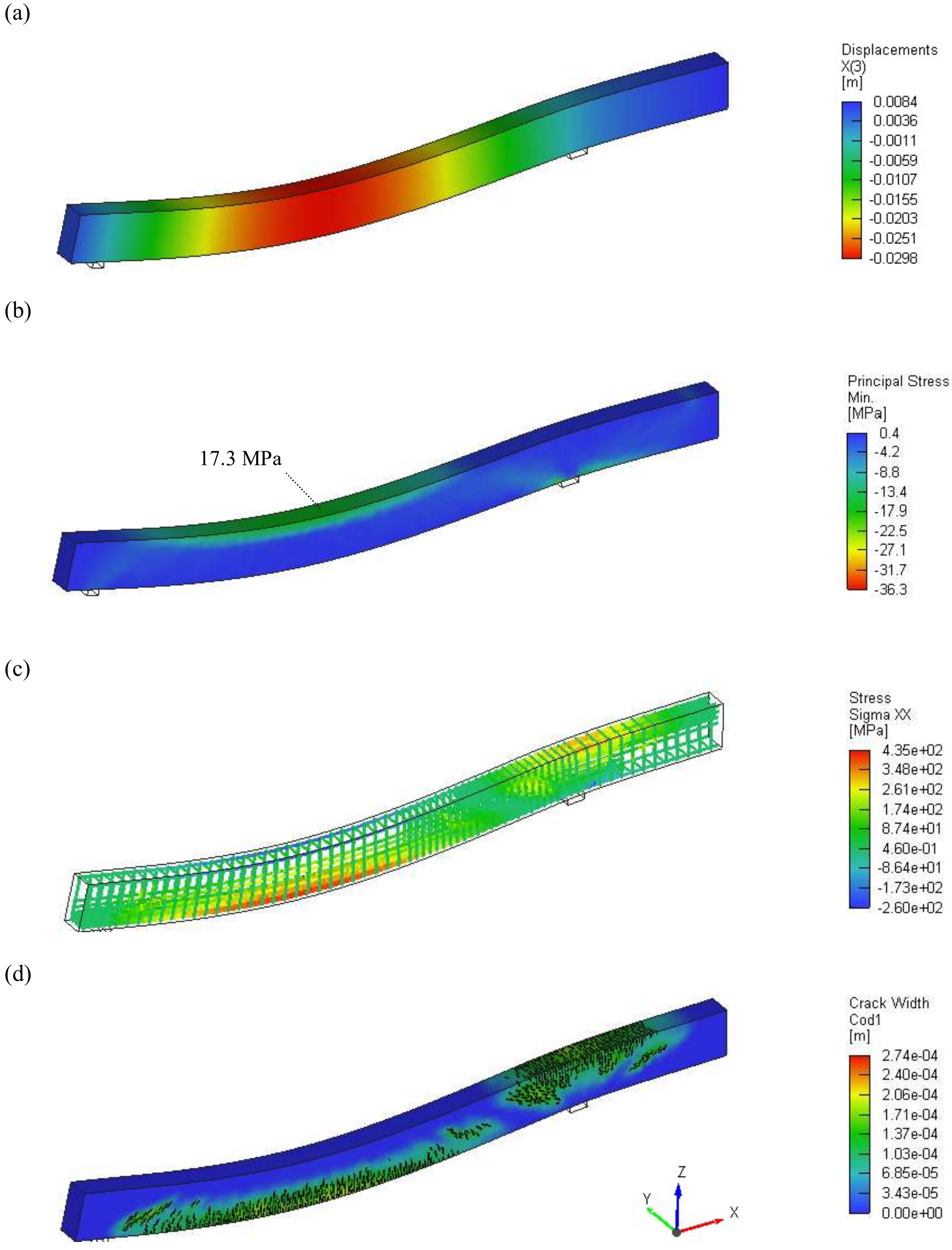

Figure 96 – Cantilever beam NLA at *design load*: (a) deflections in the *z*-direction; (b) concrete principal stress σ_{c3}; (c) reinforcement stresses, (d) crack widths.

6.2.4 Results: service load

Selected results at service load are shown in Figure 97 and described as follows.

The maximum displacement in the *z*-direction was -1.94 cm in the midspan. The concrete maximum compressive stress reached 12.9 MPa, while the reinforcement tensile stress reached 327 MPa. The maximum crack width was 0.15 mm.

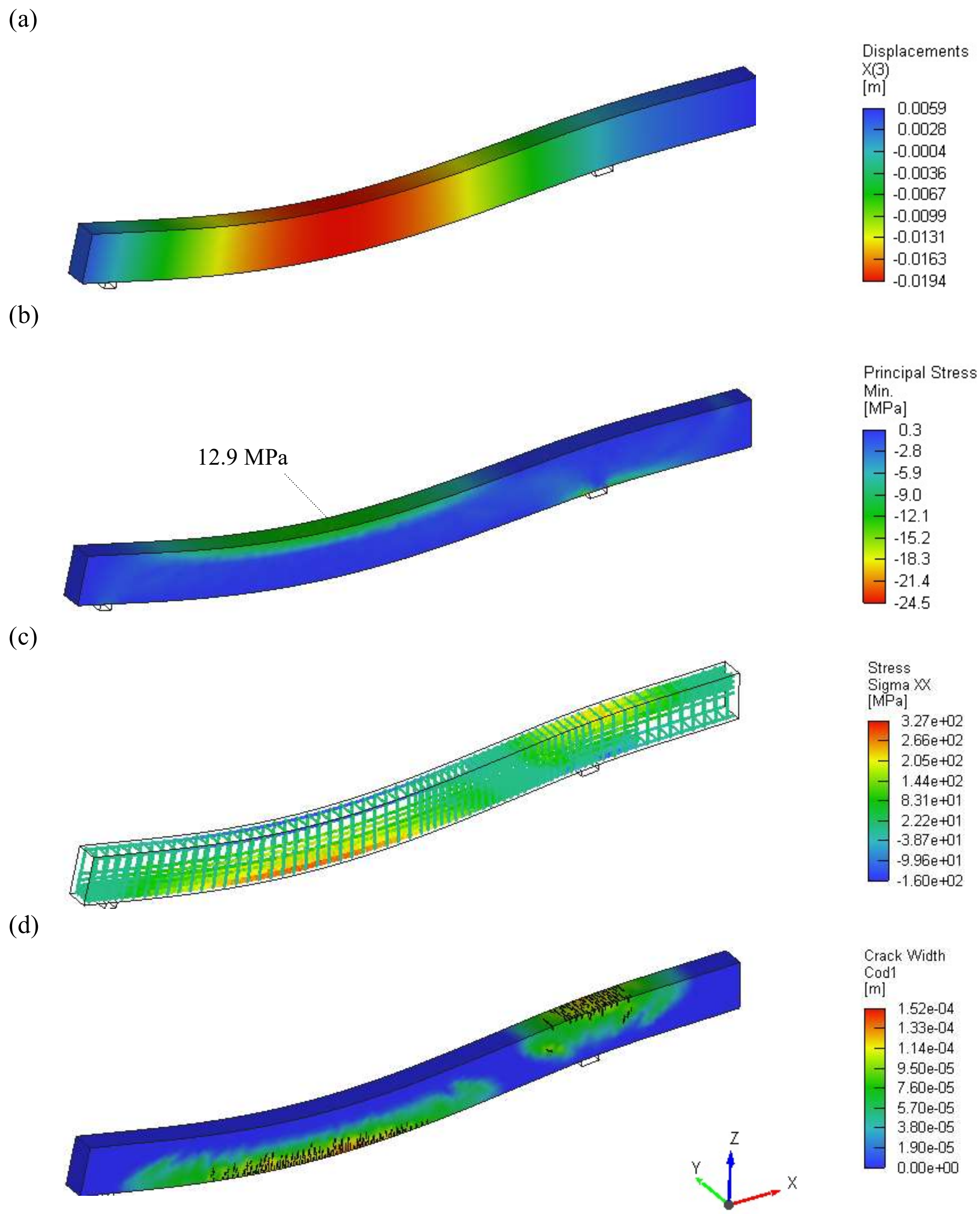

Figure 97 – Cantilever beam NLA at *service load*: (a) deflections in the *z*-direction; (b) concrete principal stress σ_{c3}; (c) reinforcement stresses; (d) crack widths.

6.2.5 Alternative solution: plastic sectional design

The beam was designed for Ultimate Limit State as a linear member, as regularly done in design practice, by the Sectional Method (SecM), which is based on a truss model with longitudinal chords and a web. Sectional design was performed for the peak sectional forces at the right support and at the midspan. Bending moment and shear force diagrams for the calculations are presented in Figure 98a.

Flexural design

The flexural moment is resisted by horizontal chords spaced at a distance z. A plastic design where concrete in compression is utilized up to the material capacity was performed using a rectangular stress block. The design values of the bending moments and the corresponding required reinforcement were:

$$\begin{aligned} M_d^+ &= 727\ kN.m; x = 0.186\ m; A_s^+ = 24.9\ cm^2 \rightarrow 8\ \phi 20 \\ M_d^- &= 567\ kN.m; x = 0.141\ m; A_s^- = 18.9\ cm^2 \rightarrow 6\ \phi 20 \end{aligned} \tag{6.9}$$

Shear design

Four sections were analyzed for the shear design, assuming the angle of the inclined struts θ = 45°. The maximum shear forces and the resulting designed reinforcement were:

$$\begin{aligned} V_{d,span,left} &= 405\ kN; \frac{A_{sw}}{s} = 5.60\ \frac{cm^2}{m} && \rightarrow stirrup\ \phi 8/15 \\ V_{d,span,mid} &= 240\ kN; \left(\frac{A_{sw}}{s}\right)_{\min} = 4.63\ \frac{cm^2}{m} && \rightarrow stirrup\ \phi 8/20 \\ V_{d,span,right} &= 540\ kN; \frac{A_{sw}}{s} = 10.23\ \frac{cm^2}{m} && \rightarrow stirrup\ \phi 10/15 \\ V_{d,cantilever} &= 270\ kN; \left(\frac{A_{sw}}{s}\right)_{\min} = 4.63\ \frac{cm^2}{m} && \rightarrow stirrup\ \phi 8/20 \end{aligned} \tag{6.10}$$

Reinforcement for crack control

Longitudinal skin reinforcement was distributed uniformly on both side faces of the beam to control cracking in the web. According to NBR-6118 (2014):

$$A_h = 0.10\% \times A_c = 4.00\ \frac{cm^2}{m} \quad \rightarrow \phi 10/20\ each\ face \tag{6.11}$$

The final arrangement for the sectional design of the cantilever beam is presented in Figure 98b.

(a)

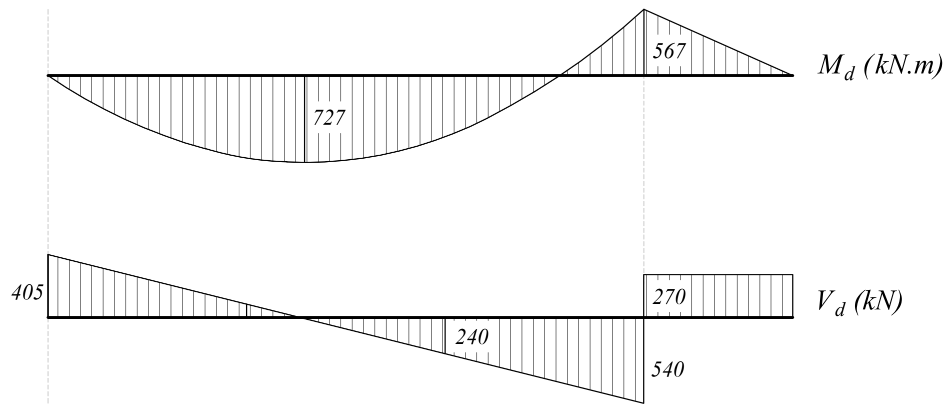

(b)

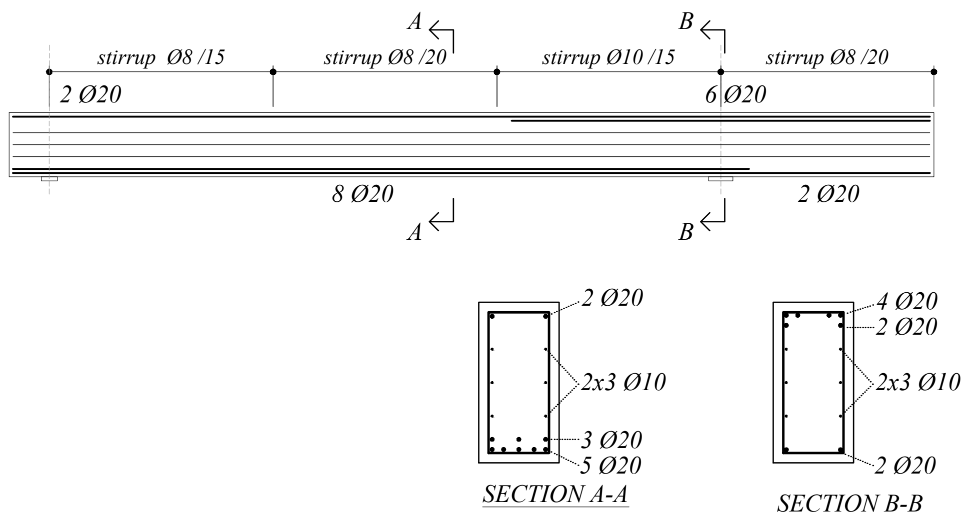

Figure 98 – Cantilever beam designed by the SecM: (a) bending moment and shear force diagrams; (b) reinforcement layout.

Nonlinear analysis of the alternative solution

The solution achieved by the sectional design was assessed by a nonlinear analysis so that a direct comparison could be established between the SFM e SecM solutions. The structural model elaborated for the analysis was named 'model B'; it considered the reinforcement modeled as 1D elements as presented in Figure 99.

Selected results at service load are shown in Figure 100 and described as follows: the maximum beam displacement in the *z*-direction was -1.89 cm, and the maximum crack width reached 0.19 mm.

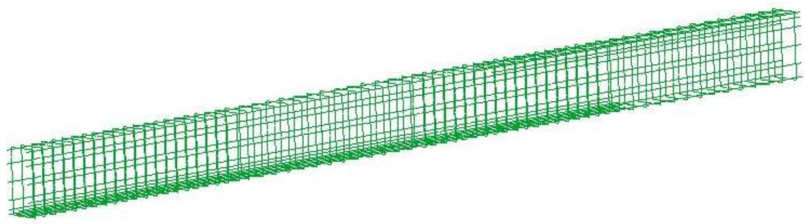

Figure 99 – Cantilever beam designed by the SecM: NLA – 1D elements.

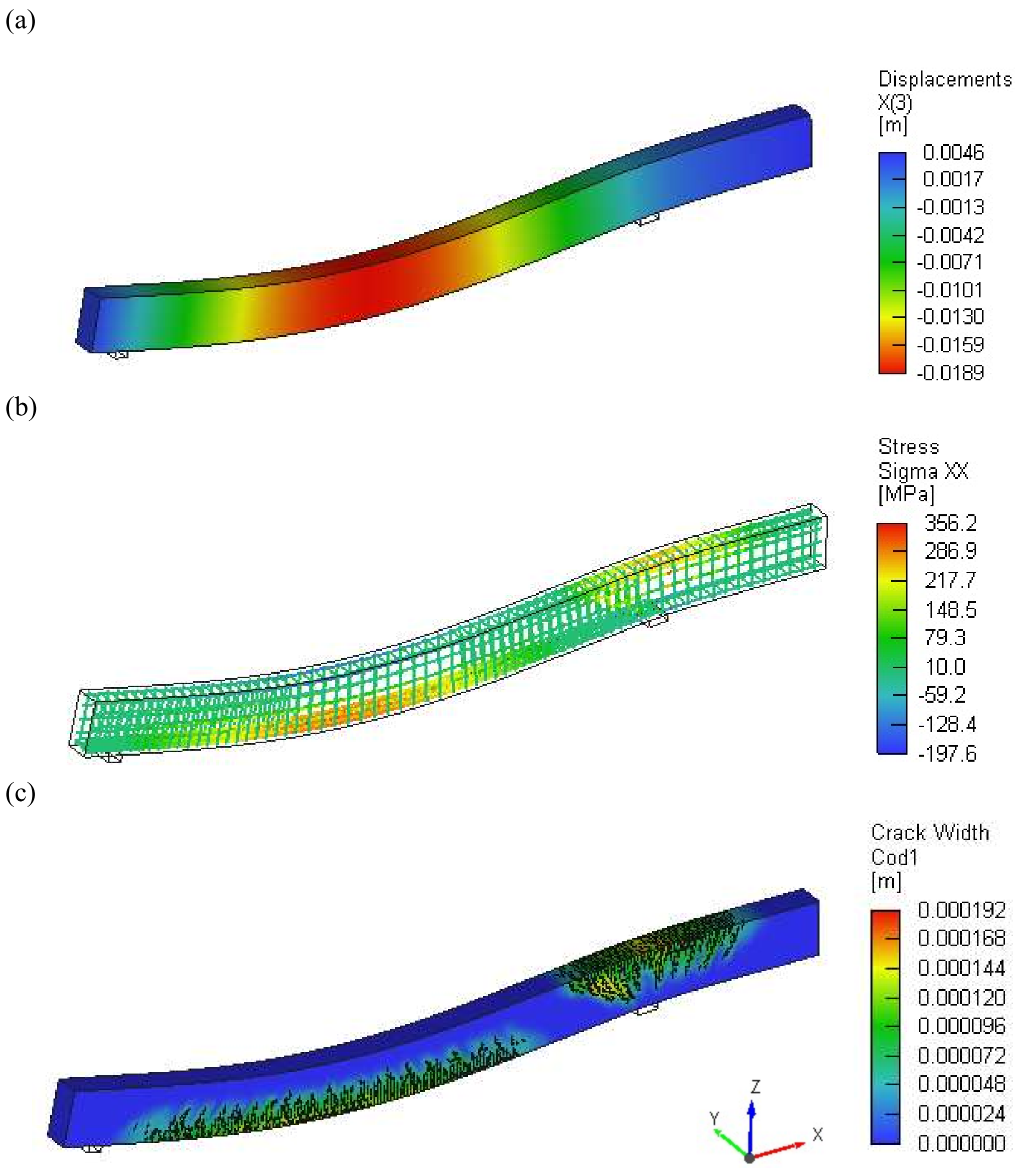

Figure 100 – Cantilever beam designed by the SecM: NLA results at *service load* - (a) deflections in the *z*-direction; (b) reinforcement stresses; (c) crack widths.

6.2.6 Discussion

The behavior of the beams is visualized in four load-displacement curves (Figure 101): the ordinate plots the reaction of the right support, and the abscissa the vertical displacement, either at midspan or at the extremity of the cantilever beam (in this case, the computed displacement adequately discounted the parcel attributed to the rigid body movement of the hangover which resulted from the rotation of the section at the right support: $\delta^{*}_{cant} = \delta_{cant} - \theta_{righ\ supp.}\ \ell_{hang}$). The load-displacement curves show similar stiffness responses of the beams designed by the SFM and the SecM.

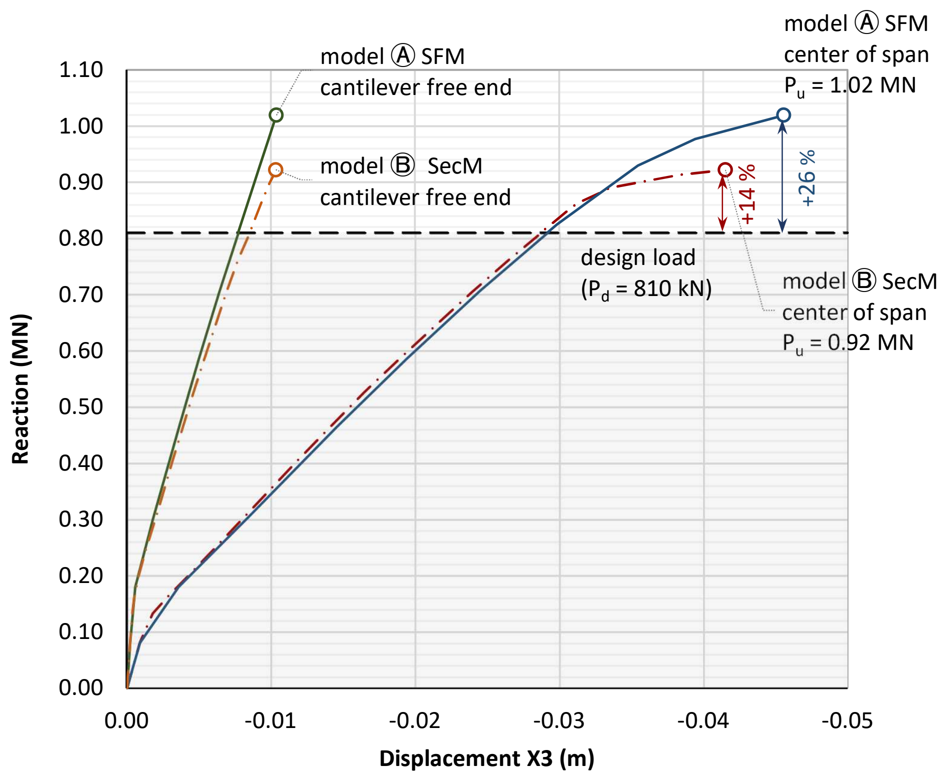

Figure 101 – Cantilever beam NLA: load-displacement curves.

The maximum sustained load in the beam designed by the SFM was 26% higher than the design load, and 11% higher than the failure load of the beam designed by the SecM.

The beam designed by the SFM presented a better performance in service conditions. This was observed by the crack widths, which were 26% smaller, and by the crack pattern, which did not extend up to the beam mid height, as in the SecM, but was concentrated at the bottom of the beam.

Reinforcement consumption

The SFM design required more reinforcement compared to the SecM design:

- The total area of flexural reinforcement was 35% higher at a midspan section, and 53% higher at a section passing through the right support:

$$\frac{A_{sx,positive,SFM}}{A_{sx,positive,SECT}} = \frac{34.0}{25.2} = 1.35; \quad \frac{A_{sx,negative,SFM}}{A_{sx,negative,STM}} = \frac{28.9}{18.9} = 1.53 \tag{6.12}$$

  The difference is explained by the fact that the sectional design for flexure assumes optimized lever arms between compressive and tension chords in each cross-section.
- The SFM design resulted in a more conservative stirrup arrangement for shear reinforcement. It did not account, as in the SecM design, for the portion of the shear resistance provided by concrete ($V_{Rd,c}$) which, after cracking, is “attributed to aggregate interlock, dowel action, and the shear transmitted across the concrete compression zone” (ACI, 2019, p. 401).

Remarks

The nonlinear analyses confirmed the safety of the SFM for the ULS design of the cantilever beam. The SFM design required more flexural and shear reinforcement but yielded a better performance in service conditions. The sectional method is certainly preferable for designing regular beams in B-regions for its efficiency, economy, and validated results. This first example, however, clearly demonstrated the feasibility of applying the SFM to provide an alternative design solution.

6.3 Example 2: corbel

6.3.1 Structural model for the nonlinear analysis

Column and corbel were meshed with elements with dimension of 0.05 m, so that at least six elements were distributed along the corbel depth, and eight elements were distributed along the corbel width and length (Figure 102a). All the rebars from the reinforcement layout presented in Figure 49 were discretized as linear elements, as shown in Figure 102b. Steel plates were meshed with elements with dimension of 0.025 m, yielding two elements along its height. The resulting structural model for the nonlinear analysis summed 31,186 tetrahedral elements and 1,006 linear elements. It was named 'model A'.

Concerning the boundary conditions, displacements were constrained in the *x*-, *y*- and *z*-directions in four points below the steel plate at the bottom of the column, as presented in Figure 103. Concrete was modeled with a "solid concrete" material model (f_{cd} = 20 MPa, f_{ctd} = 1.33 MPa, E_c = 26,070 MPa, a_g = 20 mm, ε_{cp} = -1.54‰, f_{co} = -2.8 MPa, W_d = 5 mm). Embedded rebars were modeled with a "1D reinforcement" material model (f_{yd} = 435 MPa, E_s = 210 GPa, ε_{su} = 10‰). Steel plates above the corbel faces and at the bottom of the column were modeled with a "solid elastic" material model with increased modulus of 10 E_s = 2 100 GPa, to distribute the concentrated applied forces.

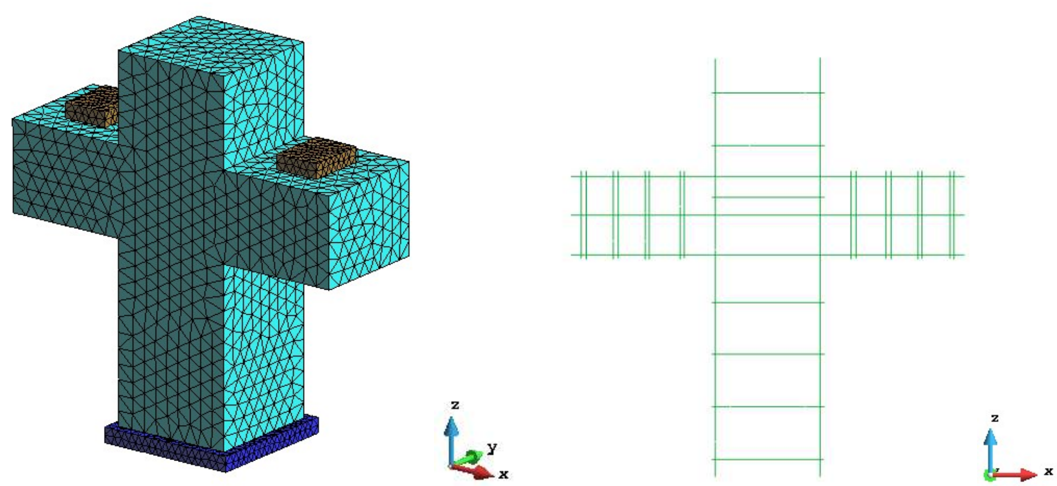

(a) (b)

Figure 102 – Corbel NLA structural model: (a) volume elements; (b) linear elements.

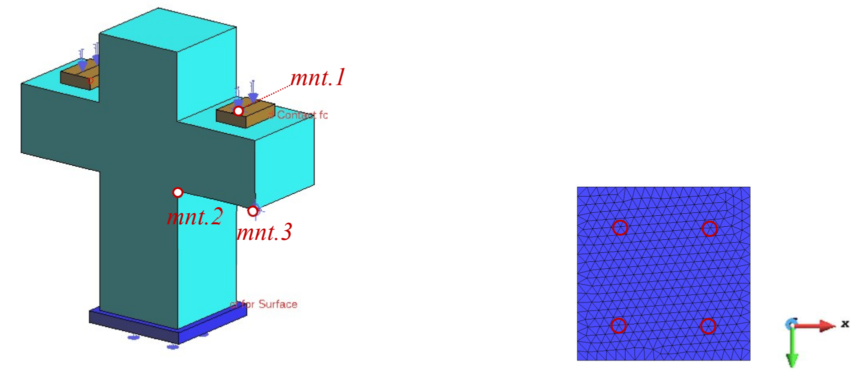

(a) (b)

Figure 103 – Corbel NLA structural model: (a) applied loads and monitoring points; (b) points of application of the boundary conditions at the bottom of the lower steel plate.

Loads were applied as a pair of concentrated loads for each top steel plate. Analysis was performed with the *arc-length* solution method, utilizing the *PARDISO* solver for loads increasing incrementally up to failure. The behavior of the structural model was assessed with the aid of the three monitoring points: one monitoring point (*mnt.1*) located on the surface of the top steel plate to read the concentrated applied force in the *z*-direction, and the other ones (*mnt.2* and *mnt.3*) located at the bottom corners of the corbel to read displacements in the *z*-direction. Loads and monitoring points are shown in Figure 103.

6.3.2 Results: failure load

The corbel failed by the yielding of the main tie at a load of 740 kN (1.47 times the design load). Selected results of the numerical simulation at failure load are shown in Figure 104 and Figure 105, and described as follows.

At the maximum sustained load of the analysis, the maximum displacement in the *z*-direction was -0.28 cm; tie reinforcement was stressed up to the yield stress (f_{yd} = 435 MPa). Stirrups confined the compression zone such that the concrete maximum compressive stress could reach 35.0 MPa. Cracks formed in the region extending from the support areas to the corbel-column interface, and propagated into the column above the corbel, with a maximum width of 0.36 mm. In the last converged iteration, plastic strains summed 0.30‰ in concrete, and 5.67‰ in the reinforcement

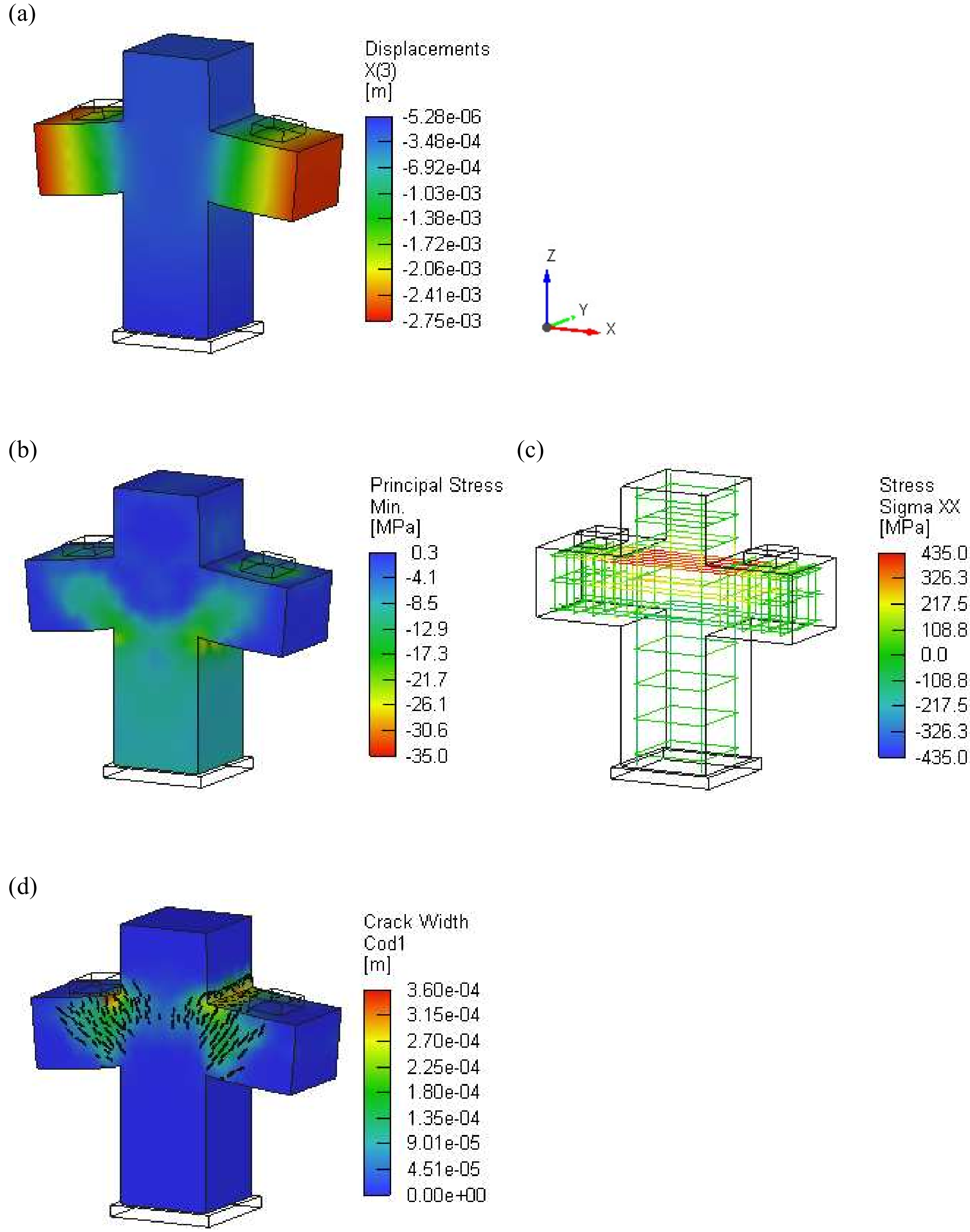

Figure 104 – Corbel NLA results at *failure load*: (a) deflections in the *z*-direction; (b) concrete principal stress σ_{c3}, (c) reinforcement stresses; (d) crack widths.

(a)

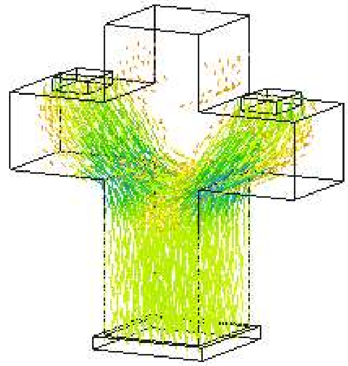

(b)

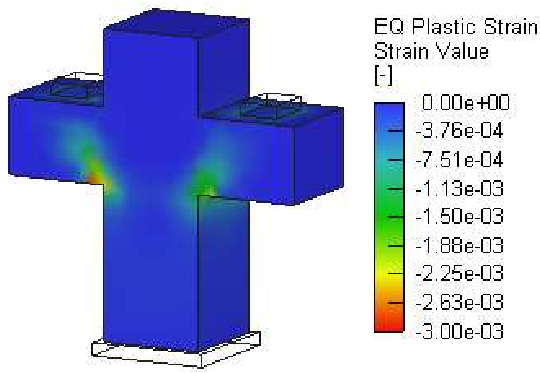

(c)

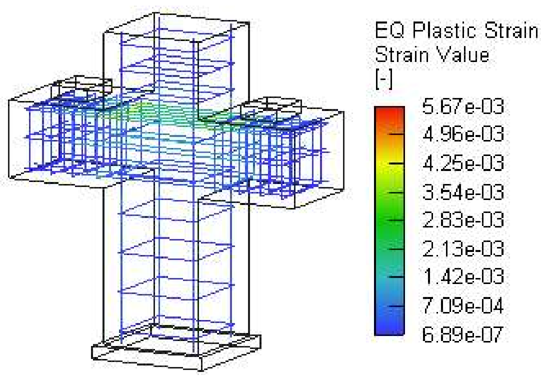

Figure 105 – Corbel NLA results at *failure load*: (a) concrete principal stress tensors; (b) concrete plastic strains; (c) reinforcement plastic strains.

6.3.3 Results: design load

Selected results at design load are shown in Figure 106 and described as follows.

The maximum displacement in the z-direction was -0.14 cm. The concrete maximum compressive stress was 24.5 MPa, while the main reinforcement tensile stress reached 409 MPa. The maximum crack width was 0.17 mm.

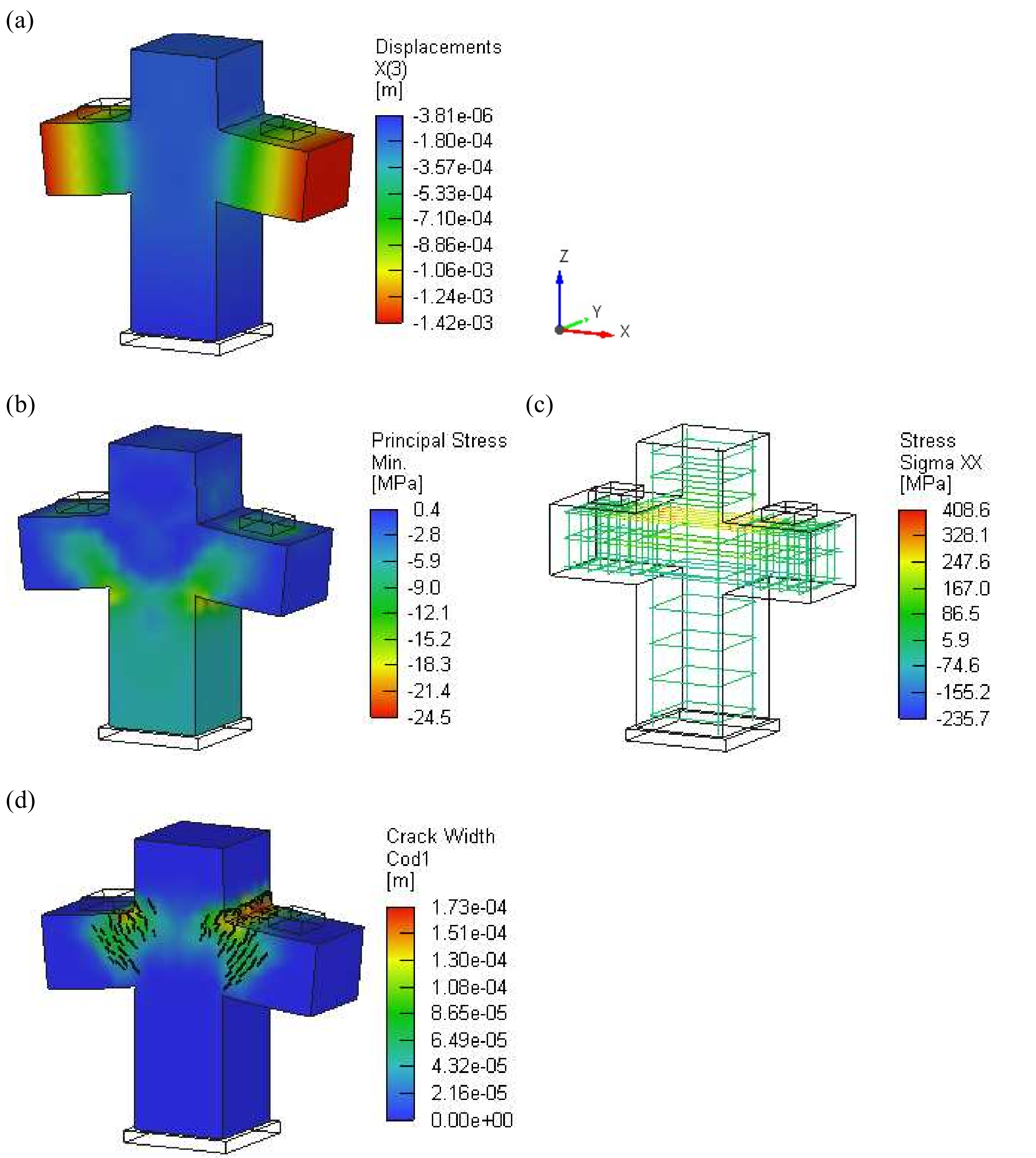

Figure 106 – Corbel NLA results at *design load*: (a) deflections in the z-direction; (b) concrete principal stress σ_{c3}; (c) reinforcement stresses, (d) crack widths.

6.3.4 Results: service load

Selected results at service load are shown in Figure 107 and described as follows.

The maximum displacement in the *z*-direction was -0.11 cm. The concrete maximum compressive stress was 20.2 MPa, while the main reinforcement tensile stress reached 359 MPa. The maximum crack width was 0.13 mm.

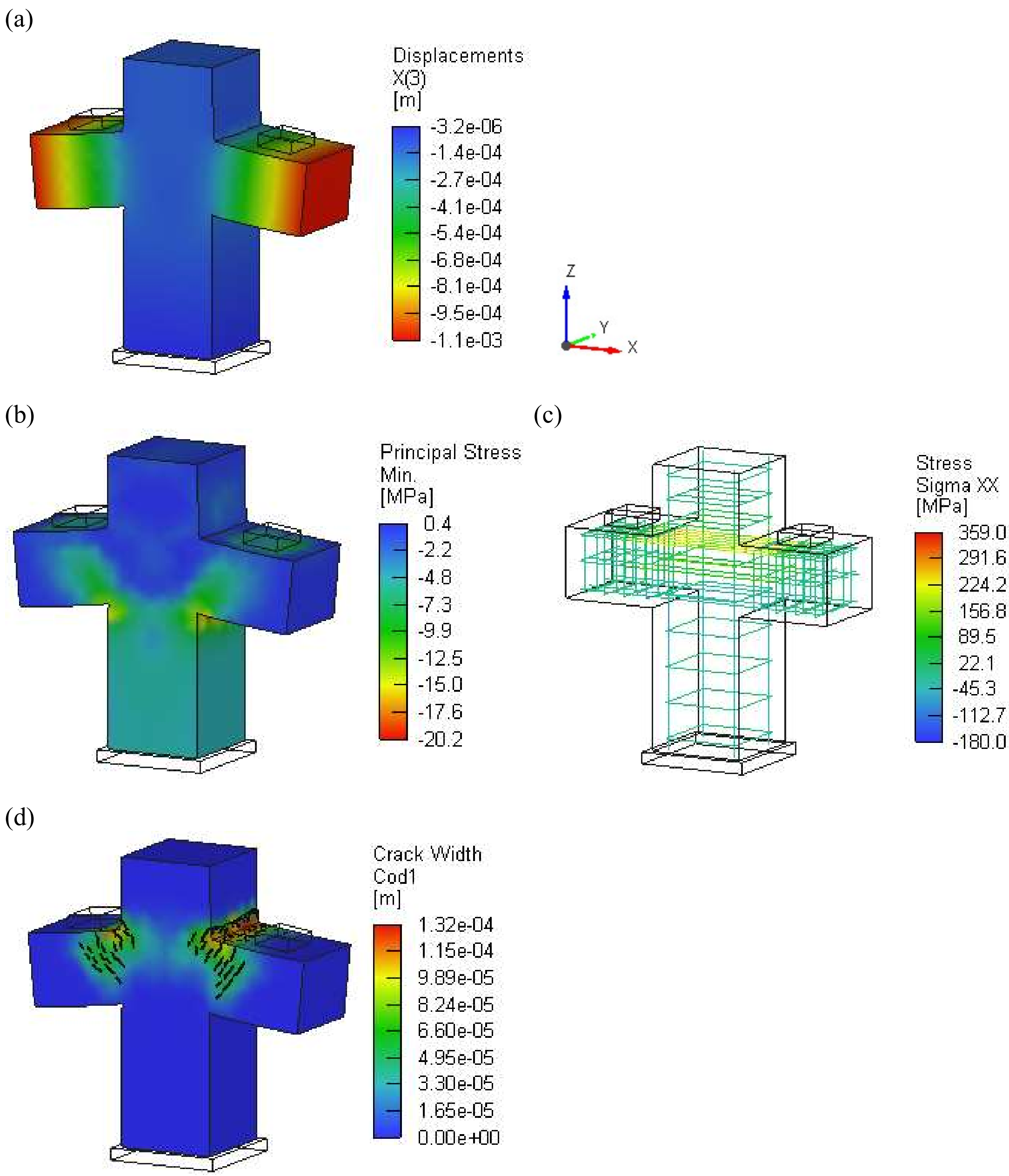

Figure 107 – Corbel NLA results at *service load*: (a) deflections in the *z*-direction; (b) concrete principal stress σ_{c3}; (c) reinforcement stresses; (d) crack widths.

6.3.5 Alternative solution: structure designed by the STM

Applying the strut-and-tie method (STM) for designing corbels is allowed by design codes such as Eurocode 2 (CEN, 2004), MC2010 (*fib,* 2013), ACI-315 (2014), and NBR-6118 (2023), assuming that the applied load is transferred directly to the support by means of an inclined strut, as illustrated in Figure 108a. The main tensile reinforcement was initially designed according to Brazilian Code NBR-9062 (2017, Section 7.3.5.3), following the design rules for short corbels:

$$A_{s,tir} = \left(0.10 + \frac{a_c}{d}\right)\frac{F_d}{f_{yd}} = 0.855 \times \frac{500}{43.48} = 9.82\ cm^2 \tag{6.13}$$

Complementarily, it was designed according to the *fib* Practical design of structural concrete (1999, Section 6.5.2.3). The assigned design steps are listed below:

- Step 1: determination of the lever arm, a:

$$\begin{aligned} a_1 &= \frac{F_d}{b\nu_1 f_{cd}} = \frac{500}{0.40 \times (1 - 30/250) \times 30{,}000/1.5} = 0.071\ m \\ a &= a_c + \frac{a_1}{2} = 0.236\ m \end{aligned} \tag{6.14}$$

- Step 2: determination of the compressive height:

$$a_2 = d - \sqrt{d^2 - 2a\,a_1} = 0.073\ m \tag{6.15}$$

- Step 3: determination of the longitudinal reinforcement, A_1:

$$\begin{aligned} \cot\theta &= \frac{a_2}{a_1} = \frac{0.073}{0.071} = 1.03 \\ T_1 &= F\cot\theta = 500 \times 1.03 = 514.1\ kN \\ A_1 &= \frac{514.1}{43.48} = 11.8\ cm^2 \cong A_{s,tir} \end{aligned} \tag{6.16}$$

The longitudinal reinforcement was detailed for the highest value from the two different approaches. An arrangement of 6 ϕ16 straight bars anchored with welded transverse bars at the extremities was chosen. Additional horizontal closed ties parallel to the primary tension reinforcement, uniformly distributed within two-thirds of the effective depth, were detailed for crack control according to ACI 318 (2014, section 16.5.5.2). The total area, A_h, was:

$$A_h = 0.5 \times (A_1 - A_n) = 0.5 \times 11.8 = 5.9\ cm^2 \tag{6.17}$$

which was covered by 8 ϕ10 rebars.

At the bottom of the corbel, 4 ϕ8 rebars were arranged:

$$A_{s,\inf} = 0.15\% \times A_c = 0.0015 \times 40 \times 30 = 1.8\ cm^2 \tag{6.18}$$

The transverse reinforcement, A_w, was designed for the following part of the load:

$$F_w = F\left(2a / z - 1\right)/3 = 0.35F \tag{6.19}$$

$$A_w = \frac{F_w}{f_{yd}} = 0.35 \times \frac{500}{43.48} = 4.02\ cm^2 \tag{6.20}$$

which was detailed with 2 stirrups ϕ8 mm with four legs each, enclosing the longitudinal tension reinforcement and the compression zone and distributed over length a_w:

$$a_w = 0.85a - d/4 = 0.13\ cm \tag{6.21}$$

The final reinforcement arrangement is presented in Figure 108b. The reinforcement area in the x-direction arrangement summed:

$$A_{sx,corbel} = 6 \times 2.00 + 6 \times 1.13 + 4 \times 0.50 = 20.8\ cm^2 \tag{6.22}$$

which was approximately equal to the total area obtained from the SFM design (20.5 cm²).

(a)

(b)

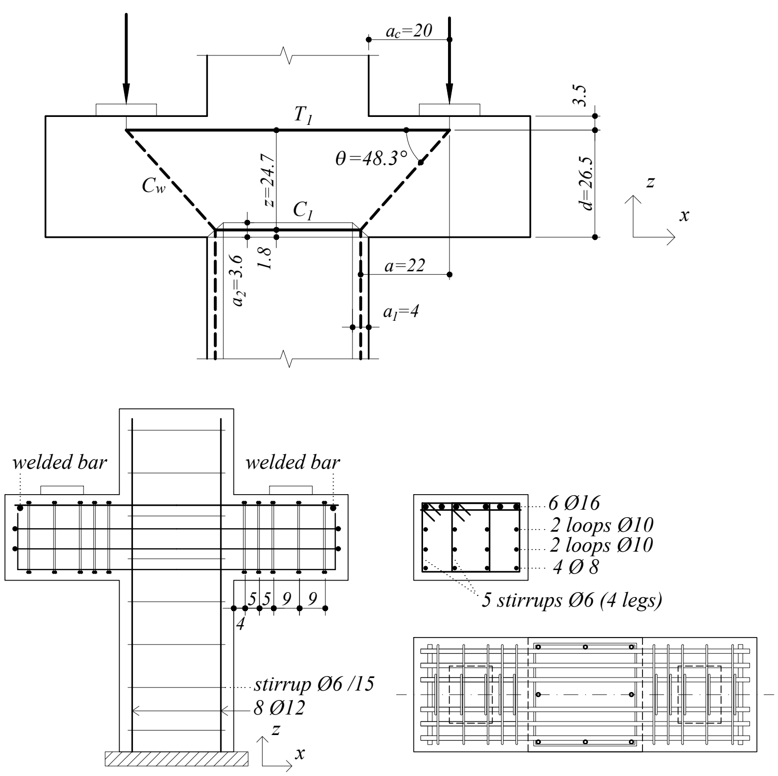

Figure 108 – Corbel designed by the STM: (a) structural model; (b) detailing.

Nonlinear analysis of the alternative solution

The STM solution was then assessed by a nonlinear analysis. The structural model elaborated for this analysis, 'model B', was identical to the one elaborated to assess the SFM solution, except for the reinforcement arrangement presented in Figure 109. Selected results at service load are shown in Figure 110: the maximum vertical displacement was -0.11 cm; the main tie reached a stress of 396 MPa; and the maximum crack width was 0.14 mm.

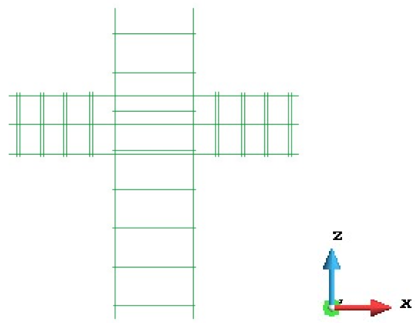

Figure 109 – Corbel designed by the STM: nonlinear structural model – 1D elements.

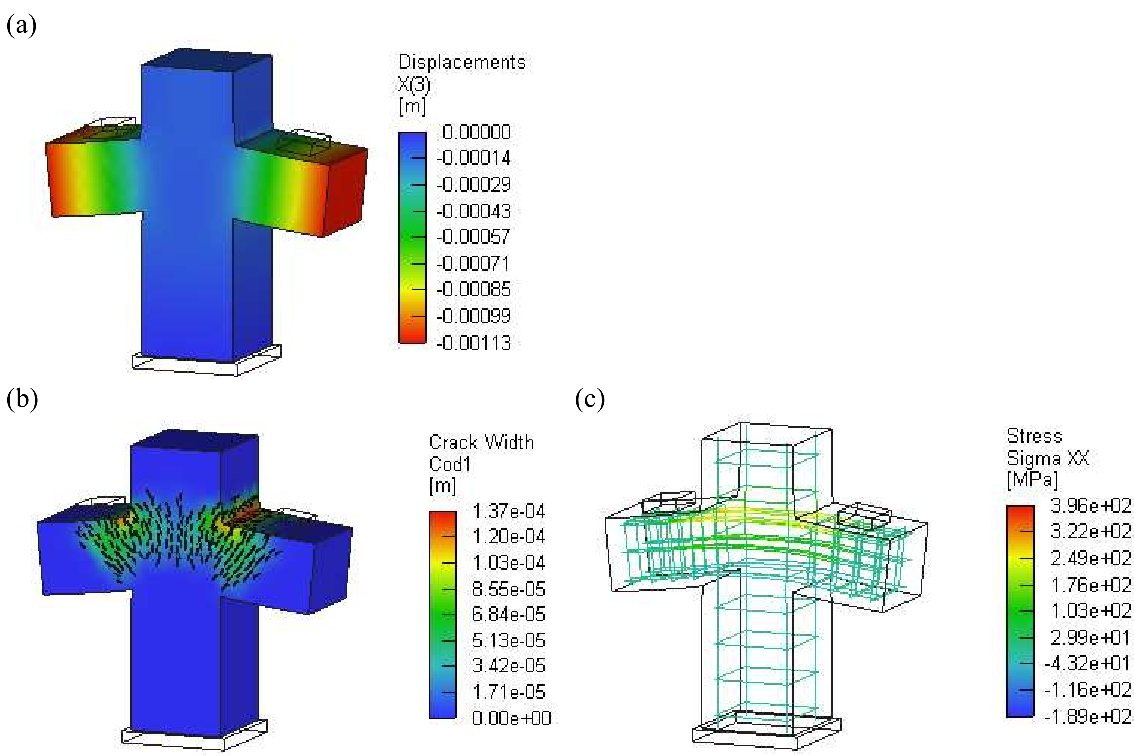

Figure 110 – Corbel designed by the STM: NLA results at *service load* - (a) deflections in the *z*-direction; (b) reinforcement stresses; (c) crack widths.

6.3.6 Discussion

The behavior of the corbels is visualized in the load-displacement curves of Figure 111, where the ordinate plots the total applied force, and the abscissa the relative vertical displacement (difference between measurements from *mnt.2* and *mnt.3*). The load-displacement curves show a slightly stiffer response of the corbel designed by the SFM.

The maximum sustained load in the beam designed by the SFM was 47% higher than the design load, and 10% higher than the failure load of the corbel designed by the STM.

The beam designed by the SFM presented a better performance in service conditions. Although the absolute value of the maximum crack widths and vertical displacements were similar in both simulated corbels, the crack pattern developed in the one designed by the STM was noticeably more pronounced, extending through the column-corbel intersection volume.

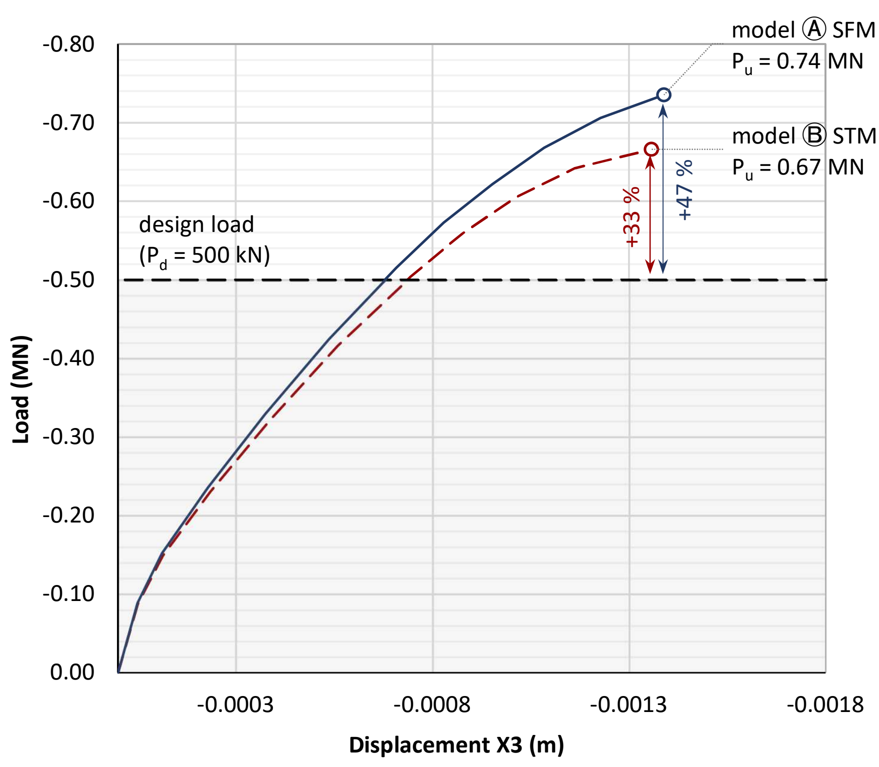

Figure 111 – Corbel NLA: load-displacement curves.

Reinforcement consumption

The SFM design used similar total horizontal reinforcement as the STM design, but it was more concentrated towards the top face of the corbel. The procedure adopted for treating the singularities turned out to be appropriate, since a safe design was achieved.

Vertical reinforcement in the SFM design was provided by a total amount 2.15 times larger than the STM design; additional stirrups in the column above the corbel were needed to equilibrate the forces deriving from the structural analysis, which assumed elastic material behavior.

Two complementary comments are presented concerning the reinforcement detailing. First, it is noted that there is experimental evidence that horizontal tensile stresses and cracks develop in the column above the corbel, as observed in the tests performed by Urban and Krawczyk (2016). The introduction of complementary column stirrups in the SFM design is justified theoretically and observed practically. Second, the SFM yields reinforcement in three orthogonal directions by following elastic stress lines; it can be considered an intermediate solution to the design method proposed by Hoffmann, Käseberg and Holschemacher (2023) giving fanned-out reinforcement layouts.

Remarks

The nonlinear analyses confirmed the safety of SFM for the ULS design of the corbel. The SFM design required more flexural and shear reinforcement, but yielded a better performance in service conditions. This second example demonstrated the feasibility of application of the SFM to provide a competitive alternative design solution for this simple D-region.

6.4 Example 3: beam under axial forces

6.4.1 Structural model for the nonlinear analysis

The structural model for the nonlinear analysis was meshed with elements with dimension of 0.04 m; at least five elements were distributed along each dimension of the cross-section.

- For beam *I*: 408 linear and 21,476 tetrahedral elements, as shown in Figure 112.
- For beam *II*: 376 linear and 21,156 tetrahedral elements, as shown in Figure 113.
- For beam *III*: 536 linear and 21,175 tetrahedral elements, as shown in Figure 114.

Concerning boundary conditions, displacements were constrained in the *x*-, *y*- and *z*-directions on the faces of the steel plates of the extremities of the beam.

Concrete was modeled with a "solid concrete" material model (f_{cd} = 21.4 MPa, f_{ct} = 1.33 MPa, E_c = 26,070 MPa, a_g = 20 mm, ε_{cp} = -1.54‰, f_{co} = -2.8 MPa, W_d = 5 mm). Embedded rebars were modeled with a "1D reinforcement" material model (f_{yd} = 435 MPa, E_s = 210 GPa, ε_{su} = 10‰). Steel plates, in turn, were modeled with a "solid elastic" material model with increased modulus of 10 x E_s = 2 100 GPa.

Loads were applied as a set of ten concentrated loads at the central steel plate, as indicated in the cross-sections of Figure 50. They were incrementally increased up to failure. Analyses were performed with the *arc-length* solution method, utilizing the *PARDISO* solver. The behavior of the structural model was assessed with the aid of one monitoring point (*mnt.1)* located at the central steel plate to read displacements in the *x*-direction, and two monitoring surfaces at the lateral steel plates (*mnt.2* and *mnt.3)* to read support reactions (Figure 112c).

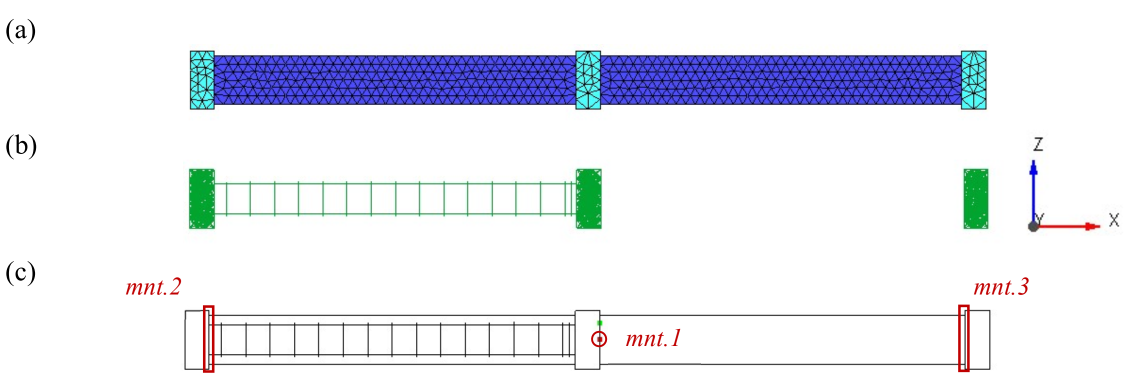

Figure 112 – Beam *I* model for theNLA: (a) mesh; (b) steel plates and linear elements; (c) monitoring points.

(a)

(b)

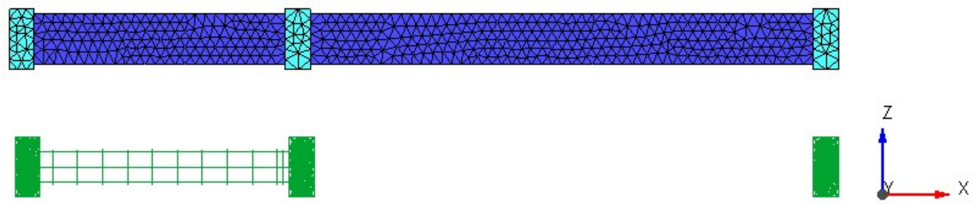

Figure 113 – Beam *II* model for the NLA: (a) mesh; (b) steel plates and linear elements.

(a)

(b)

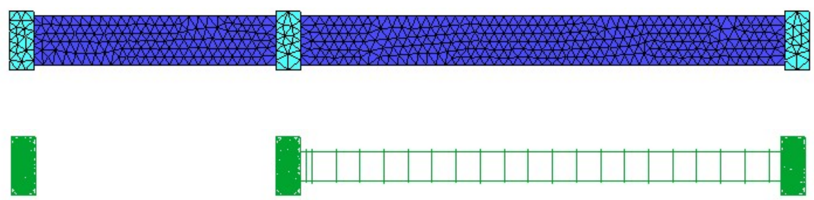

Figure 114 – Beam *III* model for the NLA: (a) mesh; (b) steel plates and linear elements.

6.4.2 Results: *beam I*

The maximum sustained load in the numerical analysis was 1,410 kN, which corresponded to 1.39 times the design load. The concrete beam failed by the yielding of the reinforcement in the tension span (see Section 6.4.6).

Selected results at the *maximum sustained load* in the analysis are shown in Figure 115: the maximum horizontal displacement was 0.34 cm at the central plate; reinforcement in the tension span was stressed up to the yield stress (f_{yd} = 435 MPa). The concrete compressive stress reached 21.9 MPa at the compression midspan. Cracks throughout the tension span reached widths of 0.41 mm.

Selected results at *design load* are shown in Figure 116: the maximum horizontal displacement was 0.19 cm; concrete compressive stresses reached 17.8 MPa; reinforcement stresses reached 272 MPa; and the maximum crack width was 0.06 mm.

Selected results at *service load* are shown in Figure 117: the maximum horizontal displacement was 0.12 cm; concrete compressive stresses reached 13.5 MPa; reinforcement stresses reached 173 MPa; and the maximum crack width was 0.04 mm.

(a)

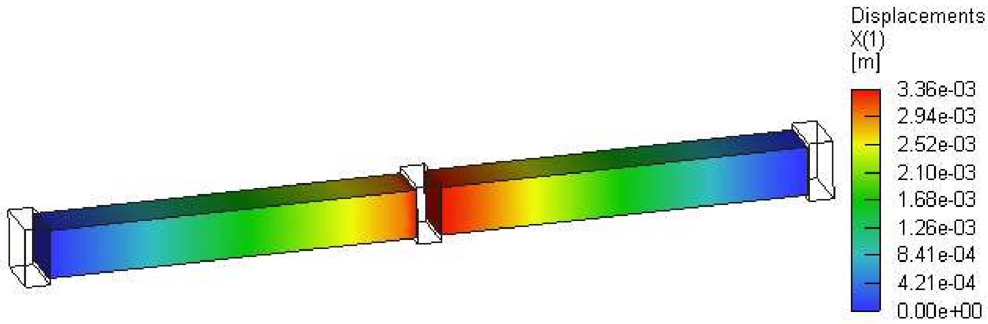

(b)

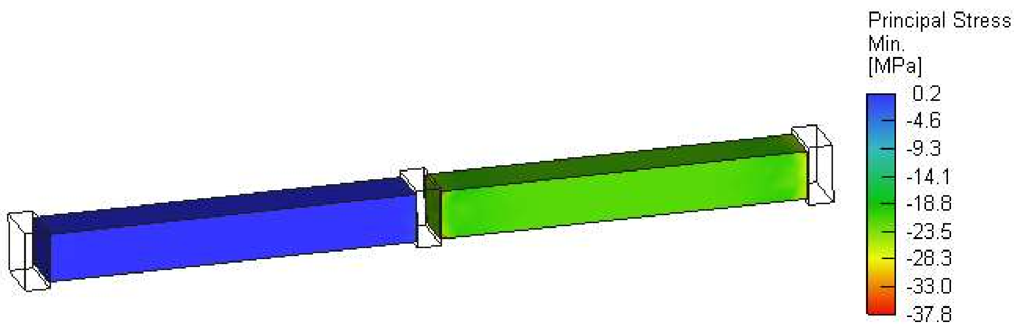

(c)

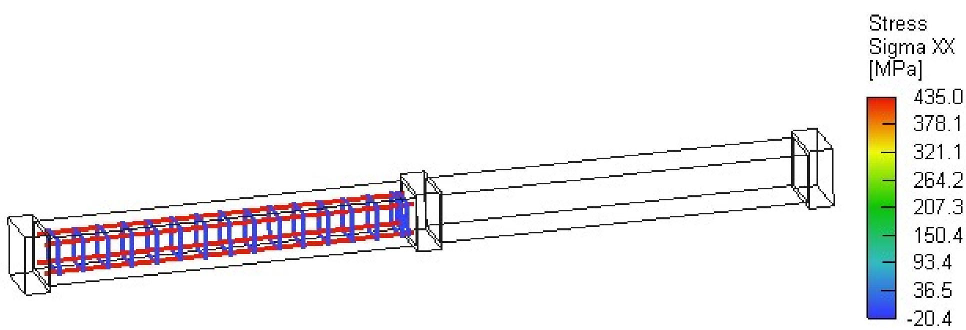

(d)

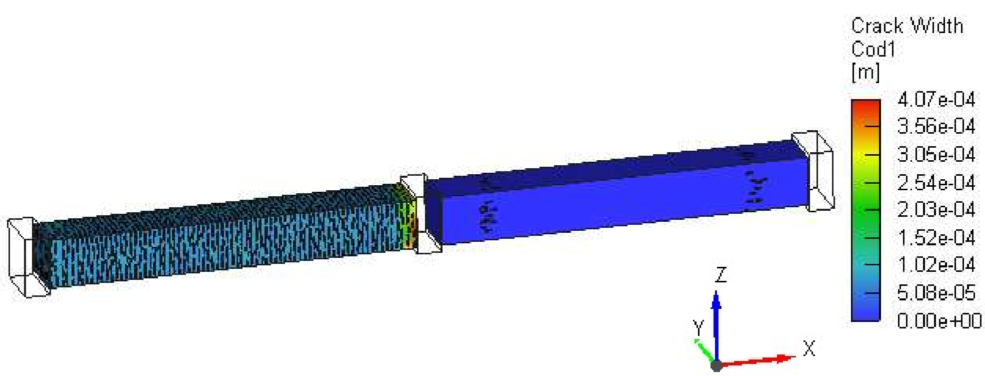

Figure 115 – Beam *I* NLA results at *maximum load*: (a) deflections in the *x*-direction; (b) concrete principal stress σ_{c3}; (c) reinforcement stresses; (d) crack widths.

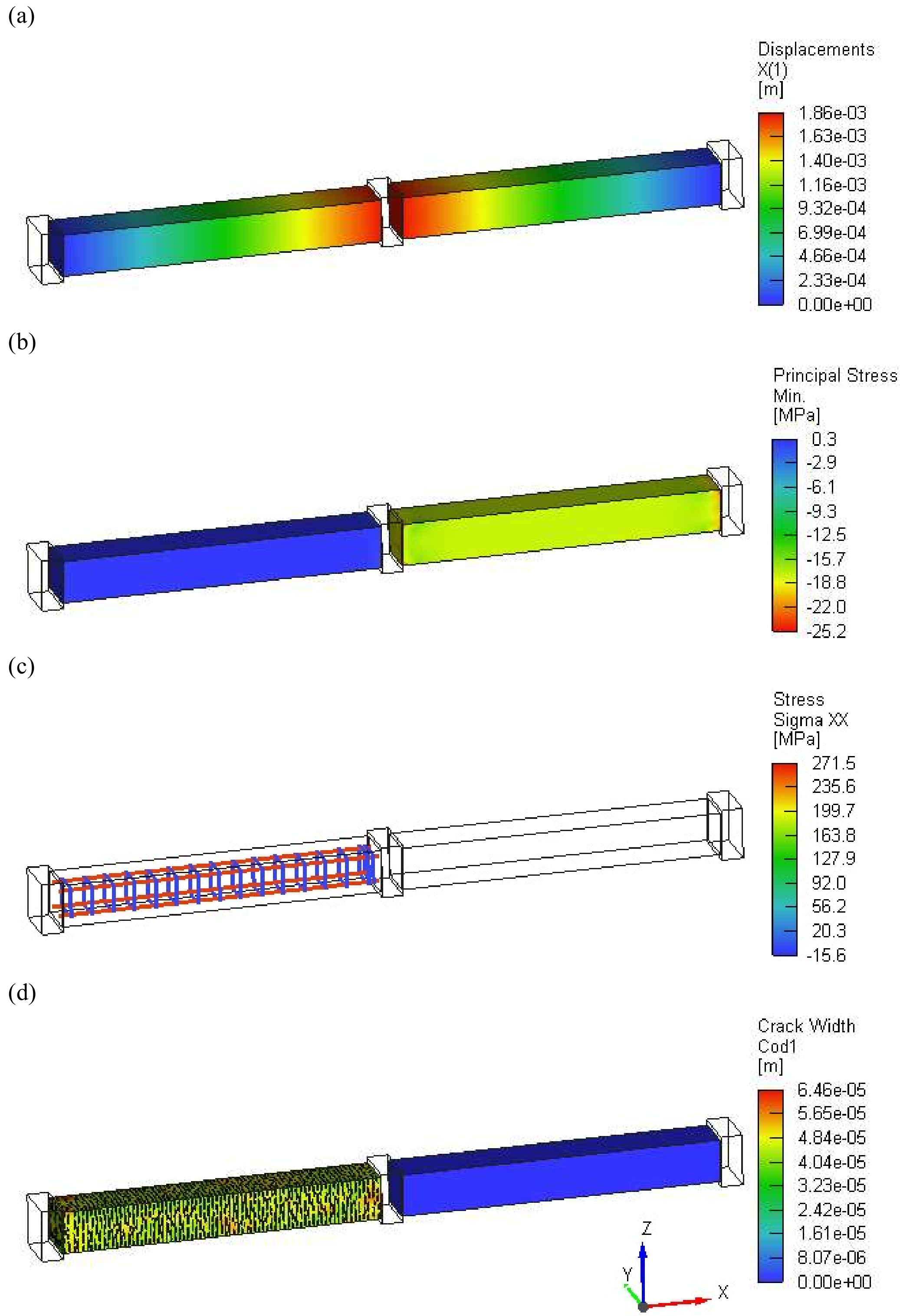

Figure 116 – Beam *I* NLA results at *design load*: (a) deflections in the x-direction; (b) concrete principal stress σ_{c3}; (c) reinforcement stresses; (d) crack widths.

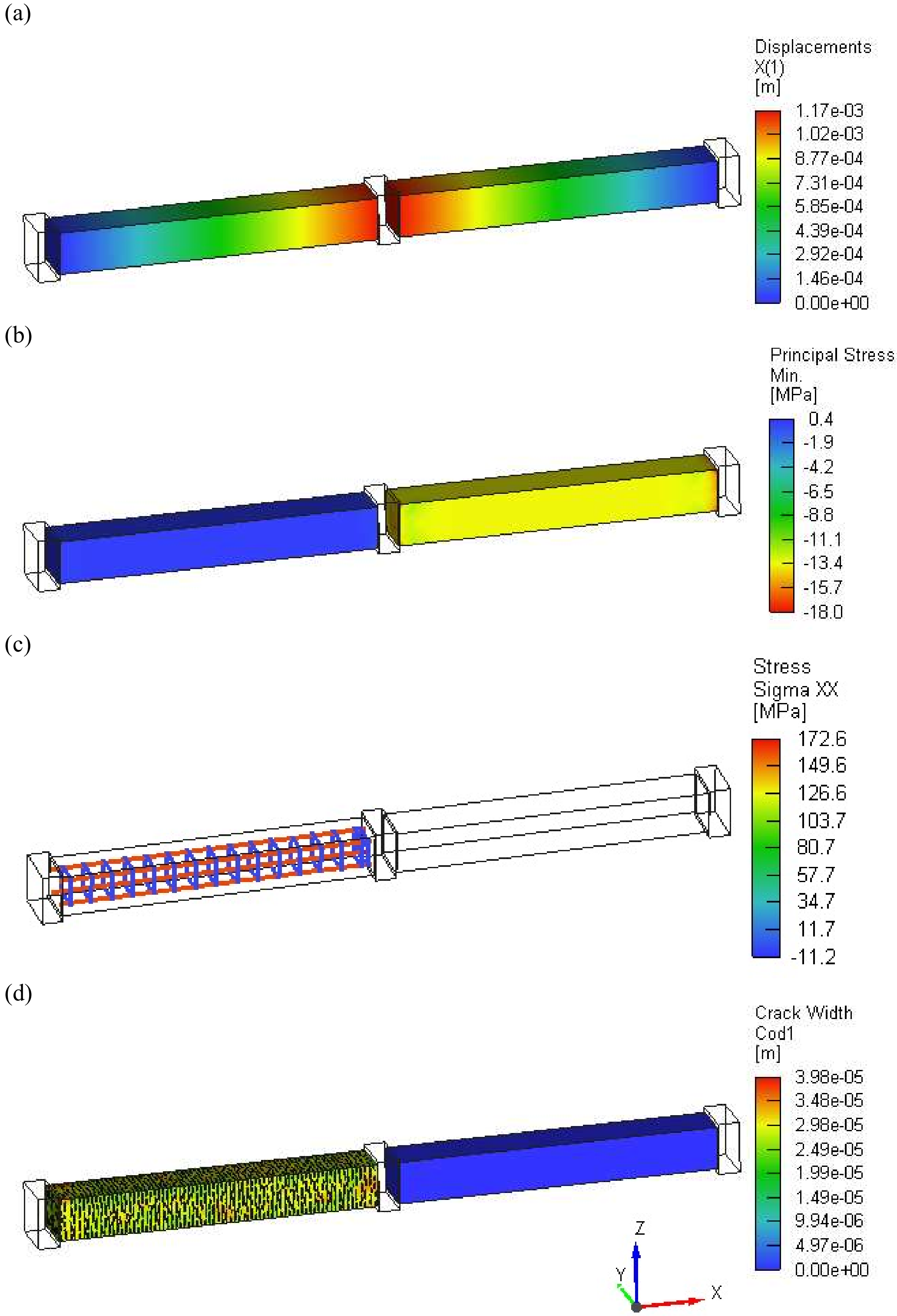

Figure 117 – Beam *I* NLA results at *service load*: (a) deflections in the x-direction; (b) concrete principal stress σ_{c3}; (c) reinforcement stresses; (d) crack widths.

6.4.3 Results: beam *II*

The maximum sustained load in the numerical analysis was 1,503 kN, which corresponded to 1.47 times the design load. The concrete beam failed by the yielding of the reinforcement in the tension span (see Section 6.4.6).

Selected results at the ***maximum sustained load*** in the analysis are shown in Figure 118 and described as follows: the maximum horizontal displacement was 0.22 cm at the central plate. Concrete compressive stresses reached 16.4 MPa (representative value, outside the zone of the central plate), while reinforcement stresses in the tension span reached the yield stress (f_{yd} = 435 MPa). Cracks throughout the tension span reached widths of 0.18 mm.

Selected results at ***design load*** are shown in Figure 119 and described as follows: the maximum horizontal displacement was 0.15 cm; concrete compressive stresses reached 13.3 MPa; reinforcement stresses reached 326 MPa; and the maximum crack width was 0.07 mm.

Selected results at ***service load*** are shown in Figure 120 and described as follows: the maximum horizontal displacement was 0.12 cm; concrete compressive stresses reached 11.1 MPa; reinforcement stresses reached 251 MPa; and the maximum crack width was 0.06 mm.

6.4.4 Results: beam *III*

The maximum sustained load in the numerical analysis was 1,087 kN, which corresponded to 1.06 times the design load. The concrete beam failed by concrete crushing (see Section 6.4.6).

Selected results at the ***maximum sustained load*** in the analysis are shown in Figure 120: the maximum horizontal displacement was 0.22 cm; concrete compressive stress reached 22.0 MPa; reinforcement stresses in the tension span reached 233 MPa; and cracks widths throughout the tension span reached 0.06 mm.

(a)

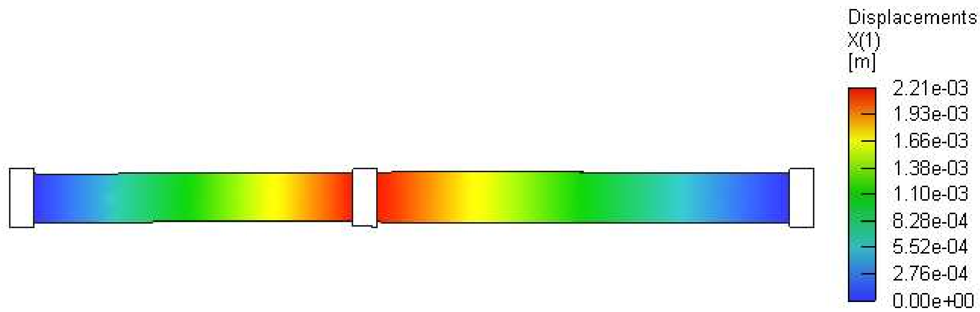

(b)

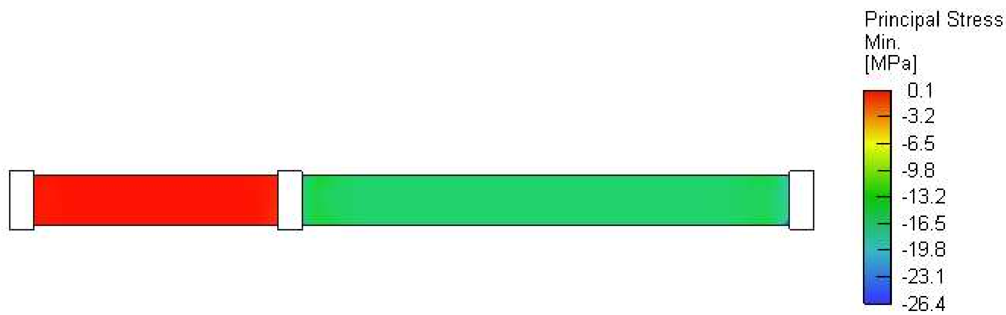

(c)

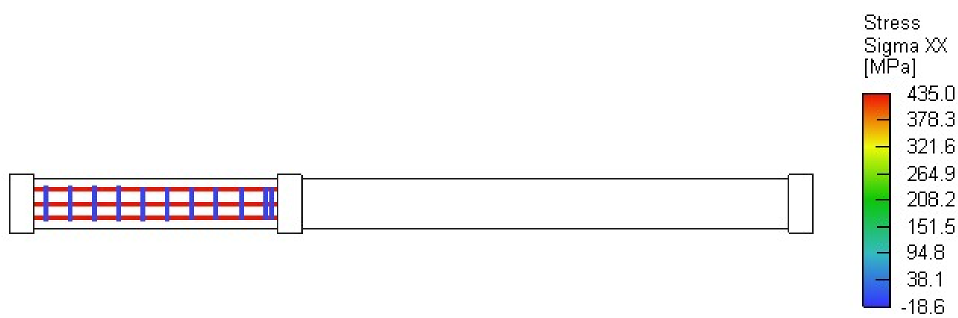

(d)

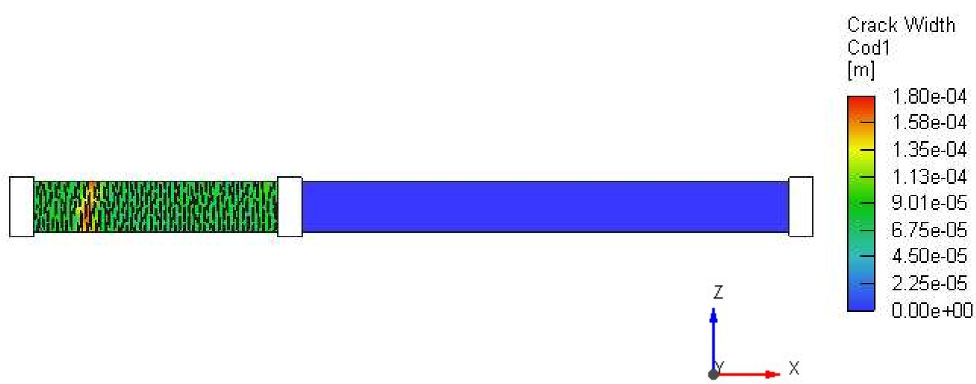

Figure 118 – Beam *II* NLA results at *maximum load*: (a) deflections in the *x*-direction; (b) concrete principal stress σ_{c3}; (c) reinforcement stresses; (d) crack widths.

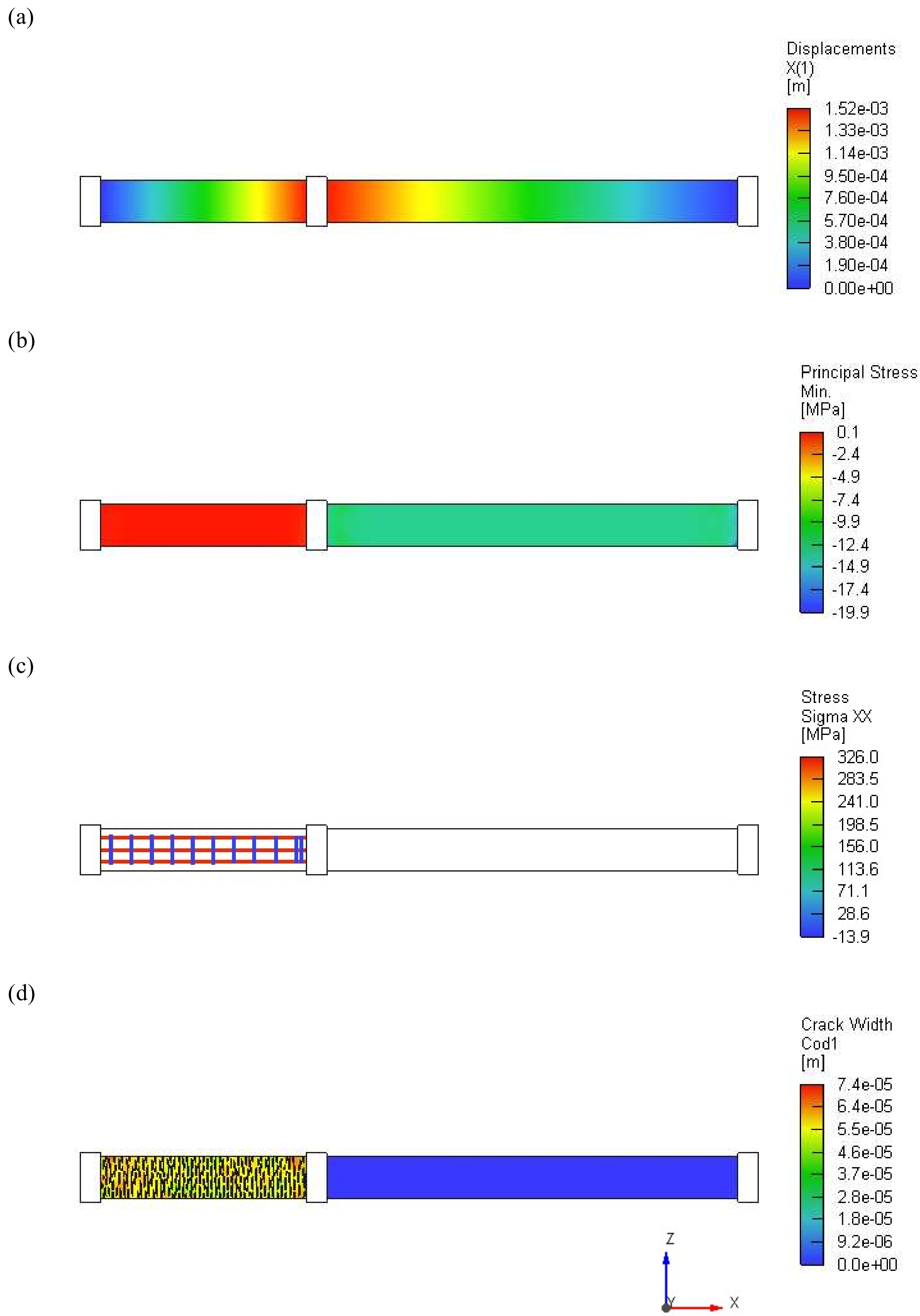

Figure 119 – Beam *II* NLA results at *design load*: (a) deflections in the x-direction; (b) concrete principal stress σ_{c3}; (c) reinforcement stresses; (d) crack widths.

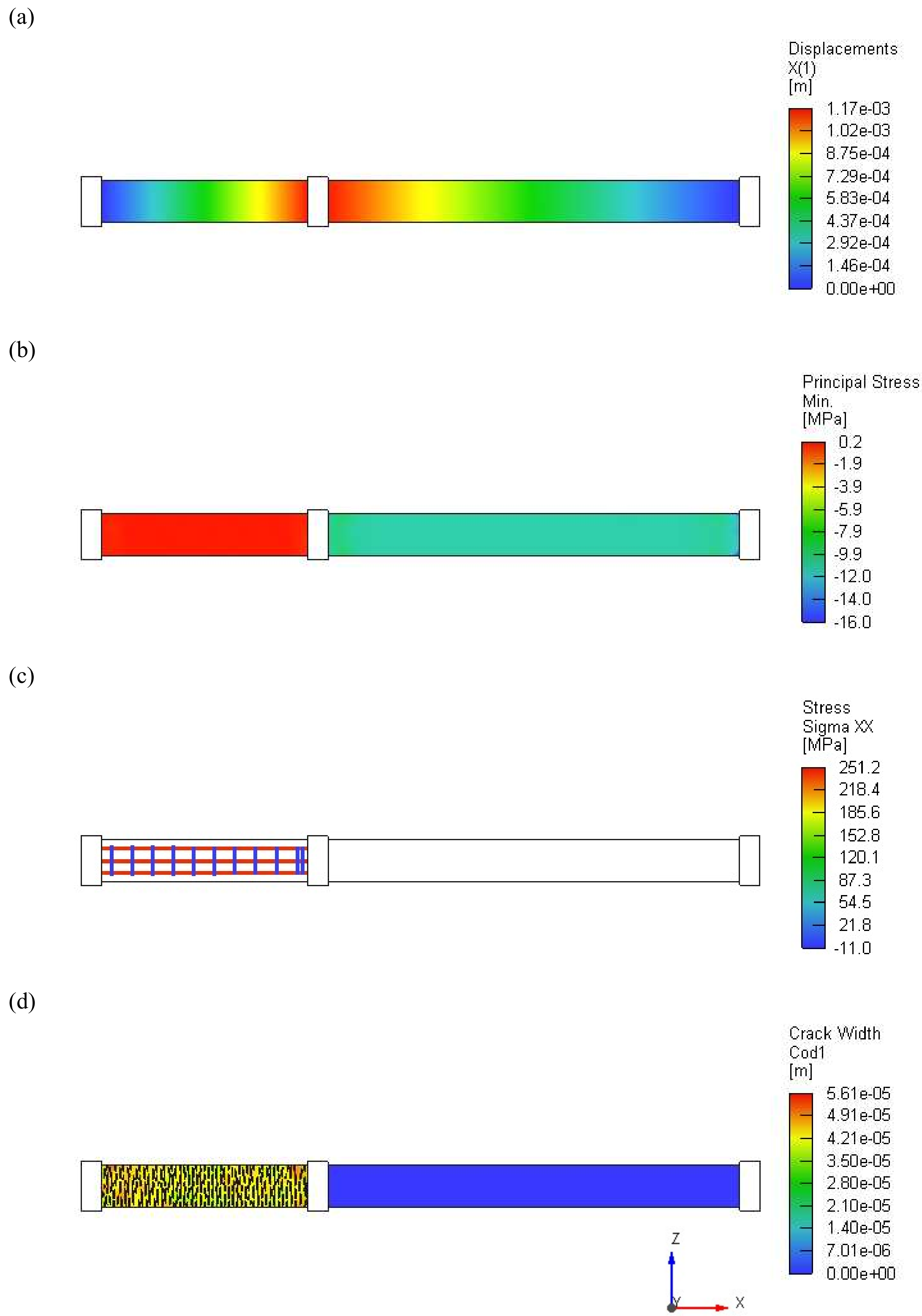

Figure 120 – Beam *II* NLA results at *service load*: (a) deflections in the x-direction; (b) concrete principal stress σ_{c3}; (c) reinforcement stresses; (d) crack widths.

(a)

(b)

(c)

(d)

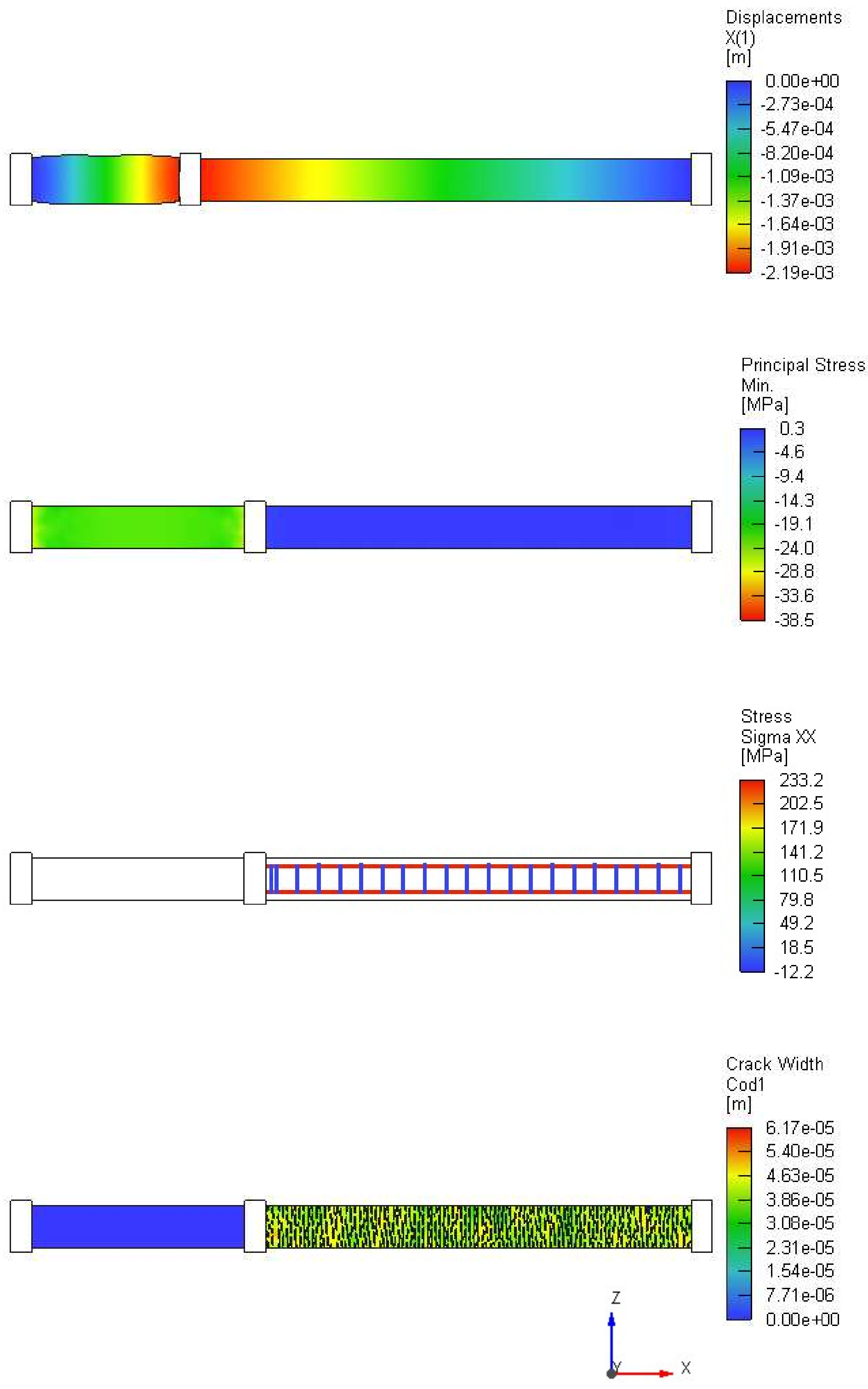

Figure 121 – Beam *III* NLA results at *maximum load*: (a) deflections in the *x*-direction; (b) concrete principal stress σ_{c3}, (c) reinforcement stresses; (d) crack widths.

Selected results at <u>*design load*</u> are shown in Figure 122: the maximum horizontal displacement was 0.20 cm; concrete compressive stresses reached 21.7 MPa, while reinforcement stresses reached 214 MPa; and the maximum crack width was 0.06 mm.

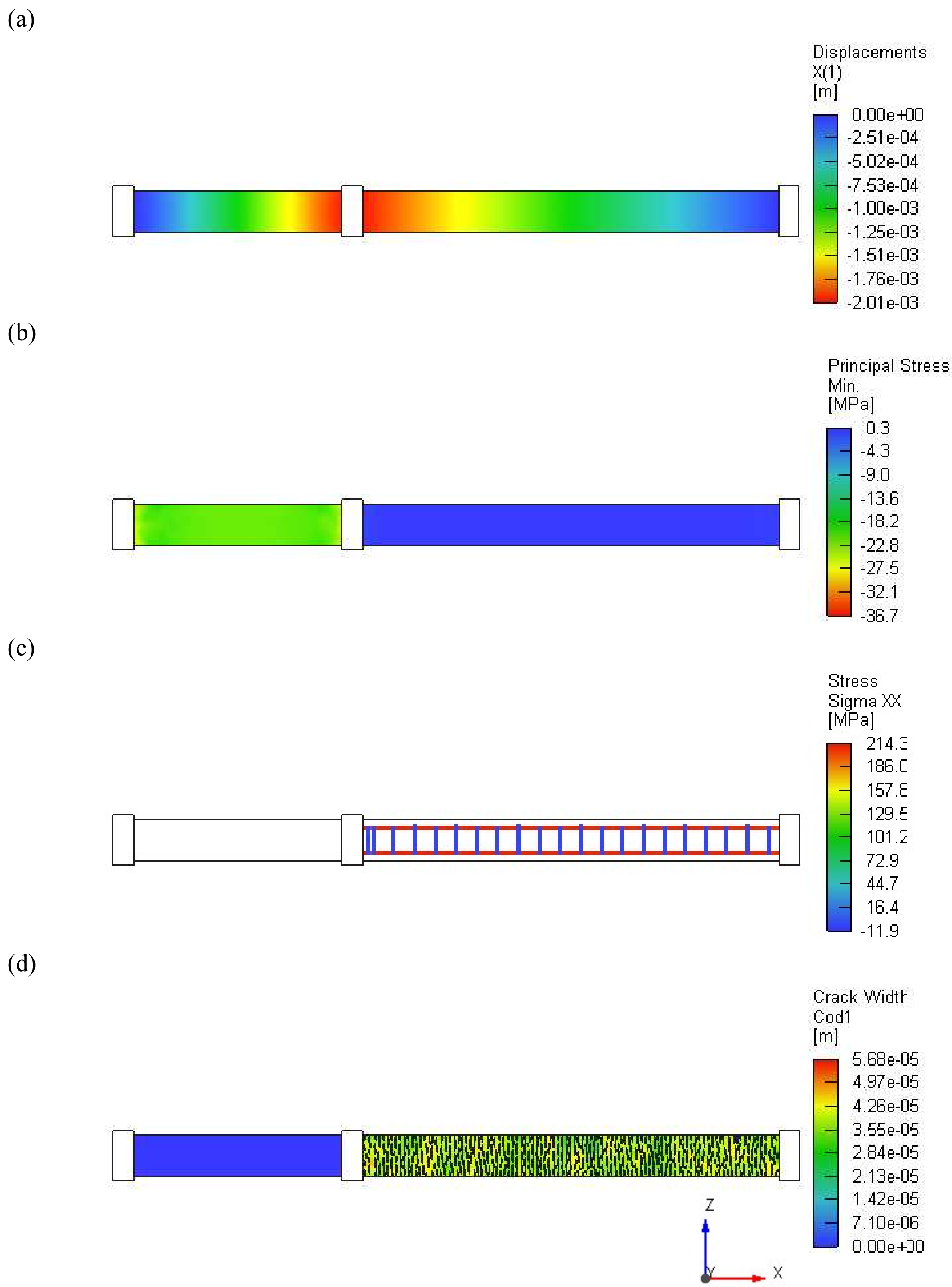

Figure 122 – Beam *III* NLA results at *design load*: (a) deflections in the x-direction; (b) concrete principal stress σ_{c3}; (c) reinforcement stresses, (d) crack widths.

Selected results at <u>*service load*</u> are shown in Figure 123: the maximum horizontal displacement was 0.09 cm; concrete compressive stresses reached 15.1 MPa, while reinforcement stresses reached 105 MPa; and the maximum crack width was 0.03 mm.

(a)

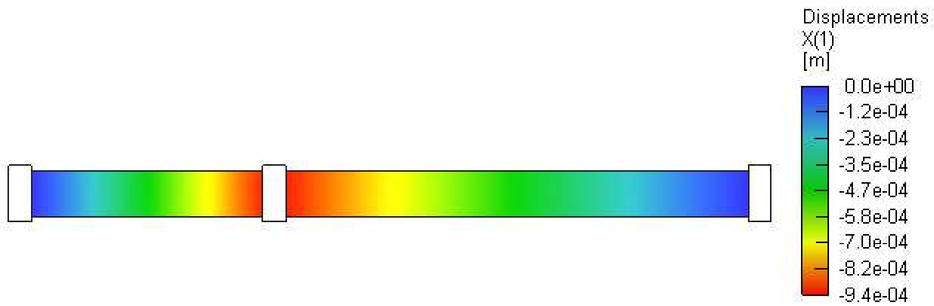

(b)

(c)

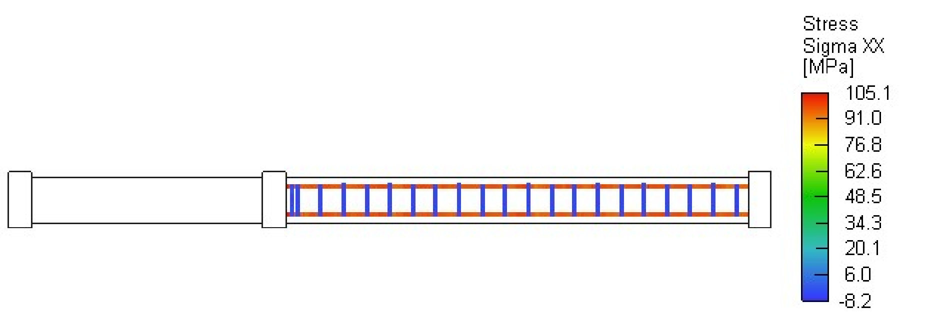

(d)

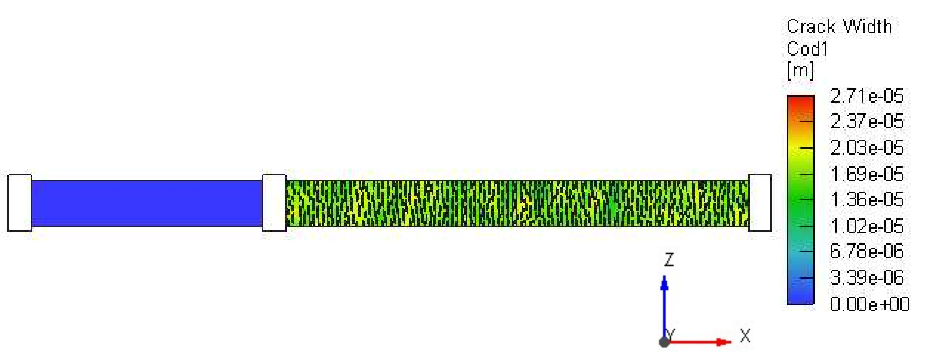

Figure 123 – Beam *III* NLA results at *service load*: (a) deflections in the x-direction; (b) concrete principal stress σ_{c3}; (c) reinforcement stresses; (d) crack widths.

6.4.5 Alternative solution: concrete limit design (CLD)

The alternative solution adopted for this worked example was a plastic limit design for concrete. It assumed that concrete presented no tensile strength, and that concrete was utilized up to its maximum strength in compression.

Assuming a parabola-rectangle stress-strain relation for the concrete, the maximum sustained load in the beam was obtained for concrete strains reaching the value:

$$\varepsilon_{c2} = -2.00‰ \tag{6.23}$$

The compressed spans, therefore, were subjected to the maximum force:

$$F_{cu} = -\left(1.00 \times f_{cd}\right) A_c = -857\ kN \tag{6.24}$$

The tension span was designed for the portion of the applied force not resisted by concrete:

$$F_{su} = F_d - \left|F_{cu}\right| = 1020 - 857 = 163\ kN \tag{6.25}$$

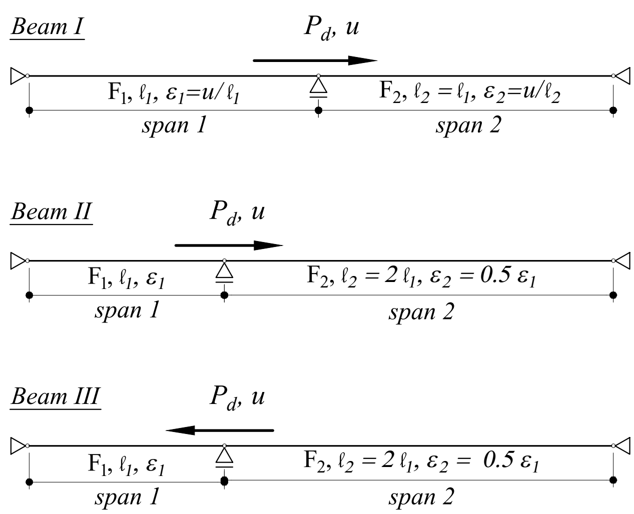

Figure 124 – Beam under axial forces: parameters for the alternative plastic design.

Beam I

The tensioned span was subjected to the same strain as the one in the compressed span:

$$\varepsilon_{su} = -\varepsilon_{c2} = +2.00‰ \tag{6.26}$$

This deformation was smaller than the reinforcement yielding strain $\varepsilon_{yd} = f_{yd} / E_s = = 2.07‰$, so that the force mobilized in the reinforcement was calculated from:

$$F_{1u} = \left(\varepsilon_{su} E_s\right) A_s = (2‰ \times 210{,}000) A_s = 420 A_s \tag{6.27}$$

The total area of required reinforcement was then calculated as:

$$A_s = \frac{F_{1u}}{420{,}000 \times 10^{-4}} = \frac{163}{42} = 3.9\ cm^2 \tag{6.28}$$

which was arranged with 4 ϕ12 longitudinal rebars.

Beam II

The tensioned span was subjected to:

$$\varepsilon_{su} = -2 \times \varepsilon_{cu} = -2 \times (-2.00‰) = +4‰ \tag{6.29}$$

meaning that reinforcement was yielding, and the force mobilized in the reinforcement was:

$$F_{1u} = f_{yd} A_s = 434.8 \times A_s \tag{6.30}$$

The total area of required reinforcement was then calculated as:

$$A_s = \frac{F_{1u}}{43.48} = \frac{163}{43.48} = 3.7\ cm^2 \tag{6.31}$$

which was arranged with 4 ϕ16 longitudinal rebars.

Beam III

The tensioned span was subjected to:

$$\varepsilon_{su} = -0.5\ \varepsilon_{cu} = +1.00‰ \tag{6.32}$$

This deformation was smaller than the yield strain ε_{yd}, so that the force mobilized in the reinforcement was calculated from:

$$F_{2u} = \left(\varepsilon_s \times E_s\right) A_s = (1.00‰ \times 210{,}000) A_s = 210 A_s \qquad [unit = MN] \tag{6.33}$$

The total area of required reinforcement was then calculated as:

$$A_s = \frac{F_{2u}}{210{,}000 \times 10^{-4}} = \frac{163}{21} = 7.8\ cm^2 \tag{6.34}$$

which was arranged with 4 ϕ16 longitudinal rebars, that is, the same arrangement of the beam designed by the SFM.

Nonlinear analysis of the alternative solution

Selected results at *service load* are shown in Figure 125: the maximum crack widths for beams *I*, *II* and *III* were, respectively, 0.04 mm, 0.07 mm and 0.03 mm, approximately identical to those observed in the simulations of the SFM design.

(a)

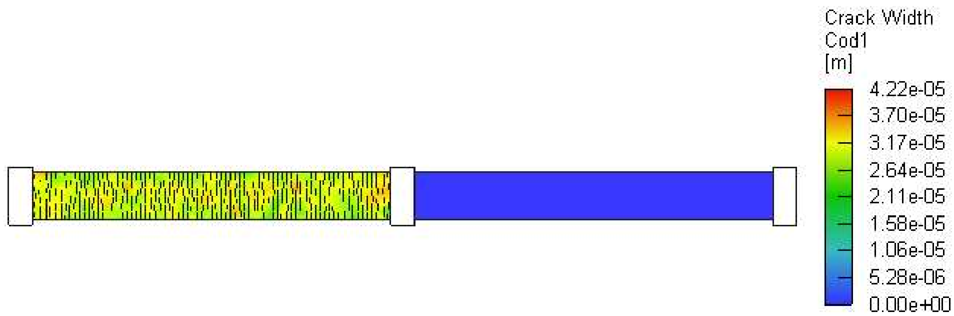

(b)

(c)

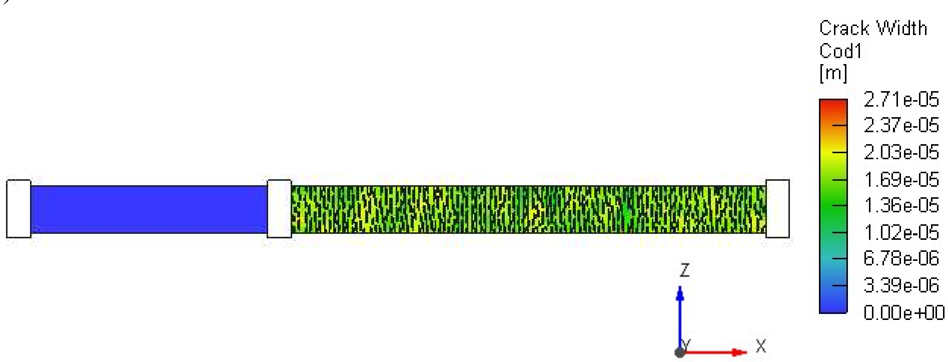

Figure 125 – Beams designed by the concrete limit design - NLA results: crack widths at *service* load: (a) beam *I*; (b) beam *II*; and (c) beam *III*.

6.4.6 Discussion

The behavior of the beams is visualized in the load-displacement curves of Figure 126, where the ordinate plots the total applied force (as the sum of reaction forces measured from *mnt.2* and *mnt.3*), and the abscissa the horizontal displacement measured by *mnt.1*. The curves in blue correspond to the beam designed by the SFM, and the curves in red, to the beam designed by the concrete limit design (cld). Forces equilibrated by the compression span (C) and tension span (T) appear in dashed lines, while their sum appear in continuous line.

(a)

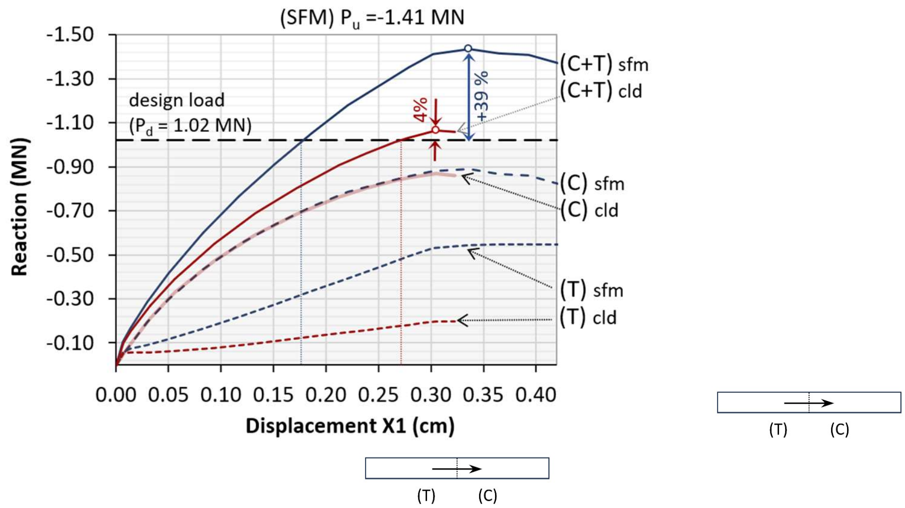

(b)

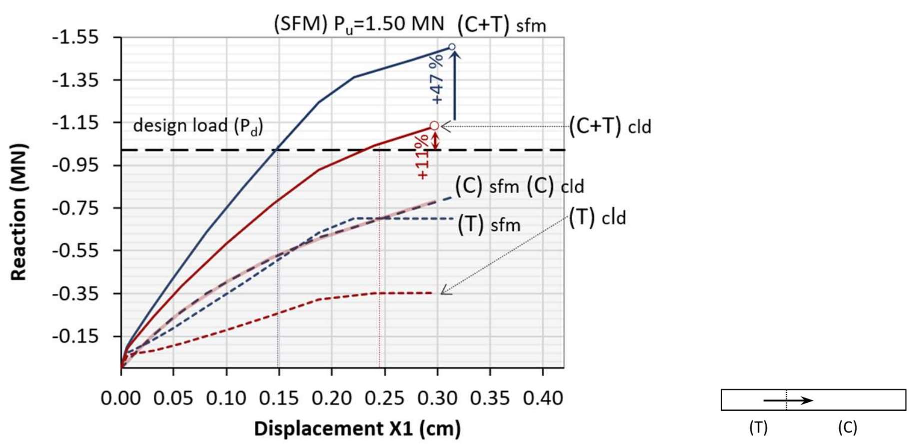

(c)

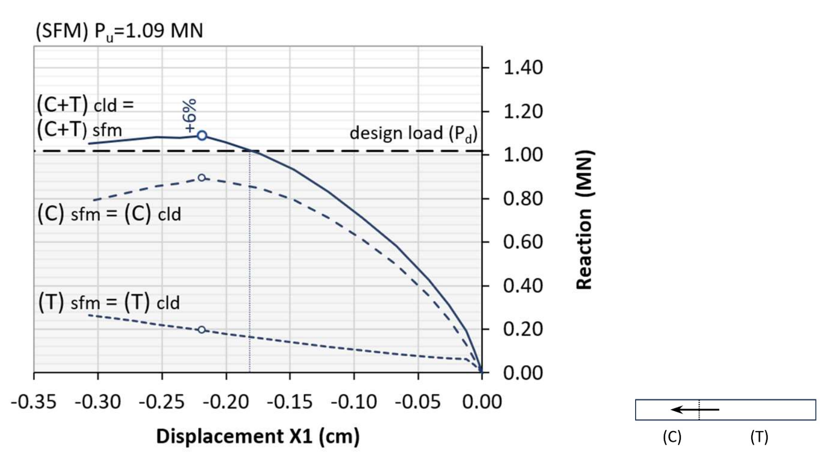

Figure 126 – Beam under axial load NLA: load-displacement curves for (a) beam *I*; (b) beam *II*; and (c) beam *III*.

Beams *I* and *II* designed by the SFM required more reinforcement compared to the ones designed by CLD. They showed stiffer responses.

Beam *III* designed by the SFM required the same reinforcement as the one designed by the CLD. The SFM assumed uncracked concrete in the structural analysis, and limit design for the reinforcement, which was assumed to be yielding. The nonlinear analysis showed, however, that it did not occur. Even so, plastic stress redistribution of concrete in the compression span allowed for the development of a strain state in the beam that was sufficient to mobilize the design load. This example was purposedly conceived to illustrate an extreme case in which a short beam in compression is associated with a long beam in tension. It is recalled that the beam ultimate capacity would have been further increased if minimum reinforcement in the compression span were provided as prescribed by normative codes.

Uncracked and cracked stiffnesses

The SFM assumed uncracked stiffness for the structural analysis determining the applied stress field for the design. Questions may arise as to whether this assumption is adequate to check strength criteria: it could be argued that concrete stiffness in areas of anticipated cracking should be reduced. The ACI (2019, p.72) recognizes the difficulty of reflecting the degree of cracking along each member before yielding: “complexities involved in selecting different stiffnesses for all member of a frame would make frame analyses inefficient in the design process”. Complexities would be even more pronounced in selecting different stiffnesses for individual solid elements: (i) composing massive structural members; (ii) with their stiffness largely affected by the loading history and load cases, which in a real structure may lead to the formation of new cracks, or widening or closure of existing ones.

Simpler assumptions are, therefore, required in the definition of material stiffnesses. Assuming uncracked stiffnesses for the structural analyses was adequate in the three examples.

Remarks

The nonlinear analyses confirmed the safety of the SFM for the ULS design of the beams subjected to axial forces. The third worked example showed that by assuming uncracked stiffness, a safe design was achieved.

6.5 Example 4: six-pile cap

6.5.1 Structural model for the nonlinear analysis

For the nonlinear structural model, additional steel plates were modeled at the top of the columns, so that the concentrated applied loads could be uniformly distributed to the concrete column elements. Columns, pile cap, piles and rebars were meshed with elements with dimension of 0.25 m, while steel plates were meshed with elements with dimension of 0.10m. The resulting structural model for the nonlinear analysis summed 74,218 tetrahedral elements and 14,708 linear elements, as presented in Figure 127a, and was named 'model A1'. Boundary conditions were assumed as in the elastic model. The contact between steel plates and column, column and pile cap, pile cap and piles, and piles and steel plates were all modeled as *master-slave* fixed contacts.

Pile cap elements were modeled with a "*solid concrete*" material model (f_{cd} = 20 MPa, E_c = 26,070 MPa). Embedded rebars were modeled with a "1D reinforcement" material model (f_{yd} = 435 MPa, E_s = 210 GPa, ε_{su} = 10‰). Steel plates were modeled with a "*solid elastic*" material model (increased modulus of 10 x E_s = 2 100 GPa, to better distribute the applied forces). Column elements, in turn, were modeled with a "*reinforced concrete*" material model, which combined C30 concrete (f_{cd} = 20 MPa, f_{ct} = 1.33 MPa, E_c = 26,070 MPa, a_g = 20 mm, ε_{cp} = -1.54‰, f_{co} = -2.8 MPa, W_d = 5 mm) with smeared reinforcement at a ratio of 1% in the *x*- and *y*-directions; additionally, embedded rebars in the *z*-direction were modeled: 32 #20 for *C1* and *C2*, and 24 #10 for *C3*. This reinforcement amount was assumed to avert loss of convergence in the column elements throughout the loading process and thus focusing the nonlinear analysis on the pile cap element. Piles were modeled with a softened a "solid concrete" material model (f_{cd} = 20.0 MPa, E_c = 650 MPa), for the same purpose as discussed in the linear structural model.

Vertical loads were applied on top of the columns differently from the elastic model. They were applied as concentrated forces, so that they could be more easily monitored throughout the analysis. The nonlinear analysis was performed with the *arc-length* solution method, utilizing the *ICCG* solver for loads increasing up to failure. The behavior of the structural model was assessed with the aid of monitoring points: three at the top *C1, C2* and *C3* to read the applied loads, six at the bottom of the piles to read the reaction forces, and two on top piles *P1* and *P2* to read vertical displacements in the cap (*mnt.2* and *mnt.3*). The monitoring point to read the applied load to *C3*, specifically, was named *mnt.1* (see Figure 127c).

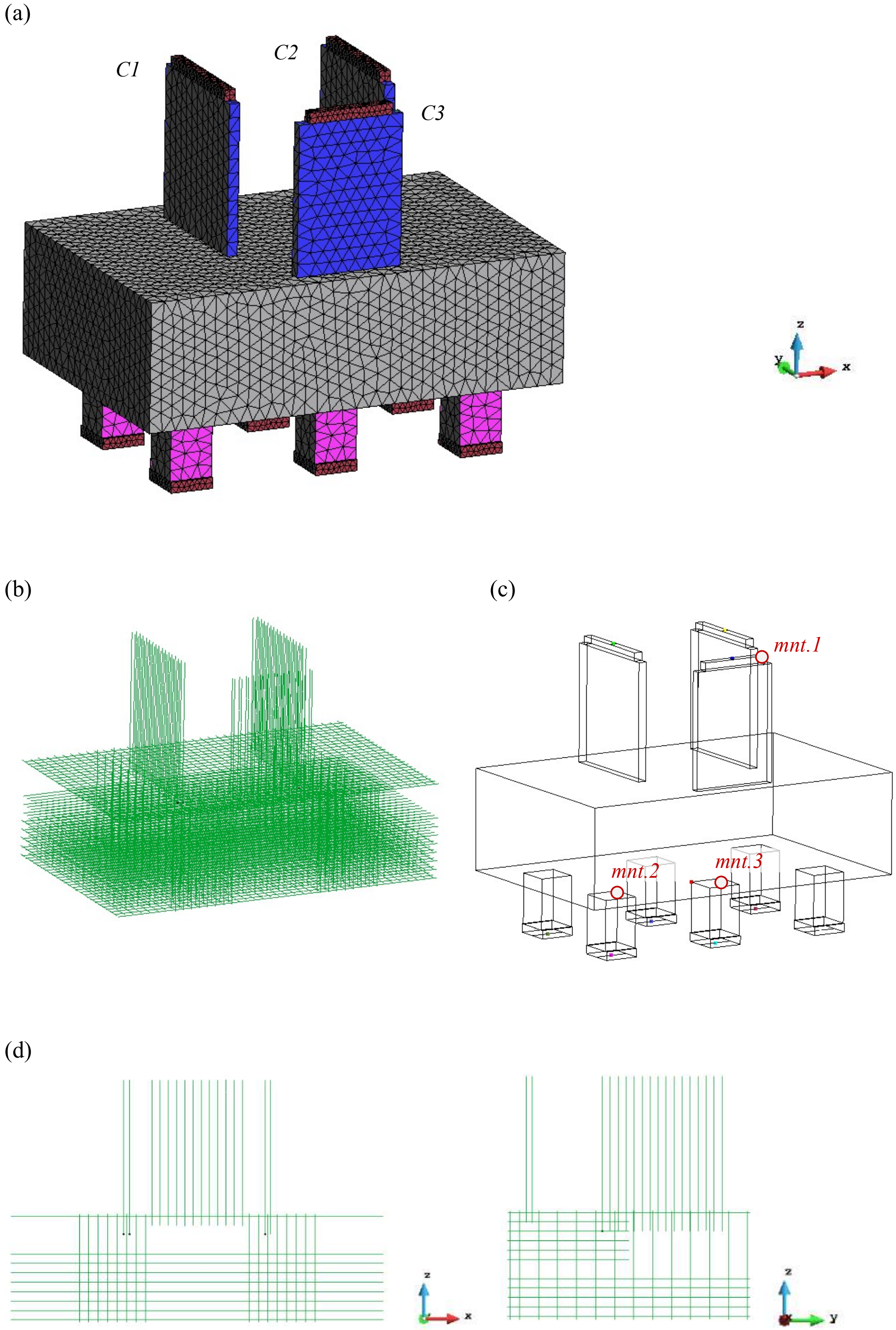

Figure 127 – Six-pile cap NLA structural model: (a) volume elements; (b) linear elements; (c) monitoring points *mnt.1* to *mnt.3*; (d) reinforcement side views.

6.5.2 Results: maximum simulation load

The pile cap was loaded up to 1.8 times the design load without failing. Clearly, analysis was performed focusing on the cap; to that aim, columns were reinforced to really high reinforcement ratios so that applied loads could be attained. In a real scenario, the structural member could have failed due to excessive column/pile compression, or disqualified for excessive cracking and deformation, or insufficient load bearing capacity of the soil. Selected results of the numerical analysis at failure load are shown in Figure 128 and Figure 129 and described as follows.

The maximum vertical total displacement was 2.11 cm. Several layers of reinforcement in the *x*-direction yielded (f_{yd} = 435 MPa); localized yielding of reinforcement in the *y*-direction was localized below the extremities of column C3; reinforcement in the z-direction was subjected to low stresses. The concrete maximum compressive stress was 13.6 MPa. Flexural cracks developed throughout the cap volume, along the full depth of the member; the maximum crack width was 0.49 mm. Plastic strains summed 0.33‰ in concrete, and 5.67‰ in the reinforcement in the last converged iteration.

6.5.3 Results: design load

Selected results at design load are shown in Figure 130 and described as follows.

The maximum vertical total displacement was 1.11 cm; stresses of the tensioned reinforcement reached 295 MPa. Concrete compressive stress reached 6.7 MPa. The maximum crack width was 0.26 mm.

6.5.4 Results: service load

Selected results at failure load are shown in Figure 131 and described as follows.

The maximum vertical total displacement was 0.70 cm; stresses of the tensioned reinforcement reached 111 MPa. Concrete compressive stress reached 4.2 MPa, and the maximum crack width was 0.04 mm.

(a)

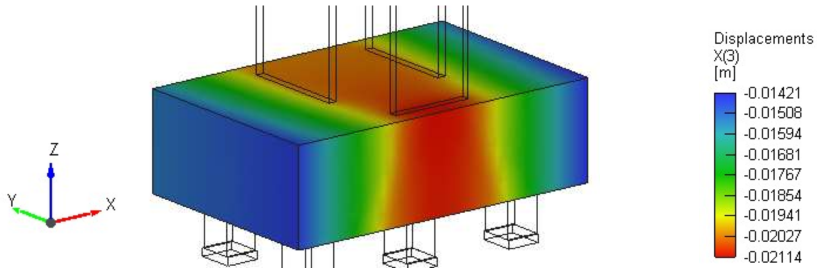

(b)

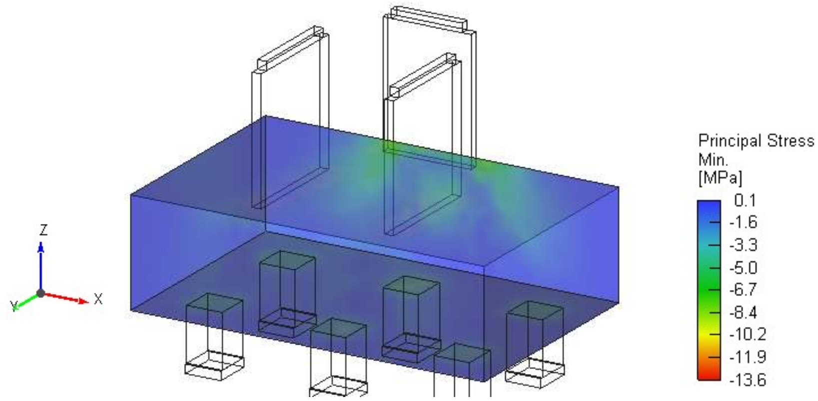

(c)

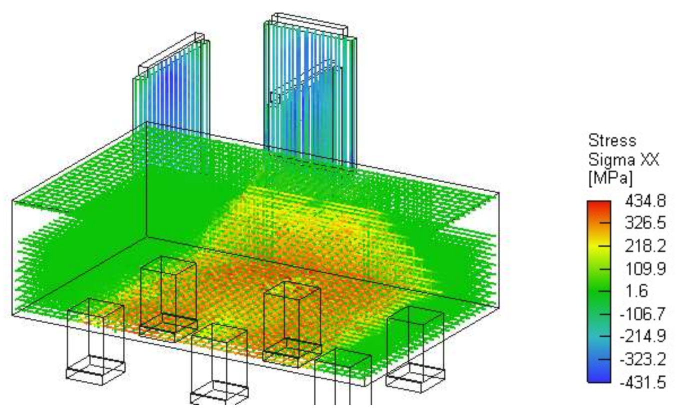

(d)

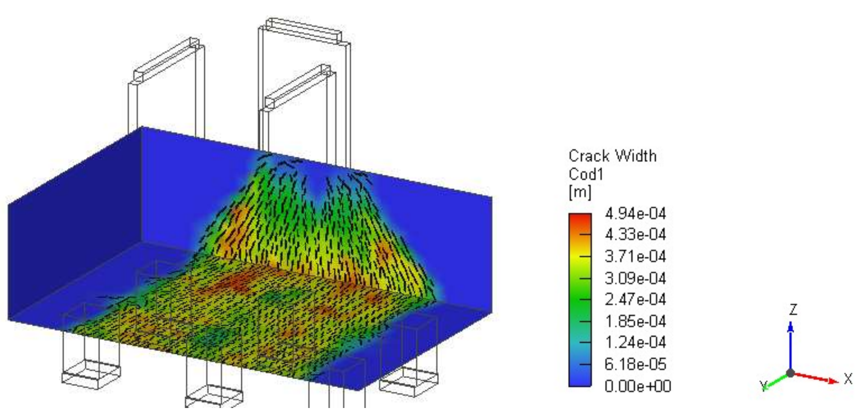

Figure 128 – Pile cap NLA results at *failure load*: (a) deflections in the *z*-direction; (b) concrete principal stress σ_{c3}; (c) reinforcement stresses; (d) crack widths.

(a)

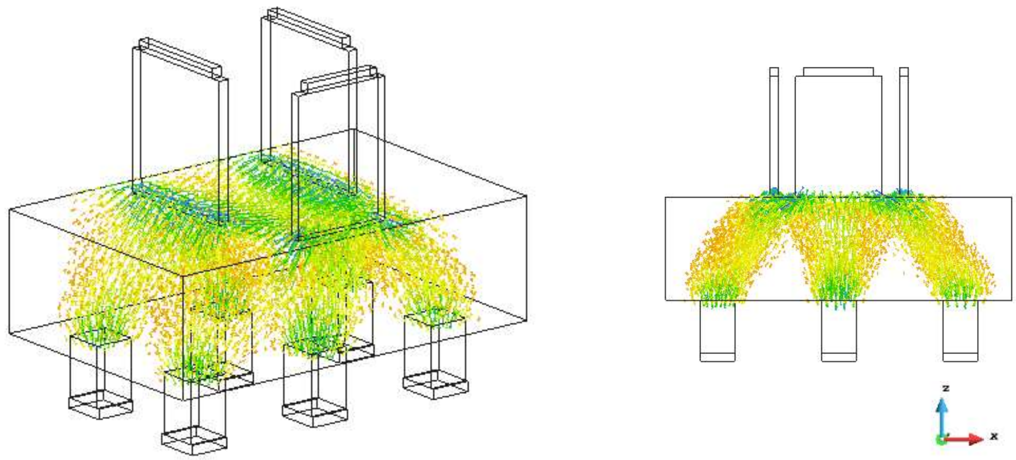

(b)

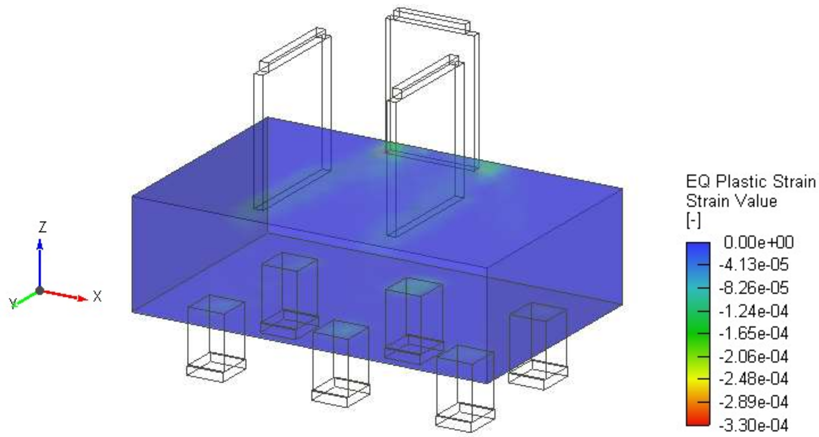

(c)

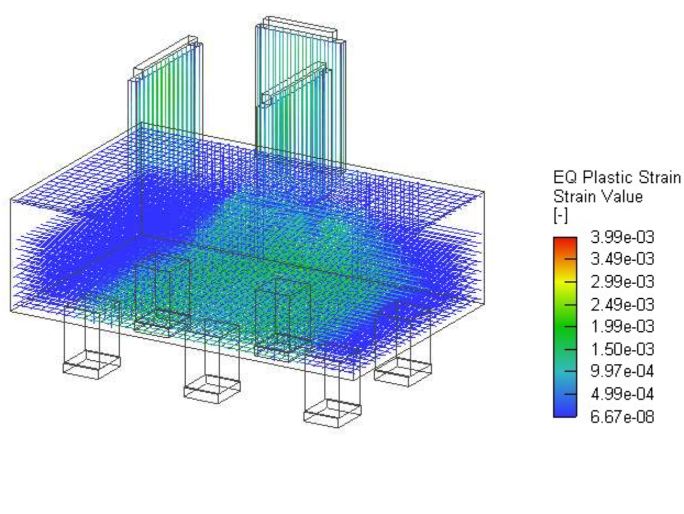

Figure 129 – Pile cap NLA results at failure load: (a) principal concrete stresses; (b) concrete plastic strains; (c) reinforcement plastic strains.

(a)

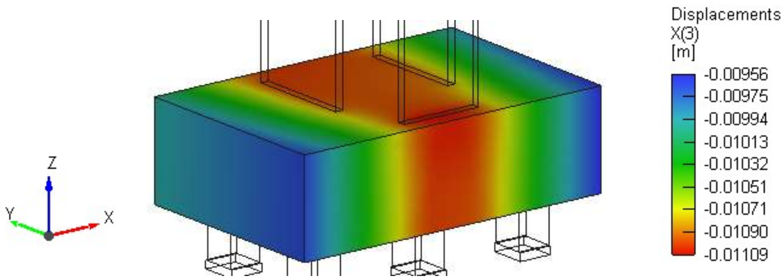

(b)

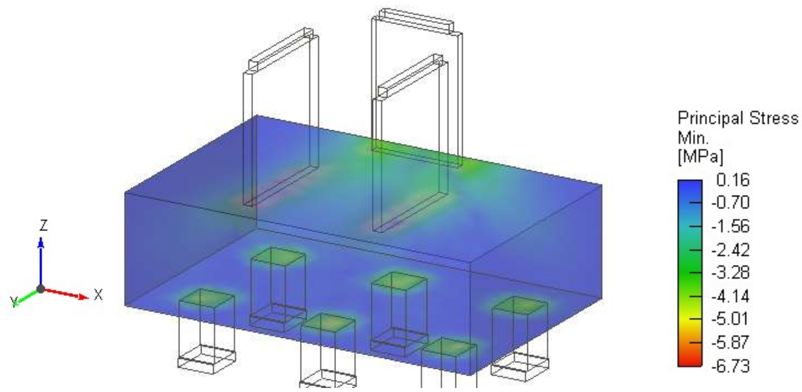

(c)

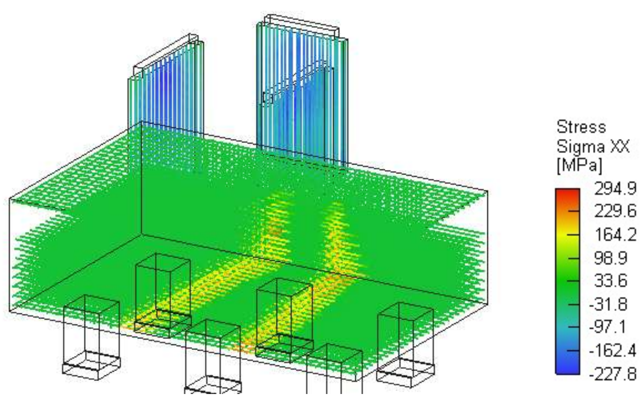

(d)

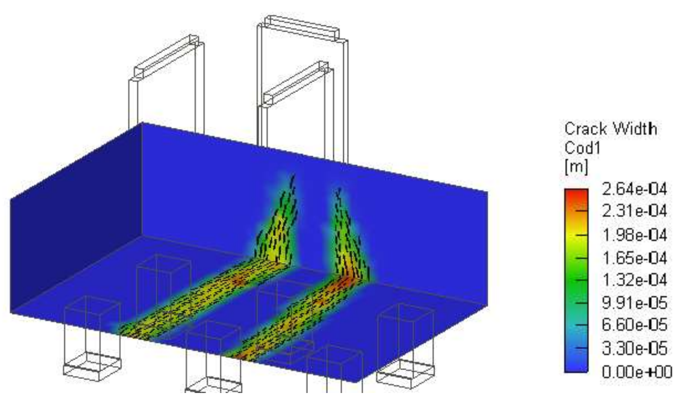

Figure 130 – Pile cap NLA results at *design load*: (a) deflections in the *z*-direction; (b) concrete principal stress σ_{c3}; (c) reinforcement stresses; (d) crack widths.

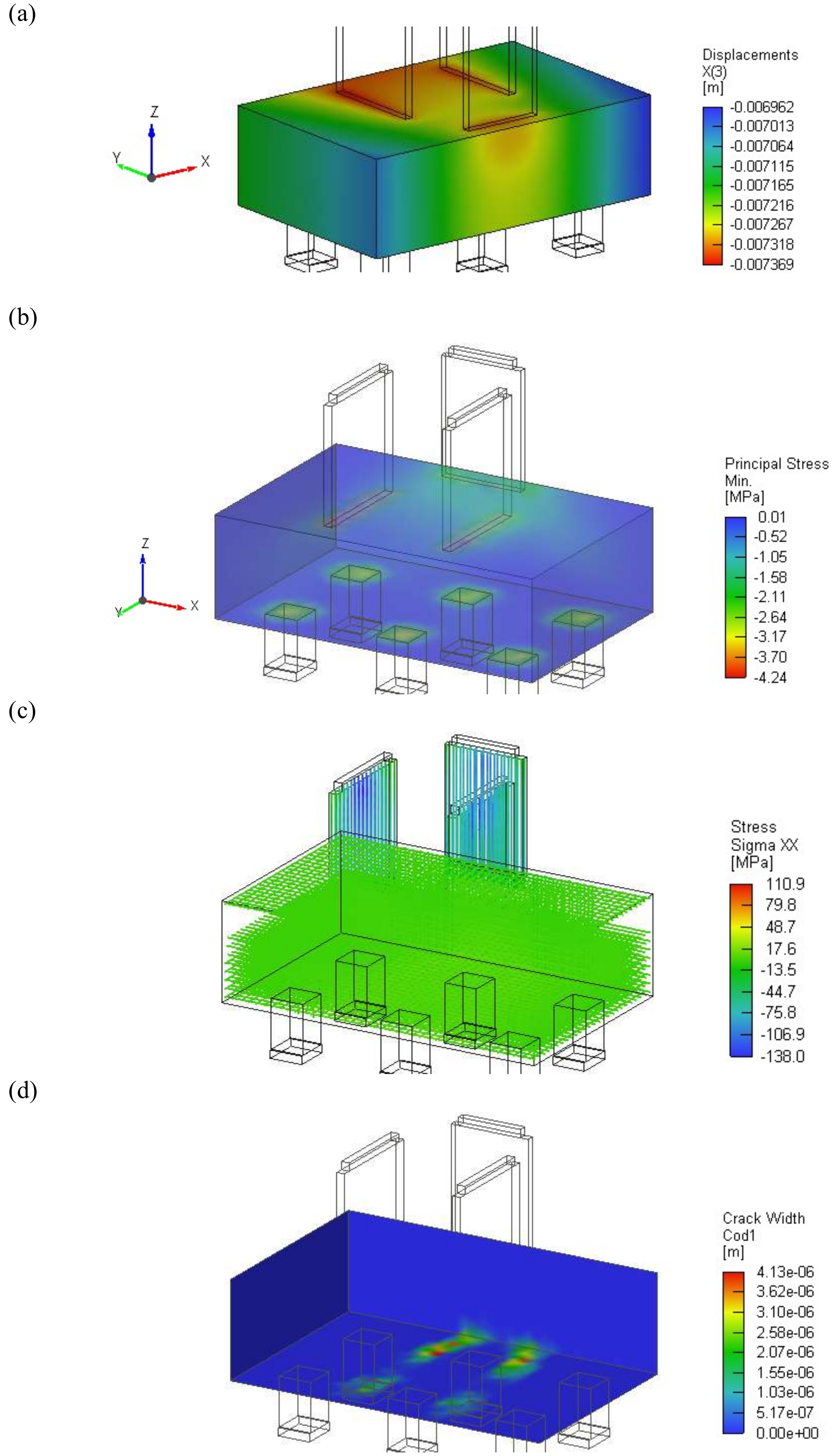

Figure 131 – Pile cap NLA results at *service load*: (a) deflections in the *z*-direction; (b) concrete principal stress σ_{c3}; (c) reinforcement stresses; (d) crack widths.

6.5.5 Alternative solution: structure designed by the STM

In order to quantitatively assess the solution obtained from the SFM, the pile cap was designed by the STM for *Load combination 1*. The resistant model, presented in Figure 132, was conceived as follows:

- At the bottom of the cap, ties were placed above the piles (blue lines), along with two diagonal struts (purple lines).
- At the top of the cap, compressive struts connected horizontally the nodes of *C1* and *C2* applied forces; two complementary diagonal struts (red lines) and two complementary ties were arranged to transfer the load from column *C3* to the rear face of the cap (blue lines).
- Finally, inclined struts connected the nodes at the top of the cap to the nodes corresponding to the supporting piles (light green lines), along with two complementary diagonal struts (purple lines).

Vertical restraint for the model was provided by spring supports with $k_v = 2{,}600/0.009 \approx 285{,}000$ kN/m for each pile. Forces at each bar resulting from the analysis are presented in Figure 133.

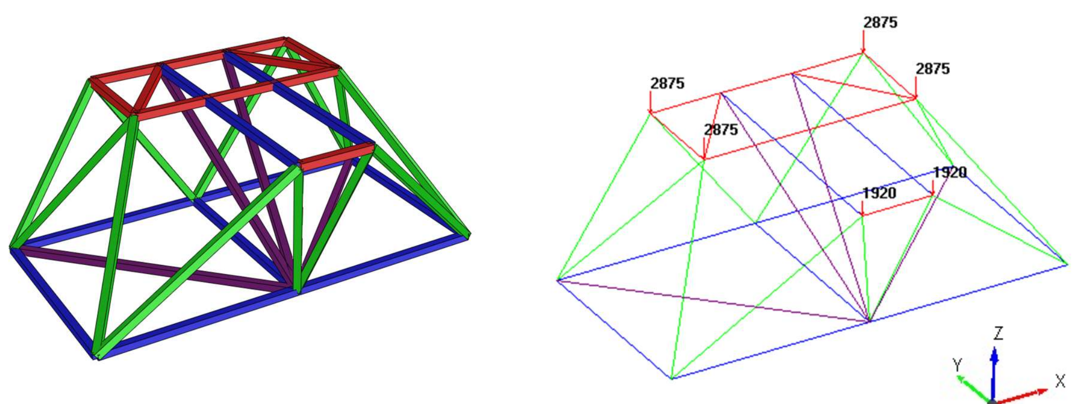

(a) (b)

Figure 132 – Six-pile cap designed by the STM: (a) perspective view; (b) loads.

Reinforcement was then calculated to resist the tie forces. At the bottom face of the pile cap, the main ties in the *x*-direction were detailed with 11ϕ25 each, whereas the main outer ties in the outer *y*-direction ties were detailed with 11ϕ20:

$$A_{sx,tie\_\inf} = \left(1{,}875 \times 1.4/43.48\right) x0.85 = 51.3\ cm^2 \quad \rightarrow 11\ \phi 25$$
$$A_{sy,tie\_\inf} = 1{,}113 \times 1.4/43.48 = 35.8\ cm^2 \quad \rightarrow 11\ \phi 20 \tag{6.35}$$

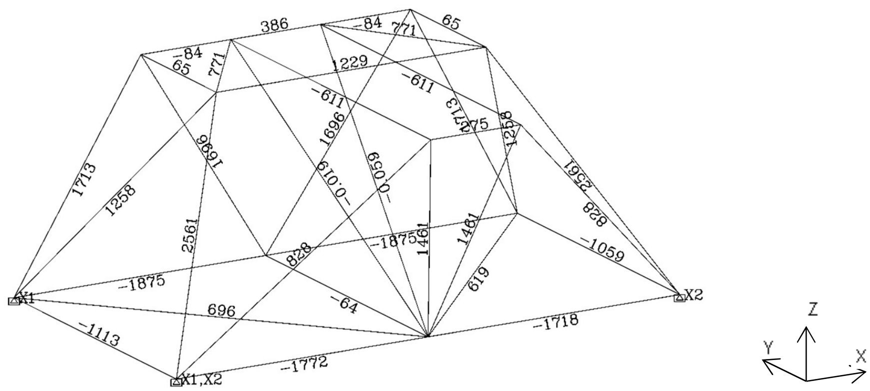

Figure 133 – Six-pile cap designed by the STM: forces (characteristic values).

Secondary rebars at the bottom of the pile cap were arranged as a uniformly distributed mesh for crack control. The ratio of 0.20% of the total tie cross-sectional area in the *x*-direction was considered:

$$A_{sx,\inf\_second} = 0.20 \times (22 \times 5.00) = 22.0\ cm^2 / 2.00\ m \quad \rightarrow \text{adopted}\ \ \phi 16/20$$
$$A_{sy,\inf\_second} = 0.20 \times (22 \times 3.15) = 13.9\ cm^2 / 4.80\ m \quad \rightarrow \text{adopted}\ \ \phi 16/20 \tag{6.36}$$

At the top face of the pile cap, the axial forces acting on the ties were resisted by 13ϕ20 in the *y*-direction; additional rebars in a ϕ12 /20 mm mesh completed the reinforcement distribution:

$$A_{sx,\sup} = 0.20 \times (26 \times 5.00) = 26.0\ cm^2 = 26/5.20 = 5.0\ cm^2/m \quad \rightarrow \phi 12/20$$
$$A_{sy,tie\_\sup} = (611 \times 2) \times 1.4/43.48 = 39.3\ cm^2 \quad \rightarrow 13\ \phi 20 \tag{6.37}$$
$$A_{sy,secondary} = A_{sx,\sup} \quad \rightarrow \phi 12/20$$

The reinforcement layout obtained from the STM design is presented in Figure 134. The proposed arrangement was quantified in terms of the sum of cross-sectional areas of rebars in each direction:

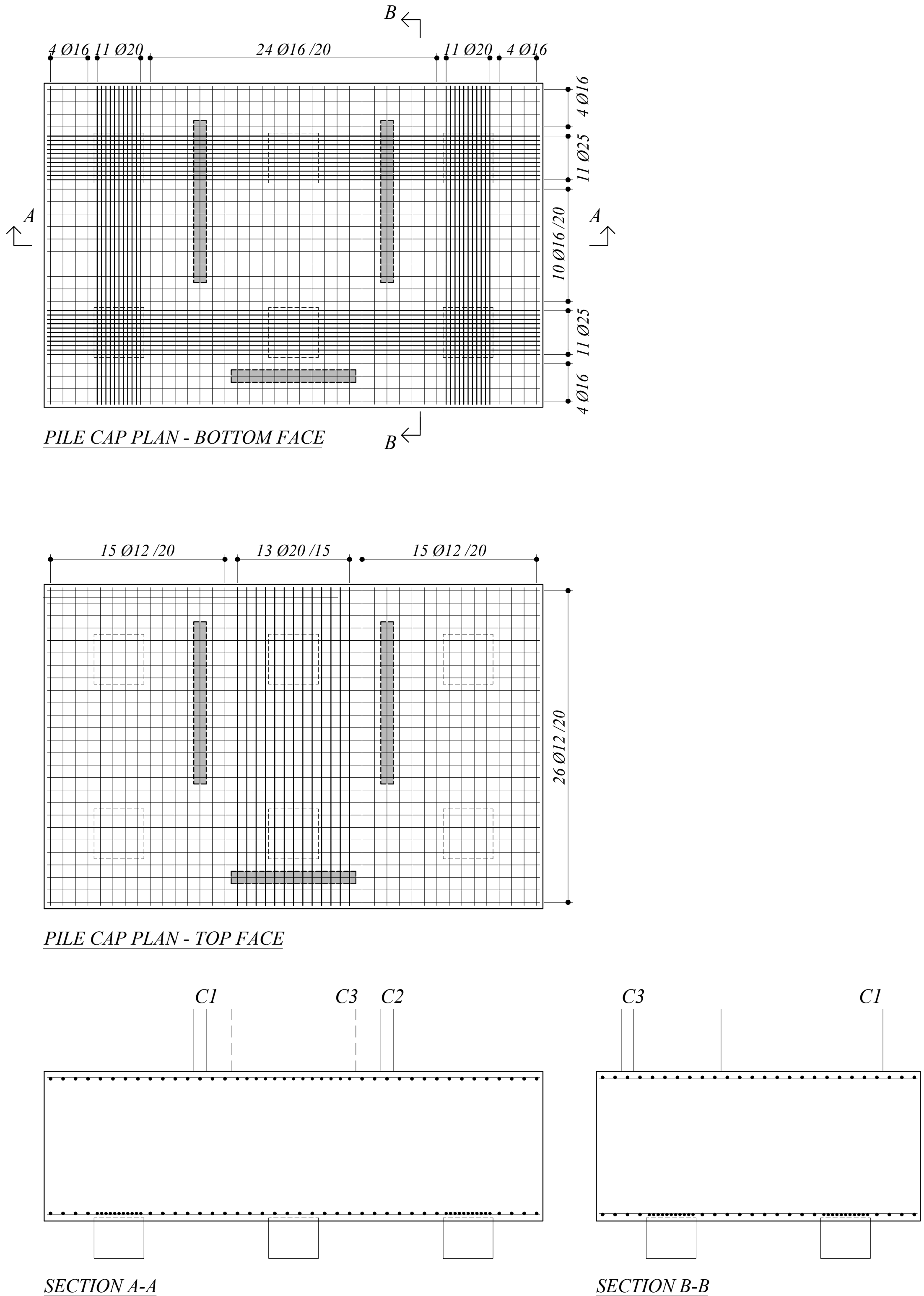

Figure 134 – Six-pile cap designed by the STM: reinforcement layout.

$$\begin{aligned}
A_{sx,\inf} &= 22 \times 5.00 + 18 \times 2.00 = 146.0\ cm^2 \\
A_{sy,\inf} &= 22 \times 3.15 + 32 \times 2.00 = 133.3\ cm^2 \\
A_{sx,\sup} &= 26 \times 1.13 = 29.4\ cm^2 \\
A_{sy,\sup} &= 30 \times 1.13 + 13 \times 3.15 = 74.9\ cm^2
\end{aligned} \tag{6.38}$$

Nonlinear analysis of the alternative solution

The STM solution was also assessed by a nonlinear analysis for comparison purposes. The elaborated model, 'model B1', was similar to the one elaborated to assess the SFM solution, but considered the rebar arrangement from Figure 134, which were modeled as presented in Figure 135.

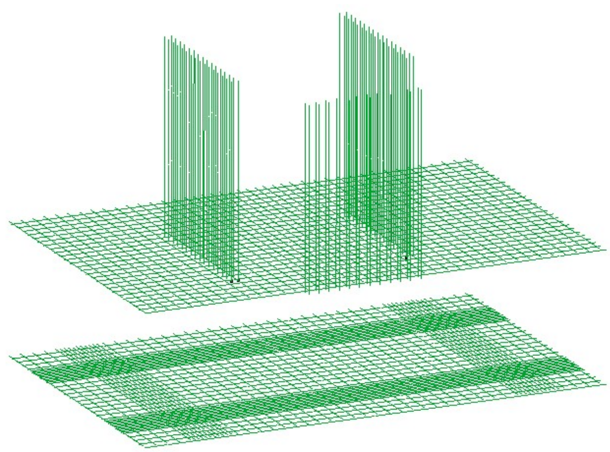

Figure 135 – Six-pile cap designed by the STM: nonlinear model – 1D elements.

Selected results at service load are shown in Figure 136 and described as follows: the maximum vertical displacement 0.74 cm; reinforcement stresses were considerably higher (334 MPa); and, surprisingly, the maximum crack width reached 0.49 mm, which does not respect the limit of 0.30 mm established in the MC2010 (*fib*, 2013) for the least aggressive exposure class.

(a)

(b)

(c)

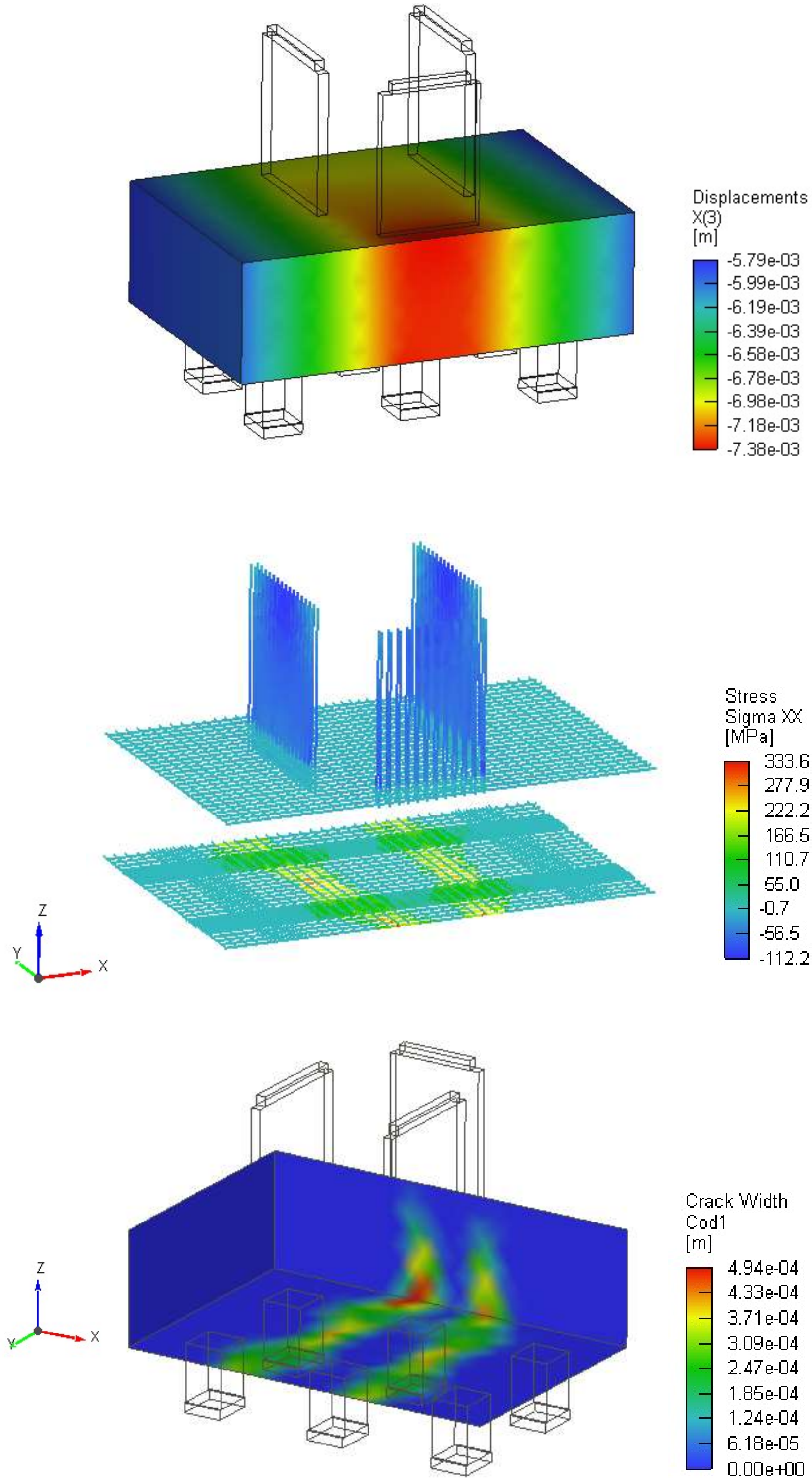

Figure 136 – Six-pile cap designed by the STM: NLA results at *service load* – (a) displacements in the *z*-direction; (b) reinforcement stresses; (c) crack widths.

6.5.6 Discussion

The behavior of the pile caps is visualized in the load-displacement curves of Figure 137, where the ordinate plots the applied load at the top of column *C1* measured by *mnt.1*, and the abscissa the relative vertical displacement (difference between measurements from *mnt.2* and *mnt.3*).

- **Model A1** was elaborated with the reinforcement designed by the SFM, and with a material model for concrete with its full tensile strength (f_{ctd} = 1.33 MPa). The numerical simulation was performed up to a load 80% higher than the design load. Yet, the failure of the pile cap was not reached, which confirmed the safety of the SFM by a large margin.
- **Model A2** was elaborated with the reinforcement designed by the SFM, and with a material model for concrete whereby its tensile strength was artificially reduced to 20% of the original strength ($f_{ctd,red}$ = 0.20 f_{ctd} = 0.27 MPa; $G_{f,red}$ = 0.20 G_f = 6.67e-06). The pile cap did not fail in the numerical simulation. Note: the value of 20 % was defined by trial-and-error - loss of convergence successively occurred in simulations with lower tensile strength due to localized effects of partially loaded regions.
- **Model B1** was elaborated with the reinforcement designed by the STM, and concrete with its full tensile strength (f_{ctd} = 1.33 MPa). In the numerical simulation, the pile cap failed at an ultimate load 68% higher than the design load. The STM, as the SFM, underestimated the capacity of the pile cap by not computing the concrete tensile strength.
- **Model B2** was elaborated with the reinforcement designed by the STM, and with a material model for concrete whereby its tensile strength was artificially reduced to 20% of the original strength ($f_{ctd,red}$ = 0.2 x f_{ctd} = 0.27 MPa; $G_{f,red}$ = 0.20 x G_f = 6.67e-06). The pile cap failed at an ultimate load 17% higher than the design load.

The load-displacement curves show a slightly stiffer response of the cap designed by the SFM. The increased strength of the cap designed by this method is attributed to the concrete tensile strength and to the reinforcement working in compression.

Reinforcement consumption

The total required reinforcement for the pile cap arranged by the SFM design was greater compared to the STM design:

$$\frac{A_{s,\inf,SFM}}{A_{s,\inf,STM}} = \frac{252.0+156.0}{146.0+133.3} = 1.46; \quad \frac{A_{s,\sup,SFM}}{A_{s,\sup,STM}} = \frac{14.7+99.4}{29.4+74.9} = 1.09 \tag{6.39}$$

Those increased values of +46% and +9% are considered justified by the increased performance brought by the SFM solution.

Bar spacing in the arrangement

Some discussion is proposed on the spacing of rebars in the SFM design. An initial macroscopic insight is obtained from Vincent et al. (2018, p. 555), who stated that "Provided that the spacing between two neighboring reinforcements is sufficiently small as compared with the size of the reinforced zone, the latter may be replaced by a zone where the homogenized constituent material obeys a macroscopic strength condition".

Further information is required, however, to delimit the area of influence of individual rebars. For combining pure tension and flexure, the FIP Recommendations (FIP, 1999, p. 95) establishes an effective concrete area *for crack control* extending 6ϕ from the axis of a rebar. Inside massive elements (outside the zone influenced by the concrete cover), that would result in an influence length of 12 ϕ (that means, for ϕ10/12/16/20/25 rebars, influence lengths of 12/14/19/24/30 cm, respectively). Evaluation of an effective concrete area *for ultimate limit state homogenized behavior*, however, is still missing. As an assumed guideline, however, spacing between layers was limited to 0.20 m, and spacing between bars within a horizontal grid and between vertical stirrups were limited to 0.40 m. The numerical analyses confirmed the adequacy of this procedure.

The arrangement of the bottom reinforcement in a *grid layout*, rather than concentrated above the pile lines in a *banded layout*, did not compromise the pile cap overall strength, as shown by the numerical simulation. This acknowledgement assent to an experimental test program conducted by Kim et al. (2023) for four-pile caps which indicated that "the ultimate strength of the footings were comparable when the bottom mat reinforcement was properly developed, regardless of the type of layouts and anchorage details" (KIM et al., 2023, p. 285) Surprisingly, the program concluded that "The grid layout provided the best performance based on considerations of strength, serviceability, and constructability" (KIM et al., 2023, p.299).

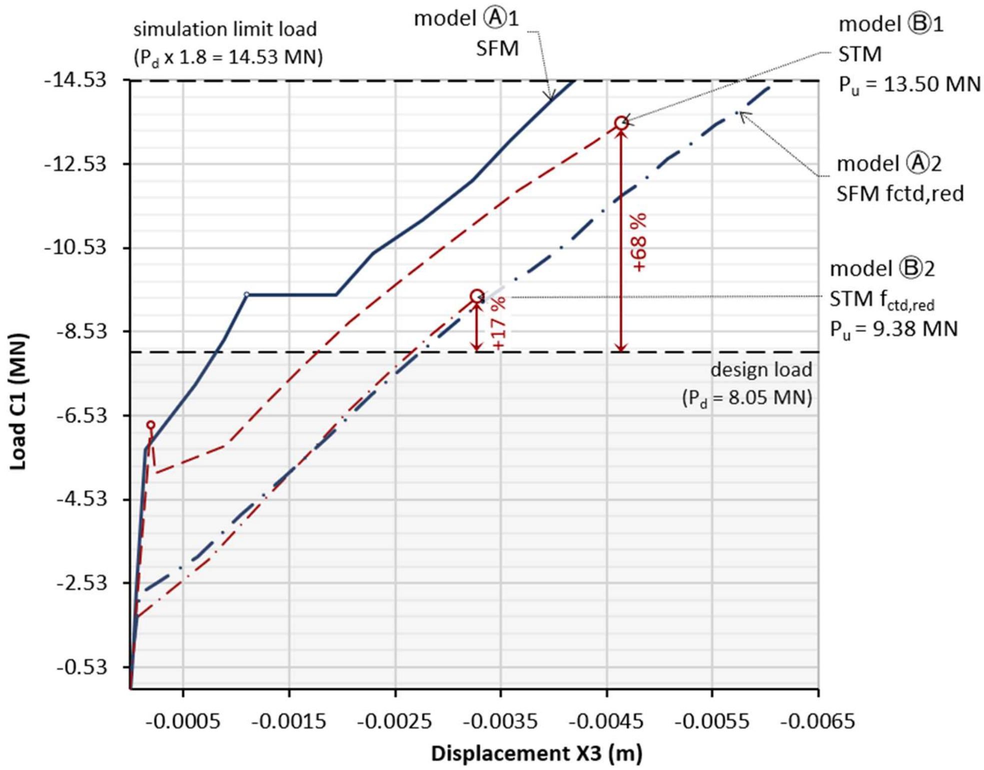

Figure 137 – Six-pile cap NLA: load-displacement curves.

Remarks

The limited applicability of the STM was already signalized by Schlaich, Schäfer, Jennewein reviewing their proposed design approach. They stated that "The resulting models are quite often kinematic which means that equilibrium in a given model is possible only for the specific load cases" (1987, p. 93).

The nonlinear analyses confirmed the safety of the SFM for the ULS design of the six-pile cap. The SFM design required more flexural and shear reinforcement but yielded a better performance in service conditions. It proposed a novel configuration for the arrangement of reinforcement inside the massive member, with reinforcement distributed uniformly in the horizontal planes and distributed in multiple layers over the cap depth. Reinforcement arrangements may yet be optimized to reduce the reinforcement consumption and the distance between failure and design loads.

6.6 Example 5: trunnion girder

6.6.1 Structural model for the nonlinear analysis

Concrete column and girder structure were meshed with elements with dimensions of 0.40 m, while steel plates were meshed with elements of 0.10 m, as presented in Figure 138. Each bar in the *x*-, *y*- and *z*-directions from the reinforcement layout presented in Section 5.6.4 was discretized as a linear element (see Figure 139). The complete structural model summed 170,796 tetrahedral elements and 12,080 linear elements, and was named 'model A1'. Boundary conditions were assumed as in the elastic model. The contact between anchor steel plates and girder, and between column and girder were modeled as *master-slave* fixed contacts.

Trunnion girder solid elements were modeled with a "solid concrete" material model (f_{cd} = 20 MPa, f_{ct} = 1.33 MPa, E_c = 26,070 MPa, a_g = 20 mm, ε_{cp} = -1.54‰, f_{co} = -2.8 MPa, W_d = 5 mm). Embedded rebars were modeled with a "1D reinforcement" material model (f_{yd} = 435 MPa, E_s = 210 GPa, ε_{su} = 10‰), while anchor and trunnion plates with a "solid elastic" material model (increased modulus of 10 x E_s = 2 100 GPa, to better distribute the applied forces). Column elements, on the other hand, were modeled with a "reinforced concrete" material model with smeared reinforcement at a ratio of 4% in the x, y-, and z-directions. This reinforcement amount did not derive from specific calculations, but was rather assumed to avert loss of convergence in the column elements throughout the loading process and, therefore, to focus the nonlinear analysis on the trunnion girder.

Trunnion forces were applied with the aid of a complementary resource of the nonlinear software: the definition of load stages composing a loading history. In the first stage, post-tensioning in both longitudinal and transverse directions were applied to the structure in 4 steps. In the second stage, the loads from the trunnion were applied sequentially in 4 steps until reaching the loads corresponding to Gate position #2; in the following stages, loads were applied to compose the sequence: Gate position #3 – Gate position #4 – back to Gate position #3 – back to Gate position #2 – back to Gate position #1 (for each of these 5 stages, 2 load steps were considered). Thereafter, the load was increased up to the maximum simulation load.

For nonlinear analysis of the trunnion girder, the loading history should meet predefined values of both post-tensioning and tainter gate applied forces, and should account for the girder dead load. Therefore, the arc-length method for solving the nonlinear equations was no longer applicable, and analysis was performed with the Newton-Raphson Method instead.

The behavior of the structural model was assessed with the aid of two monitoring points: the first one (*mnt.1*) was located under the FN_{sup} closer to the column (see Figure 73), to read the applied load in the x-direction; the second one (*mnt.2*) was located under the FN_{sup} more distant from the column, to read girder displacements in the x-direction.

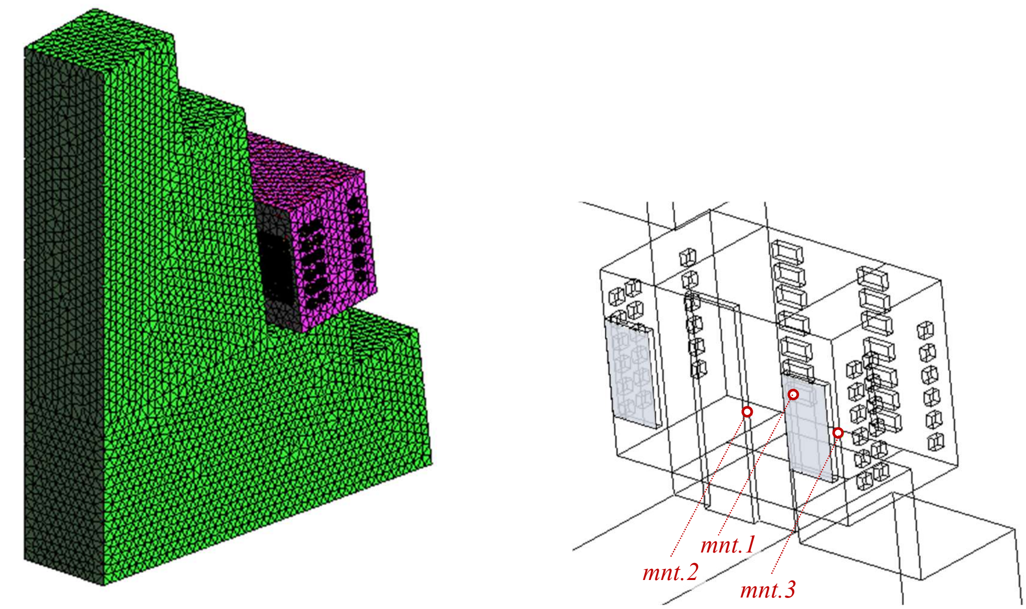

(a) (b)

Figure 138 – Trunnion girder NLA structural model: (a) volume elements; (b) trunnion girder and monitoring point; (c) linear elements.

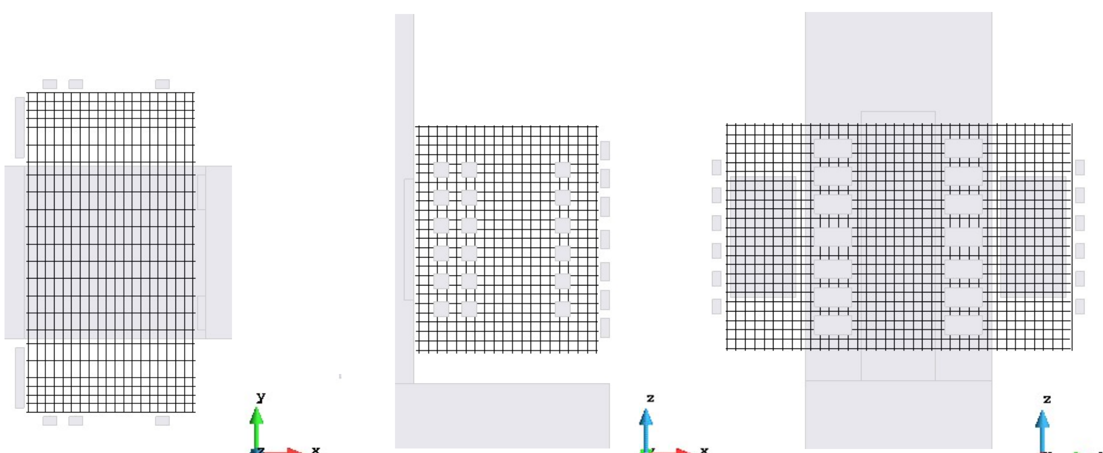

(a) (b) (c)

Figure 139 – Trunnion girder NLA: reinforcement - (a) *xy*-, (b) *xz*-; (c) *yz*-plane views.

6.6.2 Results: post-tensioning load

Selected results of the numerical analysis after application of the post-tensioning forces are shown in Figure 140 and described as follows: the maximum displacement in the *x*-direction was 0.17 cm. Vertical cracks were formed at the upstream vertical corners of the girder, with widths reaching 0.10 mm. Stresses at the girder-column contact surface were about 7.0 MPa. The main lines of the concrete principal stress tensor clearly indicate transmission of the post-tensioning force through the interface.

(a) (b)

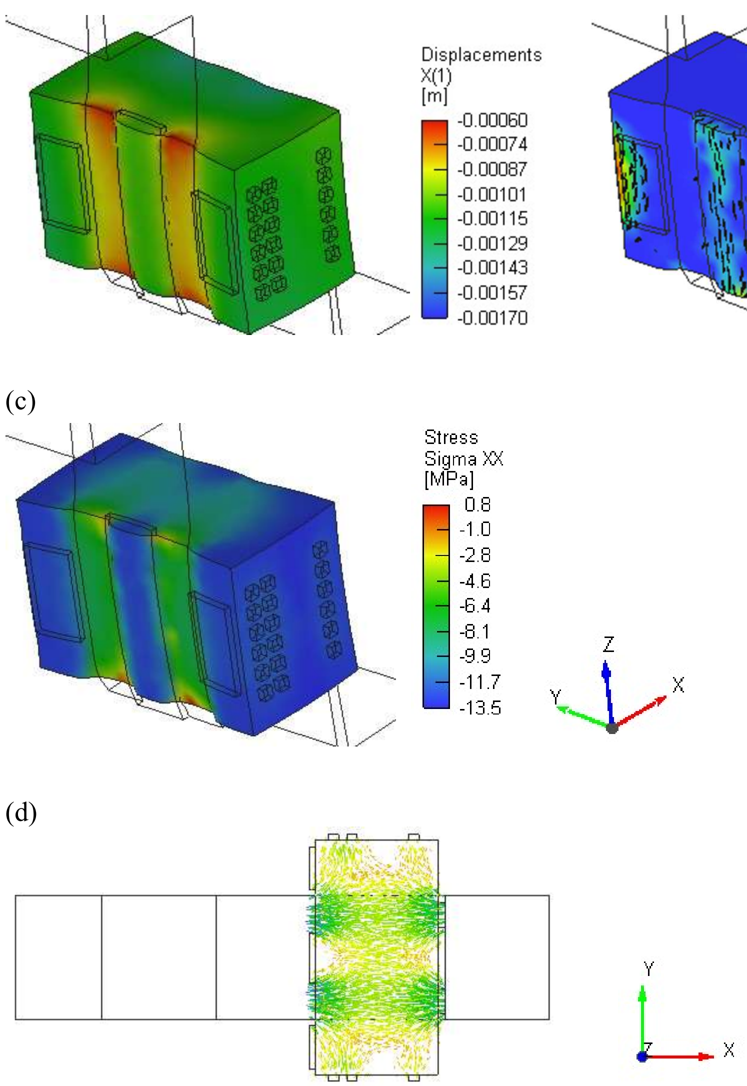

Figure 140 – Trunnion girder NLA results at *post-tensioning load*: (a) displacements; (b) crack widths; (c) normal stresses σ_x; (d) plan view concrete stress tensor.

6.6.3 Results: maximum simulation load

The girder was loaded up to 2.1 times the design load without failing. Selected results of the numerical analysis at the maximum simulation load are shown in Figure 142 and Figure 141 and described as follows.

The accumulated displacement in the x-direction under the trunnion steel plate was 0.06 cm. No reinforcement yielded; maximum reinforcement stress was 104 MPa. The concrete maximum compressive stress was 13.6 MPa. Vertical cracks developed throughout the girder volume, mainly behind the PT anchors and in the vicinities of the column-girder interface; the maximum crack width was 0.10 mm (only cracks in the first principal direction were presented for better visualization). Plastic strains summed 0.11‰ in concrete.

(a)

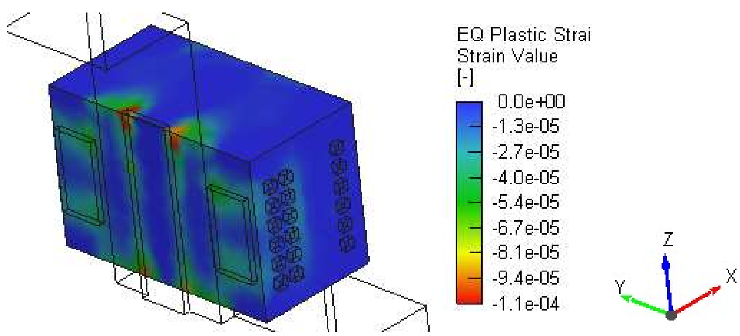

(b)

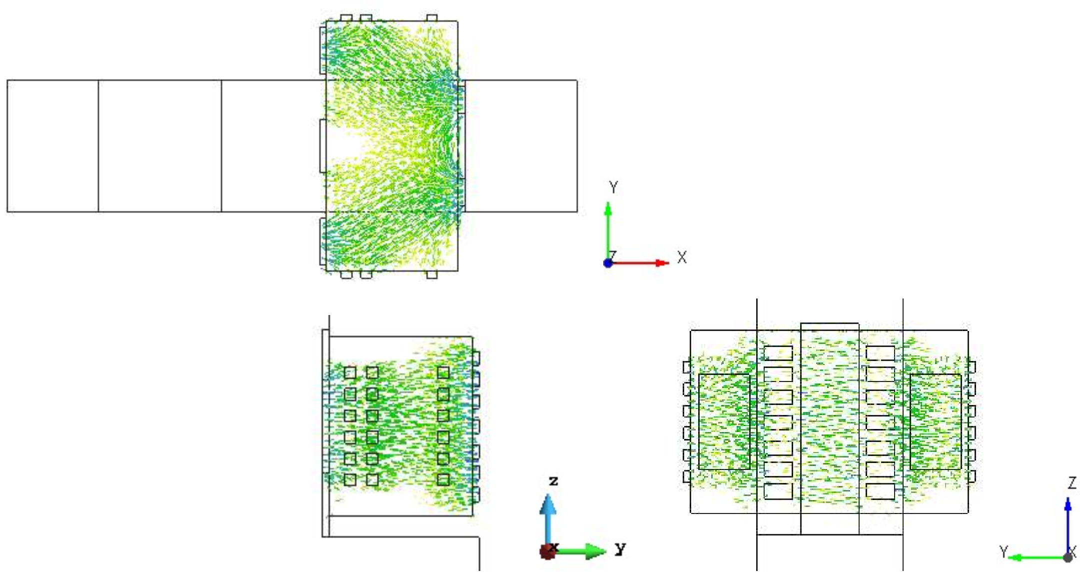

Figure 141 – Trunnion girder NLA results at the *maximum load of the simulation*: (a) concrete equivalent plastic strain; (b) principal stress tensor.

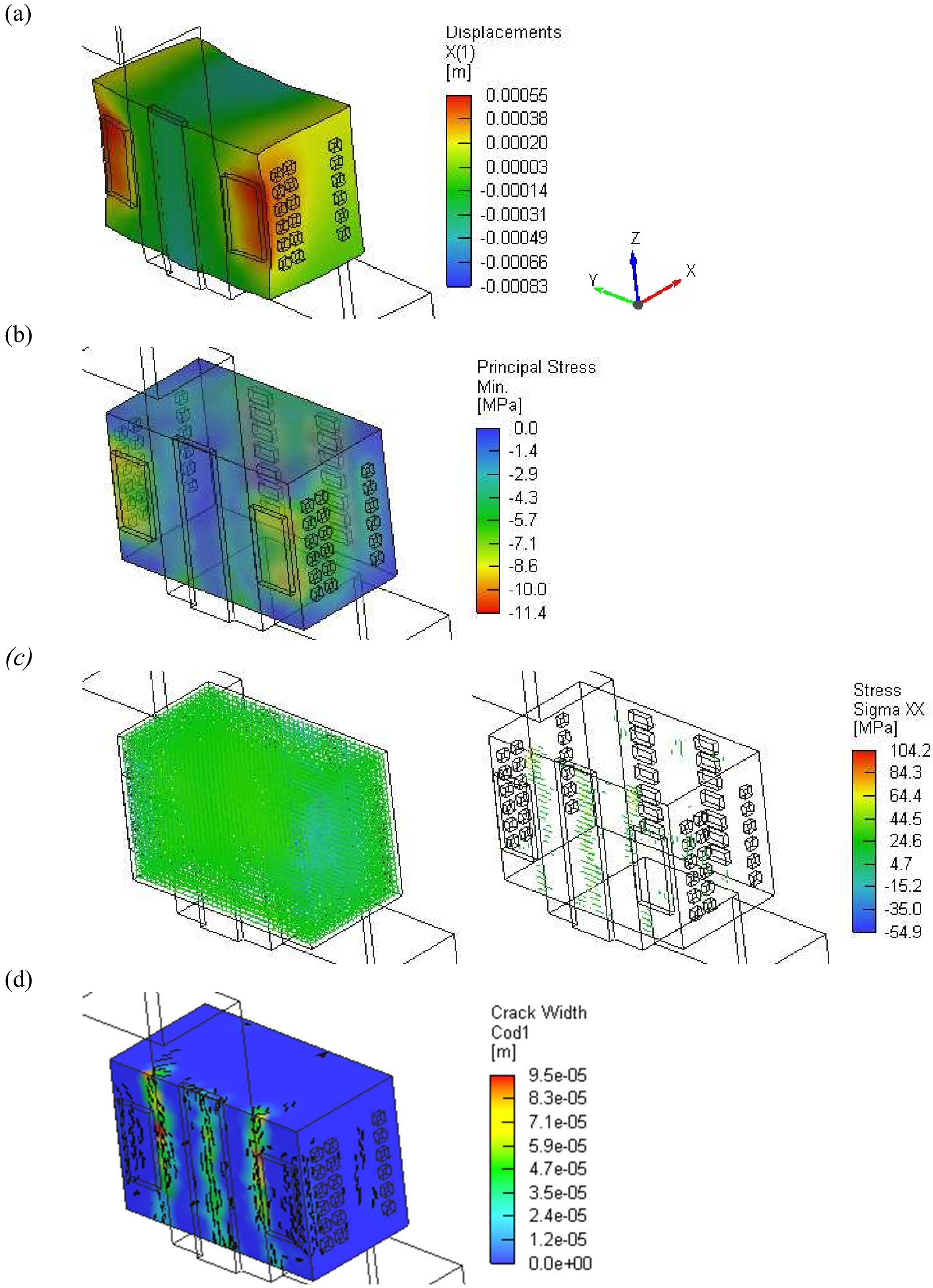

Figure 142 – Trunnion girder NLA results at the <u>*maximum load of the simulation*</u>: (a) displacements; (b) minimum principal stresses; (c) reinforcement stresses; (d) crack widths.

6.6.4 Results: design load

Selected results at design load are shown in Figure 143 and described as follows: the accumulated displacement in the *x*-direction under the trunnion steel plate was -0.03 cm; stresses in the reinforcement reached 115 MPa. Principal concrete compressive stress reached 10.4 MPa, and the maximum crack width was 0.05 mm.

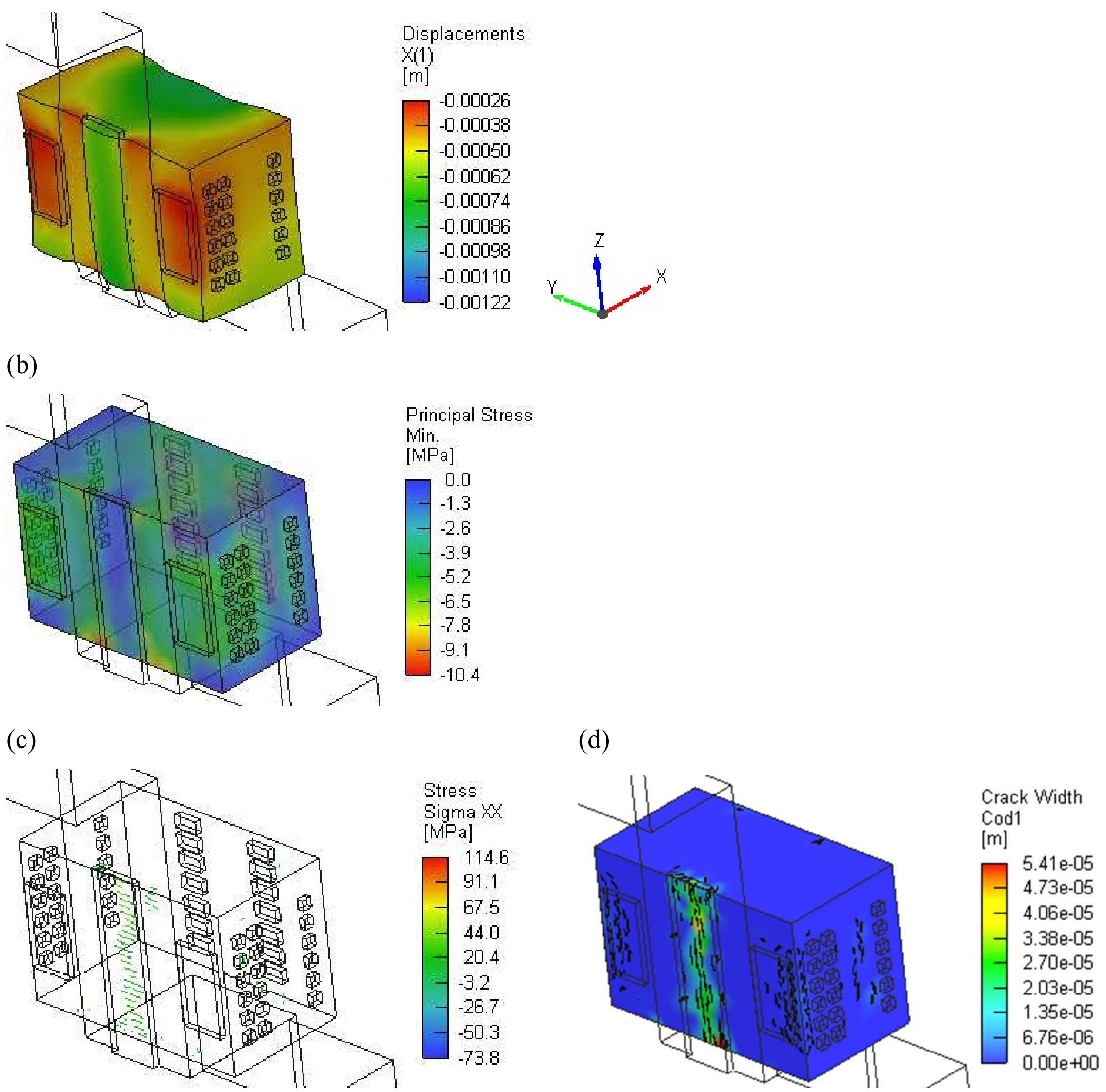

Figure 143 – Trunnion girder NLA results at *design load*: (a) displacements; (b) minimum principal stresses; (c) reinforcement stresses; (d) crack widths.

6.6.5 Results: service load

Selected results at service load are shown in Figure 144 and described as follows: the accumulated displacement in the *x*-direction under the trunnion steel plate was -0.04 cm; stresses in the reinforcement reached 123 MPa. Principal concrete compressive stress reached 10.4 MPa, and the maximum crack width was 0.05 mm.

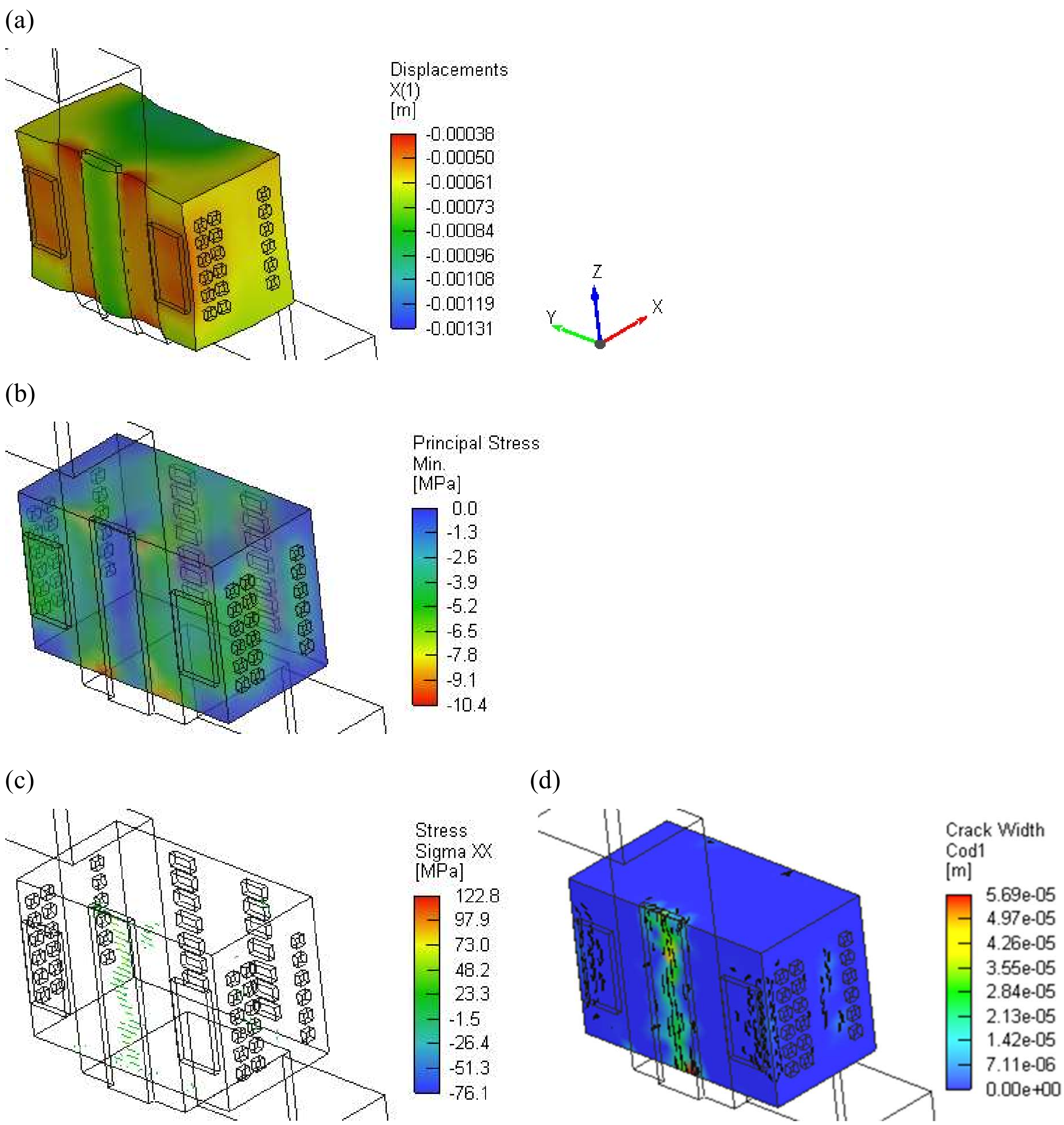

Figure 144 – Trunnion girder NLA results at *service load*: (a) displacements; (b) minimum principal stresses; (c) reinforcement stresses; (d) crack widths.

6.6.6 Discussion

The behavior of the girder is visualized in the load-displacement curves of Figure 145, where the ordinate plots the total applied force measured by *mnt.1*, and the abscissa the relative displacement in the x-direction (difference between measurements from *mnt.2* and *mnt.3*).

- **Model A1** was elaborated with the reinforcement designed by the SFM, and with a material model for concrete with its full tensile strength (f_{ctd} = 1.33 MPa). The numerical simulation was performed up to a load 110% higher than the design load. Yet, failure of the girder was not reached, which confirmed the safety of the SFM by a large margin. The increased strength of the girder is attributed to the concrete tensile strength and the reinforcement compressive strengths accounted for in the simulation.
- **Model A2** was elaborated with the reinforcement designed by the SFM, and with a material model for concrete where its tensile strength was artificially reduced to 1% of the original strength ($f_{ctd,red}$ = 0.01 f_{ctd} = 0.01 MPa; $G_{f,red}$ = 0.01 G_f = 3.33e-07). In the numerical simulation, the girder failed at a load 100% higher than the design load. Note: the value of 1%, much inferior to the 20% assumed in the pile cap analyses, could be assumed without causing convergence issues because reinforcement was distributed throughout the girder in the three orthogonal directions.

Discussion on the computational aspects for both the SFM design and the validation NLA are addressed as follows:

- The linear analysis of the model described in Section 5.6.1 was performed in 40 minutes (on a personal computer with i5 processor, 16 Gb of RAM, and 2.90 GHz clock speed).
- The computation of the reinforcement stresses by the application developed for this research was performed in additional 40 minutes.
- Each individual nonlinear analysis in ATENA took approximately 40 minutes (on a personal computer with i7 processor, 32 Gb of RAM, and 3.50 GHz clock speed). More than thirty analyses were performed to build an adequate model, in a trial-and-error process, especially when convergence matters occurred. Testing of parameters for the material models, solution methods, solvers, and load step sizes: all these activities required critical reasoning.

These numbers corroborate that the assessment of structures by NLFEA is still quite time-consuming and computationally expensive.

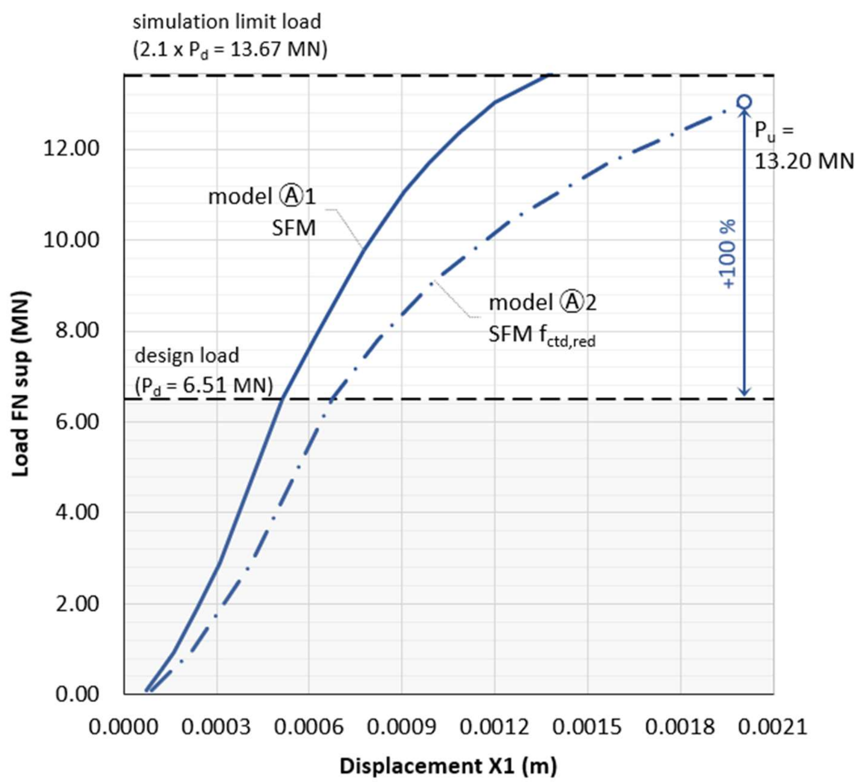

Figure 145 – Trunnion girder NLA: load-displacement curves.

Remarks

In complex and massive structures, with reinforcement distributed over the volume, forces are equilibrated in three dimensional schemes that are not directly visualized or simplified by strut-and-ties schemes. The SFM provided a lower bound safe solution for the ULS design of the trunnion girder. This fifth example demonstrated the feasibility of applying the SFM to provide an alternative design solution for structures with complex loading. More economical solutions would be obtained with more sectorized arrangements.

The SFM automatically provided the girder with resisting mechanisms to equilibrate tensile forces and bending moments, combined effects of shear and torsion, and tensile stresses originated by the effects of three-dimensional partially loaded blocks. The concrete tensile strength was adequately neglected for the ULS design, as explicitly recommended for flexural and axial strength calculations (ACI, 2014, Section 22.2.2.2) and in the calculation of reinforcement for anchorage zones for post-tensioned tendons (ACI, 2019, Section 25.9.4.4).

7 Summary and conclusions

7.1 Summary

The text from Sections 7.1.1 to 7.1.3 is reproduced from Chen, Nogueira Bittencourt and Della Bella (2023b).

7.1.1 Limit analysis (theory of plasticity)

The formulation presented for the concrete design started from a stress field satisfying the equilibrium conditions in the structure volume and its boundary, particularly obtained from a linear analysis. Moreover, the stresses in concrete and steel were limited by their yield conditions (or plastic values). These are the two conditions required by the lower bound theorem of the Theory of Plasticity to guarantee that, in this way, the structure collapse load is equal to or greater than the design load.

7.1.2 Limit analysis and structural concrete

Limit analysis assumes that materials have a rigid-perfectly plastic behavior. Its application to reinforced concrete, which is not straightforward since concrete and reinforcement steel are materials of limited ductility, was carefully reviewed by several researchers. Limit analysis may be applied to reinforced concrete if there is "sufficient deformation capacity to develop the plastic stress redistribution required in the element." Specific provisions for evaluating and quantifying the plastic redistribution are currently restricted to parameter δ measuring the change in the direction of the compression of the concrete, as proposed by Marti et al. (2002). Further research is required, however, to validate the proposed limit of 15 degrees, and to conceivably introduce complementary plastic parameters.

7.1.3 Proposed framework of the design equations

The design equations were initially deduced analytically for crack directions in each octant. It was shown that, by means of an artifice relative to the shear stress components, the equations for a crack direction in the first octant can be alternatively used, simplifying the application in design practice to a great extent. There was no need to resort to axis transformations, or to deal with design formulas with absolute value combinations for the shear stress components in the reinforcement computation. The proposed formulas were accompanied by the physical interpretation of the contribution of each term of the applied stress tensor, discerning shear stress components increasing or alleviating the reinforcement stresses. Furthermore, limits of design equation were clearly defined in terms of the required reinforcement and concrete stress invariants.

7.1.4 Design of structural members

The SFM was applied to the design of five selected structural members. For each example important features of the design were investigated:

- Example 1 showed all the steps completing the design of a structural member and allowed for discussing anchorage of reinforcement during the detailing process. It also showed that the method does not yield the most economical design for linear members in B-regions. For those elements, sectional plastic design methods remain more suitable.
- Example 2 showed that the SFM provided a competitive solution when applied to the design of a simple D-region. Singularities inherent to the numerical model were adequately maneuvered by averaging required reinforcement between neighboring elements.
- Example 3 showed that by assuming uncracked axial stiffness in the structural analysis safe results were obtained. The three beams underwent plastic deformations capable enough to mobilize the design forces.
- Example 4 showed that the SFM handled complex loads and geometries with ease and efficiency by naturally accounting for the flow of forces three-dimensionally. It also showed the feasibility of provisioning reinforcement in grid and/or multiple layered layouts.
- Example 5 showed, once more, that the SFM handled complex loads easily, and that it required considerably less computational effort compared to full nonlinear analyses.

Detailing into constructive arrangements

From the experience acquired from the design of the five worked examples, a detailing procedure is proposed for detailing of massive structural members: (i) identify regions with maximum reinforcement stresses and assure that a corresponding arrangement can be detailed; (ii) identify regions with zero reinforcement stress; (iii) establish a minimum arrangement and identify the regions covered by it; (iv) allocate supplementary rebars locally or define new arrangements covering the remaining regions; (v) check if code requirements of minimum reinforcement and detailing rules specific for the structural member being designed are fulfilled.

Concerning material consumption, solutions brought by the SFM indeed led to higher required reinforcement quantities. Lower-bound solutions might be too conservative.

Assessment by NLA

NLA of the structural members designed by the SFM assumed a fracture-plastic material model for concrete and an orthotropic smeared crack formulation. They were performed by the software *ATENA*. In all the cases, the maximum sustained load was higher than the design load. The reason for the increased strength of the member in the numerical simulation is attributed to the contribution of: (i) the concrete tensile strength; (ii) the reinforcement working in compression; and (iii) the assumed arrangements, which were calculated for peak values, but covered delimited zones where less reinforcement was required.

The nonlinear analyses showed that the structural members presented a good performance in serviceability conditions, whereby crack widths were controlled to meet prescribed normative limits.

7.2 Conclusions

"Equations for designing reinforcement based on three-dimensional stress fields have been deduced analytically and grouped into four main design cases according to the internal stresses equilibrating the applied stresses. Any applied stress state can be resisted by stresses in concrete and reinforcement distributed in up to three mutually orthogonal directions. A deep understanding of the physics of both applied and resisting stresses oriented the assemblage of a framework suited for implementation in design practice. The formulation for the Ultimate Limit State design presented herein is justified by the static method, based on the Lower Bound Theorem of the Limit Analysis of the Theory of Plasticity, and yields safe solutions" (CHEN; NOGUEIRA BITTENCOURT; DELLA BELLA, 2023a) provided that ductility requirements are met.

Further investigations are required to outline the limits of application of the method, since reinforced concrete is not a rigid plastic material, as idealized by the Lower Bound Theorem. These investigations should evaluate the plastic redistribution capacity of structural members, considering the necessary ductility of concrete and steel reinforcement to attain assumed stress plastic limits.

The SFM design was successfully applied to the design of structural members and the main relevant aspects of the detailing process were discussed, including singularities, anchorage of rebars, bar spacings, concrete assumed stiffnesses, load cases and load combinations, failure load, and structural performance in SLS. The *Partial Safety Factor* method was used in the analysis of the design examples, but the *Global Resistance Factor* safety format, which assumes the global resistance of a structure as a random variable and requires the input of mean properties of materials, could have been used as well (de BOER et al., 2014).

The *strengths* of the SFM may be outlined: (i) the method does not rely on the definition of strut-and-tie models; (ii) it predicates that all the structural regions participate in the resisting scheme, differently from the STM, where stress fields are developed in idealized linear elements; (iii) the method does not rely on the definition of complex material models and nonlinear analyses; (iv) it does not require the input of predetermined reinforcement arrangements for the calculations; (v) it can handle complex geometries and loadings efficiently; (vi) it is far less computationally demanding compared to the NLFEA.

The *weaknesses* of the method are also identified. First, it is remarked that the detailing process from the maps of required reinforcement turned out to be a handcrafted activity. Second, the application of the SFM demands that ductility requirements are met; the proposed limitation of δ_i to 15 degrees is still not clear and lacks experimental confirmation. Third, the effectiveness factor for the concrete compressive strength, which accounts for the limited ductility of the material, requires further assessment. Braestrup (2021, p. 2512) explicitly states "the effectiveness factor for a given type of structural element will have to be evaluated by comparing the predictions of plastic analysis with experimental evidence."

The SFM can be applied to a wide *range of reinforced concrete structures*. Although the Brazilian Code NBR-6118 (ABNT, 2023) does not recognize the method, there is background for its utilization in the Model Code 2010 (*fib*, 2013) for the general 3D case, and in Eurocode 2 (CEN, 2004) for the specific 2D case. The method is best applied to the design of complex structures or structural members subjected to complex loads and various load combinations. It could also be applied to the design of simpler structures, such as 1D linear members in B-regions, or 2D frame nodes in D-regions; for those elements, however, established and tested plastic solutions exist which yield more economical arrangements. It is noted that the method is not suited for members conceived to work without shear reinforcement, since the tensile strength of the concrete is totally disregarded in the formulation. Also, the method is not suited for the design of members relying on the resistance provided by aggregate interlock.

The SFM is a standalone method since, starting from a linear analysis, a full detailing is achieved. It can, however, be more efficiently used in conjunction with other design methods. For example, the STM may help with the visualization of rebar anchor regions in the SFM; or the SFM may help with the visualization of lines of reinforcement and thus orient the construction of three-dimensional STM models.

At this point, the original *research questions* posed in Section 1.3 can be answered: the existing method based on three-dimensional stress fields (the SFM) has been rarely used in practice due to difficulties in dealing with and interpreting the design equations. Design tools, up to the moment of the conclusion of this work, were not available to help engineers automate the design process. The SFM provides solutions that are safe and show good performance in SLS in terms of crack widths. The *gaps in the knowledge* identified in Section 1.3 were filled: (i) the use of design formulas was highly simplified with the proposed rules dealing with positive and negative signs of the shear stresses; (ii) the physical interpretation of the formulas was presented; (iii) the method was applied to the design of real structural members, and (iv) several detailing aspects were discussed in the worked examples.

This dissertation *originally contributes to knowledge* by further extending the existing design method combining linear analysis and limit design for reinforced concrete structures. First, by deducing and interpreting the design equations of the resisting mechanism in a novel and simpler approach, at a point level. Second, by applying them to design real structural members, from the initial stage of determining the applied stresses to the last stage of reinforcement detailing.

The SFM has the potential to change the way engineers design and detail complex D-regions. Designers need not (and should not) be restricted to a design based on sectional forces, or on the construction of intricate three-dimensional strut-and-tie models. Those who do not have access to expensive nonlinear finite element software may benefit from the method.

It may take a decade until commercial software implement the SFM formulation into their finite element packages, and even longer until they implement the powerful graphical resources such as those provided by *ParaView*. Meanwhile, engineers need to resort to tools similar to those utilized in this work (an application for the automatic point-to-point design, and a graphical post-processor) to take full advantage of the method.

This dissertation is expected to contribute to draw the attention of the engineering community to the, albeit underestimated, practical and powerful design method based on three-dimensional stress fields.

7.3 Recommendations for future work

Future work may be developed to further improve the SFM design.

Concerning the formulation of the resisting mechanism

- To extend the SFM formulation for reinforcement working in compression.
- To extend the SFM formulation for reinforcement arranged in directions other than the three mutually orthogonal directions coinciding with the coordinate axes: either in non-orthogonal directions, following an inclined face of a member, for example; or in a complementary diagonal direction following an arbitrary prevalent inclined principal direction.
- To further investigate the concrete effectiveness factor v.
- To further investigate the concrete plasticization criteria in the point-to-point design, in order to confirm the normative limitation of δ_i to 15 degrees.

Concerning detailing aspects

- To optimize reinforcement layouts from the reinforcement maps. Optimization algorithms could be developed to automatically delimit zones with uniform reinforcement minimizing the overall consumption, balancing constructive aspects.
- To establish rigorous criteria for plasticization in the solutions obtained by the SFM, which would allow for adopting more spaced rebars within a horizontal grid, or more spaced layers along the depth of a member.
- To establish criteria for minimum reinforcement in massive members.

Concerning serviceability conditions

- To implement SLS verifications in the automatic ULS routine.
- To estimate deflections from the elastic three-dimensional stress fields.

REFERENCES[1]

ABRA, O.M.B.; FTIMA, M.B. Development of a new design approach of reinforced concrete structures based on strength reduction method. **Engineering Structures**, v. 207, p. 110192, 2020. doi: 10.1016/j.engstruct.2020.110192.

ABRA, O.M.B.; FTIMA, M.B. Strength reduction design method for reinforced concrete structures: Generalization. **Engineering Structures**, v. 258, p. 114134, 2022. doi:10.1016/ j.engstruct.2022.114134.

AHRENS, J.; GEVECI, B.; LAW, C. **ParaView**: An end-user tool for large data visualization. In: Visualization Handbook. Elsevier, 2005.

AMERICAN CONCRETE INSTITUTE (ACI) Committee 318. **ACI 318-19**: building code requirements for structural concrete and commentary. Detroit: American Concrete Institute (ACI); 2019.

AMERICAN CONCRETE INSTITUTE (ACI) Committee 350. **ACI 350-06**: Code requirements for environmental engineering and concrete structures and commentary. 2006.

ANDRITZ. **Andritz News No. 36**. Vienna: Andritz Hydro GmbH; 2022. Available at: https://www.andritz.com/ hydro-en/hydronews/hn36/lauca-angola.

ASSOCIAÇÃO BRASILEIRA DE NORMAS TÉCNICAS. **ABNT NBR-6118**: Projeto de estruturas de concreto. Rio de Janeiro, Brazil: ABNT, 2023.

ATIR. **STRAP Structural Analysis Programs** – User´s Manual. Israel: ATIR Eng. Software Dev., Dec. 2005.

BALÁZS, G. et al. Design for SLS according to *fib* Model Code 2010. **Structural Concrete**, v. 14, n. 2, p. 99-123, 2013.

BASTESKÅR, M.; ENGEN, M.; KANSTAD, T.; FOSSÅ, K.T. A review of literature and code requirements for the crack width limitations for design of concrete structures in serviceability limit states. **Structural Concrete**, v. 20, n. 3, p. 678–688, 2019. doi:10.1002/ suco.201800183.

BASTESKÅR, M.; ENGEN, M.; KANSTAD, T.; JOHANSEN, H.; FOSSÅ, K.T. Serviceability limit state design of large concrete structures: Impact on reinforcement amounts and consequences of design code ambiguity. **Engineering Structures**, v. 201, p. 109816:1-10, 2019.

BAUMANN, T. Tragwirkung orthogonaler Bewehrungsnetze beliebiger Richtung in Flächentragwerken aus Stahlbeton. v. 217. Berlin (Deutschland): Deutscher Ausschuss für Stahlbeton, p. 1-53, 1972. (Heft / Deutscher Ausschuss für Stahlbeton).

[1] In ABNT style.

BAUMANN, T. Zur Frage der Netzbewehrung von Flächentragwerken. **Der Bauingenieur**, v. 47, n. 10, p. 367-377, 1972.

BAŽANT, Z.P.; OH, B.H. Crack band theory for fracture of concrete. **Materials and Structures**, v. 16, n. 94, p. 155-177, 1983. (RILEM)

BENES, S.; MIKOLÁŠKOVÁ, J.; ALTMAN, T. **ATENA Program Documentation**, Part 12, User's manual for ATENA Studio. Prague: Cervenka Consulting, 2015. 75 p.

BLOMFORS, M.; ENGEN, M.; PLOS, M. Evaluation of safety formats for non-linear finite element analyses of statically indeterminate concrete structures subjected to different load paths. **Structural Concrete**, v. 17, n. 1, p. 44-51, 2016. doi: 10.1002/suco.201500059

BRAESTRUP, M.W. Concrete plasticity – A historical perspective. **Structural Concrete**, v. 22, n. 12, p. 2508-2525, 2021. doi: 10.1002/suco.202100444

BRAESTRUP, M.W. **Concrete plasticity** – the Copenhagen shear group 1973-79. Bygningsstatiske Meddelelser, v. 65, n. 2,3,4, p. 33-87, 1994.

CEB-FIP. **Model Code 90.** CEB-FIP Bulletins No. 213/214. London: Thomas Telford Ltd., 1993. 460 p.

CEN (European Committee for Standardization). **Eurocode 2**: Design of concrete structures - Part 1-1: General rules and rules for Buildings (EN 1992-1-1:2004). Brussels, Belgium.

ČERVENKA, V.; ČERVENKA, J.; JANDA, Z.; PRYL, D. **ATENA Program Documentation**, Part 8: User's Manual for ATENA-GiD Interface. Prague, Czech Republic: Červenka Consulting, 2017. 139 p.

ČERVENKA, V.; JENDELE, L.; ČERVENKA, J. **ATENA Program Documentation**, Part 1: Theory. Prague, Czech Republic: Červenka Consulting, 2020. 340 p.

CHEN, R.; BITTENCOURT, T.N.; DELLA BELLA, J.C. Design of reinforced concrete structures from three-dimensional stress fields. **Revista IBRACON de Estruturas e Materiais**, v. 16, n. 4, e16407, 2023. doi: 10.1590/S1983-41952023000400007

CHEN, R.; NOGUEIRA BITTENCOURT, T.; DELLA BELLA, J.C. Design of reinforced concrete structures based on three-dimensional stress fields. **Structural Concrete**, v. 24, n. 5, p. 5963-5988, 2023. doi: 10.1002/suco.202300156

CHEN, W.-F.; DRUCKER, D. C. Bearing capacity of concrete blocks or rock. **Journal of the Engineering Mechanics Division**, v. 95, n. 4, p. 955-978, 1969.

COLAS, C.; PERLONGO, A.; NGUYEN, T.N.; BLEYER, J. Stress-based method for concrete solids' reinforcement design. In: TINCE 2023 - Technological Innovations in Nuclear Civil Engineering, 2023, Gif-sur-Yvette, France.

COLL, A. et al. **GiD v.14 Reference Manual**. Barcelona: International Center for Numerical Methods in Engineering (CIMNE), 2018.

COLLINS, M.P.; MITCHELL, D. Rational approach to shear design – The 1984 Canadian code provisions. **ACI Structural Journal**, v. 83, n. 6, p. 925-933, 1986.

COWAN, H.J. The strength of plain, reinforced and prestressed concrete under the action of combined stresses, with particular reference to the combined bending and torsion of rectangular sections. **Magazine of Concrete Research**, v. 5, n. 17, p. 75-86, 1953.

de BOER, A. **Design strategy structural concrete in 3D: focusing on uniform forces results and sequential analysis**. 2010. Dissertation (Doctorate) - Delft University of Technology, Delft.

de BOER, A. et al. Nonlinear FEA guideline for modelling of concrete infrastructure objects. In: BIĆANIĆ et al. (Eds.). **Computational Modelling of Concrete Structures**. London: Taylor & Francis Group, 2014. p. 977-986.

de BORST, R. **Non-linear analysis of frictional materials**. Dissertation (Doctorate) - Delft University of Technology, Delft, 1986.

DEBERNARDI, P.G.; TALIANO, M. An improvement of the Eurocode 2 and *fib* Model Code 2010 methods for the calculation of crack width in R. C. structures. **Structural Concrete**, v. 17, n. 3, p. 365-376, 2016. doi: 10.1002/suco.201500033.

DIANAFEA. Clinker silo. [online]. 2017. Available at: https://dianafea.com/book/export/html/140. Accessed: Feb 9, 2017.

DOLGIKH, A.P.; PODVYSOTSKII, A. Strength analysis of massive reinforced concrete structures using the method of equivalent shells. **Power Technology and Engineering**, v. 44, n. 5, p. 365-368, 2011.

DRUCKER, D.C.; PRAGER, W.; GREENBERG, H.J. Extended limit analysis theorems for continuous media. **Quarterly of Applied Mathematics**, v. 9, p. 381-389, 1952.

ENGEN, M. et al. Solution strategy for non-linear finite element analyses of large reinforced concrete structures. **Structural Concrete**, v. 16, n. 3, p. 389-397, 2015.

FIP (FÉDÉRATION INTERNATIONALE DU PRÉCONTRAINT). **FIP Recommendations** (1999): Practical design of structural concrete. FIP Commission 3 “Practical design”. London: SETO, 1996.

FERNÁNDEZ RUIZ, M.; MUTTONI, A. On development of suitable stress fields for structural concrete. **ACI Structural Journal**, v. 104, n. 4, p. 495-500, 2007.

fib. B**ulletin 45**: Practitioners’ guide to finite element modelling of reinforced concrete structures. Lausanne, Switzerland: *fib*, 2008. 344 p.

fib. **Bulletin 61**: Design examples for strut-and-tie models. Lausanne, Switzerland: *fib*, 2011. 220 p.

fib. **Bulletin 100**: Design and assessment with strut-and-tie models and stress fields: from simple calculations to detailed numerical analysis. Lausanne, Switzerland: *fib*, 2021. 235 p.

fib. **Model Code for concrete structures 2010**. Lausanne, Switzerland: Ernst & Sohn, 2013. 434 p.

FOSTER, S.J.; MARTI, P.; MOJSILOVIĆ, N. Design of reinforced concrete solids using stress analysis. **ACI Structural Journal**, v. 100, n. 6, p. 758-764, 2003.

GERSTLE, K.B. et al. Behavior of concrete under multiaxial stress states. **Journal of Engineering Mechanics Division**, v. 106, n. 6, p. 1383-1403, 1980.

GVOZDEV, A.A. Opredelenie velichiny razrushayushchei nagruzki dlya statischeski neopredelimykh sistem, preterpevayushchikh plasticheskie deformatsii. Svornik trudov konferentsii po plasticheskim deformatsiyam, Akademia Nauk SSSR, pp.19-30, Moscow-Leningrad (English translation: the determination of the value of the collapse load for statically indeterminate systems undergoing plastic deformation). **International Journal of Mechanical Sciences**, v. 1, p. 322-333, 1938.

HENDRIKS, M.A.N.; de BOER, A.; BELLETTI, B. et al. Guidelines for nonlinear finite element analysis of concrete structures. Rijkswaterstaat Centre for Infrastructure, Report RTD:1016-1:2016. Utrecht, Nederland, 2016. 66 p.

HOFFMANN, L.; KÄSEBERG, S.; HOLSCHEMACHER, K. Reinforcement detail: Stress trajectory-oriented corbel reinforcement. **Structural Concrete**, v. 24, n. 1, p. 1-11, 2023. doi: 10.1002/suco.202200920

HOOGENBOOM, P.C.J.; de BOER, A. Computation of optimal concrete reinforcement in three dimensions. In: BIĆANIĆ, N. et al. (Eds.). **Computational modelling of concrete structures**. London: Taylor & Francis Group, 2010. p. 639-646.

HOOGENBOOM, P.C.J. **Discrete elements and nonlinearity in design of structural concrete walls**. 1998. Dissertation (Doctorate) - Delft University of Technology, Delft.

HOOGENBOOM, P.C.J.; de BOER, A. Computation of reinforcement for solid concrete. **Heron**, v. 53, n. 4, p. 247-271, 2008.

HORDJIK, D.A. **Local approach to fatigue of concrete**. 1991. Dissertation (Doctorate) - Delft University of Technology, Delft.

INTERTECHNE. AH Lauca. Available at: https://www.intertechne.com.br/project/ah-lauca/. Accessed April 13, 2024.

JOHANSEN, K.W. Brudbetingelser for sten og beton (Failure criteria for rock and concrete). **Bygningsstatiske Meddelelser**, v. 29, n. 2, p. 25–44, 1958.

Momentos do Presidente da República em Malanje. **Jornal de Angola**. 2023. Available at: https://www.jornaldeangola.ao/ao/noticias/momentos-do-presidente-da-republica-em-malanje/. Published May 13, 2023. Accessed April 13, 2024.

KAMEZAWA, Y.; HAYASHI, N.; IWASAKI, I.; TADA, M. A study on design methods of RC structures based on FEM analysis. Proceedings of the Japan Society of Civil Engineers, v. 25, n. 502, p. 103-122, 1994. (in Japanese)

KAUFMANN, W. **Strength and deformations of structural concrete subjected to in-plane shear and normal forces**. 1998. Dissertation (Doctorate) - Institute of Structural Engineering, Swiss Federal Institute of Technology, Zurich.

KAUFMANN, W.; MATA-FALCÓN, J. Structural concrete design in the 21st century: are limit analysis methods obsolete? In: 24th Czech concrete days, Litomyšl. 2017.

KIM, H. et al. Effects of reinforcement details on behavior of drilled shaft footings. **ACI Structural Journal**, v. 120, n. 1, p. 285-302, 2023.

KLEISSL, K. C.; RAVN, U. G. Crack width verification of large disturbed regions in practice. Nordic mini seminar: Crack width calculation methods for large concrete structures. Oslo, 2017.

KOTSOVOS, M.D.; SPILIOPOULOS, K.V. Evaluation of structural-concrete design-concepts based on finite-element analysis. **Computers & Mechanics**, v. 21, p. 330-338, 1998.

KUPFER, H.; HILSDORF, H.K.; RUSCH, H. Behaviour of concrete under biaxial stresses. **Journal of the American Concrete Institute**. Proceedings, v. 66, n. 8, p. 656-666, 1969.

LARSEN, K. P. **Numerical limit analysis of reinforced concrete structures**: computational modeling with finite elements for lower bound limit analysis of reinforced concrete structures. 2010. Dissertation (Doctorate) - Technical University of Denmark, Kongens Lyngby.

Life application Bible: New International Version. Wheaton: Tyndale House Publishers, Inc., 2011.

LISICHKIN, S.E. Safety enhancement in large hydraulic structures from new spatial reinforcement methods. **Hydrotechnical Construction**, v. 35, n. 3, p. 116-123, 2001.

LOURENÇO, M.S., ALMEIDA, J.F. Adaptive stress field models: formulation and validation. **ACI Structural Journal**, v. 110, n. 1, p. 71-81, 2013.

LOURENÇO, M.S. et al. Design and assessment of concrete structures with strut-and-tie models and stress fields: From simple calculations to detailed numerical analysis. **Structural Concrete**, v. 24, n. 3, p. 3760-3778, 2023.

MARTI, P. Zur plastischen Berechnung von Stahlbeton. Eidgenössisches Technische Hochschule, Institut für Baustatik und Konstruktion. Ther Ber. No. 104, 1980.

MARTI, P., ALVAREZ, M., KAUFMANN, W., SIGRIST, V. Tension Chord Model for Structural Concrete. **Structural Engineering International**, v. 8, n. 4, p. 287-298, 1998. doi: 10.2749/101686698780488875.

MARTI, P., MOJSILOVIĆ, N., FOSTER, S.J. Dimensioning of orthogonally reinforced concrete solids. In: **Structural concrete in Switzerland**, *fib*-CH, *fib*-congress, Osaka, Japan, 2002.

MARTI, P., THÜRLIMANN, B. Fliessbedingungen für Stahlbeton mit Berücksichtigung der Betonzugfestifkeit. **Beton-Stahlbeton**, v. 72, n. 1, p. 7–12, 1977.

MÉLENDEZ, C., MIGUEL, P.F., PALLARÉS, L. A simplified approach for the ultimate limit state analysis of three-dimensional reinforced concrete elements. **Engineering Structures**, v. 123, p. 330-340, 2016. doi: 10.1016/j.engstruct.2016.05.039.

MENÉTREY, P., WILLAM, K.J. Triaxial failure criterion for concrete and its generalization. **ACI Structural Journal**, v. 92, n. 3, p. 311–318, 1995. doi:10.14359/1132.

MERGNY, E. et al. Stress analysis for the reinforcement of concrete massive structures, compatible with building methods. In Proceedings of the International Association for Shell and Spatial Structures (IASS): Symposium 2015, Future Visions, p. 17-20. Amsterdam, The Netherlands, 2015.

MEYBOOM, J. **Limit analysis of reinforced concrete slabs**. 2002. Dissertation (Doctorate) - Institute of Structural Engineering, Swiss Federal Institute of Technology, Zurich.

MONOTTI, M.N. **Reinforced concrete slabs** – Compatibility Limit Design. 2004. Dissertation (Doctorate) - Institute of Structural Engineering, Swiss Federal Institute of Technology, Zurich.

MÖRSCH, E. Der Eisenbetonbau – Seine Theorie und Anwendung, Verlag von Konrad Wittwer, Stuttgart, 3. Aufl. 1908, 4. Aufl. 1912, 5. Aufl. 1.Bd., 1. Hälfte, 1920, 2. Hälfte 1922.

MUTTONI, A., SCHWARTZ, J., THÜRLIMANN, B. **Design of concrete structures with stress fields**. Birkhäuser, 1996. 143 p.

NIELSEN, M.P. **Limit analysis and concrete plasticity**. NJ: Prentice-Hall, Inc., 1984.

NIELSEN, M.P.; BRAESTRUP, M.W.; JENSEN, B.C.; BACH, F. Concrete plasticity, beam shear, shear in joints, punching shear. Lyngby: Danish Society for Structural Science and Engineering, 1978. (Special Publication)

NIELSEN, M.P.; HOANG, L.C. **Limit analysis and concrete plasticity**. 3. ed. Boca Raton, FL: CRC Press, Taylor & Francis Group, 2011.

OTTOSEN, N.S. A failure criterion for concrete. **Journal of Engineering Mechanics**, v. 103, n. 4, p. 527-534, 1977.

PALOMO I.R.I et al. Prediction of the ultimate capacity of reinforced concrete elements using nonlinear analysis methodologies. **Rev IBRACON Estrut Mater**, v. 17, n. 2, p. 1-19, 2024. doi:10.1590/S1983-41952024000200010.

PAUL, B. A modification of the Coulomb-Mohr Theory of Fracture. **Journal of Applied Mechanics**, 1961, v. 28, p. 259-268.

REINECK, K.-H. (org.). **SP-208**, Strut-and-tie models. Farmington Hills, MI: American Concrete Institute, 2002. 250 p.

REINECK, K.-H.; NOVAK, L.C. (orgs.). **SP-273**, Further examples for the design of structural concrete with strut-and-tie models. Farmington Hills, MI: American Concrete Institute, 2010. 288 p.

ROSPARS, C.; CHAUVEL, D. CEOS.fr experimental programme and reference specimen tests results. **European Journal of Environmental and Civil Engineering**, v. 18, n. 7, p. 738-753, 2014. doi: 10.1080/19648189.2014.912163.

SAYIR, M.; ZIEGLER, H. Der Verträglichkeitssatz der Plastizitätstheorie und seine Anwendung auf räumlich unstetige Felder. **Journal of Applied Mathematics and Mechanics**, 1969, v. 20, p. 79-93.

SCHLAICH, J.; SCHÄFER, K. Towards a Consistent Design of Reinforced Concrete Structures. In: 12th Congress of IABSE. Vancouver, 1984.

SCHLAICH, J.; SCHÄFER, K.; JENNEWEIN, M. Toward a consistent design of structural concrete. **PCI Journal**, v. 32, n. 3, p. 74-150, 1987. doi: 10.15554/pcij.05011987.74.150.

SELBY, R.B.; VECCHIO, F.J. A constitutive model for analysis of reinforced concrete solids. **Canadian Journal of Civil Engineering**, v. 24, p. 460-470, 1997.

SMIRNOV, S.B. Problems of calculating the strength of massive concrete and reinforced concrete elements of complex hydraulic structures. **Power Technology and Engineering**, v. 17, n. 9, p. 471-476, 1983.

SU, R.K.L. et al. The provision of reinforcement in concrete solids using the generalized genetic algorithm. **Journal of Computing in Civil Engineering**, v. 25, n. 3, p. 211-217, 2010.

TAN, R.; HENDRIKS, M.; KANSTAD, T. Evaluation of current crack width calculation methods according to Eurocode 2 and *fib* Model Code 2010. In: Hordijk, D.; Luković, M. (orgs**.). High Tech Concrete**: Where Technology and Engineering Meet. Springer, Cham. 2018. p. 1610-18. doi: 10.1007/978-3-319-59471-2_185.

THÜRLIMANN, B. Plastic analysis of reinforced concrete beams. IABSE Colloquium, Copenhagen, 1979, **Plasticity in Reinforced Concrete**, Introductory Report, Zürich, Int. Assoc. Bridge Struct. Eng., Reports of the Working Commissions, v.28, p. 71-90, 1978.

U.S. ARMY CORPS OF ENGINEERS. **Engineer Manual EM 1110-2-2702** - Design of spillway tainter gates. 2000.

URBAN, T.; KRAWCZYK, Ł. Strengthening corbels using post-installed threaded rods. **Structural Concrete**, v. 18, n. 2, p. 303-315, 2017. doi: 10.1002/suco.201500215.

van der ESCH, A. et al. Categorization of formulas for calculation of crack width and spacing in reinforced concrete elements. **Structural Concrete**. 2023. doi: 10.1002/suco.202300535.

VECCHIO, Frank J.; COLLINS, MICHAEL P. The modified compression-field theory for reinforced concrete elements subjected to shear. **ACI Structural Journal**, v. 83, n. 2, p. 219-231, 1986.

VIDOSA, F.G.; KOTSOVOS, M.D.; PAVLOVIĆ, M.N. Nonlinear finite-element analysis of concrete structures: performance of a fully three-dimensional brittle model. **Computers & Structures**, v. 40, n. 5, p. 1287-306, 1991.

VINCENT et al. Ultimate limit state design of three-dimensional reinforced concrete structures: A numerical approach. Computational modelling of concrete structures. London: Taylor & Francis Group, 2018. p. 553-560.

W. COMMONS. [Internet]. Avaiable at: https://commons.wikimedia.org/wiki/File: Hydroelectric_dam_animation_esp.ogv. (accessed May 1, 2022).

ZALESOV, A.S.; RUBIN, O.D. Higher safety of massive hydraulic structures based on improved design norms. **Hydrotechnical Construction**, v. 28, n. 9, p. 554-558, 1994.

Appendices

APPENDIX A - Biaxial compression with reinforcement in three directions: crack direction in the 2nd to the 8th octants

For a crack direction in the ***second octant***, (ℓ_1,m_1,n_1) = (-0.577, 0.577, 0.577). The reinforcement equivalent stresses, from Equation (3.9), are:

$$\begin{cases} f_{tx} = \sigma_x - \tau_{xy} - \tau_{xz} \\ f_{ty} = \sigma_y - \tau_{xy} + \tau_{yz} \\ f_{tz} = \sigma_z - \tau_{xz} + \tau_{yz} \end{cases} \tag{A.1}$$

The invariants of the concrete stress tensor are:

$$\begin{aligned} I_{c2} &= 3\left(-\tau_{xy}\tau_{yz} + \tau_{xy}\tau_{xz} - \tau_{xz}\tau_{yz}\right) \\ I_{c1} &= 2\left(\tau_{xy} + \tau_{xz} - \tau_{yz}\right) \end{aligned} \tag{A.2}$$

The conditions $I_{c2} > 0$ and $I_{c1} < 0$ are simultaneously met for the following sign combinations: sgn(τ) = (-,-,+), (-,-,-), (-,+,+), or (+,-,+). The internal stresses developed in concrete and reinforcement are further analyzed:

- When τ_{xy}, $\tau_{xz} < 0$, and $\tau_{yz} > 0$, i.e., when sgn(τ) = (-,-,+) as indicated in Figure 146a, all shear stress components increase the tensile stresses in the reinforcement. The results of the 2nd trihedron can be obtained with the expressions of the 1st trihedron if we adopt positive values for all shear components.
- When sgn(τ) = (-,-,-), (-,+,+), or (+,-,+), the stress with the smallest absolute value τ_1 alleviates the tensile stresses in the corresponding reinforcement. Condition (3.24)a must be satisfied to guarantee that ($\sigma_{c1} = 0$, $\sigma_{c2} < 0$, $\sigma_{c3} < 0$). The results of the 2nd trihedron can be obtained with the expressions of the 1st trihedron admitting a negative value for τ_1, and positive values for τ_2, τ_3.

For a crack direction in the ***third octant***, (ℓ_1,m_1,n_1) = (-0.577, -0.577, 0.577). The reinforcement equivalent stresses, from Equation (3.9), are:

$$\begin{cases} f_{tx} = \sigma_x + \tau_{xy} - \tau_{xz} \\ f_{ty} = \sigma_y + \tau_{xy} - \tau_{yz} \\ f_{tz} = \sigma_z - \tau_{xz} - \tau_{yz} \end{cases} \tag{A.3}$$

The invariants of the concrete stress tensor are:

$$I_{c2} = 3\left(-\tau_{xy}\tau_{xz} - \tau_{xy}\tau_{yz} + \tau_{xz}\tau_{yz}\right)$$
$$I_{c1} = 2\left(-\tau_{xy} + \tau_{xz} + \tau_{yz}\right) \tag{A.4}$$

Conditions $I_{c2} > 0$ and $I_{c1} < 0$ are simultaneously met for the following sign combinations: sgn(τ)= (+,-,-), (-,-,-), (+,+,-), or (+,-,+).

- When $\tau_{xy} > 0$, and τ_{xz}, $\tau_{yz} < 0$, i.e., when sgn(τ) = (+,-,-) as indicated in Figure 146b, all shear stress components increase the tensile stresses in the reinforcement. The results of the 3rd trihedron can be obtained with the expressions of the 1st trihedron if we adopt positive values for all shear components.
- When sgn(τ)= (-,-,-), (+,+,-), or (+,-,+), the stress with the smallest absolute value τ_1 alleviates the tensile stresses in the corresponding reinforcement. Condition (3.24)a must be satisfied to guarantee that ($\sigma_{c1} = 0$, $\sigma_{c2} < 0$, $\sigma_{c3} < 0$). The results of the 3rd trihedron can be obtained with the expressions of the 1st trihedron if we adopt a negative value for τ_1, and positive values for τ_2, τ_3.

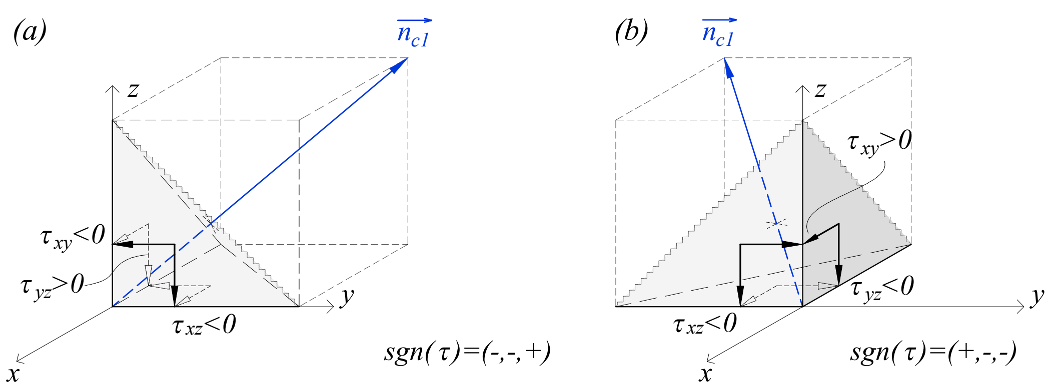

Source: Chen, Nogueira Bittencourt, and Della Bella (2023a).

Figure 146 – Trihedrons defined for crack directions on the (a) second and (b) third octants.

For a crack direction on the ***fourth octant***, (ℓ_1,m_1,n_1) = (0.577, -0.577, 0.577). The reinforcement equivalent stresses, from Equation (3.9), are:

$$\begin{cases} f_{tx} = \sigma_x - \tau_{xy} + \tau_{xz} \\ f_{ty} = \sigma_y - \tau_{xy} - \tau_{yz} \\ f_{tz} = \sigma_z + \tau_{xz} - \tau_{yz} \end{cases} \tag{A.5}$$

The invariants of the concrete stress tensor are:

$$\begin{aligned} I_{c2} &= 3\left(\tau_{xy}\tau_{yz} - \tau_{xy}\tau_{xz} - \tau_{xz}\tau_{yz}\right) \\ I_{c1} &= 2\left(\tau_{xy} - \tau_{xz} + \tau_{yz}\right) \end{aligned} \tag{A.6}$$

Conditions $I_{c2} > 0$ and $I_{c1} < 0$ are simultaneously met for the following sign combinations: sgn(τ)= (-,+,-), (+,+,-), (-,-,-), or (-,+,+).

- When τ_{xy}, $\tau_{yz} < 0$, and $\tau_{xz} > 0$ (-,+,-) as indicated in Figure 147a, all shear stress components increase the tensile stresses in the reinforcement. The results of the 4th trihedron can be obtained with the expressions of the 1st trihedron if we adopt positive values for all shear components.
- When sgn(τ)= (+,+,-), (-,-,-), or (-,+,+), the stress with the smallest absolute value τ_1 alleviates the tensile stresses in the corresponding reinforcement. Condition (3.24) must be satisfied to guarantee that ($\sigma_{c1} = 0$, $\sigma_{c2} < 0$, $\sigma_{c3} < 0$). The results of the 4th trihedron can be obtained with the expressions of the 1st trihedron if we adopt a negative value for τ_1, and positive values for τ_2, τ_3.

For crack directions in the ***fifth*** to the ***eighth octants***: each inferior trihedron, formed by a crack plane with n = -0.577 defining the crack direction, is opposite by the origin of the coordinate system to a superior trihedron. Both represent the same stress state. The 7th trihedron, for example, is constructed with a crack plane with (ℓ_1, m_1, n_1) = (-0.577, -0.577, -0.577), as shown in Figure 147b. It is opposed by the origin to the 1st trihedron. The expressions for I_{c2}, I_{c1}, f_{tx}, f_{ty} and f_{tz} are the same as those obtained for the design in the 1st trihedron.

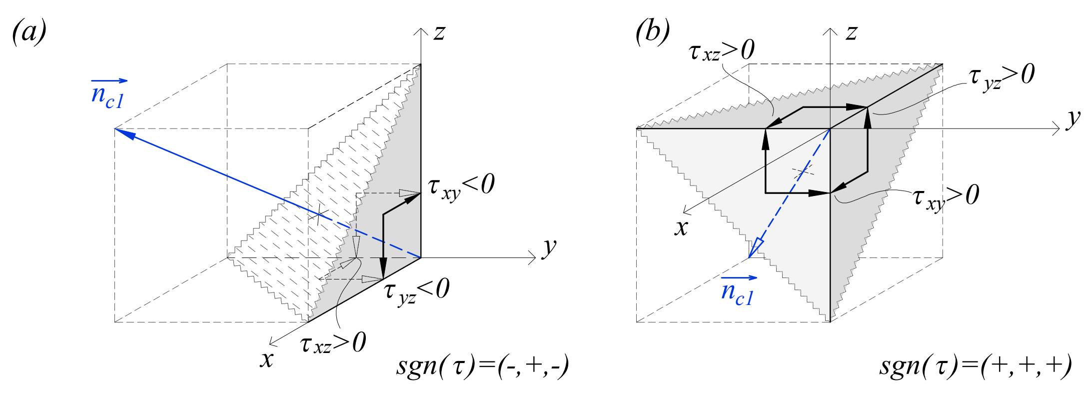

Source: Chen, Nogueira Bittencourt, and Della Bella (2023a).

Figure 147 – Trihedrons defined for crack directions on the (a) fourth and (b) seventh octants.

APPENDIX B - Derivation of the equations for the plane stress state

The equations for designing a membrane element subjected to a plane stress state can be derived from the general formulation presented in equation (3.9). For example, when $\sigma_z = \tau_{xz} = \tau_{yz} = 0$:

$$\begin{cases} f_{tx} = \sigma_x + \tau_{xy} m_1 / \ell_1 & (a) \\ f_{ty} = \sigma_y + \tau_{xy} \ell_1 / m_1 & (b) \\ f_{tz} = 0 & (c) \end{cases} \quad \text{(B.1)}$$

The economical solution is obtained when:

$$\begin{cases} \dfrac{\partial}{\partial \ell_1} \sum f_t = -\tau_{xy} \dfrac{m_1}{\ell_1^2} + \tau_{xy} \dfrac{1}{m_1} = -\tau_{xy} \left(\dfrac{m_1}{\ell_1^2} - \dfrac{1}{m_1} \right) = 0 \\ \dfrac{\partial}{\partial m_1} \sum f_t = \tau_{xy} \dfrac{1}{\ell_1} - \tau_{xy} \dfrac{\ell_1}{m_1^2} = -\tau_{xy} \left(\dfrac{\ell_1}{m_1^2} - \dfrac{1}{\ell_1} \right) = 0 \end{cases}$$

i.e., when $\ell_1 = \pm m_1$. For a crack direction on the ***first octant***, $\ell_1 = m_1 = 1$. Retaking (B.1):

$$\begin{cases} f_{tx} = \sigma_x + \tau_{xy} \\ f_{ty} = \sigma_y + \tau_{xy} \\ f_{tz} = 0 \end{cases} \quad \text{(B.2)}$$

This case is illustrated in Figure 148. The unit vector of the crack plane is $\overrightarrow{n_{c1}} = (1/\sqrt{2}, 1/\sqrt{2}, 0)$. When the calculated reinforcement in the *x*-direction in (B.2) is smaller than zero, i.e., when $\sigma_x < \tau_{xy} .\ m_1/\ell_1$ in Equation (B.1), then f_{tx} is set to zero, and no reinforcement is required in the *x*-direction (see Figure 149).

$$\begin{cases} f_{tx} = \sigma_x + \tau_{xy} m_1 / \ell_1 = 0 & (a) \\ f_{ty} = \sigma_y + \tau_{xy} \ell_1 / m_1 & (b) \\ f_{tz} = 0 & (c) \end{cases} \quad \text{(B.3)}$$

From equation (B.3)a, it is found that the direction of principal stress σ_{c1} is such that:

$$\frac{m_1}{\ell_1} = -\frac{\sigma_x}{\tau_{xy}} \quad \text{(B.4)}$$

which, substituted in (B.1), allows calculating the reinforcement in the *y*-direction:

$$\begin{cases} f_{tx} = 0 \\ f_{ty} = \sigma_y - \dfrac{\tau_{xy}^2}{\sigma_x} \end{cases} \tag{B.5}$$

The last term of f_{ty} is always positive because σ_x is negative. Similarly, the expressions for the x-reinforcement may be found when f_{ty} yields negative in equation (B.1):

$$\begin{cases} f_{tx} = \sigma_x - \dfrac{\tau_{xy}^2}{\sigma_y} \\ f_{ty} = 0 \end{cases} \tag{B.6}$$

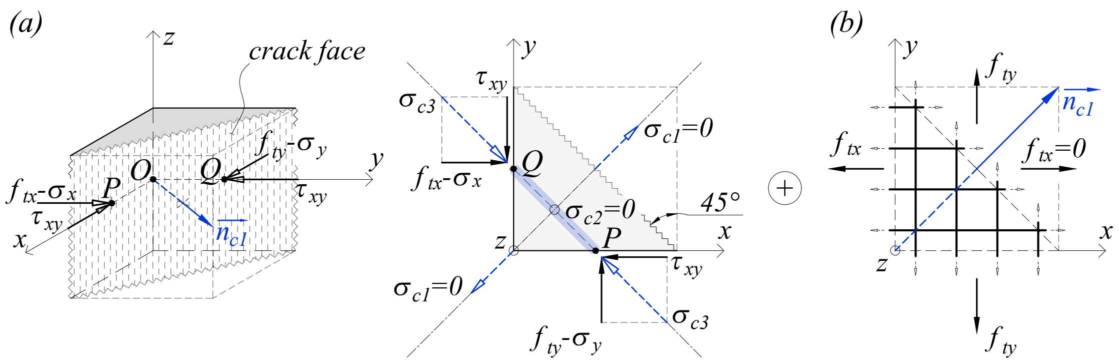

Source: Chen, Nogueira Bittencourt, and Della Bella (2023a).

Figure 148 – Plane stress state: (a) concrete stresses in 3D view and in (b) plane view; (c) equivalent reinforcement stresses.

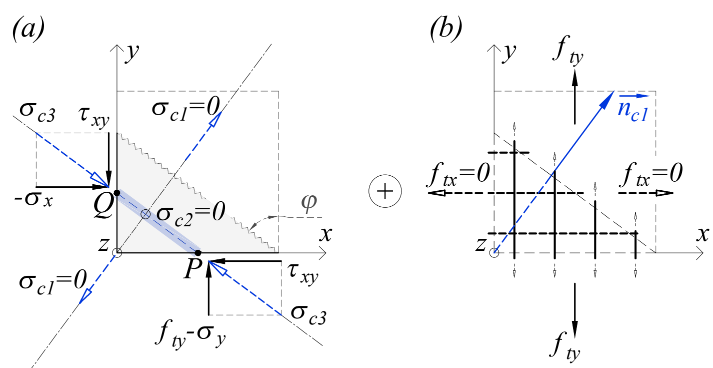

Source: Chen, Nogueira Bittencourt, and Della Bella (2023a).

Figure 149 – Plane stress state and reinforcement required in one direction: (a) concrete and (b) reinforcement stresses.

APPENDIX C - Zero shear stresses and crack directions in the 2nd to the 8th octants

When one shear stress component is zero, concrete is assumed to be subjected to a biaxial compression stress state. However, when two shear stress components are zero, concrete is assumed to be subjected to a uniaxial compression stress state. By comparing the sign of the allowable shear stress components (column 6) with the corresponding reinforcement design equations (col. 7) in Table C1, independently of the crack direction, shear stress components are observed to increase reinforcement stresses. Therefore, reinforcement is designed from equation (3.17) admitting the non-zero shear stresses components with positive values.

Table C1 – Design equations when shear stress components are zero.

(1)	(2)	(3)	(4)	(5)	(6)	(7)
Oct.	**Zero shear stress**	**Invariants**		**sgn(τ) satisfying**		**Reinforcement design equation**
		I_{c2}	I_{c1}	$I_{c2} > 0$	$I_{c2} > 0$ & $I_{c1} < 0$	
2nd	$\tau_{xy} = 0$	$-3\tau_{xz}\tau_{yz}$	$2(\tau_{xz} - \tau_{yz})$	(0, +, -), (0, -, +)	(0, -, +)	$f_{tx} = \sigma_x - \tau_{xy} - \tau_{xz}$ $f_{ty} = \sigma_y - \tau_{xy} + \tau_{yz}$ (A.1) $f_{tz} = \sigma_z - \tau_{xz} + \tau_{yz}$
	$\tau_{xz} = 0$	$-3\tau_{xy}\tau_{yz}$	$2(\tau_{xy} - \tau_{yz})$	(+, 0, -), (-, 0, +)	(-, 0, +)	
	$\tau_{yz} = 0$	$3\tau_{xy}\tau_{xz}$	$2(\tau_{xy} + \tau_{xz})$	(+, +, 0), (-, -, 0)	(-, -, 0)	
3rd	$\tau_{xy} = 0$	$3\tau_{xz}\tau_{yz}$	$-2(-\tau_{xz} - \tau_{yz})$	(0, +, +), (0, -, -)	(0, -, -)	$f_{tx} = \sigma_x + \tau_{xy} - \tau_{xz}$ $f_{ty} = \sigma_y + \tau_{xy} - \tau_{yz}$ (A.3) $f_{tz} = \sigma_z - \tau_{xz} - \tau_{yz}$
	$\tau_{xz} = 0$	$-3\tau_{xy}\tau_{yz}$	$-2(\tau_{xy} - \tau_{yz})$	(+, 0, -), (-, 0, +)	(+, 0, -)	
	$\tau_{yz} = 0$	$-3\tau_{xy}\tau_{xz}$	$-2(\tau_{xy} - \tau_{xz})$	(+, -, 0), (-, +, 0)	(+, -,0)	
4th	$\tau_{xy} = 0$	$-3\tau_{xz}\tau_{yz}$	$-2(\tau_{xz} - \tau_{yz})$	(0, +, -), (0, -, +)	(0, +, -)	$f_{tx} = \sigma_x - \tau_{xy} + \tau_{xz}$ $f_{ty} = \sigma_y - \tau_{xy} - \tau_{yz}$ (A.5) $f_{tz} = \sigma_z + \tau_{xz} - \tau_{yz}$
	$\tau_{xz} = 0$	$3\tau_{xy}\tau_{yz}$	$-2(-\tau_{xy} - \tau_{yz})$	(+, 0, +), (-, 0, -)	(-, 0, -)	
	$\tau_{yz} = 0$	$-3\tau_{xy}\tau_{xz}$	$-2(-\tau_{xy} + \tau_{xz})$	(-, +, 0), (+, -, 0)	(-, +,0)	
2nd	$\tau_{xy} = \tau_{xz} = 0$	0	$-2\tau_{yz}$	-	(0, 0,+)	$f_{tx} = \sigma_x - \tau_{xy} - \tau_{xz}$ $f_{ty} = \sigma_y - \tau_{xy} + \tau_{yz}$ (A.1) $f_{tz} = \sigma_z - \tau_{xz} + \tau_{yz}$
	$\tau_{xz} = \tau_{yz} = 0$	0	$2\tau_{xy}$	-	(–, 0, 0)	
	$\tau_{xy} = \tau_{yz} = 0$	0	$2\tau_{xz}$	-	(0, –, 0)	
3rd	$\tau_{xy} = \tau_{xz} = 0$	0	$2\tau_{yz}$	-	(0, 0, –)	$f_{tx} = \sigma_x + \tau_{xy} - \tau_{xz}$ $f_{ty} = \sigma_y + \tau_{xy} - \tau_{yz}$ (A.3) $f_{tz} = \sigma_z - \tau_{xz} - \tau_{yz}$
	$\tau_{xz} = \tau_{yz} = 0$	0	$-2\tau_{xy}$	-	(+,0, 0)	
	$\tau_{xy} = \tau_{yz} = 0$	0	$2\tau_{xz}$	-	(0, –, 0)	
4th	$\tau_{xy} = \tau_{xz} = 0$	0	$2\tau_{yz}$	-	(0, 0, –)	$f_{tx} = \sigma_x - \tau_{xy} + \tau_{xz}$ $f_{ty} = \sigma_y - \tau_{xy} - \tau_{yz}$ (A.5) $f_{tz} = \sigma_z + \tau_{xz} - \tau_{yz}$
	$\tau_{xz} = \tau_{yz} = 0$	0	$2\tau_{xy}$	-	(–, 0, 0)	
	$\tau_{xy} = \tau_{yz} = 0$	0	$-2\tau_{xz}$	-	(0,+, 0)	

Note: a trihedron with crack direction in the 5th to the 8th octant yields the same design equations as those defined for a trihedron opposed by the origin.